Mechanisms of Lysosome Biogenesis and Regulation

by

Weichao Zhang

A dissertation submitted in partial fulfillment
of the requirements for the degree of
Doctor of Philosophy
(Molecular, Cellular, and Developmental Biology)
in The University of Michigan
2022

Doctoral Committee:

Assistant Professor Ming Li, Chair
Assistant Professor Jacob Kitzman
Professor Daniel Klionsky
Professor Yanzhuang Wang
Professor Haoxing Xu

Weichao Zhang

zhangwc@umich.edu

ORCID ID: 0000-0002-0835-890X

Dedication

This dissertation is dedicated to the 67-year-old lysosome and scientists who devoted their careers to studying such an amazing organelle.

Acknowledgements

I want to thank my Ph.D. advisor Dr. Ming Li for his guidance and support for my research. I am grateful for the opportunity to take risks and challenges in his lab. Along the way, I have honed my skills to work independently and collaboratively. It is also my great pleasure to work with members of the Ming Li Lab, including Dr. Xi Yang, Felichi (Peach) Mae Arines, Varsha Venkatarangan, Liang Chen, and many undergraduate students who assist and support our work.

I would like to thank my dissertation committee members, Dr. Jacob Kitzman, Dr. Daniel Klionsky, Dr. Haoxing Xu, and Dr. Yanzhuang Wang for their invaluable suggestions and support. I also want to thank Dr. Mara Duncan who previously served on my committee for the past four years.

I want to give my special thanks to Dr. Yanzhuang Wang and his lab members. Dr. Wang is extremely generous in supporting our mammalian studies. Most of my initial study was performed in Wang Lab. Dr. Xiaoyan Zhang and Dr. Leibin Wang trained me on mammalian cell culture techniques. Dr. Jianchao Zhang and Dr. Sarah Bui are wonderful collaborators to work with. Without their help, this dissertation would not be possible.

Lastly, I would like to thank my amazing wife, my parents, parents-in-law, my relatives, my friends, and most importantly, my lovely daughter Mirica named after "*miracle*".

Preface

Chapter 1 summarizes lysosome function, lysosome-related diseases, and mechanisms of lysosome regulation. Zhang., W wrote and organized this chapter. Zhang., B generated figures in this Chapter.

Chapter 2 is reprinted from Yang, X*., Zhang, W.*, Wen, X., Bulinski, P. J., Chomchai, D. A., Arines, F. M., Liu, Y. Y., Sprenger, S., Teis, D., Klionsky, D. J., & Li, M. (2020). **TORC1 regulates vacuole membrane composition through ubiquitin- and ESCRT-dependent microautophagy**. *The Journal of cell biology*, *219*(3), e201902127. https://doi.org/10.1083/jcb.201902127. (* These authors contributed equally to this paper).

Chapter 3 is reprinted from Zhang, W., Yang, X., Chen, L., Liu, Y. Y., Venkatarangan, V., Reist, L., Hanson, P., Xu, H., Wang, Y., & Li, M. (2021). **A conserved ubiquitin- and ESCRT-dependent pathway internalizes human lysosomal membrane proteins for degradation.** *PLoS biology*, *19*(7), e3001361. https://doi.org/10.1371/journal.pbio.3001361

Chapter 4 describes our recent discovery of a novel protein factor essential for lysosome biogenesis. Zhang., W. wrote the majority of this Chapter. Yang., X, Lin., Y, Bui., S, Zhang., J, and Chen., L contributed to the Materials & Methods in this chapter. Li., M edited this chapter. This manuscript is in preparation.

Table of Contents

List of Tables

List of Figures

Abstract

Lysosomes are the central catabolic organelles that contain acidic hydrolases to break down macromolecules. On the membrane surface, lysosomal transporters and channels shuttle nutrients and metabolites across the membrane to maintain cellular homeostasis. Pathogenic mutations of these lysosomal proteins lead to inherited disorders called lysosomal storage diseases. In addition, lysosomes serve as signaling hubs that sense nutrient availability and environmental cues to control cellular activities, including protein synthesis, cell growth & differentiation, and autophagy. Thus, dysregulation of lysosomal function is frequently associated with neurodegeneration diseases and cancers.

Despite the significance of lysosomal proteins in maintaining lysosome integrity and cellular hemostasis, the mechanisms of their regulation and turnover are largely unknown. Previously, my research mentor Dr. Ming Li showed that transporters on the yeast vacuole (functionally equivalent to human lysosome) were selectively downregulated in response to a specific substrate level. These pioneering discoveries laid the foundation to understand how cells regulate their lysosomal membrane proteins (LMPs) in response to environmental cues.

For this dissertation, we sought to explore the mechanisms of lysosome regulation in both yeast and human cells. In Chapter 2, we asked how cells regulate lysosome proteome in response to environmental stresses, such as starvation or TORC1 inactivation. In yeast, we showed that TORC1 inactivation leads to upregulation of vacuole biogenesis and autophagy pathways; however, it also triggers the downregulation of many vacuolar membrane proteins to support

vacuole remodeling. We further demonstrated that the degradation of these vacuolar membrane proteins is mediated by the ubiquitin- and ESCRT-dependent microautophagy process.

As our yeast studies consistently demonstrated the importance of the ubiquitination process and ESCRT machinery in regulating LMPs, we wondered if such mechanisms are evolutionarily conserved in human cells. In Chapter 3, we performed a cycloheximide chase screen and identified two short-living lysosomal membrane proteins, RNF152 and LAPTM4A. We showed that the degradation of RNF152 is triggered by its autoubiquitination and the LAPTM4A is ubiquitinated by NEDD4. Furthermore, the ESCRT-machinery is required to internalize the ubiquitinated RNF152 and LAPTM4A into the lysosome lumen.

In Chapter 4, we conducted a CRISPR-Cas9 screen to identify uncharacterized genes involved in the degradation of LMPs and lysosome function. Our screen revealed a novel factor, TMEM251, required for lysosome function. Ablation of TMEM251 leads to defective mannose-6-phosphate (M6P) formation of lysosomal enzymes, a critical process for targeting acidic hydrolases to lysosomes. Our study further indicated that TMEM251 is necessary for the processing and activation of the GlcNAc-1-phosphotransferase, which catalyzes the first-step reaction of M6P formation.

In this dissertation, we present novel mechanisms of lysosome biogenesis and regulation. We discovered a conserved ubiquitin- and ESCRT-dependent pathway to turnover LMPs in yeast and human cells. Our studies on LMP regulation provide a better understanding of lysosomal protein quality control and how lysosomes adapt to environmental changes. In addition, our discovery of TMEM251 sheds light on understanding the mechanisms of lysosome biogenesis.

Chapter 1: Introduction to Lysosome Function and Regulation

Lysosomes are single membrane-bound organelles that digest and recycle cellular materials. Lysosomes contain ~70 different hydrolases that are active in an acidic environment (Saftig & Puertollano, 2021). The lysosomal pH (4.5-5) is maintained by the multi-subunit v-ATPase complexes that pump protons into the lysosomal lumen at the expense of ATP. Other than the v-ATPase complexes, previous studies have identified hundreds of lysosomal membrane proteins (LMPs) (Bagshaw et al., 2005; Schröder et al., 2007; Wyant et al., 2018). Among them, there are more than 60 lysosomal transporters and channels that transport nutrients and metabolites across the lysosomal membrane (Chapel et al., 2013; Bissa et al., 2016).

1.1 Lysosome biogenesis

Lysosomal luminal hydrolases and LMPs are essential for maintaining lysosome function and integrity. Multiple cellular pathways ensure the proper targeting and delivery of lysosomal enzymes and LMPs. This section gives a summary of cellular pathways involved in lysosome biogenesis.

1.1.1 Trafficking of lysosomal enzymes

Lysosome luminal hydrolases contain signal peptide sequences which allow their synthesis and translocation into the ER. The ER-Golgi transport of lysosome hydrolases is mediated by COP-II vesicles. A recent study from Macro Sardiello's group suggested that CLN8, an ER-resident protein, served as a receptor for lysosome hydrolases to facilitate their ER exit (di Ronza et al., 2018). At the cis-Golgi, the N-acetylglucosamine-1 phosphotransferase

(GlcNAc-1 phosphotransferase) catalyzes the addition of GlcNAc-1 phosphate onto a mannose group of lysosome enzymes (Qian et al., 2010). GlcNAc-1-phosphotransferase (GNPT) is a $\alpha_2\beta_2\gamma_2$ hexamer (Bao et al., 1996). The *GNPTAB* gene encodes the α/β precursor and the *GNPTG* gene encodes the soluble γ subunit (Raas-Rothschild et al., 2000; Kudo et al., 2005; Tiede et al., 2005). The complex assembles at the ER and is transported to the Golgi via COP-II vesicles (Franke et al., 2013). At the cis-Golgi, GNPT α/β precursor is cleaved and activated by MBTPS1 (membrane bound transcription factor peptidase, site 1) (Marschner et al., 2011).

At the trans-Golgi network (TGN), the uncovering enzyme (UCE) removes the GlcNAc group, exposing the mannose-6-phosphate (M6P) (Rohrer & Kornfeld, 2001). Two types of M6P receptors, including cation-dependent (46kDa)- and cation-independent (300kDa) M6P receptors (CD-MPR and CI-MPR) bind to M6P tags of lysosomal hydrolases and deliver them to the endosomal trafficking pathway (Kang et al., 2010; Coutinho et al., 2012).

Most lysosome hydrolases reach lysosomes via M6P receptor-dependent pathways (Fig. 1). Both CD-MPR and CI-MPR contain the "acidic-cluster-dileucine" motifs (DXXLL, where X is any amino acid) that recruit GGA proteins (clathrin adaptors) and the AP-1 adaptor complex (Chen et al., 1993; Johnson & Kornfeld, 1992). These adaptor complexes mediate the formation of clathrin-coated vesicles, facilitating their endosomal trafficking. At the endosomes, lysosomal enzymes dissociate from M6P receptors due to a relatively low pH. Lysosomal enzymes reach lysosomes via the endosomal trafficking pathway and the M6P receptors are recycled back to the TGN by the retromer complex (Arighi et al., 2004). Previous cell culture studies suggested that ~5-20% of lysosomal hydrolases may escape from the M6P receptor recognition and become secreted (Braulke & Bonifacino, 2009). At the plasma membrane, a small fraction of CI-MPR

can bind to those secreted lysosomal enzymes and re-direct them to lysosomes via endocytosis (see section 1.2) (Lin et al., 2004).

A small number of luminal hydrolases can also reach lysosomes through M6P receptor-independent pathways (Dittmer et al., 1999). For example, β-glucocerebrosidase (βGC), a lysosome enzyme does not contain the M6P modification, whose lysosomal targeting is mediated by a lysosomal localized protein, LIMP-2 (Reczek et al., 2007). In addition, lysosome acid phosphatase is synthesized as a transmembrane protein. This precursor protein is first targeted to the plasma membrane and further endocytosed to reach lysosomes, where its luminal domain is cleaved and activated (Peters et al., 1990).

1.1.2 Trafficking of LMPs

LMPs contain cytosolic sorting signals that facilitate their trafficking. There are two well-characterized signal motifs: dileucine-based motif (DXXLL) and tyrosine-based motif (YXXØ, where Ø is a bulky hydrophobic residue). The adaptor complexes AP-1 and AP-3 can bind to both DXXLL and YXXØ motifs of LMPs and deliver them to lysosomes via the endosomal trafficking pathway and the AP-3 pathway, respectively (Braulke & Bonifacino, 2009). Some LMPs, (ex: LIMP-2, LAMP2) can take both pathways to lysosomes (Laulagnier et al., 2011), and others displayed more specificity. For example, the trafficking of PQLC2, a lysosomal cationic amino acid exporter, is mainly mediated by the AP-3 dependent pathway (Llinares et al., 2015). Alternatively, some LMPs can be targeted to the cell surface first and further delivered to the lysosome via endocytosis. In this case, the endocytosis adaptor complex AP-2 is required for the LMP targeting (Rappoport et al., 2005). A recent study from Juan Bonifacino's group demonstrated that LAMP1 (Lysosome-associated membrane protein 1) could transport to

lysosomes via this indirect pathway (Chen et al., 2017). Thus far, how LMPs decide which trafficking pathway to take is still not fully understood.

1.2 Cellular pathways that deliver cargoes to the lysosome for degradation

1.2.1 Endocytosis

Many cellular pathways, such as endocytosis, phagocytosis, and autophagy, deliver cargoes to lysosomes for degradation (Fig. 2). Endocytosis is often triggered by the binding of extracellular ligands to specific receptors at the plasma membrane. The invagination of the receptors is mediated by either the clathrin-dependent or clathrin-independent pathways (Mayor et al., 2014). The endocytosed vesicles then fuse to early endosomes. If endosomal cargoes are decorated by the degradation signals (i.e., ubiquitination), the ESCRT (endosomal sorting complexes required for transport) machinery internalizes these ubiquitinated cargoes to generate multivesicular bodies (MVBs), also known as late endosomes (Vietri et al., 2020). The late endosomes further fuse with lysosomes, targeting the intraluminal vesicles for degradation.

Endocytosis contributes to signal transduction from growth factors, hormones, and cytokines to regulate cell growth, differentiation, and motility (Sorkin & Waters, 1993; Morcavallo et al., 2014; Cendrowski et al., 2016). Further, it allows the uptake of extracellular nutrients such as LDL particles (Brown & Goldstein, 1979). At endo-lysosomal compartments, the lysosomal acid lipase type A (LIPA) hydrolyzes the cholesteryl esters and triglycerides, releasing free cholesterol and fatty acids from LDL particles (Dubland & Francis, 2015). The lysosomal cholesterol transporter NPC1 (Niemann-Pick Type C 1), accompanied by NPC2, exports cholesterol out of lysosomes (Subramanian & Balch, 2008). Recently, many studies performed genome-wide screens (RNAi & CRISPR-Cas9 KO) to identify uncharacterized regulators for lipids/cholesterol pathways, and their results consistently emphasized the

importance of endo-lysosomal compartments in regulating cellular lipid/cholesterol homeostasis (Chu et al., 2015; Trinh et al., 2020; van den Boomen et al., 2020; Lu et al., 2022).

Endocytosis also regulates plasma membrane protein composition in response to environmental cues. Such examples are established in yeast. Mup1, a methionine transporter, one of the most well-characterized cargoes, undergoes endocytosis when excess methionine is present outside of cells (Lin et al., 2008; Guiney et al., 2016; Lee et al., 2019). A similar substrate-dependent regulatory mechanism is also observed for other transporters at the plasma membrane, including Can1 (arginine), Fur4 (uracil), and Lyp1 (lysine) (Lin et al., 2008). More interestingly, a recent study from David Teis's group demonstrated that amino acids and nitrogen starvation triggered a broad downregulation of amino acid transporters and glucose transporters at the plasma membrane (Ivashov et al., 2020). This study provides further insights on how cells regulate plasma membrane protein composition in response to cellular stress; however, it remains puzzling if such a regulatory mechanism is conserved in higher organisms.

1.2.2 Phagocytosis

Phagocytosis eliminates large (>0.5μm) extracellular particles, such as bacteria, fungi, foreign substances, and apoptotic bodies (Uribe-Querol & Rosales, 2020). Similar to endocytosis, phagocytosis is also triggered by ligand-receptor interactions at the cell surface. To ingest microorganisms, phagocytic receptors such as CD14, dectin1/2, and CD33, recognize specific surface molecules of microbes such as lipopolysaccharide (LPS) or β-glucans (Saijo & Iwakura, 2011; Zanoni & Granucci, 2013; Zhao, 2019). Alternatively, opsonic receptors, such as Fc receptors and complement receptors, recognize molecules (antibodies or complement components) that decorate the particles for phagocytosis (Uribe-Querol & Rosales, 2020). Phagocytosis is mediated by actin-polymerization and exocytosis near the plasma membrane

(Masters et al., 2013; Jaumouillé & Waterman, 2020). As phagosome matures inside the cells, the engulfed particles are delivered to lysosomes for degradation (Abe & Kuwahara, 2021). In higher organisms, a group of specialized cells are dedicated for phagocytosis with high efficiency. Such cell types include macrophages, dendritic cells, osteoclasts, etc. These specialized cells are commonly involved in removing pathogens, maintaining tissue homeostasis, and presenting antigens to initiate an adaptive immune response (Lim et al., 2017).

1.2.3 Autophagy

Autophagy is a conserved cellular pathway that delivers intracellular cargoes to lysosomes for degradation. It is classified into three types: macroautophagy, chaperone-mediated autophagy, and microautophagy.

Macroautophagy is characterized by the formation of double-membrane bound structures (autophagosomes) to engulf cellular materials, including damaged organelles, protein aggregation, and pathogens (Feng et al., 2014; Yin et al., 2016). Macroautophagy can be induced by cellular stress such as nutrient starvation, growth factor deprivation, and invasion of pathogens. Autophagy could be selective against damaged/excessive organelles, e.g., mitochondria (mitophagy) and ribosomes (ribophagy), and pathogenic particles (Xenophagy) (Ding et al., 2012; Wyant et al., 2018; Sharma et al., 2018). Upon activation, autophagic cargoes are ubiquitinated and recognized by autophagy receptors p62 which further deliver cargoes to form autophagosomes (Shaid et al., 2013; Chen et al., 2019). Then, the autophagosome fuse to the lysosome forming an autolysosome, so that the engulfed cargoes are targeted to degradation.

Chaperone-mediated autophagy (CMA) involves the Hsc70 chaperone that recognizes the KFERQ canonical motif of cytosolic proteins (Kirchner et al., 2019). Under cellular stress, such as nutrient starvation, oxidative stress, DNA damage, etc., Hsc70 delivers substrates to the

lysosome surface and interacts with the lysosome-associated membrane protein type 2A (LAMP-2A) (Kaushik and Cuervo, 2018). The substrates are then unfolded and translocated into lysosomes by LAMP-2A complexes for degradation (Massey et al., 2006).

Microautophagy refers to a process by which endo-lysosomes directly engulf and digest small volumes of cytosolic substrates. The mechanisms of microautophagy are least understood (Li et al., 2012). In yeast cells, microautophagy invaginates diverse cellular organelles including ER (Schäfer et al., 2020), peroxisomes (Sakai et al., 1998), lipid droplets (van Zutphen et al., 2014), and part of the nucleus (Krick et al., 2008). Notably, my research mentor, Dr. Ming Li's pioneer studies highlighted the importance of microautophagy in regulating the vacuolar membrane protein composition (Li et al., 2015a; Li et al., 2015b, Zhu et al., 2017). This will be further discussed in the later sections and Chapters 2 & 3. In mammalian cells, microautophagy is only reported to recycle cytosolic proteins, lipid droplets, and ER-derived vesicles (Mejlvang et al., 2018; Loi et al., 2019; Schulze et al., 2020). Recently, converging evidence suggested the importance of the ESCRT machinery and Hsc70 chaperones in regulating some of the microautophagy processes mentioned above (Mejlvang et al., 2018; Loi et al., 2019; Schäfer et al., 2020). However, it remains elusive what other mechanisms may contribute to these diverse processes. More importantly, given the size difference between yeast vacuole (~2-4 μm in diameter) and human lysosomes (0.2-0.3 μm in diameter), one can imagine that they may have different capacities for microautophagy. It is unclear if those mechanisms of microautophagy are fully conserved in yeast and human cells.

1.3 The lysosome serves as a signaling hub

The mechanistic target of rapamycin complex 1 (MTORC1) is an evolutionarily conserved kinase regulator of diverse cellular pathways. When active, MTORC1 is recruited to

the lysosomal surface to activate anabolic pathways such as protein and lipid synthesis, energy metabolism, and cell growth, while inhibiting catabolic processes such as autophagy (Saxton & Sabatini, 2018). For example, MTORC1 phosphorylates 4E-BP1, a translation repressor, which in turn activates elF4E (eukaryotic translation initiation factor 4E) to initiate protein synthesis (Choo et al., 2008). MTORC1 also promotes the phosphorylation of S6 Kinase 1 (S6K1) which further activates S6 Ribosome protein to increase translation efficiency (Holz et al., 2005). On the other hand, MTORC1 inhibits macroautophagy by directly phosphating ULK1 (Unc-51-like kinase 1, ATG1 in yeast) and ATG13 (Jung et al., 2010). Further, active MTORC1 promotes the nuclear export of TFEB (transcription factor EB) via phosphorylation on S142 and S211 residues (Napolitano et al., 2018). As TFEB is the master transcription factor that controls lysosome biogenesis and autophagy, inactivation of TFEB by MTORC1 inhibits these cellular catabolic pathways (Martina et al., 2012).

MTORC1 receives inputs from two distinct GTPase complexes, Rag GTPases and Rheb (Fig. 3). Rag GTPases are heterodimeric complexes that respond to cellular amino acid availability. When active, RagA/B binds to GTP and RagC/D is in GDP-bound form. This recruits MTORC1 to the lysosome (Sancak et al., 2010). Under amino acid starvation, Rag GTPases swap their nucleotide state, so the MTORC1 remains inactive in the cytosol (Kim & Kim, 2016). The Rheb GTPase regulates MTORC1 in response to hormones and growth factors. Under the growth condition, Rheb allosterically binds to MTORC1 and promotes its kinase activity (Heard et al., 2014). Therefore, MTORC1 activation requires signals from both nutrients and growth factors.

The nucleotide state of Rag GTPases is further regulated by three GAP (GTPase-activating protein) complexes: the GATOR1/2, the FLCN (folliculin) complex, and leucyl-tRNA

synthetase 1 (LRS). Under starvation, GATOR1 promotes GTP hydrolysis of RagA/B, resulting in MTORC1 inactivation. Ablation of GATOR1 components constitutively activates MTORC1 in the cell (Bar-Peled et al., 2013). Additionally, GATOR1 is inhibited by the GATOR2 complex. On the other hand, the FLCN complex promotes the GTP hydrolysis of Rag C/D (Tsun et al., 2013). Although the detailed mechanism is not fully understood, the FLCN complex is essential for MTORC1 activation by promoting its recruitment to the lysosomal surface (Lawrence et al., 2019). Further, LRS1, an intracellular leucine sensor, also serves as a GAP for RagD. The presence of leucine promotes the interaction of LRS with Rag D; therefore, activates MTORC1 (Han et al., 2012).

Besides LRS, many amino acid sensors contribute to the MTORC1 signaling through the GATOR1/2-Rag GTPases pathway. Such sensors include Sestrins1/2 (SESN1/2, leucine sensors), CASTORs (cytosolic arginine sensor for MTORC1), and SAMTOR (S-adenosylmethionine sensor upstream of MTORC1). During leucine starvation, SESN2 binds to and inhibits GATOR2, therefore, inactivates MTORC1. Under the leucine-rich condition, SESN2 dissociates from GATOR2, resulting in MTORC1 activation (Kim et al., 2015). It is worth noting that similar mechanisms are also established for CASTORs and SAMTOR to regulate MTORC1 activities in response to cytosolic arginine and methionine level, respectively (Chantranupong et al., 2016; Gu et al., 2017). Importantly, lysosomal membrane proteins also contribute to MTORC1 signaling in response to amino acid levels. SLC38A9 (sodium-coupled neutral amino acid transport 9) promotes MTORC1 activation through interaction with the RagA/B-Regulator complex (Rebsamen et al., 2015). Recent studies further characterized that SLC38A9 senses intraluminal arginine level and promotes leucine export to the cytosol, thereby activating MTORC1 (Wyant et al. 2017).

The TSC1/2 (Tuberous sclerosis 1 and 2) complex serves as a GAP for Rheb GTPase activities. Dysfunction of the TSC complex also leads to constitutive activation of MTORC1. TSC1/2 integrates signals from growth factor signaling through PI3K-ATK and Ras/Raf/Mek/Erk pathways. Akt and ERK1/2 phosphorylate TSCs, thereby inhibiting its GAP activity towards Rheb (Vires & Howe, 2007). In contrast, the TSC complex also responds to DNA damage and low energy level through the AMPK signaling pathway. AMPK phosphorylates TSC2, promoting its GAP activity to inhibit MTORC1 (van Veelen et al., 2011).

Recently, evidence has emerged that lysosomal E3 ligases also play critical roles in modulating MTORC1 signaling at different stages. Under amino acid starvation, the lysosomal localized E3 ligase RNF152 and the Skp2-SCF E3 ligase ubiquitinate RagA, and recruit GATOR1 to the lysosome surface, thereby inactivating MTORC1 (Deng et al., 2015; Jin et al., 2015). Chen and colleagues further indicated that the CUL3-KLHL22 E3 ubiquitin ligase activated MTORC1 by promoting ubiquitination and degradation of DEPDC5 (a subunit of GATOR1) when amino acids are present (Chen et al., 2018). Recently, two independent studies identified another lysosomal E3 ligase, RNF167, which regulates the stability of amino acid sensors, Sestrin2 (Wang et al. 2022) and CASTOR1 (Li et al., 2021), in response to nutrients level. Although further studies are still required to understand how E3 ligase responds to amino acid levels, it is undoubted that ubiquitination by E3 ligases is an essential regulatory mechanism for MTORC1 signaling.

1.4 Lysosome-associated diseases

Lysosomes are essential for maintaining nutrient homeostasis and regulating cell signaling. Malfunction of lysosomal proteins leads to inherited disorders called lysosomal

storage diseases (LSDs). In addition, growing evidence shows that lysosomal dysfunction is associated with neurodegeneration diseases and cancers.

1.4.1 Lysosomal storage diseases

LSDs are metabolic disorders characterized by the accumulation of toxic materials/wastes in lysosomes. There are more than 70 different LSDs that have been identified and they are often caused by mutations in a single lysosome-related gene (Platt et al., 2018). These genes could encode lysosome hydrolases, lysosomal membrane proteins/transporters, or essential factors for lysosome biogenesis. LSDs are also frequently associated with the early onset of neurodegeneration (Onyenwoke et al., 2016).

Defects in a lysosomal enzyme cause accumulation of a specific type of undigested substrates. For example, Fabry disease, one of the most common LSDs, is caused by mutations in α-galactosidase A (GLA), which breaks down complex glycolipid globotriaosylceramide (Gb3) (Masson et al., 2004). GLA deficiency leads to Gb3 build-up in cells, resulting in severe organ dysfunction in the cardiovascular and renal systems (Schiffmann et al., 2017). Similarly, mutations in lysosomal acid β-galactosidase (GLB) cause accumulation of glycosphingolipids (ex: Gangliosides) in lysosomes of neurons, leading to GM1 gangliosidosis (Brunetti-Pierri & Scaglia, 2008). Patients with GM1 gangliosidosis suffer psychomotor retardation, loss of vision, and defects in skeletal development (Rha et al., 2021).

As LMPs are critical for transporting lysosomal cargoes and maintaining lysosome function and integrity, mutations in LMPs also lead to diverse LSDs. For example, mutations in CTNS (cystinosin), a lysosomal cystine transport, causes cystinosis, which is characterized by the accumulation of cystine in the lysosome. The excessive cystine can form crystals in the lysosomes, resulting in lysosome dysfunction (Cherqui et al., 2002). Further, lysosome pathways

also regulate cellular lipid homeostasis. The lysosomal cholesterol transporter NPC1 (Niemann-Pick Type C 1) exports cholesterol out of lysosomes. Mutations in NPC1 cause accumulation of cholesterol and lipids in lysosomes, resulting in progressive neurological dysfunction including ataxia, dysphagia, and dementia (Vanier. 2010).

Lysosomal enzymes are synthesized at the ER and transported to lysosomes through endosomal trafficking pathways. Defects in transporting or sorting of lysosomal hydrolases also lead to severe LSDs. CLN8, whose mutation leads to neuronal ceroid lipofuscinosis 8, is recently characterized as a lysosomal enzyme receptor that mediates ER-Golgi trafficking of lysosomal hydrolases (di Ronza et al., 2018). Another well-known example is the GlcNAc-1-phosphotransferase (GNPT), which catalyzes the formation of M6P modifications on lysosomal enzymes. Mutations in genes encoding GNPT (*GNPTAB* and *GNPTG*) lead to Mucolipidosis type II and III (Raza et al., 2016).

1.4.2 Neurodegeneration diseases

Besides LSDs, lysosomal dysfunction is commonly associated with age-related neurodegeneration diseases, such as Alzheimer's disease and Parkinson's disease (Nixon & Cataldo, 2006; Cook et al., 2012). Alzheimer's disease is characterized by the accumulation of amyloid plaques and neurofibrillary tangles (tau) in the brain. Previous studies characterized several lysosome-related risk factors for Alzheimer's disease. For example, presenilin 1 (PSEN1), the catalytic subunit of γ-secretase complex, mediates the cleavage of amyloid precursor protein, releasing the Amyloid-beta (Aβ) peptides (Kelleher et al., 2017). However, further investigations suggested that pathogenic mutations of PSEN1 impair the stability of the lysosomal v-ATPase complexes, thereby, disrupting lysosome acidification (Lee et al., 2015). Importantly, lysosomal targeting therapy has become a promising strategy to treat Alzheimer's

diseases. Recent studies indicated that upregulation of lysosomal pathways, such as autophagy, through TFEB activation promotes the degradation of pathogenic aggregates by lysosomes and improves memory in Alzheimer's mice (Song et al., 2020).

Parkinson's disease, the second most prevalent nondegenerative disorder, is characterized by the accumulation and aggregation of α-Syn (synuclein) known as Lewy bodies (Wakabayashi et al., 2007). α-Syn can be targeted to lysosomal degradation through macroautophagy or CMA (Lopes et al., 2015). Lysosome dysfunction is commonly associated with the formation of insoluble α-Syn aggregates in the cells. Clinically, mutations in GBA, ATP13A2, and LRRK2 are the most well-known risk factors for Parkinson's disease (Navarro-Romero et al., 2020). *GBA* encodes the lysosomal acid β-glucosidase that breaks down glucosylceramide into glucose and ceramide (Riboldi et al., 2019). ATP13A2 is a lysosomal polyamine exporter and divalent cation transporter (Park et al., 2015). Although the function of LRRK2 is still not fully understood, several studies consistently suggested that LRRK2 kinase phosphorylates several Rab family GTPases and serves as a key regulator of endosomal trafficking and autophagy (Steger et al., 2016; Nguyen et al., 2020). Taken together, all of these risk factors suggested a strong correlation between lysosomal dysfunction and the early onset of Parkinson's disease.

1.4.3 Cancers

The relationship between lysosome function and cancer is rather complicated. First, MTORC1 integrates cellular signals to control cell proliferation. Multiple MTORC1 regulators mentioned previously are closely associated with cancer development and progression. GATOR1 and TSC1/2 complexes are tumor suppressors, whose inactivation mutations promote cancer proliferation. Similarly, a recent study indicated that the degradation of CASTOR1, the intracellular arginine senor, enhanced the progression of breast cancer cells (Li et al., 2021).

On the other hand, enhanced lysosome pathways promote cancer metastasis (Fehrenbacher & Jäättelä, 2005; Piao & Amaravadi, 2016). Increased lysosomal exocytosis releases lysosome hydrolases into the extracellular space, leading to the degradation of the extracellular matrix (Tang et al., 2020). This process is further promoted by activating the lysosomal Ca^{2+}-releasing channel mucolipin 1 (TRPML1), and/or TFEB in cancer cells (Kundu et al., 2018). Moreover, recent clinical studies suggested that high expression of lysosomal cathepsins is associated with tumor progression and metastasis and poor survival rate (Leusink et al., 2018; Fujimoto et al., 2021).

1.5 Lysosome regulation and quality control

Given the physiological and clinical significance of lysosomes, we aim to understand how cells regulate lysosomes to maintain their proper function. Recent studies have focused on three aspects of lysosome regulations: transcriptional regulation, lysosomal membrane protein degradation, and lysosome repair and turnover at the organelle level.

1.5.1 Transcriptional regulation and lysosome biogenesis

The transcriptional regulation of lysosome biogenesis was first implicated in yeast. Transcription factors, such as Gat1 and Gln3, activate the transcription of NCR (nitrogen catabolic repression)-sensitive genes. Vacuolar proteases such as Pep4 and Cps1 are direct targets of Gat1 and Gln3 (Scherens et al., 2006). Under optimal nitrogen conditions, Yeast Tor1 phosphorylates Gat1 and Gln3, preventing them from entering the nucleus (Beck et al., 1999; Crespo et al., 2002; Puria et al., 2008). Recently, Daniel Klionsky's group suggested that Gat1 and Gln3 served as transcriptional activators for macroautophagy (Bernard et al., 2015). Similarly, a TORC1-Rim15-Ume6 kinase cascade was also implicated in regulating macroautophagy (Bartholomew et al., 2012).

In higher organisms, TFEB and TFE3 are the most well-characterized transcription factors that regulate lysosome biogenesis. Both transcription factors bind to the "GTCACGTGAC" motif (Raben et al., 2016) and promote the gene expression of lysosomal biogenesis and autophagy, known as CLEAR (coordinated lysosomal expression and regulation) network (Sardiello et al., 2009, et al; Palmieri et al., 2011). Similar to those transcription factors described in yeast, TFEB nuclear translocation is also regulated by its phosphorylation status. As previously mentioned, TFEB can be directly phosphorylated by MTORC1 in response to nutrients and growth factor stimulation (Napolitano et al., 2018). Other than MTORC1, the phosphorylation of TFEB/TFE3 is also regulated by kinases such as MAPK1, GSK3β, and AKT, under varieties of cellular signals and environmental conditions (David, 2011; Palmieri et al., 2017; Pan & Valapala, 2022). Furthermore, post-translational modifications, such as acetylation and ubiquitination, also contribute to the TFEB/TFE3-dependent lysosome biogenesis pathways (Sha et al., 2017; Zhang et al., 2018).

1.5.2 Lysosome membrane repair and lysophagy

Previous mammalian studies mainly focused on revealing the lysosomal quality control system at the organelle level. Acute treatment of lysosomotropic reagent LLOMe (L-Leucyl-L-Leucine methyl ester) leads to small ruptures of the lysosomal membrane. Recently, two independent studies suggested that the ESCRT machinery are recruited to the lysosomal surface to seal these small ruptures (Skowyra et al., 2018; Radulovic et al., 2018). Phyllis Hanson's group further demonstrated that the recruitment of ESCRT machinery was Ca^{2+}-dependent. Presumably, the Ca^{2+} binding adaptor PDCD6/ALG-2 recruits PDCD6IP/ALIX (programmed cell death 6 interacting protein) and further recruits ESCRT-III components (Skowyra et al., 2018). However, the source of Ca^{2+} remains elusive. In addition, both groups suggested that

TSG101 (ESCRT-I) and PDCD6IP/ALIX acted in parallel to recruit ESCRT-III (Skowyra et al., 2018; Radulovic et al., 2018). As TSG101 contains a ubiquitin-binding domain, it remains puzzling if polyubiquitination is also a prerequisite for ESCRT-dependent lysosomal membrane repair.

Lysophagy, selective autophagy for lysosomes, is responsible for turning over damaged lysosomes that cannot be repaired by the ESCRT machinery (Maejima et al., 2013; Anding & Baehrecke, 2017). Damaged lysosomes expose the luminal β-galactosides which binds to galectin-3 (Gal3) (Aits et al., 2015). Then, Gal3 recruits ubiquitination machinery, including UBE2QL1 (E2), TRIM16 (E3), and FBOX27-SCF (E3) to ubiquitinate cargoes such as LAMP1 and LAMP2 at their luminal domain (Chauhan et al., 2016; Yoshida et al., 2017; Koerver et al., 2019). These ubiquitinated cargoes are recognized by the autophagy receptor p62 so that the damaged lysosomes are engulfed by autophagosomes and delivered to the intact lysosomes for degradation (Hung et al. 2013; Yoshida et al. 2017).

1.5.3 Lysosome membrane protein degradation

Despite the advance in understanding the mechanisms of lysosomal membrane repair and lysophagy, the regulation for lysosome membrane protein is not well understood. My research mentor Dr. Ming Li established pioneer works to characterize the turnover mechanism for LMPs using yeast as a model organism. He and colleagues identified a few vacuolar E3 ligase systems that down-regulate vacuolar membrane proteins in response to environmental cues. For example, the Rsp5-Ssh4 complex ubiquitinates Ypq1 (a vacuolar lysine transporter) when lysine is depleted from the cytosol, and Ypq1 is internalized and degraded inside the vacuole (Li et al. 2015b). Similarly, a vacuolar Zn^{2+} influx transporter Cot1 is also ubiquitinated by another E3 ligase complex, DSC, and degraded inside the vacuole (Li et al. 2015a, Yang et al. 2018). Importantly,

he and others consistently demonstrated that these vacuole membrane proteins were internalized into the vacuole by the ESCRT-dependent microautophagy (Li et al. 2015a, Li et al. 2015b, Oku et al. 2017, Zhu et al. 2017, Morshed et al. 2020).

1.6 Outlooks

Dr. Ming Li's discoveries provided an initial understanding of how lysosomal membrane transporters are regulated in response to its substrate level in yeast (Li et al., 2015a, Li et al., 2015b). However, many questions remain to be answered. In this dissertation, we aimed to further characterize the lysosomal membrane protein turnover system. Specifically, we asked how cells regulate lysosomal membrane proteome in response to environmental stresses, such as nutrient depletion or nitrogen starvation. Our studies uncovered that E3 ligases on the yeast vacuole, including Rsp5, DSC complex, and Pib1, act in concert to down-regulate vacuolar membrane proteins in response to TORC1 inactivation (Chapter 2, Yang et al. 2020). We further demonstrated that the degradation of these vacuolar membrane proteins is mediated by the ESCRT-dependent microautophagy.

Next, we asked if such mechanisms for lysosomal membrane protein regulation are evolutionarily conserved. In Chapter 3, we identified two short-living mammalian lysosomal membrane proteins RNF152 and LAPTM4A. We further demonstrated that the degradation of both proteins was mediated by a conserved ubiquitin- and ESCRT-dependent mechanism (Zhang et al., 2021).

In Chapter 4, we generated a RNF152-based reporter cell line and conducted a CRISPR-Cas9 screen to identify uncharacterized genes involved in the degradation of LMP and lysosome biogenesis. Our screen revealed a novel factor TMEM251 that regulates M6P modification of lysosomal enzymes by selectively promoting the cleavage and activation of GNPT by MBTPS1.

In summary, this thesis describes novel mechanisms of lysosome biogenesis and regulation. Our studies on LMP regulation provide knowledge to the field of lysosomal protein quality control, a field that has little available information. In addition, the characterization of TMEM251 brings fresh insights into the understanding of the mechanisms of lysosome biogenesis.

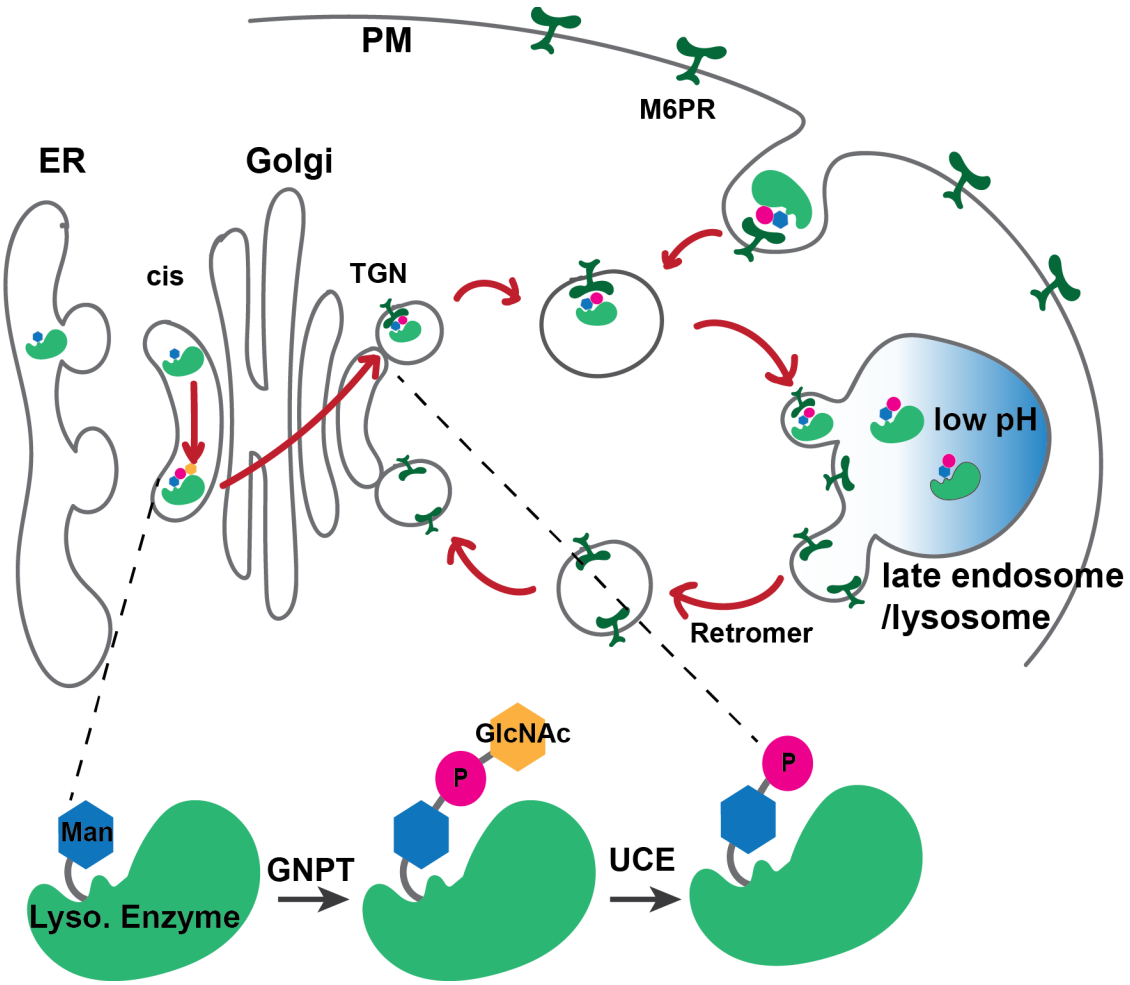

Figure 1.1: M6P sorting of lysosomal luminal enzymes. The GlcNAc-1-phosphotransferase (GNPT) catalyzes the first step reaction of M6P biogenesis of lysosomal enzymes. The uncovering enzyme (UCE) removes the GlcNAc group to expose the M6P. At the TGN, the M6P receptors (M6PRs) capture the M6P of lysosomal enzymes and deliver them to the lysosomes. The M6PR can be recycled to TGN by the retromer. Further, the M6PRs at the plasma membrane redirect extracellular hydrolases to the endosomal trafficking pathways.

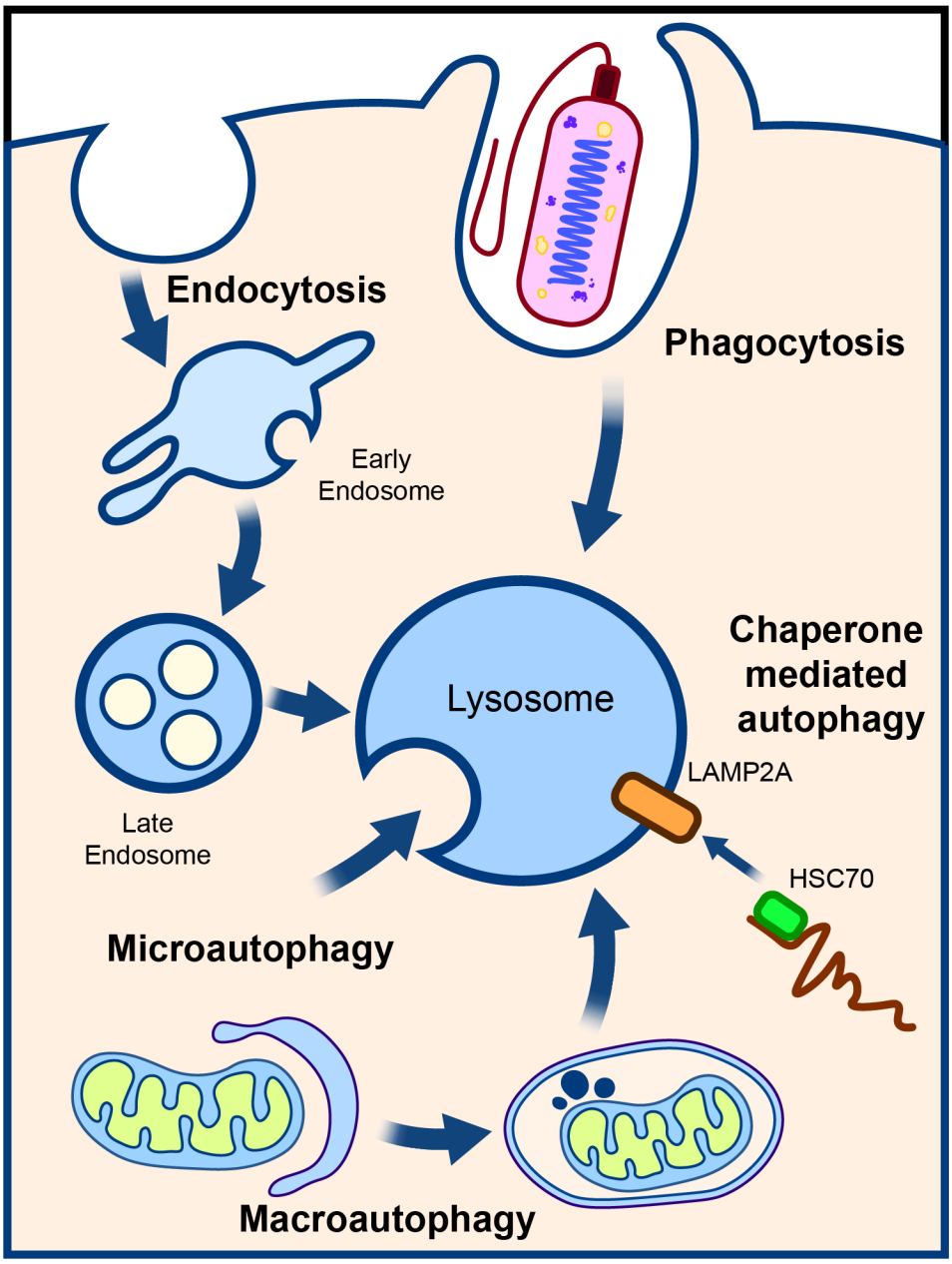

Figure 1.2: Cellular pathways that deliver cargoes to the lysosome. Endocytosis, phagocytosis, and autophagy (macroautophagy, microautophagy, and CMA) deliver substrates to lysosomes for degradation.

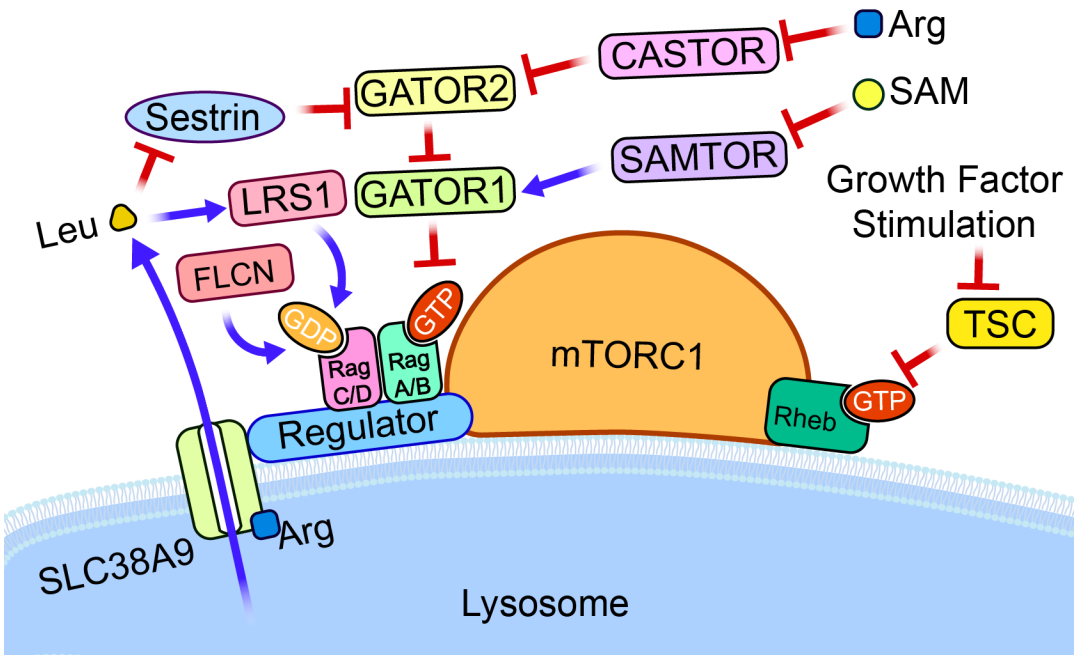

Figure 1.3: MTORC1 regulation in response to amino acid and growth factor stimulations. MTORC1 receives input from Rag GTPase and Rheb, which sense amino acids and growth factors, respectively. This figure illustrates upstream signaling that regulates Rag GTPase and Rheb.

1.7 References:

Abe T, Kuwahara T. Targeting of Lysosomal Pathway Genes for Parkinson's Disease Modification: Insights From Cellular and Animal Models. *Front Neurol*. 2021;12:681369. Published 2021 Jun 14. doi:10.3389/fneur.2021.681369

Aits S, Kricker J, Liu B, et al. Sensitive detection of lysosomal membrane permeabilization by lysosomal galectin puncta assay. *Autophagy*. 2015;11(8):1408-1424. doi:10.1080/15548627.2015.1063871

Arighi CN, Hartnell LM, Aguilar RC, Haft CR, Bonifacino JS. Role of the mammalian retromer in sorting of the cation-independent mannose 6-phosphate receptor. *J Cell Biol*. 2004;165(1):123-133. doi:10.1083/jcb.200312055

Bagshaw RD, Mahuran DJ, Callahan JW. A proteomic analysis of lysosomal integral membrane proteins reveals the diverse composition of the organelle. *Mol Cell Proteomics*. 2005;4(2):133-143. doi:10.1074/mcp.M400128-MCP200

Bao M, Booth JL, Elmendorf BJ, Canfield WM. Bovine UDP-N-acetylglucosamine:lysosomal-enzyme N-acetylglucosamine-1-phosphotransferase. I. Purification and subunit structure. *J Biol Chem*. 1996;271(49):31437-31445. doi:10.1074/jbc.271.49.31437

Bar-Peled L, Chantranupong L, Cherniack AD, et al. A Tumor suppressor complex with GAP activity for the Rag GTPases that signal amino acid sufficiency to mTORC1. *Science*. 2013;340(6136):1100-1106. doi:10.1126/science.1232044

Bartholomew CR, Suzuki T, Du Z, et al. Ume6 transcription factor is part of a signaling cascade that regulates autophagy. *Proc Natl Acad Sci U S A*. 2012;109(28):11206-11210. doi:10.1073/pnas.1200313109

Beck T, Hall MN. The TOR signalling pathway controls nuclear localization of nutrient-regulated transcription factors. *Nature*. 1999;402(6762):689-692. doi:10.1038/45287

Bernard A, Jin M, Xu Z, Klionsky DJ. A large-scale analysis of autophagy-related gene expression identifies new regulators of autophagy. *Autophagy*. 2015;11(11):2114-2122. doi:10.1080/15548627.2015.1099796

Bissa B, Beedle AM, Govindarajan R. Lysosomal solute carrier transporters gain momentum in research. *Clin Pharmacol Ther*. 2016;100(5):431-436. doi:10.1002/cpt.450

Braulke T, Bonifacino JS. Sorting of lysosomal proteins. *Biochim Biophys Acta*. 2009;1793(4):605-614. doi:10.1016/j.bbamcr.2008.10.016

Brown MS, Goldstein JL. Receptor-mediated endocytosis: insights from the lipoprotein receptor system. *Proc Natl Acad Sci U S A*. 1979;76(7):3330-3337. doi:10.1073/pnas.76.7.3330

Brunetti-Pierri N, Scaglia F. GM1 gangliosidosis: review of clinical, molecular, and therapeutic aspects. *Mol Genet Metab*. 2008;94(4):391-396. doi:10.1016/j.ymgme.2008.04.012

Cendrowski J, Mamińska A, Miaczynska M. Endocytic regulation of cytokine receptor signaling. *Cytokine Growth Factor Rev*. 2016;32:63-73. doi:10.1016/j.cytogfr.2016.07.002

Chantranupong L, Scaria SM, Saxton RA, et al. The CASTOR Proteins Are Arginine Sensors for the mTORC1 Pathway. *Cell*. 2016;165(1):153-164. doi:10.1016/j.cell.2016.02.035

Chapel A, Kieffer-Jaquinod S, Sagné C, et al. An extended proteome map of the lysosomal membrane reveals novel potential transporters. *Mol Cell Proteomics*. 2013;12(6):1572-1588. doi:10.1074/mcp.M112.021980

Chauhan S, Kumar S, Jain A, et al. TRIMs and Galectins Globally Cooperate and TRIM16 and Galectin-3 Co-direct Autophagy in Endomembrane Damage Homeostasis. *Dev Cell*. 2016;39(1):13-27. doi:10.1016/j.devcel.2016.08.003

Chen HJ, Remmler J, Delaney JC, Messner DJ, Lobel P. Mutational analysis of the cation-independent mannose 6-phosphate/insulin-like growth factor II receptor. A consensus casein kinase II site followed by 2 leucines near the carboxyl terminus is important for intracellular targeting of lysosomal enzymes [published correction appears in J Biol Chem 1994 Jun 10;269(23):16518]. *J Biol Chem*. 1993;268(30):22338-22346.

Chen J, Ou Y, Yang Y, et al. KLHL22 activates amino-acid-dependent mTORC1 signalling to promote tumorigenesis and ageing. *Nature*. 2018;557(7706):585-589. doi:10.1038/s41586-018-0128-9

Chen RH, Chen YH, Huang TY. Ubiquitin-mediated regulation of autophagy. *J Biomed Sci*. 2019;26(1):80. Published 2019 Oct 21. doi:10.1186/s12929-019-0569-y

Chen Y, Gershlick DC, Park SY, Bonifacino JS. Segregation in the Golgi complex precedes export of endolysosomal proteins in distinct transport carriers. *J Cell Biol*. 2017;216(12):4141-4151. doi:10.1083/jcb.201707172

Cherqui S, Sevin C, Hamard G, et al. Intralysosomal cystine accumulation in mice lacking cystinosin, the protein defective in cystinosis. *Mol Cell Biol*. 2002;22(21):7622-7632. doi:10.1128/MCB.22.21.7622-7632.2002

Choo AY, Yoon SO, Kim SG, Roux PP, Blenis J. Rapamycin differentially inhibits S6Ks and 4E-BP1 to mediate cell-type-specific repression of mRNA translation. *Proc Natl Acad Sci U S A*. 2008;105(45):17414-17419. doi:10.1073/pnas.0809136105

Chu BB, Liao YC, Qi W, et al. Cholesterol transport through lysosome-peroxisome membrane contacts [published correction appears in Cell. 2021 Jan 7;184(1):289]. *Cell*. 2015;161(2):291-306. doi:10.1016/j.cell.2015.02.019

Cook C, Stetler C, Petrucelli L. Disruption of protein quality control in Parkinson's disease. *Cold Spring Harb Perspect Med*. 2012;2(5):a009423. doi:10.1101/cshperspect.a009423

Coutinho MF, Prata MJ, Alves S. Mannose-6-phosphate pathway: a review on its role in lysosomal function and dysfunction. *Mol Genet Metab*. 2012b;105(4):542-550. doi:10.1016/j.ymgme.2011.12.012

de Vries PJ, Howe CJ. The tuberous sclerosis complex proteins--a GRIPP on cognition and neurodevelopment. *Trends Mol Med*. 2007;13(8):319-326. doi:10.1016/j.molmed.2007.06.003

di Ronza A, Bajaj L, Sharma J, et al. CLN8 is an endoplasmic reticulum cargo receptor that regulates lysosome biogenesis. *Nat Cell Biol*. 2018;20(12):1370-1377. doi:10.1038/s41556-018-0228-7

Ding WX, Yin XM. Mitophagy: mechanisms, pathophysiological roles, and analysis. *Biol Chem*. 2012;393(7):547-564. doi:10.1515/hsz-2012-0119

Dittmer F, Ulbrich EJ, Hafner A, et al. Alternative mechanisms for trafficking of lysosomal enzymes in mannose 6-phosphate receptor-deficient mice are cell type-specific. *J Cell Sci*. 1999;112 (Pt 10):1591-1597. doi:10.1242/jcs.112.10.1591

Dubland JA, Francis GA. Lysosomal acid lipase: at the crossroads of normal and atherogenic cholesterol metabolism. *Front Cell Dev Biol*. 2015;3:3. Published 2015 Feb 2. doi:10.3389/fcell.2015.00003

Fehrenbacher N, Jäättelä M. Lysosomes as targets for cancer therapy. *Cancer Res*. 2005;65(8):2993-2995. doi:10.1158/0008-5472.CAN-05-0476

Feng Y, He D, Yao Z, Klionsky DJ. The machinery of macroautophagy. *Cell Res*. 2014;24(1):24-41. doi:10.1038/cr.2013.168

Franke M, Braulke T, Storch S. Transport of the GlcNAc-1-phosphotransferase α/β-subunit precursor protein to the Golgi apparatus requires a combinatorial sorting motif. *J Biol Chem*. 2013;288(2):1238-1249. doi:10.1074/jbc.M112.407676

Fujimoto T, Tsunedomi R, Matsukuma S, et al. Cathepsin B is highly expressed in pancreatic cancer stem-like cells and is associated with patients' surgical outcomes. *Oncol Lett*. 2021;21(1):30. doi:10.3892/ol.2020.12291

Gu X, Orozco JM, Saxton RA, et al. SAMTOR is an *S*-adenosylmethionine sensor for the mTORC1 pathway. *Science*. 2017;358(6364):813-818. doi:10.1126/science.aao3265

Guiney EL, Klecker T, Emr SD. Identification of the endocytic sorting signal recognized by the Art1-Rsp5 ubiquitin ligase complex. *Mol Biol Cell*. 2016;27(25):4043-4054. doi:10.1091/mbc.E16-08-0570

Han JM, Jeong SJ, Park MC, et al. Leucyl-tRNA synthetase is an intracellular leucine sensor for the mTORC1-signaling pathway. *Cell*. 2012;149(2):410-424. doi:10.1016/j.cell.2012.02.044

Heard JJ, Fong V, Bathaie SZ, Tamanoi F. Recent progress in the study of the Rheb family GTPases. *Cell Signal*. 2014;26(9):1950-1957. doi:10.1016/j.cellsig.2014.05.011

Holz MK, Ballif BA, Gygi SP, Blenis J. mTOR and S6K1 mediate assembly of the translation preinitiation complex through dynamic protein interchange and ordered phosphorylation events. *Cell*. 2005;123(4):569-580. doi:10.1016/j.cell.2005.10.024

Ivashov V, Zimmer J, Schwabl S, et al. Complementary α-arrestin-ubiquitin ligase complexes control nutrient transporter endocytosis in response to amino acids. *Elife*. 2020;9:e58246. Published 2020 Aug 3. doi:10.7554/eLife.58246

Jaumouillé V, Waterman CM. Physical Constraints and Forces Involved in Phagocytosis. *Front Immunol*. 2020;11:1097. Published 2020 Jun 12. doi:10.3389/fimmu.2020.01097

Jin G, Lee SW, Zhang X, et al. Skp2-Mediated RagA Ubiquitination Elicits a Negative Feedback to Prevent Amino-Acid-Dependent mTORC1 Hyperactivation by Recruiting GATOR1. *Mol Cell*. 2015;58(6):989-1000. doi:10.1016/j.molcel.2015.05.010

Johnson KF, Kornfeld S. A His-Leu-Leu sequence near the carboxyl terminus of the cytoplasmic domain of the cation-dependent mannose 6-phosphate receptor is necessary for the lysosomal enzyme sorting function. *J Biol Chem*. 1992;267(24):17110-17115.

Jung CH, Ro SH, Cao J, Otto NM, Kim DH. mTOR regulation of autophagy. *FEBS Lett*. 2010;584(7):1287-1295. doi:10.1016/j.febslet.2010.01.017

Kim J, Kim E. Rag GTPase in amino acid signaling. *Amino Acids*. 2016;48(4):915-928. doi:10.1007/s00726-016-2171-x

Kim JS, Ro SH, Kim M, et al. Sestrin2 inhibits mTORC1 through modulation of GATOR complexes [published correction appears in Sci Rep. 2015;5:14029]. *Sci Rep*. 2015;5:9502. Published 2015 Mar 30. doi:10.1038/srep09502

Laulagnier K, Schieber NL, Maritzen T, Haucke V, Parton RG, Gruenberg J. Role of AP1 and Gadkin in the traffic of secretory endo-lysosomes. *Mol Biol Cell*. 2011;22(12):2068-2082. doi:10.1091/mbc.E11-03-0193

Kang C, Riazuddin S, Mundorff J, et al. Mutations in the lysosomal enzyme-targeting pathway and persistent stuttering. *N Engl J Med*. 2010;362(8):677-685. doi:10.1056/NEJMoa0902630

Kaushik S, Cuervo AM. The coming of age of chaperone-mediated autophagy. *Nat Rev Mol Cell Biol*. 2018;19(6):365-381. doi:10.1038/s41580-018-0001-6

Kelleher RJ 3rd, Shen J. Presenilin-1 mutations and Alzheimer's disease. *Proc Natl Acad Sci U S A*. 2017;114(4):629-631. doi:10.1073/pnas.1619574114

Krick R, Muehe Y, Prick T, et al. Piecemeal microautophagy of the nucleus requires the core macroautophagy genes. *Mol Biol Cell*. 2008;19(10):4492-4505. doi:10.1091/mbc.e08-04-0363

Kudo M, Bao M, D'Souza A, et al. The alpha- and beta-subunits of the human UDP-N-acetylglucosamine:lysosomal enzyme N-acetylglucosamine-1-phosphotransferase [corrected] are encoded by a single cDNA [published correction appears in J Biol Chem. 2005 Dec 23;280(51):42476]. *J Biol Chem*. 2005;280(43):36141-36149. doi:10.1074/jbc.M509008200

Kundu ST, Grzeskowiak CL, Fradette JJ, et al. TMEM106B drives lung cancer metastasis by inducing TFEB-dependent lysosome synthesis and secretion of cathepsins. *Nat Commun*. 2018;9(1):2731. Published 2018 Jul 16. doi:10.1038/s41467-018-05013-x

Lawrence RE, Fromm SA, Fu Y, et al. Structural mechanism of a Rag GTPase activation checkpoint by the lysosomal folliculin complex. *Science*. 2019;366(6468):971-977. doi:10.1126/science.aax0364

Lee JH, McBrayer MK, Wolfe DM, et al. Presenilin 1 Maintains Lysosomal Ca(2+) Homeostasis via TRPML1 by Regulating vATPase-Mediated Lysosome Acidification. *Cell Rep*. 2015;12(9):1430-1444. doi:10.1016/j.celrep.2015.07.050

Lee S, Ho HC, Tumolo JM, Hsu PC, MacGurn JA. Methionine triggers Ppz-mediated dephosphorylation of Art1 to promote cargo-specific endocytosis. *J Cell Biol*. 2019;218(3):977-992. doi:10.1083/jcb.201712144

Leusink FK, Koudounarakis E, Frank MH, Koole R, van Diest PJ, Willems SM. Cathepsin K associates with lymph node metastasis and poor prognosis in oral squamous cell carcinoma. *BMC Cancer*. 2018;18(1):385. Published 2018 Apr 5. doi:10.1186/s12885-018-4315-8

Li M, Koshi T, Emr SD. Membrane-anchored ubiquitin ligase complex is required for the turnover of lysosomal membrane proteins. *J Cell Biol*. 2015;211(3):639-652. doi:10.1083/jcb.201505062

Li M, Rong Y, Chuang YS, Peng D, Emr SD. Ubiquitin-dependent lysosomal membrane protein sorting and degradation. *Mol Cell*. 2015;57(3):467-478. doi:10.1016/j.molcel.2014.12.012

Li T, Wang X, Ju E, et al. RNF167 activates mTORC1 and promotes tumorigenesis by targeting CASTOR1 for ubiquitination and degradation. *Nat Commun*. 2021;12(1):1055. Published 2021 Feb 16. doi:10.1038/s41467-021-21206-3

Li WW, Li J, Bao JK. Microautophagy: lesser-known self-eating. *Cell Mol Life Sci*. 2012;69(7):1125-1136. doi:10.1007/s00018-011-0865-5

Lim JJ, Grinstein S, Roth Z. Diversity and Versatility of Phagocytosis: Roles in Innate Immunity, Tissue Remodeling, and Homeostasis. *Front Cell Infect Microbiol*. 2017;7:191. Published 2017 May 23. doi:10.3389/fcimb.2017.00191

Lin CH, MacGurn JA, Chu T, Stefan CJ, Emr SD. Arrestin-related ubiquitin-ligase adaptors regulate endocytosis and protein turnover at the cell surface. *Cell*. 2008;135(4):714-725. doi:10.1016/j.cell.2008.09.025

Lin SX, Mallet WG, Huang AY, Maxfield FR. Endocytosed cation-independent mannose 6-phosphate receptor traffics via the endocytic recycling compartment en route to the trans-Golgi network and a subpopulation of late endosomes. *Mol Biol Cell*. 2004;15(2):721-733. doi:10.1091/mbc.e03-07-0497

Llinares E, Barry AO, André B. The AP-3 adaptor complex mediates sorting of yeast and mammalian PQ-loop-family basic amino acid transporters to the vacuolar/lysosomal membrane. *Sci Rep*. 2015;5:16665. Published 2015 Nov 18. doi:10.1038/srep16665

Loi M, Raimondi A, Morone D, Molinari M. ESCRT-III-driven piecemeal micro-ER-phagy remodels the ER during recovery from ER stress. *Nat Commun*. 2019;10(1):5058. Published 2019 Nov 7. doi:10.1038/s41467-019-12991-z

Lopes da Fonseca T, Villar-Piqué A, Outeiro TF. The Interplay between Alpha-Synuclein Clearance and Spreading. *Biomolecules*. 2015;5(2):435-471. Published 2015 Apr 14. doi:10.3390/biom5020435

Lu A, Hsieh F, Sharma BR, Vaughn SR, Enrich C, Pfeffer SR. CRISPR screens for lipid regulators reveal a role for ER-bound SNX13 in lysosomal cholesterol export. *J Cell Biol*. 2022;221(2):e202105060. doi:10.1083/jcb.202105060

Maejima I, Takahashi A, Omori H, et al. Autophagy sequesters damaged lysosomes to control lysosomal biogenesis and kidney injury. *EMBO J*. 2013;32(17):2336-2347. doi:10.1038/emboj.2013.171

Marschner K, Kollmann K, Schweizer M, Braulke T, Pohl S. A key enzyme in the biogenesis of lysosomes is a protease that regulates cholesterol metabolism. *Science*. 2011;333(6038):87-90. doi:10.1126/science.1205677

Martina JA, Chen Y, Gucek M, Puertollano R. MTORC1 functions as a transcriptional regulator of autophagy by preventing nuclear transport of TFEB. *Autophagy*. 2012;8(6):903-914. doi:10.4161/auto.19653

Massey AC, Kaushik S, Sovak G, Kiffin R, Cuervo AM. Consequences of the selective blockage of chaperone-mediated autophagy. *Proc Natl Acad Sci U S A*. 2006;103(15):5805-5810. doi:10.1073/pnas.0507436103

Masson C, Cissé I, Simon V, Insalaco P, Audran M. Fabry disease: a review. *Joint Bone Spine*. 2004;71(5):381-383. doi:10.1016/j.jbspin.2003.10.015

Masters TA, Pontes B, Viasnoff V, Li Y, Gauthier NC. Plasma membrane tension orchestrates membrane trafficking, cytoskeletal remodeling, and biochemical signaling during phagocytosis. *Proc Natl Acad Sci U S A*. 2013;110(29):11875-11880. doi:10.1073/pnas.1301766110

Mayle KM, Le AM, Kamei DT. The intracellular trafficking pathway of transferrin. *Biochim Biophys Acta*. 2012;1820(3):264-281. doi:10.1016/j.bbagen.2011.09.009

Mayor S, Parton RG, Donaldson JG. Clathrin-independent pathways of endocytosis. *Cold Spring Harb Perspect Biol*. 2014;6(6):a016758. Published 2014 Jun 2. doi:10.1101/cshperspect.a016758

Mejlvang J, Olsvik H, Svenning S, et al. Starvation induces rapid degradation of selective autophagy receptors by endosomal microautophagy. *J Cell Biol*. 2018;217(10):3640-3655. doi:10.1083/jcb.201711002

Palmieri M, Impey S, Kang H, et al. Characterization of the CLEAR network reveals an integrated control of cellular clearance pathways. *Hum Mol Genet*. 2011;20(19):3852-3866. doi:10.1093/hmg/ddr306

Palmieri M, Pal R, Nelvagal HR, et al. mTORC1-independent TFEB activation via Akt inhibition promotes cellular clearance in neurodegenerative storage diseases [published correction appears in Nat Commun. 2017 Jun 13;8:15793]. *Nat Commun*. 2017;8:14338. Published 2017 Feb 6. doi:10.1038/ncomms14338

Pan HY, Valapala M. Regulation of Autophagy by the Glycogen Synthase Kinase-3 (GSK-3) Signaling Pathway. *Int J Mol Sci*. 2022;23(3):1709. Published 2022 Feb 1. doi:10.3390/ijms23031709

Morcavallo A, Stefanello M, Iozzo RV, Belfiore A, Morrione A. Ligand-mediated endocytosis and trafficking of the insulin-like growth factor receptor I and insulin receptor modulate receptor function. *Front Endocrinol (Lausanne)*. 2014;5:220. Published 2014 Dec 17. doi:10.3389/fendo.2014.00220

Napolitano G, Esposito A, Choi H, et al. mTOR-dependent phosphorylation controls TFEB nuclear export. *Nat Commun*. 2018;9(1):3312. Published 2018 Aug 17. doi:10.1038/s41467-018-05862-6

Navarro-Romero A, Montpeyó M, Martinez-Vicente M. The Emerging Role of the Lysosome in Parkinson's Disease. *Cells*. 2020;9(11):2399. Published 2020 Nov 2. doi:10.3390/cells9112399

Nguyen APT, Tsika E, Kelly K, et al. Dopaminergic neurodegeneration induced by Parkinson's disease-linked G2019S LRRK2 is dependent on kinase and GTPase activity. *Proc Natl Acad Sci U S A*. 2020;117(29):17296-17307. doi:10.1073/pnas.1922184117

Nixon RA, Cataldo AM. Lysosomal system pathways: genes to neurodegeneration in Alzheimer's disease. *J Alzheimers Dis*. 2006;9(3 Suppl):277-289. doi:10.3233/jad-2006-9s331

Onyenwoke RU, Brenman JE. Lysosomal Storage Diseases-Regulating Neurodegeneration. *J Exp Neurosci*. 2016;9(Suppl 2):81-91. Published 2016 Apr 5. doi:10.4137/JEN.S25475

Pan HY, Valapala M. Regulation of Autophagy by the Glycogen Synthase Kinase-3 (GSK-3) Signaling Pathway. *Int J Mol Sci*. 2022;23(3):1709. Published 2022 Feb 1. doi:10.3390/ijms23031709

Park JS, Blair NF, Sue CM. The role of ATP13A2 in Parkinson's disease: Clinical phenotypes and molecular mechanisms. *Mov Disord*. 2015;30(6):770-779. doi:10.1002/mds.26243

Peters C, Braun M, Weber B, et al. Targeting of a lysosomal membrane protein: a tyrosine-containing endocytosis signal in the cytoplasmic tail of lysosomal acid phosphatase is necessary and sufficient for targeting to lysosomes. *EMBO J*. 1990;9(11):3497-3506.

Piao S, Amaravadi RK. Targeting the lysosome in cancer. *Ann N Y Acad Sci*. 2016;1371(1):45-54. doi:10.1111/nyas.12953

Platt FM, d'Azzo A, Davidson BL, Neufeld EF, Tifft CJ. Lysosomal storage diseases [published correction appears in Nat Rev Dis Primers. 2018 Oct 18;4(1):36] [published correction appears in Nat Rev Dis Primers. 2019 May 17;5(1):34]. *Nat Rev Dis Primers*. 2018;4(1):27. Published 2018 Oct 1. doi:10.1038/s41572-018-0025-4

Puria R, Zurita-Martinez SA, Cardenas ME. Nuclear translocation of Gln3 in response to nutrient signals requires Golgi-to-endosome trafficking in Saccharomyces cerevisiae. *Proc Natl Acad Sci U S A*. 2008;105(20):7194-7199. doi:10.1073/pnas.0801087105

Qian Y, Lee I, Lee WS, et al. Functions of the alpha, beta, and gamma subunits of UDP-GlcNAc:lysosomal enzyme N-acetylglucosamine-1-phosphotransferase. *J Biol Chem*. 2010;285(5):3360-3370. doi:10.1074/jbc.M109.068650

Raas-Rothschild A, Cormier-Daire V, Bao M, et al. Molecular basis of variant pseudo-hurler polydystrophy (mucolipidosis IIIC). *J Clin Invest*. 2000;105(5):673-681. doi:10.1172/JCI5826

Radulovic M, Schink KO, Wenzel EM, et al. ESCRT-mediated lysosome repair precedes lysophagy and promotes cell survival. *EMBO J*. 2018;37(21):e99753. doi:10.15252/embj.201899753

Rappoport JZ, Benmerah A, Simon SM. Analysis of the AP-2 adaptor complex and cargo during clathrin-mediated endocytosis. *Traffic*. 2005;6(7):539-547. doi:10.1111/j.1600-0854.2005.00280.x

Raza MH, Domingues CE, Webster R, et al. Mucolipidosis types II and III and non-syndromic stuttering are associated with different variants in the same genes. *Eur J Hum Genet*. 2016;24(4):529-534. doi:10.1038/ejhg.2015.154

Raben N, Puertollano R. TFEB and TFE3: Linking Lysosomes to Cellular Adaptation to Stress. *Annu Rev Cell Dev Biol*. 2016;32:255-278. doi:10.1146/annurev-cellbio-111315-125407

Rebsamen M, Pochini L, Stasyk T, et al. SLC38A9 is a component of the lysosomal amino acid sensing machinery that controls mTORC1. *Nature*. 2015;519(7544):477-481. doi:10.1038/nature14107

Reczek D, Schwake M, Schröder J, et al. LIMP-2 is a receptor for lysosomal mannose-6-phosphate-independent targeting of beta-glucocerebrosidase. *Cell*. 2007;131(4):770-783. doi:10.1016/j.cell.2007.10.018

Rha AK, Maguire AS, Martin DR. GM1 Gangliosidosis: Mechanisms and Management. *Appl Clin Genet*. 2021;14:209-233. Published 2021 Apr 9. doi:10.2147/TACG.S206076

Riboldi GM, Di Fonzo AB. *GBA*, Gaucher Disease, and Parkinson's Disease: From Genetic to Clinic to New Therapeutic Approaches. *Cells*. 2019;8(4):364. Published 2019 Apr 19. doi:10.3390/cells8040364

Rohrer J, Kornfeld R. Lysosomal hydrolase mannose 6-phosphate uncovering enzyme resides in the trans-Golgi network. *Mol Biol Cell*. 2001;12(6):1623-1631. doi:10.1091/mbc.12.6.1623

Saijo S, Iwakura Y. Dectin-1 and Dectin-2 in innate immunity against fungi. *Int Immunol*. 2011;23(8):467-472. doi:10.1093/intimm/dxr046

Sakai Y, Koller A, Rangell LK, Keller GA, Subramani S. Peroxisome degradation by microautophagy in Pichia pastoris: identification of specific steps and morphological intermediates. *J Cell Biol*. 1998;141(3):625-636. doi:10.1083/jcb.141.3.625

Sancak Y, Bar-Peled L, Zoncu R, Markhard AL, Nada S, Sabatini DM. Ragulator-Rag complex targets mTORC1 to the lysosomal surface and is necessary for its activation by amino acids. *Cell*. 2010;141(2):290-303. doi:10.1016/j.cell.2010.02.024

Sardiello M, Palmieri M, di Ronza A, et al. A gene network regulating lysosomal biogenesis and function. *Science*. 2009;325(5939):473-477. doi:10.1126/science.1174447

Saxton RA, Sabatini DM. mTOR Signaling in Growth, Metabolism, and Disease [published correction appears in Cell. 2017 Apr 6;169(2):361-371]. *Cell*. 2017;168(6):960-976. doi:10.1016/j.cell.2017.02.004

Schäfer JA, Schessner JP, Bircham PW, et al. ESCRT machinery mediates selective microautophagy of endoplasmic reticulum in yeast. *EMBO J*. 2020;39(2):e102586. doi:10.15252/embj.2019102586

Scherens B, Feller A, Vierendeels F, Messenguy F, Dubois E. Identification of direct and indirect targets of the Gln3 and Gat1 activators by transcriptional profiling in response to nitrogen availability in the short and long term. *FEMS Yeast Res*. 2006;6(5):777-791. doi:10.1111/j.1567-1364.2006.00060.x

Schiffmann R, Hughes DA, Linthorst GE, et al. Screening, diagnosis, and management of patients with Fabry disease: conclusions from a "Kidney Disease: Improving Global Outcomes" (KDIGO) Controversies Conference. *Kidney Int*. 2017;91(2):284-293. doi:10.1016/j.kint.2016.10.004

Schröder B, Wrocklage C, Pan C, et al. Integral and associated lysosomal membrane proteins. *Traffic*. 2007;8(12):1676-1686. doi:10.1111/j.1600-0854.2007.00643.x

Schulze RJ, Krueger EW, Weller SG, et al. Direct lysosome-based autophagy of lipid droplets in hepatocytes. *Proc Natl Acad Sci U S A*. 2020;117(51):32443-32452. doi:10.1073/pnas.2011442117

Sha Y, Rao L, Settembre C, Ballabio A, Eissa NT. STUB1 regulates TFEB-induced autophagy-lysosome pathway. *EMBO J*. 2017;36(17):2544-2552. doi:10.15252/embj.201796699

Shaid S, Brandts CH, Serve H, Dikic I. Ubiquitination and selective autophagy. *Cell Death Differ*. 2013;20(1):21-30. doi:10.1038/cdd.2012.72

Sharma V, Verma S, Seranova E, Sarkar S, Kumar D. Selective Autophagy and Xenophagy in Infection and Disease. *Front Cell Dev Biol*. 2018;6:147. Published 2018 Nov 13. doi:10.3389/fcell.2018.00147

Skowyra ML, Schlesinger PH, Naismith TV, Hanson PI. Triggered recruitment of ESCRT machinery promotes endolysosomal repair. *Science*. 2018;360(6384):eaar5078. doi:10.1126/science.aar5078

Song JX, Malampati S, Zeng Y, et al. A small molecule transcription factor EB activator ameliorates beta-amyloid precursor protein and Tau pathology in Alzheimer's disease models. *Aging Cell*. 2020;19(2):e13069. doi:10.1111/acel.13069

Sorkin A, Waters CM. Endocytosis of growth factor receptors. *Bioessays*. 1993;15(6):375-382. doi:10.1002/bies.950150603

Steger M, Tonelli F, Ito G, et al. Phosphoproteomics reveals that Parkinson's disease kinase LRRK2 regulates a subset of Rab GTPases. *Elife*. 2016;5:e12813. Published 2016 Jan 29. doi:10.7554/eLife.12813

Saftig P, Puertollano R. How Lysosomes Sense, Integrate, and Cope with Stress. Trends Biochem Sci. 2021 Feb;46(2):97-112. doi: 10.1016/j.tibs.2020.09.004. Epub 2020 Oct 1. PMID: 33012625; PMCID: PMC7855039.

Subramanian K, Balch WE. NPC1/NPC2 function as a tag team duo to mobilize cholesterol. *Proc Natl Acad Sci U S A*. 2008;105(40):15223-15224. doi:10.1073/pnas.0808256105

Takahara T, Amemiya Y, Sugiyama R, Maki M, Shibata H. Amino acid-dependent control of mTORC1 signaling: a variety of regulatory modes. *J Biomed Sci*. 2020;27(1):87. Published 2020 Aug 17. doi:10.1186/s12929-020-00679-2

Tang T, Yang ZY, Wang D, et al. The role of lysosomes in cancer development and progression. *Cell Biosci*. 2020;10(1):131. Published 2020 Nov 18. doi:10.1186/s13578-020-00489-x

Tiede S, Storch S, Lübke T, et al. Mucolipidosis II is caused by mutations in GNPTA encoding the alpha/beta GlcNAc-1-phosphotransferase. *Nat Med*. 2005;11(10):1109-1112. doi:10.1038/nm1305

Trinh MN, Brown MS, Goldstein JL, et al. Last step in the path of LDL cholesterol from lysosome to plasma membrane to ER is governed by phosphatidylserine. *Proc Natl Acad Sci U S A*. 2020;117(31):18521-18529. doi:10.1073/pnas.2010682117

Tsun ZY, Bar-Peled L, Chantranupong L, et al. The folliculin tumor suppressor is a GAP for the RagC/D GTPases that signal amino acid levels to mTORC1. *Mol Cell*. 2013;52(4):495-505. doi:10.1016/j.molcel.2013.09.016

Uribe-Querol E, Rosales C. Phagocytosis: Our Current Understanding of a Universal Biological Process. *Front Immunol*. 2020;11:1066. Published 2020 Jun 2. doi:10.3389/fimmu.2020.01066

van den Boomen DJH, Sienkiewicz A, Berlin I, et al. A trimeric Rab7 GEF controls NPC1-dependent lysosomal cholesterol export. *Nat Commun*. 2020;11(1):5559. Published 2020 Nov 3. doi:10.1038/s41467-020-19032-0

van Veelen W, Korsse SE, van de Laar L, Peppelenbosch MP. The long and winding road to rational treatment of cancer associated with LKB1/AMPK/TSC/mTORC1 signaling. *Oncogene*. 2011;30(20):2289-2303. doi:10.1038/onc.2010.630

van Zutphen T, Todde V, de Boer R, et al. Lipid droplet autophagy in the yeast Saccharomyces cerevisiae. *Mol Biol Cell*. 2014;25(2):290-301. doi:10.1091/mbc.E13-08-0448

Vanier MT. Niemann-Pick disease type C. *Orphanet J Rare Dis*. 2010;5:16. Published 2010 Jun 3. doi:10.1186/1750-1172-5-16

Vietri M, Radulovic M, Stenmark H. The many functions of ESCRTs. *Nat Rev Mol Cell Biol*. 2020;21(1):25-42. doi:10.1038/s41580-019-0177-4

Xiao Q, Yan P, Ma X, et al. Neuronal-Targeted TFEB Accelerates Lysosomal Degradation of APP, Reducing Aβ Generation and Amyloid Plaque Pathogenesis. *J Neurosci*. 2015;35(35):12137-12151. doi:10.1523/JNEUROSCI.0705-15.2015

Wakabayashi K, Tanji K, Mori F, Takahashi H. The Lewy body in Parkinson's disease: molecules implicated in the formation and degradation of alpha-synuclein aggregates. *Neuropathology*. 2007;27(5):494-506. doi:10.1111/j.1440-1789.2007.00803.x

Wang D, Xu C, Yang W, et al. E3 ligase RNF167 and deubiquitinase STAMBPL1 modulate mTOR and cancer progression [published online ahead of print, 2022 Jan 25]. *Mol Cell*. 2022;S1097-2765(22)00002-8. doi:10.1016/j.molcel.2022.01.002

Wyant GA, Abu-Remaileh M, Wolfson RL, et al. mTORC1 Activator SLC38A9 Is Required to Efflux Essential Amino Acids from Lysosomes and Use Protein as a Nutrient. *Cell*. 2017;171(3):642-654.e12. doi:10.1016/j.cell.2017.09.046

Wyant GA, Abu-Remaileh M, Frenkel EM, et al. NUFIP1 is a ribosome receptor for starvation-induced ribophagy. *Science*. 2018;360(6390):751-758. doi:10.1126/science.aar2663

Yang X, Zhang W, Wen X, et al. TORC1 regulates vacuole membrane composition through ubiquitin- and ESCRT-dependent microautophagy. *J Cell Biol*. 2020;219(3):e201902127. doi:10.1083/jcb.201902127

Yin Z, Pascual C, Klionsky DJ. Autophagy: machinery and regulation. *Microb Cell*. 2016;3(12):588-596. Published 2016 Dec 1. doi:10.15698/mic2016.12.546

Zanoni I, Granucci F. Role of CD14 in host protection against infections and in metabolism regulation. *Front Cell Infect Microbiol*. 2013;3:32. Published 2013 Jul 24. doi:10.3389/fcimb.2013.00032

Zhang J, Wang J, Zhou Z, et al. Importance of TFEB acetylation in control of its transcriptional activity and lysosomal function in response to histone deacetylase inhibitors. *Autophagy*. 2018;14(6):1043-1059. doi:10.1080/15548627.2018.1447290

Zhang W, Yang X, Chen L, et al. A conserved ubiquitin- and ESCRT-dependent pathway internalizes human lysosomal membrane proteins for degradation. *PLoS Biol*. 2021;19(7):e3001361. Published 2021 Jul 23. doi:10.1371/journal.pbio.3001361

Zhao L. CD33 in Alzheimer's Disease - Biology, Pathogenesis, and Therapeutics: A Mini-Review. *Gerontology*. 2019;65(4):323-331. doi:10.1159/000492596

Zhu L, Jorgensen JR, Li M, Chuang YS, Emr SD. ESCRTs function directly on the lysosome membrane to downregulate ubiquitinated lysosomal membrane proteins. *Elife*. 2017;6:e26403. Published 2017 Jun 29. doi:10.7554/eLife.26403

Chapter 2: TORC1 Regulates Vacuole Membrane Composition through Ubiquitin- and ESCRT-dependent Microautophagy

Cellular adaptation in response to nutrient limitation requires the induction of autophagy and lysosome biogenesis for the efficient recycling of macromolecules. Here, we discovered that starvation and TORC1 inactivation not only lead to the upregulation of autophagy and vacuole proteins involved in recycling, but also result in the downregulation of many vacuole membrane proteins to supply amino acids as part of a vacuole remodeling process. Downregulation of vacuole membrane proteins is initiated by ubiquitination, which is accomplished by the coordination of multiple E3 ubiquitin ligases, including Rsp5, the Dsc complex, and a newly characterized E3 ligase, Pib1. The Dsc complex is negatively regulated by TORC1 through the Rim15-Ume6 signaling cascade. After ubiquitination, vacuole membrane proteins are sorted into the lumen for degradation by ESCRT-dependent microautophagy. Thus, our study uncovered a complex relationship between TORC1 inactivation and vacuole biogenesis.

2.1 Introduction

The lysosome is a central catabolic station that breaks down and recycles cellular materials to maintain nutrient homeostasis (Lim & Zoncu, 2016; Settembre et al., 2013). Emerging evidence suggests that the lysosome is a dynamic organelle, which constantly adjusts its membrane composition according to environmental cues. In yeast, changes in substrate concentration can lead to the degradation of their corresponding vacuole (yeast lysosome) membrane transporters. For example, depleting lysine from the cytoplasm triggers a selective degradation of the vacuolar lysine importer Ypq1 to stop lysine from being transported from the cytoplasm into the vacuole lumen (Li et al., 2015b; Sekito et al., 2014). Similarly, a low cytoplasmic Zn^{2+} level leads to the downregulation of a vacuolar Zn^{2+} importer, Cot1 (Li et al., 2015a).

Our understanding of the underlying mechanisms for vacuole membrane regulation is still incomplete. However, it has been shown that protein ubiquitination serves as a sorting signal to initialize the degradation process. In yeast, two independent vacuole E3 ligases are involved in the substrate-triggered degradation of transporters. Specifically, a cytosolic NEDD4 family E3 ligase, Rsp5, and its vacuole membrane adapter, Ssh4, are responsible for the ubiquitination of Ypq1 (Li et al., 2015b), whereas Dsc, a multi-subunit transmembrane ubiquitin ligase complex, is required for the ubiquitination of Cot1 (Li et al., 2015a; Yang et al., 2018). After ubiquitination, vacuole membrane proteins are delivered into the lumen by the endosomal sorting complexes required for transport (ESCRT) pathway (Li et al., 2015a; Li et al., 2015b; Zhu et al., 2017). With this selective degradation mechanism, the vacuole membrane composition is regulated accurately in response to specific transporting substrates. Besides this fine level adjustment of individual transporters, how do other environmental stresses such as starvation regulate vacuole membrane composition?

Beyond catabolism, the lysosome also plays a major role in cellular stress response. The evolutionarily conserved mechanistic target of rapamycin kinase complex 1 (MTORC1), a lysosome membrane-associated kinase complex, serves as the signaling hub to sense different stresses and regulate cellular metabolism accordingly (Laplante & Sabatini, 2009; Perera & Zoncu, 2016). In mammalian cells, under nutrient-rich conditions, MTORC1 is recruited to the lysosome membrane and activated to phosphorylate the ribosomal RPS6 kinases (RPS6KB1/S6K1, RPS6KB2/S6K2) and ElF4EBP1 (eukaryotic translation initiation factor 4E binding protein 1) to promote protein synthesis, leading to cell growth and proliferation (Holz et al., 2005). In addition, active MTORC1 inhibits the transcription of various stress response genes involved in autophagy, lysosome biogenesis, and endoplasmic reticulum (ER) stress by phosphorylating TFEB (transcription factor EB) and TFE3 (Rehi et al., 1999; Sardiello et al., 2009; Settembre et al., 2011; Settmebre et al., 2012). Similarly, in yeast, active TORC1 directly phosphorylates Sch9, an analog of the mammalian RPS6 kinases, to stimulate protein translation when nutrients are available (Jin et al., 2014; Urban et al., 2007). Meanwhile, TORC1 also inhibits autophagy through Atg13 phosphorylation, thereby inhibiting its ability to activate the Atg1 kinase (Fujioka et al., 2014; Kraft et al., 2012).

Conversely, when TORC1/MTORC1 is inactive under stress conditions, catabolic processes such as proteasome degradation, autophagy, and endocytosis of plasma membrane proteins are elevated. In addition, lysosome biogenesis is upregulated to boost its degradative and recycling function. In mammalian cells, when MTORC1 is inactive, dephosphorylated TFEB translocates into the nucleus to promote the transcription of numerous target genes, including those encoding lysosomal hydrolases, pumps, permeases, and lysosome positioning regulators (Martina et al., 2014; Puertollano et al., 2018; Sardiello et al., 2009; Settembre et al., 2009; Settembre et al.,

2011; Settembre et al., 2012; Willett et al., 2017). In yeast, many vacuolar proteases such as Prb1, Ape1, Cps1, and Pep4 are upregulated to enhance the digestion function during starvation (Müller et al., 2015; Parzych & Klionsky 2018). All these studies point to a direct correlation between MTORC1/TORC1 inactivation and the enhancement of lysosomal/vacuolar biogenesis. However, two recent studies suggested the complexity of their relationship in yeast. Sakai and colleagues observed that glucose depletion leads to the invagination and degradation of two vacuole membrane proteins, Vph1 (a V_0 subunit of the vacuolar ATPase) and Pho8 (vacuolar phosphatase), in an ESCRT-dependent manner (Oku et al., 2017). Similarly, De Virgilio and colleagues observed that rapamycin treatment leads to the ESCRT-dependent degradation of Pho8 (Hatakeyama et al., 2019). These observations indicated that remodeling the vacuole proteome after TORC1 inactivation might be more complex than previously anticipated, and raised several interesting questions: First, is the downregulation of vacuole membrane proteins a general response to TORC1 inactivation? Second, what machinery is involved? And third, how does TORC1 regulate this machinery?

In this study, we report that TORC1 plays a critical role in regulating vacuole membrane composition. In contrast to the simplified model that TORC1 inactivation leads to a global upregulation of vacuole biogenesis, we discovered that TORC1 inactivation also triggers the concomitant downregulation of numerous vacuole membrane proteins. Further analysis revealed that multiple E3 ligase systems, including Rsp5, the Dsc complex, and a third E3 ligase, Pib1, function together on the vacuole membrane to ubiquitinate proteins. Moreover, our results showed that TORC1 can regulate the activity of the vacuole ubiquitin machinery. Specifically, TORC1 regulates the production and assembly of the vacuolar Dsc complex. After ubiquitination, cargoes are sorted into the lumen for degradation in an ESCRT-dependent manner. This study thus extends

our understanding of the complexity of how TORC1 regulates vacuole composition according to environmental cues.

2.2 Results

2.2.1 TORC1 inactivation triggers downregulation of many vacuole membrane proteins

The TORC1 complex is responsible for regulating numerous stress responses according to environmental cues. However, how TORC1 regulates the vacuole protein composition is only partially understood. To answer this question, we set out to understand how vacuole membrane composition responds to environmental stresses such as starvation, and its relationship with TORC1 inactivation. As an initial test, we monitored the levels of five vacuole membrane proteins, including Vba4 (a putative amino acid permease), Fet5 (a subunit of the putative iron transporter complex, which dimerizes with Fth1), Fth1, Vph1, and Zrt3* (a variant of the zinc exporter Zrt3, please see Li et al., 2015a for details), after yeast cells enter the stationary phase. All five vacuole membrane proteins were chromosomally tagged with the green fluorescent protein (GFP), and they properly localized to the vacuole membrane (Fig. S1A) (Li et al., 2015a). We then used a GFP antibody to measure the protein level changes. As shown in Fig. 1A-B, we took four time points (16, 20, 24, and 36 h) in the stationary phase and compared them to mid-log cells (1 h, with OD_{600} ~0.7). All five proteins were significantly downregulated after cells entered the stationary phase. During degradation, free GFP accumulated due to its resistance to vacuolar proteases (Fig. 1A-B and S1A). Longer incubation in the stationary phase led to a higher level of protein degradation and more accumulation of free GFP (Fig. 1A, 16-36 h). In contrast, very little degradation was observed in mid-log cells (Fig. 1A, 1 h). Together, our results suggested that long-term nutrient starvation can trigger the downregulation of many vacuole membrane proteins.

The downregulation of vacuole membrane proteins in response to nutrient starvation is a surprising finding, especially because it has been widely assumed that starvation promotes vacuole biogenesis and autophagy to boost the recycling of intracellular materials (Noda, 2017). Consistently, previous studies have shown that vacuolar hydrolases, components of the autophagic machinery, and the vacuole membrane amino acid exporter Atg22, are indeed upregulated under starvation conditions (Müller et al., 2015; Yang et al., 2006).

To verify those reported observations, we collected antibodies against endogenous vacuolar/autophagic proteins, including Vph1, Pep4, Cps1, and Atg8, and checked their response to natural starvation. Due to the lack of an Atg22 antibody, we chromosomally tagged Atg22 with GFP at its C terminus. As shown in Fig. S1B-C, vacuolar proteases (Pep4 and Cps1) and autophagic machinery (Atg8 and Atg22) were indeed induced by starvation. In contrast, the protein level of untagged Vph1 decreased, which was consistent with the observation made in Fig. 1A where Vph1-GFP was partially degraded. Together, our data indicated that vacuoles undergo extensive remodeling in response to nutrient limitation. Proteins involved in the digestion and recycling functions are upregulated, while many other membrane proteins are downregulated. Interestingly, an accumulation of free GFP was also observed for Atg22-GFP (Fig. S1D), indicating that even a protein directly involved in recycling can still be subjected to degradation after long-term starvation.

To directly test if the downregulation is due to TORC1 inactivation, we treated the mid-log phase cells with rapamycin. In this experiment, we expanded the substrate list to ten GFP-tagged vacuole membrane proteins by adding Cot1, Ypq1, Ypl162c (a putative transporter with unknown function), Ypq2 (a homolog of Ypq1), and Zrc1 (another zinc importer, and a homolog of Cot1) (Fig. 1C-E). To focus on the pre-existing pool of vacuole membrane proteins, we

expressed them under the control of a TET-OFF system (Garí et al., 1997) and pretreated yeast cells with doxycycline to stop their gene transcription before rapamycin treatment. In this assay, nine out of ten tested vacuole membrane proteins were downregulated to different levels, and the accumulation of a luminal GFP signal was observed (Fig. 1C-E). The only exception was seen with Zrc1, which was unchanged after rapamycin treatment. This result suggested that maintaining the Zn^{2+} import capability is important for the recycling function of the vacuole, which contains many zinc-dependent metalloenzymes (Simm et al., 2007; Hecht et al., 2013; Hecht et al., 2014). Nevertheless, our results strongly suggested that TORC1 inactivation triggers the downregulation of many vacuole membrane proteins, which is in contrast to the long-held view that vacuole biogenesis will be globally upregulated after TORC1 inactivation.

2.2.2 The degradation of vacuole membrane proteins depends on luminal proteases

The accumulation of a luminal GFP signal corresponding to the various chimeric reporters we tested (Fig. 1E) after rapamycin treatment indicated that the degradation happens inside the vacuole. To confirm this, we chose four vacuole membrane proteins (Ypl162c-GFP, Ypq1-GFP, Vph1-GFP, and Cot1-GFP) and performed the degradation assay in a *pep4*Δ strain. Pep4 is the master protease that processes and activates other vacuolar zymogens (Ammerer et al., 1986; Woolford et al., 1986). Deleting the *PEP4* gene results in general defects in the vacuolar protease activity. As shown in Fig. 2, for all four tested substrates, full-length proteins were stabilized in the *pep4*Δ strain, and the accumulation of free GFP was entirely abolished. In addition, we observed a band shift for Ypl162c-GFP in the *pep4*Δ strain (Fig. 2A), suggesting that after reaching the vacuole membrane, Ypl162c undergoes a proteolytic cleavage by luminal proteases for its maturation. In conclusion, these results indicated that the degradation depends on vacuolar protease activities.

2.2.3 The ESCRT machinery is required for invagination into the vacuole lumen

So far, three pathways have been suggested in yeast for delivering proteins to the vacuole lumen: macroautophagy, ESCRT-dependent sorting of ubiquitinated cargoes via the MVB pathway or microautophagy, and the ESCRT-independent intralumenal fragment (ILF) pathway. Among them, the ILF pathway proposes that the single vesicle (named as an intralumenal fragment) created by vacuole-vacuole homotypic fusion is responsible for selectively sorting membrane proteins into the lumen for degradation (McNally et al., 2017). Although the protein sorting mechanism has not been addressed, the ILF pathway has been reported to be blocked by rapamycin treatment and stimulated by cycloheximide-triggered hyperactivation of TORC1 (McNally et al., 2017), hence making it unlikely to be responsible for internalizing vacuole membrane proteins after TORC1 inactivation.

We then tested whether macroautophagy or ESCRT machinery were responsible for the degradation. Deleting *ATG1*, an essential gene for macroautophagy, had little effect on the degradation of all tested membrane substrates (Cot1-GFP, Vph1-GFP, Ypl162c-GFP, and Ypq1-GFP, Fig. S2A-D). In contrast, all the substrates were stabilized when two independent ESCRT components, *VPS4 (*the AAA-ATPase that disassembles the ESCRT-III filaments) and *VPS27* (a component of the ESCRT-0 subcomplex), were deleted (Fig. S2A-D and S3). These results showed that the ESCRT machinery, but not macroautophagy, is required for the degradation of vacuole membrane proteins (Zhu et al., 2017; Oku et al., 2017; Hatakeyama et al., 2019).

One caveat of using ESCRT deletion strains was the formation of class E compartments, which refers to the aberrant endosomal structures that are adjacent to vacuoles after the ESCRT machinery is inactivated. These aberrant endosomes can no longer efficiently fuse with the vacuole membrane. As such, most proteins that travel through the MVB pathway are trapped outside the

vacuole, including Vph1-GFP (MacDonald et al., 2012; Zhu et al., 2017; Yang et al., 2018). As shown in Fig. S2E and S3E, in an ESCRT deletion strain, the majority of Vph1-GFP was trapped at the class E compartment. In contrast, membrane proteins that travel through the independent AP-3 pathway, including Ypl162c-GFP, Cot1-GFP, Ypq1-GFP, and Zrc1-mCherry, are mostly localized to the vacuole membrane (Fig. S2E and S3E). This observation raises the possibility that the block of Vph1-GFP degradation is because it cannot reach the vacuole, and thus cannot be recognized by the vacuole degradation machinery.

To exclude this possibility, we performed the degradation assay in a temperature-sensitive *vps4*^{ts} strain (Babst et al., 1997). Yeast cells were first grown at the permissive temperature (26°C) to ensure all vacuole membrane proteins, including substrates and the required degradation machinery, traffick normally to the vacuole. Then the degradation assay was performed at both 26°C (permissive) and 37°C (non-permissive) temperatures. At 26°C, the degradation of all tested substrates occurred normally (Fig. 3A-E). However, after cells were shifted to 37°C, their degradation was drastically reduced, and proteins were stabilized on the vacuole membrane.

If the ESCRT machinery is responsible for increased degradation of vacuole membrane proteins, one would expect to see more ESCRTs localize (or adjacent) to the vacuole membrane after TORC1 inactivation. To test this, we tagged Vps4 with a functional 3HA-eGFP tag (Vps4-3HA-eGFP) (Adell et al., 2017) and checked its localization upon TORC1 inactivation. As shown in Fig. 3F-G, after rapamycin treatment, more Vps4-GFP puncta were localized at or in direct vicinity of the vacuole membrane (4 h, 8 h vs. 0 h), supporting a model in which the ESCRT machinery was active at the membrane to sort cargoes.

Lastly, we used transmission electron microscopy to visualize the vacuole membrane invagination after 4 hours of rapamycin treatment. As shown in Fig. 4A-C, three types of

invagination were observed in WT cells. The most prominent group was the piecemeal microautophagy of the nucleus (PMN, ~26%, n=82, Fig. 4J). Besides PMN that happens at the nucleus-vacuole junctions, we also observed cytoplasmic microautophagy of organelles such as lipid droplets (CMO, ~10%, n=82, Fig. 4K). The third group was the small tubular invagination of vacuole membrane (~14.5%, n=82, Fig. 4A-B and inserts, 4G). In addition, we also observed small vesicles inside the vacuole (Fig 4A-F, arrows). After deleting *VPS27*, the small tubular microautophagy was nearly abolished (~1.2%, Fig. 4D-F, 4G, n=74). Moreover, the number of small vesicles inside the vacuole was drastically reduced (Fig. 4H). In contrast, the other two forms of microautophagy was either unaffected (for CMO) or reduced but not abolished (for PMN). Combined with the Vps4 localization analysis, these data supported a model that the ESCRT localizes to the vacuole membrane to directly invaginate cargo proteins as small vesicles (Fig. 4A-C, 4I).

Taken together, our results indicated that the ESCRT-mediated microautophagy, but not ILF or macroautophagy, is essential for the sorting of vacuole membrane proteins into the lumen.

2.2.4 Multiple E3 ubiquitin ligases function at the vacuole

Ubiquitination is a prerequisite for cargo recognition by the ESCRT machinery, which implies that E3 ligases are important for the starvation-triggered vacuole membrane degradation. As of now, two independent E3 ligase complexes, the Ssh4-Rsp5 complex and the Dsc complex, have been identified to ubiquitinate vacuole membrane proteins (Li et al., 2015a; Li et al., 2015b; Yang et al., 2018). However, only three vacuole transporters (Ypq1, Cot1, and Zrt3*) have been shown to be their substrates. Our observation that rapamycin treatment triggers the downregulation of many vacuole membrane proteins expands their potential substrate repertoires.

To evaluate the importance of these E3 ligases in TORC1-mediated downregulation, we performed degradation assays in wild-type (WT), *ssh4*Δ, *tul1*Δ (the E3 ligase in the Dsc complex), and *ssh4*Δ *tul1*Δ double-mutant strains (Fig. 5 and S4). Interestingly, our tested substrates showed a diverse E3 ligase preference. Based on the E3 ligase dependence, we divided them into three groups: (A) Ssh4-dependent, (B) Tul1- and unknown E3 ligase-dependent, and (C) Ssh4-, Tul1-, and unknown E3 ligase-dependent.

Group A contains two substrates: Vph1 and Ypq1. For both proteins, deleting *SSH4* blocked degradation, whereas deleting *TUL1* had no impact on the kinetics (Fig. 5A and S4). In group B, after rapamycin treatment, the degradation of Cot1-GFP was significantly reduced in *tul1*Δ, but nearly unaffected in the *ssh4*Δ strain (Fig. 5B and S4), suggesting that Tul1, but not Ssh4, contributed to the degradation. However, a significant amount of Cot1-GFP was still degraded even in the *ssh4*Δ *tul1*Δ double-deletion strain, indicating the existence of either a new ubiquitin ligase or a new Rsp5 adaptor on the vacuole membrane. Of note, under zinc-depletion conditions, the degradation of Cot1-GFP is mainly dependent on Tul1 and the Dsc complex (Li et al., 2015a), suggesting the action of different recognition mechanisms under these two conditions (i.e., rapamycin vs. Zn^{2+} depletion). Zrt3* and Ypl162c represented the Ssh4-, Tul1-, and unknown E3 ligase-dependent substrates (group C). As shown in Fig. 5C, upon TORC1 inactivation, the degradation of full-length Zrt3*-GFP was partially reduced by either *SSH4* or *TUL1* deletion, and was further decreased, but not completely abolished, in the *ssh4*Δ *tul1*Δ strain, again suggesting the existence of another E3 ligase/Rsp5 adaptor. Similarly, we found that the degradation of Ypl162c also involves an unknown E3 ligase/Rsp5 adaptor, with some contribution from Ssh4 and Tul1 (Fig. 5C).

To directly demonstrate the role of vacuolar E3 ligases in cargo ubiquitination, we performed ubiquitin blots on Vph1 (group A), Cot1 (group B), and Zrt3* (group C). For western detection, the ubiquitin was labeled with a MYC tag. In order to stabilize the ubiquitinated population, we deleted *DOA4* that encodes a major deubiquitinase of the endomembrane system. Because *doa4*Δ *tul1*Δ is lethal (Tong et al., 2014; Li et al., 2015a), we generated a *doa4*Δ *vld1*Δ strain instead to study the role of the vacuolar Dsc complex. Vld1 is a bona fide Dsc component that guides the complex to the vacuole membrane through the AP3 pathway (Yang et al., 2018). Deleting *VLD1* had a similar effect on vacuole membrane degradation as *TUL1* deletion (Fig. 6A, 6C, and 6E).

As shown in Fig. 6, rapamycin treatment triggered the polyubiquitination of all three proteins. For Vph1, the deletion of *SSH4* eliminated its ubiquitination, whereas deleting *VLD1* had little effect (Fig. 6B, compare the last two lanes). In contrast, *VLD1* deletion led to a reduction (65%) of Cot1 ubiquitination, whereas *SSH4* deletion had little effect (Fig. 6D, lane 3 vs. 4). Interestingly, the temperature-sensitive *rsp5-1* mutation at 37°C resulted in a strong reduction (41%), and further deletion of *VLD1* abolished, the Cot1 ubiquitination (Fig. 6D, lane 5 vs. 6). The different effects between *SSH4* and *RSP5* mutants on Cot1 ubiquitination suggested the existence of a new Rsp5 adaptor, instead of a new E3 ligase. In the case of Zrt3*, deletion of either *SSH4* or *VLD1* caused a reduction (Fig. 6F, 40% and 18%, respectively) of its ubiquitination. However, similar to Cot1, *rsp5-1* mutant had a much stronger reduction (66%) than *ssh4*Δ (18%), and the double mutant of *rsp5-1 vld1*Δ completely abolished the ubiquitination, again suggesting the involvement of a new Rsp5 adaptor.

Our ubiquitin blots suggested the involvement of additional Rsp5 adaptors for Cot1 and Zrt3*. To confirm, we compared their degradation kinetics between the *rsp5-1 tul1*Δ strain and

*ssh4*Δ *tul1*Δ strain at a non-permissive temperature. As shown in Fig. 7A-B, the *rsp5-1 tul1*Δ double mutant completely blocked the rapamycin-triggered Cot1-GFP degradation, and no accumulation of free GFP was observed. In contrast, Cot1-GFP was still partially degraded in the *ssh4*Δ *tul1*Δ strain. Therefore, there must be a new Rsp5 adaptor to recognize Cot1.

The degradation of Zrt3*-GFP in the *rsp5-1 tul1*Δ double mutant is very intriguing. As shown in Fig. 7C, the protein levels of the full-length protein were still decreasing in the double mutant at 37°C. However, no increase of free GFP was observed. Instead, an intermediate-sized band (~33 kDa) accumulated during the rapamycin treatment (Fig. 7C, middle three lanes). These results suggested that the double mutant may have completely blocked the degradation of Zrt3*-GFP. However, Zrt3*-GFP may not be stable at high temperature and was cleaved by a luminal protease. Based on the size of the cleavage product, the digestion might have happened at the luminal loop between transmembrane helix 6 and 7 (Fig. 7E). Consistent with this hypothesis, deletion of *PEP4* in the *rsp5-1 tul1*Δ double mutant, or deletion of *PEP4* alone, abolished the accumulation of the 33-kDa band, and no decrease of the full-length protein was observed (Fig. 7C-D). Further supporting evidence was provided by imaging data. As shown in Fig. 7F, no luminal accumulation of the GFP signal was observed in the *rsp5-1 tul1*Δ double mutant despite the fact that the 33-kDa band accumulated based on the western blot. Importantly, although the *PEP4* single-deletion mutant and the triple mutant displayed a similar phenotype by western blot, they exhibited different phenotypes by fluorescence microscopy. With the triple mutant, Zrt3*-GFP was completely stabilized on the vacuole membrane. In contrast, in the *pep4*Δ mutant, Zrt3*-GFP was detected as small intravacuolar puncta, indicating that it was present on the membrane that had been invaginated, but that the resulting vesicles and their cargoes were not degraded. Together, we concluded that the *rsp5-1 tul1*Δ double mutant completely blocked the ubiquitination

of Zrt3*-GFP that was delivered into the vacuole. Furthermore, the difference between the *rsp5-1 tul1*Δ and *ssh4*Δ *tul1*Δ strains also suggested the existence of a new Rsp5 adaptor on the vacuole membrane.

In summary, our analysis indicated that Rsp5 and the Dsc complex are the two major E3 ligases that function downstream of the TORC1 complex to regulate vacuole membrane composition. In addition to Ssh4, there is strong evidence to suggest the existence of another Rsp5 adaptor on the vacuole membrane, which will be characterized and reported elsewhere.

2.2.5 Identification of a third vacuole E3 ligase, Pib1

Next, we performed the E3 ligase deletion analysis for Ypl162c. Intriguingly, unlike Cot1 and Zrt3*, the degradation of Ypl162c was not completely blocked in the *rsp5-1 tul1*Δ double mutant at 37°C (Fig. 7G-I), indicating the involvement of a third E3 ligase.

To identify the unknown E3 ligase, we generated a triple-mutant strain by further deleting the *PIB1* gene. We focused on Pib1 because this E3 ligase has been localized to the vacuole and endosome membrane but its substrates were so far unknown (Burd and Emr, 1998; Shin et al., 2001). As shown in the last three lanes of Fig. 7G, further deletion of *PIB1* completely abolished the free GFP accumulation. Pib1 is a RING domain-containing E3 ligase with a FYVE domain close to its N terminus (Fig. S5A). As reported, Pib1 is localized to the vacuole membrane and endosomes (Fig. S5B), presumably through its interaction with PtdIns3P (Burd and Emr, 1998; Shin et al., 2001). Furthermore, both ubiquitination and degradation of Ypl162c-GFP were partially reduced in the single *pib1*Δ mutant (Fig. S5C-D), indicating that Pib1 indeed participates in the ubiquitination of Ypl162c. Together, our data suggest that Pib1 plays a role in the regulation of vacuole membrane proteins.

2.2.6 TORC1 regulates vacuolar E3 ligases

What are the underlying mechanisms for TORC1 to downregulate vacuole membrane proteins? We reasoned that there might be three different levels of regulation: (1) TORC1 may regulate the phosphorylation state of vacuole membrane proteins, (2) TORC1 may regulate the activity of vacuolar ubiquitination machinery, (3) TORC1 may regulate the assembly and disassembly of the ESCRT machinery. Recently, De Virgilio and colleagues reported that TORC1 regulates ESCRT assembly through the phosphorylation of Vps27, a key component of ESCRT-0. Under nutrient-rich conditions, active TORC1 phosphorylates Vps27 and inhibits ESCRT assembly on the vacuole membrane (Hatakeyama et al., 2019). Upon starvation, Vps27 will be dephosphorylated to promote ESCRT assembly. This observation is consistent with the increase of vacuole membrane protein degradation after TORC1 inactivation. However, whether TORC1 regulates the activity of vacuolar E3 ligases is unknown.

To address the relationship between TORC1 and vacuole E3 ligases, we measured the protein levels of the three identified E3 ligase systems after natural starvation. Consistent with the increasing demand for ubiquitinating vacuole membrane proteins, the protein levels of Ssh4 and Pib1 were modestly increased after natural starvation (up to 1.8 fold, Fig. 8A-C). A similar increase was also observed for most components of the Dsc complex, including Ubx3, Tul1, Dsc2, and Dsc3 (Fig. 8D-E). Strikingly, the protein levels of Vld1 were dramatically elevated (6 fold at 12 h, Fig. 8D-E).

Because Vld1 serves as the vacuole trafficking adaptor of the Dsc complex, its upregulation suggested that TORC1 can regulate the amount of the vacuolar Dsc complex by controlling Vld1 expression. Under nutrient-rich conditions, the Vld1 protein level was low with few vacuole Dsc complexes being assembled (Fig. 8D-F). In contrast, TORC1 inactivation led to the overproduction

of Vld1 and increased assembly of the vacuole Dsc complex, as evidenced by the vacuolar localization of Ubx3 (Fig. 8D-F). To verify this model, we tested different conditions that can inactivate TORC1 activity, including rapamycin treatment, nitrogen starvation, and glucose starvation. Strikingly, Vld1 protein upregulation was observed under all conditions (Fig. 8G). As the last test, we measured the *VLD1* mRNA levels using qRT-PCR. As shown in Fig. 8H, the *VLD1* mRNA levels were increased after TORC1 inactivation.

Taken together, we concluded that TORC1 inactivation leads to the upregulation of vacuole E3 ligase systems. Focusing on the Dsc complex, we discovered that TORC1 regulates the amount of the vacuole-localized Dsc (vDsc) complex by controlling the expression of its trafficking adaptor, Vld1.

2.2.7 TORC1 regulates Vld1 expression through the Rim15-Ume6 signaling cascade

How does TORC1 control the expression of Vld1? The upregulation of *VLD1* mRNA after TORC1 inactivation (Fig. 8H) suggested that it might occur via transcriptional regulation. Using bioinformatics analysis, we identified a URS1 (upstream regulatory site 1) sequence (GGCGGC) ~500 base pairs upstream of the *VLD1* start codon (Fig. 9A), which is a putative binding site for Ume6. Ume6 is a transcription factor that forms a heterotrimeric complex with Sin3 and Rpd3 (Fig. 9A) (Williams et al., 2002). It has been reported that, under nutrient-rich conditions, Ume6 can repress the expression of *ATG8* by directly binding to the URS1 site of the *ATG8* promoter (Backues et al., 2012; Bartholomew et al., 2012). Importantly, the activity of Ume6 is regulated by TORC1. Upon starvation, Ume6 is phosphorylated through a TORC1-Rim15 cascade to relieve its inhibition of gene transcription. To investigate the importance of Ume6 on *VLD1* transcription, we first examined the *VLD1* mRNA level. In mid-log cells, the *VLD1* mRNA level was ~ 2-fold higher in the *ume6*Δ strain than the WT strain (Fig. 9B). Furthermore, upregulation of Vld1 protein

was detected after deleting either *UME6*, *RPD3*, or *SIN3* (Fig. 9C), indicating their roles in *VLD1* repression. To test the direct binding of Ume6 to the *VLD1* promoter, we applied the chromatin immunoprecipitation (ChIP) analysis using a protein A-tagged Ume6 (Ume6-PA) strain. In this assay, two regions from the *ATG8* promoter served as controls: (a) a region with a confirmed URS1 binding motif (-150) as a positive control, and (b) a region without a binding motif (-700) as a negative control (Fig. 9D). On the *VLD1* promoter, the enrichment of Ume6 was much higher in the URS1 region (-500) than in a region without the URS1 motif (-1000) and was similar to the level of the positive control (Fig. 9D). To further confirm its function with regard to Ume6 binding, we mutated the URS1 motif (GGCGGC to AAAAAA) of the *VLD1* promoter (*VLD1**, Fig. 9E) and performed another ChIP analysis. As expected, the URS1 mutation abolished the enrichment of Ume6 on the *VLD1* promoter (Fig. 9E). Taken together, these data suggested that the Ume6 ternary complex suppressed *VLD1* transcription by directly binding to its URS1 motif.

As stated above, Ume6 activity is regulated by TORC1 through the Rim15 kinase (Bartholomew et al., 2012). Based on its phosphorylation state, Rim15 can shuttle between the nucleus and cytosol. Active TORC1 and its downstream effector Sch9 phosphorylate Rim15 and prevent it from entering the nucleus (Wanke et al., 2005; Wanke et al., 2008). In contrast, TORC1 inactivation leads to the dephosphorylation and activation of Rim15 (Pedruzz et al., 2003). Active Rim15 then enters the nucleus to phosphorylate Ume6 and inhibits its repressor function (Bartholomew et al., 2012). Thus, we asked whether TORC1 is using this signaling cascade to regulate *VLD1* transcription. To this end, we subjected cells to nitrogen starvation to inactivate TORC1 and checked Vld1 protein levels in the WT, *ume6*Δ, *rim15*Δ, and *rim15*Δ *ume6*Δ strains. In WT cells, an increase of Vld1 protein was detected after nitrogen starvation (Fig. 9F-G). In *rim15*Δ cells, the basal level of Vld1 was unchanged; however, there was no upregulation after

nitrogen starvation, indicating that Rim15 works downstream of TORC1 as a positive regulator of *VLD1* transcription. Further deletion of *UME6* in the *rim15*Δ strain restored the Vld1 protein level after starvation, suggesting that Rim15 functions upstream of Ume6 (Fig. 9F-G). Interestingly, although the Vld1 protein level was already increased in *ume6*Δ cells before nitrogen starvation, it could be further upregulated after nitrogen starvation (Fig. 9F-G). This result suggested that another regulator besides Ume6 may also function downstream of Rim15 to regulate *VLD1* transcription (Fig. 9H). The identity of this regulator remains to be determined. Nevertheless, our results strongly support the hypothesis that TORC1 uses the Rim15-Ume6 signaling cascade to regulate *VLD1* transcription.

Last, we asked if overexpression of Vld1 alone is sufficient to induce a constitutive degradation of vacuole membrane proteins. Vld1 was overexpressed under the *GPD* promoter and two vacuole membrane cargoes (Cot1 and Zrt3*) were tested. As shown in Fig. 10A-B, before rapamycin treatment, protein levels of both tested substrates were similar between the WT and Vld1 overexpression strains. This indicates Vld1 overexpression alone was not sufficient to trigger a constitutive degradation of vacuole membrane proteins when TORC1 is active. After rapamycin treatment, the degradation kinetics of both Cot1 and Zrt3* were slightly faster upon overexpression. These data support the hypothesis that the TORC1 regulation of vacuole membrane proteins may be controlled at several different levels, and manipulating one condition is not sufficient to induce a dramatic change.

2.3 Discussion

2.3.1 TORC1 regulation of the vacuole membrane composition happens at different levels

In this study, we discovered that TORC1 inactivation leads to the downregulation of many vacuole membrane proteins through a ubiquitin- and ESCRT-dependent degradation

pathway. This observation is inconsistent with the model that the entire process of vacuole biogenesis will be upregulated upon TORC1 inactivation. We argue that, although lumenal hydrolases and transporters involved in the recycling function are upregulated, many other vacuolar proteins are downregulated to supply additional amino acids for cell survival.

How does TORC1 regulate the vacuole membrane composition? The latter must be controlled at several levels. First, TORC1 can affect the phosphorylation of vacuole membrane proteins. In a large scale proteomic study, Michael Hall and colleagues reported that TORC1 activity can affect the phosphorylation state of vacuole transporters, including Fth1, Ccc1, Avt4, Bpt1, and Fun26 (Soulard et al., 2010). It is conceivable that phosphorylation may prime vacuole membrane proteins for their degradation. Second, as uncovered by our study, under nutrient-rich conditions, active TORC1 inhibits the degradation of vacuole membrane proteins by repressing the activity of ubiquitination machinery. Specifically, active TORC1 inhibits the transcription of *VLD1* through the Rim15-Ume6 cascade. Consequently, very few vDsc complexes can be delivered to the vacuole. When TORC1 is inactive, the inhibition of *VLD1* is relieved, resulting in the upregulation of Vld1 and assembly of more vDsc complexes. By controlling the assembly and trafficking of ubiquitin ligases, TORC1 can regulate the abundance of vacuole membrane proteins in response to environmental cues (Fig. 10C). Third, after ubiquitination, the ESCRT machinery is recruited to the vacuole membrane to sort substrates into the lumen. Interestingly, De Virgilio and colleagues reported that active TORC1 directly phosphorylates Vps27 to inhibit its function on the vacuole membrane. Upon starvation, the dephosphorylation of Vps27 can lead to more efficient assembly of the ESCRT complex on vacuole membrane (Hatakeyama et al., 2019).

In summary, we propose that the vacuole membrane composition is regulated by TORC1

in response to environmental cues. Instead of a simple model that TORC1 inactivation leads to the upregulation of vacuole biogenesis, our study indicated that many membrane proteins are concomitantly degraded to recycle essential amino acids or possibly even "free up" space in the limiting membrane of the vacuole. The regulation may be achieved at three levels, including substrates, E3 ligases, and the ESCRT machinery. We are only at the beginning of understanding this complex relationship.

2.3.2 Different responses of v-ATPase to the (M)TORC1 inactivation between mammalian and yeast cells.

It is intriguing to observe that in yeast, after TORC1 inactivation, Vph1 is downregulated by ~30-50%. Two other recent publications also made a similar observation (Oku et al., 2017; Hatakeyama et al., 2019). This observation is surprising because, in mammalian cells, it is well established that the v-ATPase components are transcriptionally upregulated by TFEB after MTORC1 inactivation (Sardiello et al., 2009). Considering that the v-ATPase is responsible for vacuole acidification, which is essential for the vacuole's recycling function (Manolson et al., 1992), why is it downregulated in yeast?

Three reasons might explain this inconsistency. First, the yeast vacuole pH is maintained at ~5-5.5 (Li & Kane, 2009), which is less acidic than the mammalian lysosome (pH 4.5-5) (Mellman et al., 1986). This difference means the proton concentration inside the vacuole can be up to 10-fold lower than that in the lysosome. Consistent with the pH difference, GFP is quenched by the lower pH and quickly degraded in mammalian lysosomes, whereas in the yeast vacuole, GFP remains fluorescent and resistant to vacuolar proteases. As such, it may require less energy to maintain a proper vacuolar proton concentration. Second, Vph1 is an abundant protein (~ 20,000 molecules/cell) in yeast (Belle et al., 2006). Accordingly, its partial

degradation will not abolish the v-ATPase activity required for maintaining the proton gradient. Instead, this degradation may reduce ATP consumption by the v-ATPase besides supplying extra amino acids for cell survival. Third, consistent with the concept of preserving cellular ATP stores, it is well known that the yeast v-ATPase complex undergoes reversible dissociation between the V_0 and V_1 subcomplexes after glucose starvation and other stress conditions (Kane, 1995). In summary, the number of v-ATPase complexes might be more than what is required to maintain a functional vacuole pH when cells are shifted to starvation conditions. Instead, reducing ATP consumption and recycling enough amino acids might be the much more pressing issues for yeast cell survival.

2.4 Materials & Methods

Yeast strains, plasmids, media, and growth conditions

All yeast strains and plasmids used in this study are listed in Supplementary Table 1. Both Difco™ YPD broth and Difco™ Yeast Nitrogen Base (YNB) w/o Amino Acids and Ammonium Sulfate were purchased from Thermo Fisher Scientific. Yeast Nitrogen Base w/o Amino Acids was purchased from Sigma-Aldrich. All yeast strains were grown at 26°C, unless indicated otherwise, in either YPD or YNB media before further analysis.

Growth curve analysis

Yeast cells were grown in YPD medium to mid-log phase (OD_{600}: 0.5 ~ 0.7) at 28°C, which was arbitrarily defined as time point "1 h" for the growth curve analysis. Then, the growth of the yeast cells was continued at 28°C for up to 40 h. The OD_{600} was measured every 1-2 h and the same number of ODs of cells were collected at the indicated time points for further analysis.

Rapamycin-triggered degradation assay

For substrates that were tagged with GFP or 3xHA at genomic loci, yeast cells were grown in YPD medium to mid-log phase (OD_{600}: 0.5 ~ 0.7), before being incubated with 500 ng/ml rapamycin. After an appropriate amount of time, typically 4-8 h, yeast cells were collected for further analysis. For substrates that were tested under the TET-OFF system, yeast cells were grown in YNB minus uracil medium to mid-log phase (OD_{600}: 0.5 ~ 0.7). The cells were pre-incubated with 2 μg/ml doxycycline for an appropriate amount of time to allow complete ER exit (20 min for most of the substrates, and 1 h for Vph1-GFP, and Fth1-GFP). For the complete ER exit of Fet5-GFP, the plasmid was transformed into a 305-pGpd-Fth1 strain. Yeast cells were then incubated with 500 ng/ml rapamycin for an appropriate amount of time, typically 4-8 h, and collected for further analysis.

Nitrogen-starvation assay

Yeast cells were grown in YPD medium to mid-log phase (OD_{600}: 0.5 ~ 0.7), then pelleted at 3500 rpm for 5 min. After being washed with the nitrogen starvation medium (YNB without amino acids and ammonium sulfate, with 2% glucose) twice, cells were resuspended in the nitrogen starvation medium and incubated at 26°C for an appropriate amount of time (typically 3-4 h). Cells were then collected for further analysis.

Conventional transmission electron microscopy

Yeast cells were grown in YPD medium to mid-log phase (OD_{600}: 0.5 ~ 0.7), before being incubated with 500 ng/ml rapamycin for 4 h. The samples were further processed in the University of Texas Southwestern Electron Microscopy Core Facility using a published protocol (Wright, 2000; Hariri et al., 2019). Basically, cells were fixed with 2 x prefix solution (4% Glutaraldehyde in 0.2 M PIPES, 0.2 M sorbitol, 2 mM $MgCl_2$, 2 mM $CaCl_2$), then stained in uranyl acetate and embedded in Spurr Resin. After being polymerized at 60°C overnight, the specimen blocks were sectioned at 70 nm with a diamond knife (Diatome) on a Leica Ultracut UCT 6 ultramicrotome (Leica Microsystems). Sections were poststained with 2% uranyl acetate in water and lead citrate, and were placed on copper grids (Thermo Fisher Scientific). TEM images were acquired on a Tecnai G2 spirit TEM (FEI) equipped with a LaB6 source at 120 kV by using a Gatan Ultrascan charge-coupled device camera.

Chromatin immunoprecipitation (ChIP)

ChIP was performed with some modifications from a previously published paper (Aparicio et al., 2005). After the yeast cells were grown to OD_{600} ~0.8 in YPD medium, formaldehyde was added for DNA-protein cross-linking. Then the DNA was sheared by sonication, and the sheared chromatin was immunoprecipitated. Next, the protein-DNA complex

was eluted, and the cross-linking was reversed. Finally, the purified DNA was examined by RT-qPCR analysis. The information for all primers is listed in supplemental Table 2.

RNA isolation and qRT-PCR

Total RNA samples were extracted from yeast cells using TRIzol (Life Technologies, 145105) and PureLink™ RNA Mini Kit (Invitrogen, 1938678). For quantitative real-time PCR, approximately 6 μg RNA was applied for 1st-strand cDNA synthesis using PrimeScript™ RT Reagent Kit (TaKaRa, AK6003) with oligo (dT) primers. PCR was then performed using the Power SYBR Green PCR Master Mix (Thermo Fisher, 1708558D) with the primers targeting either *UBC6* (internal control) or specific genes. For each sample, the relative transcript levels were determined by normalizing them to *UBC6* levels. The information for all primers is listed in supplemental Table 2.

Microscopy and image processing

The microscopy and imaging processing was performed with a DeltaVision™ system (GE Healthcare Life Sciences) as described recently in Yang et al., 2018. The filter sets FITC (excitation 475/28, emission 525/48) and TRITC (excitation: 542/27, emission: 594/45), were used for GFP and mCherry, respectively. In brief, yeast cells were washed with milliQ water and imaged immediately at room temperature. Image acquisition and deconvolution were performed with the softWoRx program. The images were further cropped and adjusted by using ImageJ (NIH).

Immunoprecipitation and detection of cargo ubiquitination

To stabilize ubiquitinated cargoes, the gene encoding the ubiquitin hydrolase Doa4 was deleted in either WT or E3 ligase mutant background. Transient overexpression of MYC-Ub, which was under the control of a copper (*CUP1*)-inducible promoter, was induced by addition of

100 μM Cu_2SO_4 for 1 h (2 h for *ssh4-* or *rsp5-1*-related strains) before the cells were treated with rapamycin to trigger cargo ubiquitination. After 3 h of rapamycin treatment in the presence of 100 μM Cu_2SO_4, ~50 OD_{600} units of cells were collected for the IP experiment.

The IP assay was adapted from Li et al., (2015a), with some modifications. Basically, yeast cells were resuspended in 500 μl IP buffer (50 mM HEPES-KOH, pH 6.8, 150 mM KOAc, 2 mM MgOAc, 1 mM $CaCl_2$,15% glycerol) with 0.1% digitonin, supplemented with protease inhibitors and 50 mM n-ethylmalemide. Whole-cell lysates were prepared by bead beating at 4°C for 10 min, followed by addition of 500 μl of 1.9% digitonin in IP buffer. Membranes were then solubilized by nutating lysates at 4°C for 50 min. After removing the pellet by spinning at 13,000g for 10 min, the resulting lysate was incubated with 25 μl GFP-TRAP resin (Chromotek) at 4°C for 1 h. The resin was then washed four times with 0.1% digitonin in IP buffer, and bound proteins were eluted by incubating resin with sample buffer at 65°C for 5 min. The eluates were then analyzed by SDS-PAGE and probed with MYC or GFP antibody.

Sample preparation and western blot

Briefly, yeast cells were treated with ice cold 10% trichloroacetic acid (TCA) and incubated on ice for at least 1 h. After washing with 0.1% TCA, the sample pellets were dissolved in 2x boiling buffer (50 mM Tris, pH 7.5, 1 mM EDTA, 1% SDS), disrupted by glass beads using a vortex mixer for 5 min and heated at 65°C for 5 min. After addition of 2x urea sample buffer (150 mM Tris, pH 6.8, 6 M urea, 6% SDS, 40% glycerol, 100 mM DTT, bromophenol blue), samples were mixed by vortex with glass beads for 5 min and incubated at 65°C for another 5 min. The supernatants were collected, subjected to SDS-PAGE and transferred to nitrocellulose membranes for western blotting analysis.

The following antibodies were used in this study: G6PDH (1:10,000; A9521, Sigma),

Pgk1 (1:5000; 22C5D8, Invitrogen), mouse anti-GFP (1:500; sc-9996, Santa Cruz Biotechnology, Inc.), rabbit anti-GFP (1:3000; TP401, Torrey Pines Biolabs), anti-HA (1:1000; 16B12, BioLegend), mouse anti-MYC(1:500; 9E10, Santa Cruz Biotechnology, Inc.), rabbit anti-MYC(1:2,000; Sigma), Vph1 (10D7, Invitrogen), Pep4 (1:10,000), Cps1 (1:5,000) (Richter et al., 2007), and Atg8 (1:5,000). Antibodies against Dsc2, Dsc3, Ubx3, and Tul1 were generous gifts from P. Espenshade (Johns Hopkins University, Baltimore, MD).

Acknowledgments:

We thank members of the Li laboratory, including V. Venkatarangan, G. Chu, L. Reist, A. Kappagantu, and A. Hamlin for their technical support. We are also grateful to our colleagues in the Protein Folding and Disease (PFD) Hub and the MCDB department at the University of Michigan, especially M. Duncan, H. Xu, and Y. Wang for the helpful discussion and critical reading of the manuscript. We thank K. Luby-Phelps and the University of Texas Southwestern Electron Microscopy Core Facility for expert technical assistance. This research is supported by a startup fund and the MCubed 3.0 fund from the University of Michigan and NIH grant GM133873 to M. Li, by NIH grant GM131919 to DJK, and by FWF grants Y444B12, P30263, P29583, and W1101-B18 to DT.

Author contributions:

Conceptualization, X.Y., W.Z., and M.L.; Methodology, X.Y., W.Z., X.W., and M.L.; Investigation, X.Y., W.Z., X.W., P.J.B., D.A.C., S.S, F.M.A., Y.L., and M.L.; Writing – Original Draft, X.Y., W.Z., and X.W.; Writing – Review & Editing, X.Y., W.Z., D.J.K., D.T, and M.L.; Funding Acquisition, Resources, & Supervision, D.J.K., D.T, and M.L.

Declaration of interests

The authors declare no competing interests.

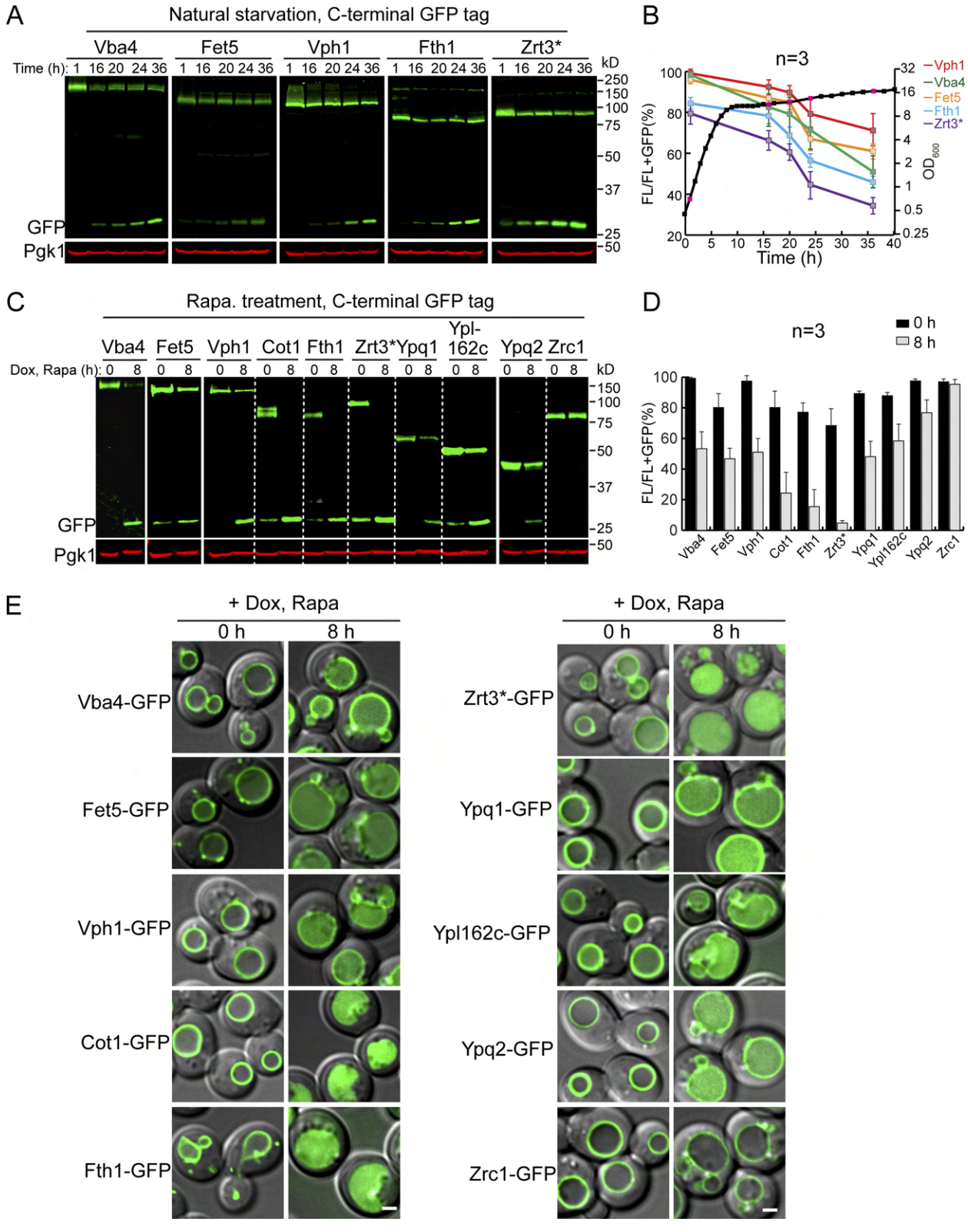
A
Natural starvation, C-terminal GFP tag
Vba4
Fet5
Vph1
Fth1
Zrt3*
Time (h): 1 16 20 24 36
kD
250
150
100
75
50
37
25
50
GFP
Pgk1
B
n=3
Vph1
Vba4
Fet5
Fth1
Zrt3*
FL/FL+GFP(%)
OD600
Time (h)
C
Rapa. treatment, C-terminal GFP tag
Vba4 Fet5 Vph1 Cot1 Fth1 Zrt3* Ypq1 Ypl-162c Ypq2 Zrc1
Dox, Rapa (h): 0 8
kD
GFP
Pgk1
D
n=3
0 h
8 h
FL/FL+GFP(%)
Vba4 Fet5 Vph1 Cot1 Fth1 Zrt3* Ypq1 Ypl162c Ypq2 Zrc1
E
+ Dox, Rapa
0 h
8 h
Vba4-GFP
Fet5-GFP
Vph1-GFP
Cot1-GFP
Fth1-GFP
Zrt3*-GFP
Ypq1-GFP
Ypl162c-GFP
Ypq2-GFP
Zrc1-GFP

Figure 2.1: TORC1 inactivation triggers the downregulation of many vacuole membrane proteins. (A) Western blots showing the downregulation of five vacuole membrane proteins in stationary phase cells. Samples were collected at the indicated time points and 1 OD_{600} units of cells were loaded in each lane. **(B)** Quantification of the protein levels in (A). The black curve represents the yeast growth curve in YPD medium at 28^{o}C, and the red squares on the growth curve represent the time points chosen for western blot analysis. FL: full-length protein fused with GFP. The relative protein levels were calculated as FL/(FL + free GFP). **(C)** Western blots showing the downregulation of TET-off-controlled vacuole membrane proteins after rapamycin treatment. The same volume of cells was loaded, with 0.5 OD_{600} units of cells loaded at 0 h. **(D)** Quantification of the protein levels in (C). **(E)** Merged images (DIC+GFP) to show subcellular localization of vacuole membrane proteins before (0 h) and after (8 h) rapamycin treatment. Scale bar: 2 μm.

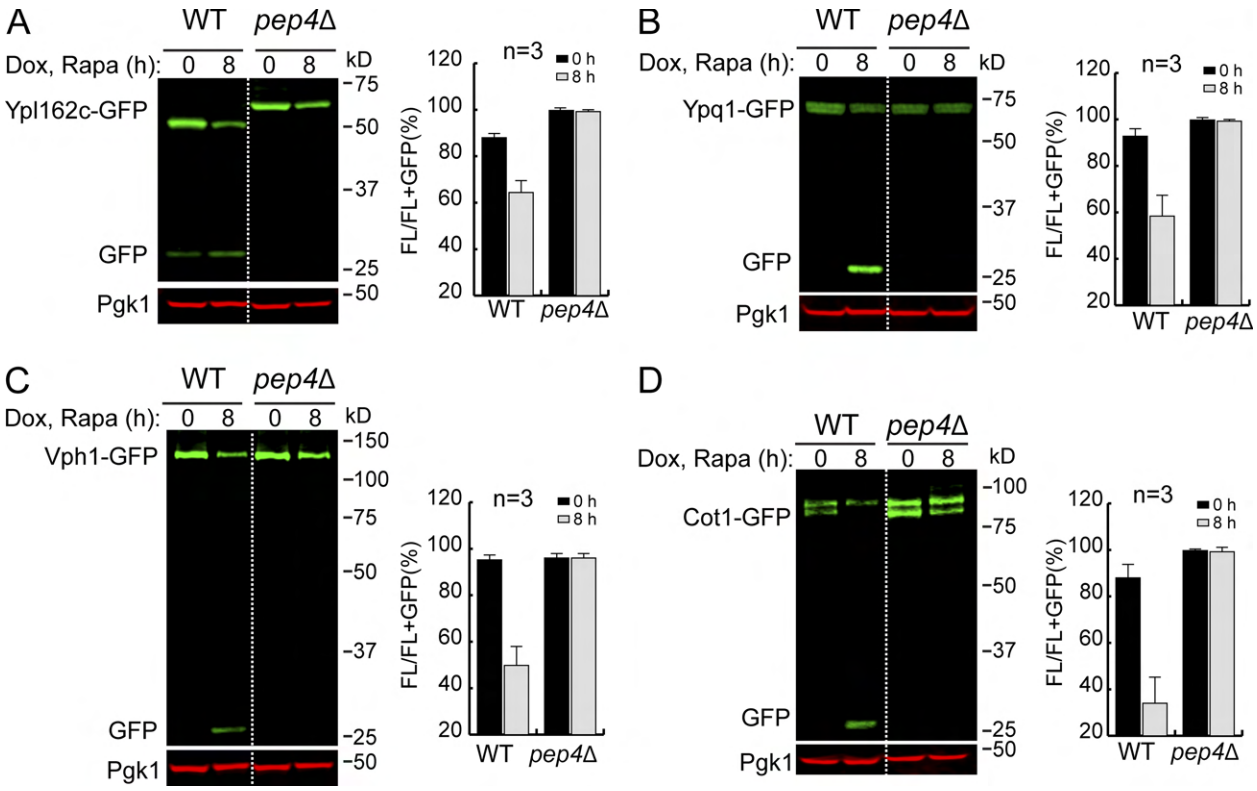

Figure 2.2: The degradation of vacuole membrane proteins depends on luminal proteases.

(A-D) Western blots (left) and corresponding quantifications (right) showing the degradation of (A) Ypl162c-GFP, (B) Ypq1-GFP, (C) Vph1-GFP or (D) Cot1-GFP in WT and *pep4*Δ strain cells. The same volume of cells was loaded, with 0.5 OD_{600} units of cells loaded at 0 h.

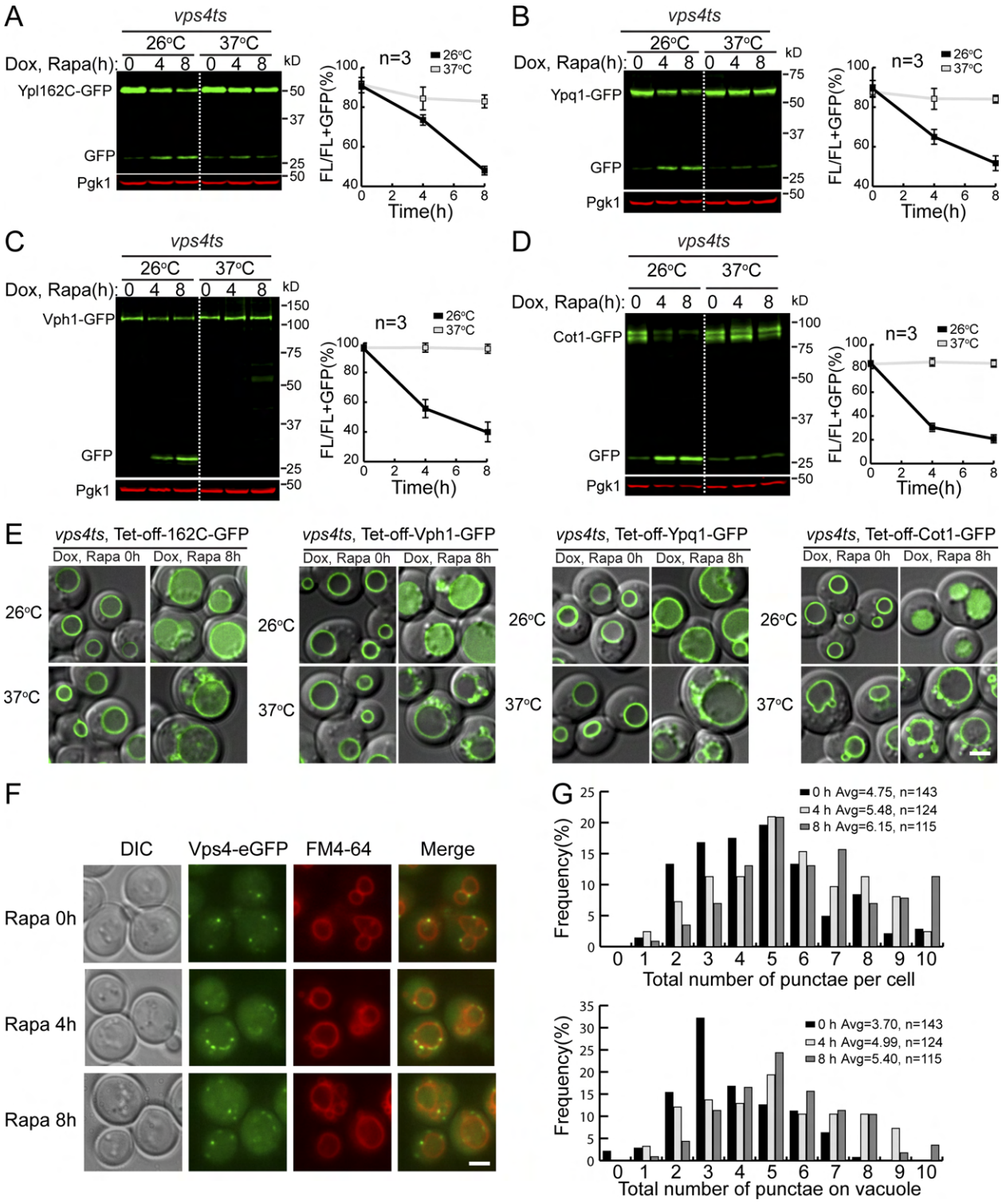

Figure 2.3: The ESCRT machinery is required for the degradation of vacuole membrane proteins. (A-D) Western blots (left) and corresponding quantifications (right) showing the degradation of (A) Ypl162c-GFP, (B) Ypq1-GFP, (C) Vph1-GFP or (D) Cot1-GFP in *vps4*^{ts} cells

at both 26°C and 37°C. The same volume of cells was loaded, with 0.5 OD_{600} units of cells loaded at 0 h. **(E)** Subcellular localization of Ypl162c-GFP, Vph1-GFP, Ypq1-GFP or Cot1-GFP in *vps4*^{ts} cells at both 26°C and 37°C after rapamycin treatment. **(F)** Subcellular localization of Vps4-eGFP before (0 h) and after (4 h, 8 h) rapamycin treatment. **(G)** Quantification of the Vps4-eGFP puncta in (F). Scale bar: 2 μm.

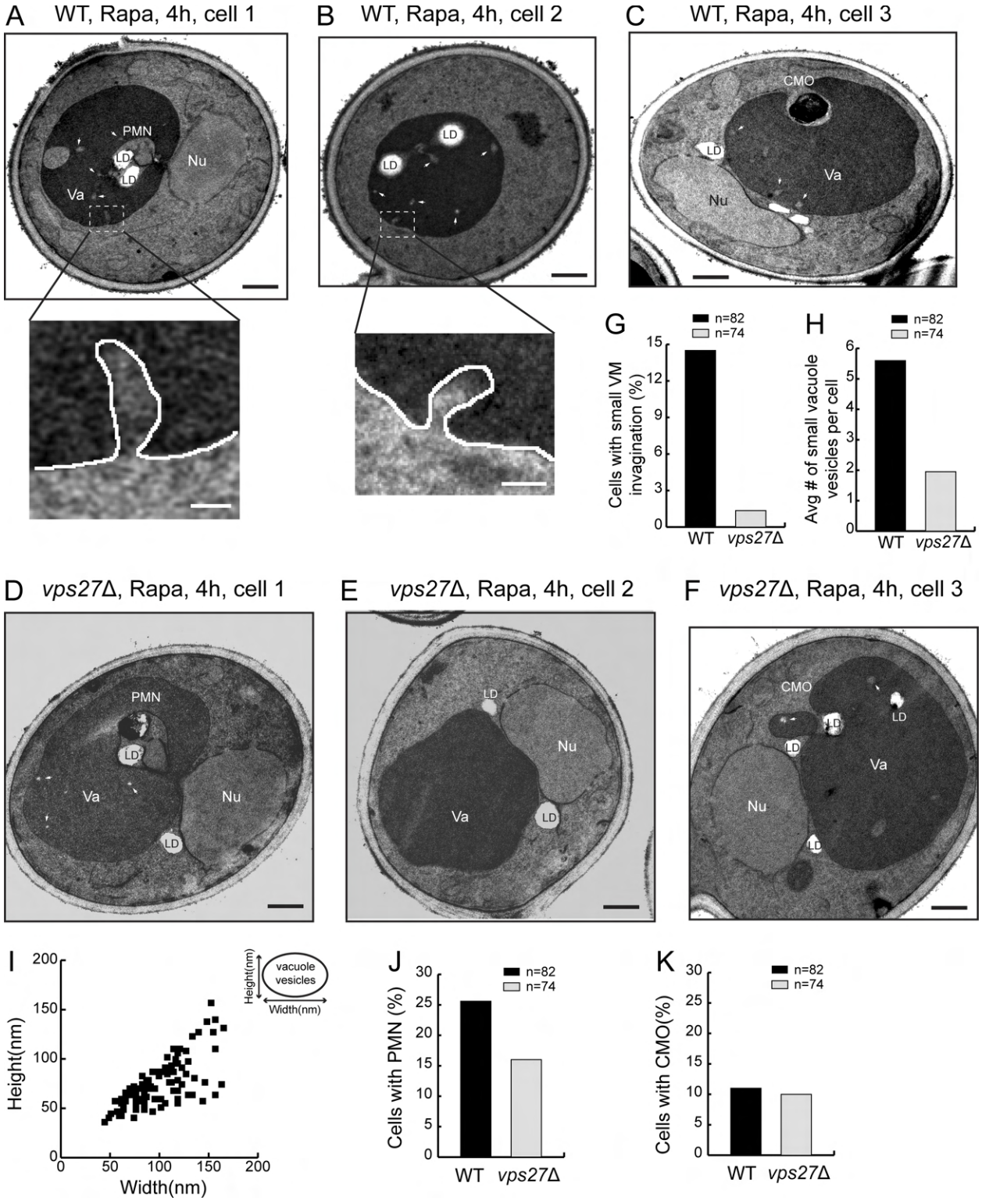

Figure 2.4: The ESCRT deletion abolished one form of microautophagy. (A-C)

Representative TEM images showing three types of microautophagy, including piecemeal

microautophagy of the nucleus (PMN), cytoplasmic microautophagy of organelles (CMO), and small vacuole membrane (VM) invagination in WT cells after rapamycin treatment. **(D-E)** Representative TEM images showing that after rapamycin treatment, PMN and CMO still happened in *vps27*Δ cells, while the small VM invagination was nearly abolished. **(G)** Frequency of observing small VM invagination in either WT or *vps27*Δ cells after rapamycin treatment. **(H)** Number of small vacuole vesicles per cell in either WT or *vps27*Δ cells after rapamycin treatment**. (I)** Size distribution of small vacuole vesicles. **(J)** Frequency of observing PMN in either WT or *vps27*Δ cells after rapamycin treatment. **(K)** Frequency of observing CMO in either WT or *vps27*Δ cells after rapamycin treatment. Va: Vacuole; Nu: Nucleus; LD: Lipid droplet. White arrows highlight small vacuole vesicles. Black scale bar: 0.5 μm. White scale bar: 50 nm.

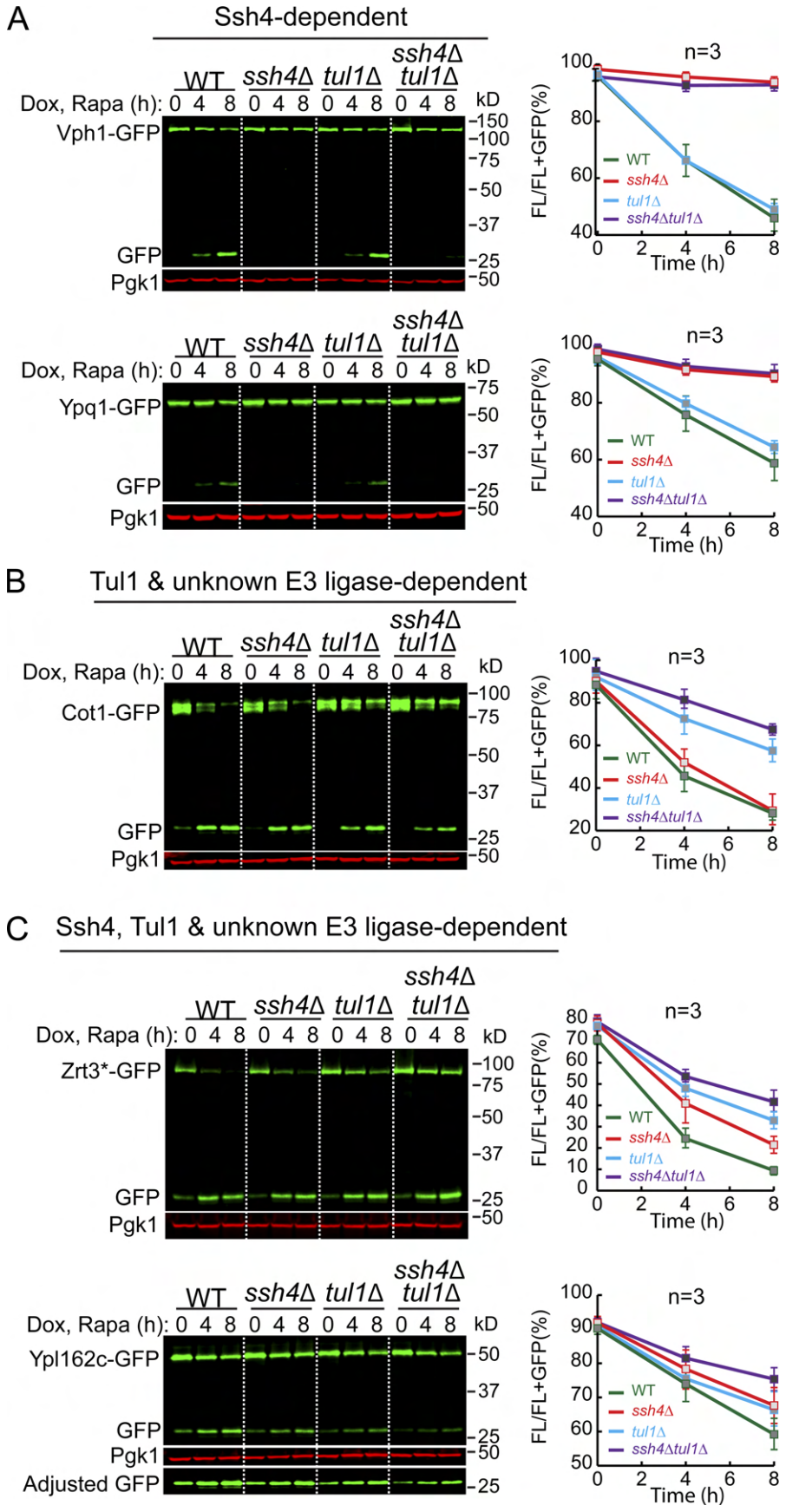
A
Ssh4-dependent
WT
ssh4Δ
tul1Δ
ssh4Δ tul1Δ
Dox, Rapa (h): 0 4 8 0 4 8 0 4 8 0 4 8
kD
Vph1-GFP
GFP
Pgk1
150
100
75
50
37
25
50
n=3
FL/FL+GFP(%)
Time (h)
WT
ssh4Δ
tul1Δ
ssh4Δtul1Δ
Ypq1-GFP
B
Tul1 & unknown E3 ligase-dependent
Cot1-GFP
C
Ssh4, Tul1 & unknown E3 ligase-dependent
Zrt3*-GFP
Ypl162c-GFP
Adjusted GFP

Figure 2.5: Multiple vacuole E3 ligases function downstream of the TORC1 kinase. (A-C) Western blots (left) and corresponding quantifications (right) showing the degradation of (A) Vph1-GFP and Ypq1-GFP, (B) Cot1-GFP, or (C) Zrt3*-GFP and Ypl162c-GFP in WT, *ssh4*Δ, *tul1*Δ, and *ssh4*Δ *tul1*Δ cells. The same volume of cells was loaded, with 0.5 OD_{600} units of cells loaded at 0 h.

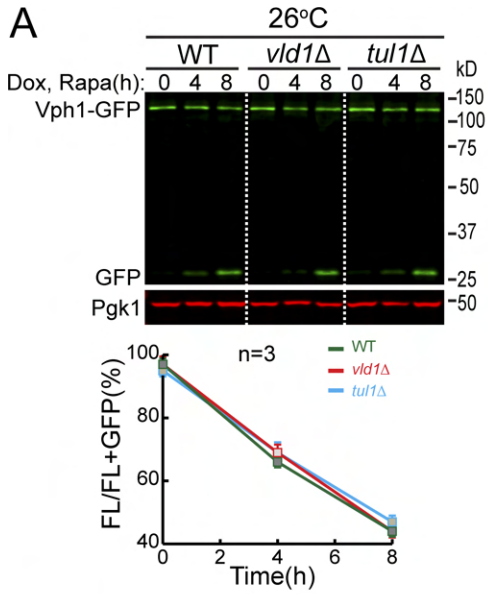
A
26°C
WT
vld1Δ
tul1Δ
Dox, Rapa(h): 0 4 8 0 4 8 0 4 8
kD
Vph1-GFP
150
100
75
50
37
GFP
25
Pgk1
50
n=3
WT
vld1Δ
tul1Δ
FL/FL+GFP(%)
100
80
60
40
0 2 4 6 8
Time(h)

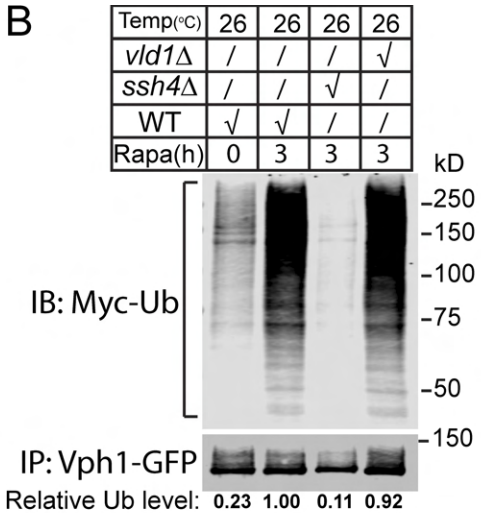
B
Temp(°C) 26 26 26 26
vld1Δ / / / √
ssh4Δ / / √ /
WT √ √ / /
Rapa(h) 0 3 3 3
kD
250
150
100
75
50
IB: Myc-Ub
150
IP: Vph1-GFP
Relative Ub level: 0.23 1.00 0.11 0.92

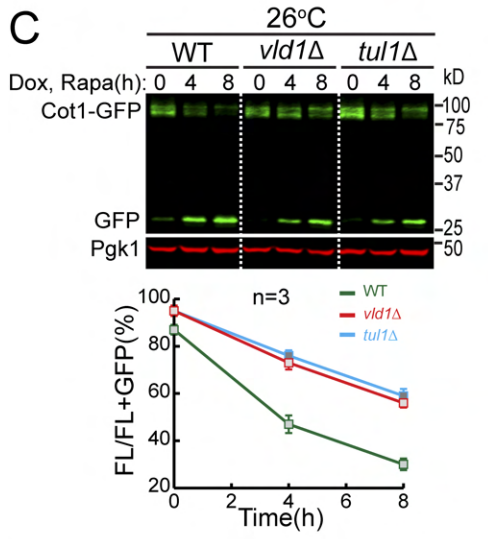
C
26°C
WT
vld1Δ
tul1Δ
Dox, Rapa(h): 0 4 8 0 4 8 0 4 8
kD
Cot1-GFP
100
75
50
37
GFP
25
Pgk1
50
n=3
WT
vld1Δ
tul1Δ
FL/FL+GFP(%)
100
80
60
40
20
0 2 4 6 8
Time(h)

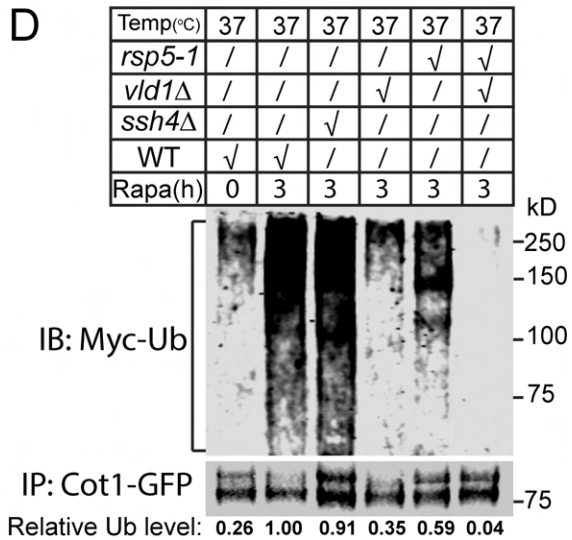
D
Temp(°C) 37 37 37 37 37 37
rsp5-1 / / / / √ √
vld1Δ / / / √ / √
ssh4Δ / / √ / / /
WT √ √ / / / /
Rapa(h) 0 3 3 3 3 3
kD
250
150
100
75
IB: Myc-Ub
IP: Cot1-GFP
75
Relative Ub level: 0.26 1.00 0.91 0.35 0.59 0.04

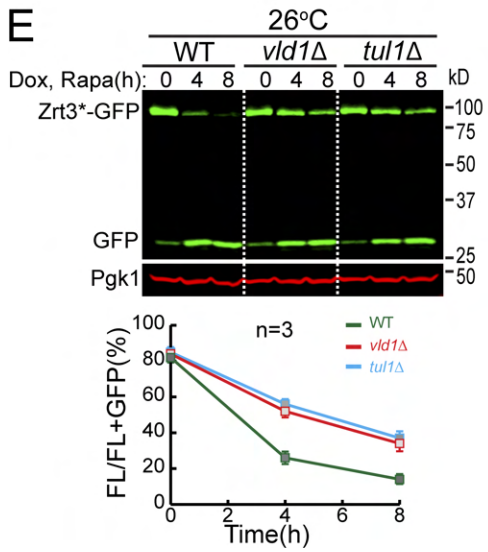
E
26°C
WT
vld1Δ
tul1Δ
Dox, Rapa(h): 0 4 8 0 4 8 0 4 8
kD
Zrt3*-GFP
100
75
50
37
GFP
25
Pgk1
50
n=3
WT
vld1Δ
tul1Δ
FL/FL+GFP(%)
100
80
60
40
20
0
0 2 4 6 8
Time(h)

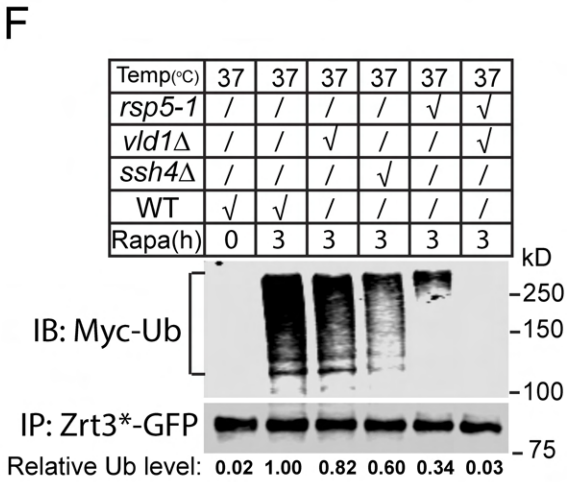
F
Temp(°C) 37 37 37 37 37 37
rsp5-1 / / / / √ √
vld1Δ / / √ / / √
ssh4Δ / / / √ / /
WT √ √ / / / /
Rapa(h) 0 3 3 3 3 3
kD
250
150
100
IB: Myc-Ub
IP: Zrt3*-GFP
75
Relative Ub level: 0.02 1.00 0.82 0.60 0.34 0.03

Figure 2.6: Vacuole membrane E3 ligases poly-ubiquitinate their membrane cargoes upon TORC1 inactivation. (A) Western blot (top) and quantification (bottom) showing the degradation of Vph1-GFP in WT, *vld1*Δ, and *tul1*Δ cells. **(B)** A representative western blot (n=3) showing the poly-ubiquitination of Vph1-GFP in WT, *ssh4*Δ, and *vld1*Δ cells at 26ºC. The relative ubiquitination level was normalized to the Vph1-GFP level. **(C)** Western blot (top) and quantification (bottom) showing the degradation of Cot1-GFP in WT, *vld1*Δ, and *tul1*Δ cells. **(D)** A representative western blot (n=2) showing the poly-ubiquitination of Cot1-GFP in WT, *ssh4*Δ, *vld1*Δ, *rsp5-1*, and *rsp5-1 vld1*Δ cells at 37ºC. **(E)** Western blot (top) and quantification (bottom) showing the degradation of Zrt3*-GFP in WT, *vld1*Δ, and *tul1*Δ cells. **(F)** A representative western blot (n=2) showing the poly-ubiquitination of Zrt3*-GFP in WT, *ssh4*Δ, *vld1*Δ, *rsp5-1*, and *rsp5-1 vld1*Δ cells at 37ºC. For (A) (C) and (E), the same volume of cells were loaded, with 0.5 OD_{600} units of cells loaded at 0 h.

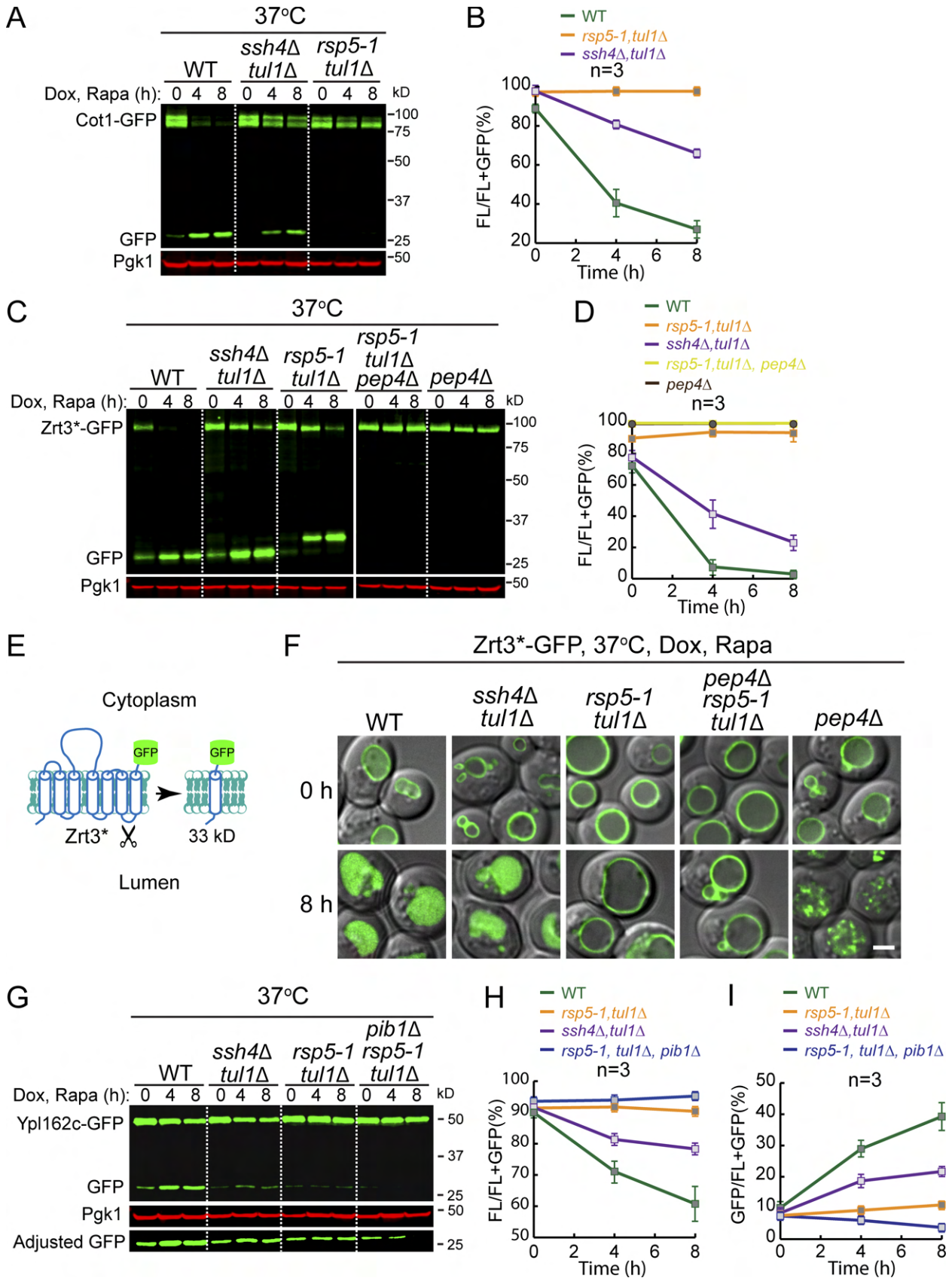
A
37°C
WT
ssh4Δ tul1Δ
rsp5-1 tul1Δ
Dox, Rapa (h): 0 4 8 0 4 8 0 4 8
kD
Cot1-GFP
GFP
Pgk1
100
75
50
37
25
50
B
WT
rsp5-1,tul1Δ
ssh4Δ,tul1Δ
n=3
FL/FL+GFP(%)
Time (h)
C
37°C
WT
ssh4Δ tul1Δ
rsp5-1 tul1Δ
rsp5-1 tul1Δ pep4Δ
pep4Δ
Dox, Rapa (h): 0 4 8 0 4 8 0 4 8 0 4 8 0 4 8
kD
Zrt3*-GFP
GFP
Pgk1
D
WT
rsp5-1,tul1Δ
ssh4Δ,tul1Δ
rsp5-1,tul1Δ, pep4Δ
pep4Δ
n=3
FL/FL+GFP(%)
Time (h)
E
Cytoplasm
GFP
GFP
Zrt3*
33 kD
Lumen
F
Zrt3*-GFP, 37°C, Dox, Rapa
WT
ssh4Δ tul1Δ
rsp5-1 tul1Δ
pep4Δ rsp5-1 tul1Δ
pep4Δ
0 h
8 h
G
37°C
WT
ssh4Δ tul1Δ
rsp5-1 tul1Δ
pib1Δ rsp5-1 tul1Δ
Dox, Rapa (h): 0 4 8 0 4 8 0 4 8 0 4 8
kD
Ypl162c-GFP
GFP
Pgk1
Adjusted GFP
H
WT
rsp5-1,tul1Δ
ssh4Δ,tul1Δ
rsp5-1, tul1Δ, pib1Δ
n=3
FL/FL+GFP(%)
Time (h)
I
WT
rsp5-1,tul1Δ
ssh4Δ,tul1Δ
rsp5-1, tul1Δ, pib1Δ
n=3
GFP/FL+GFP(%)
Time (h)

Figure 2.7: Evidence for the existence of a new Rsp5 adaptor and identification of Pib1 as the third vacuole E3 ligase. (A) Western blot showing the degradation of Cot1-GFP in WT, *ssh4*Δ *tul1*Δ, and *rsp5-1 tul1*Δ cells. **(B)** Quantification of the protein levels in (A). **(C)** Western blot showing the degradation of Zrt3*-GFP in WT, *ssh4*Δ *tul1*Δ, *rsp5-1 tul1*Δ, *pep4*Δ *rsp5-1 tul1*Δ, and *pep4*Δ cells. **(D)** Quantification of the protein levels in (C). Please note that the curves of *pep4*Δ *rsp5-1 tul1*Δ and *pep4*Δ samples are almost overlapping. **(E)** A cartoon depicting the cleavage of Zrt3* between TM6 and TM7. **(F)** Subcellular localization of Zrt3*-GFP in the indicated strains before (0 h) and after (8 h) rapamycin treatment. **(G)** Western blot showing the degradation of Ypl162c-GFP in WT, *ssh4*Δ *tul1*Δ, *rsp5-1 tul1*Δ, and *pib1*Δ *rsp5-1 tul1*Δ cells. (**H-I**) Quantification of the FL (H) or free GFP (I) levels in (G). For (A) (C) and (G), the same volume of cells was loaded, with 0.5 OD_{600} units of cells loaded at 0 h. Scale bar: 2 μm.

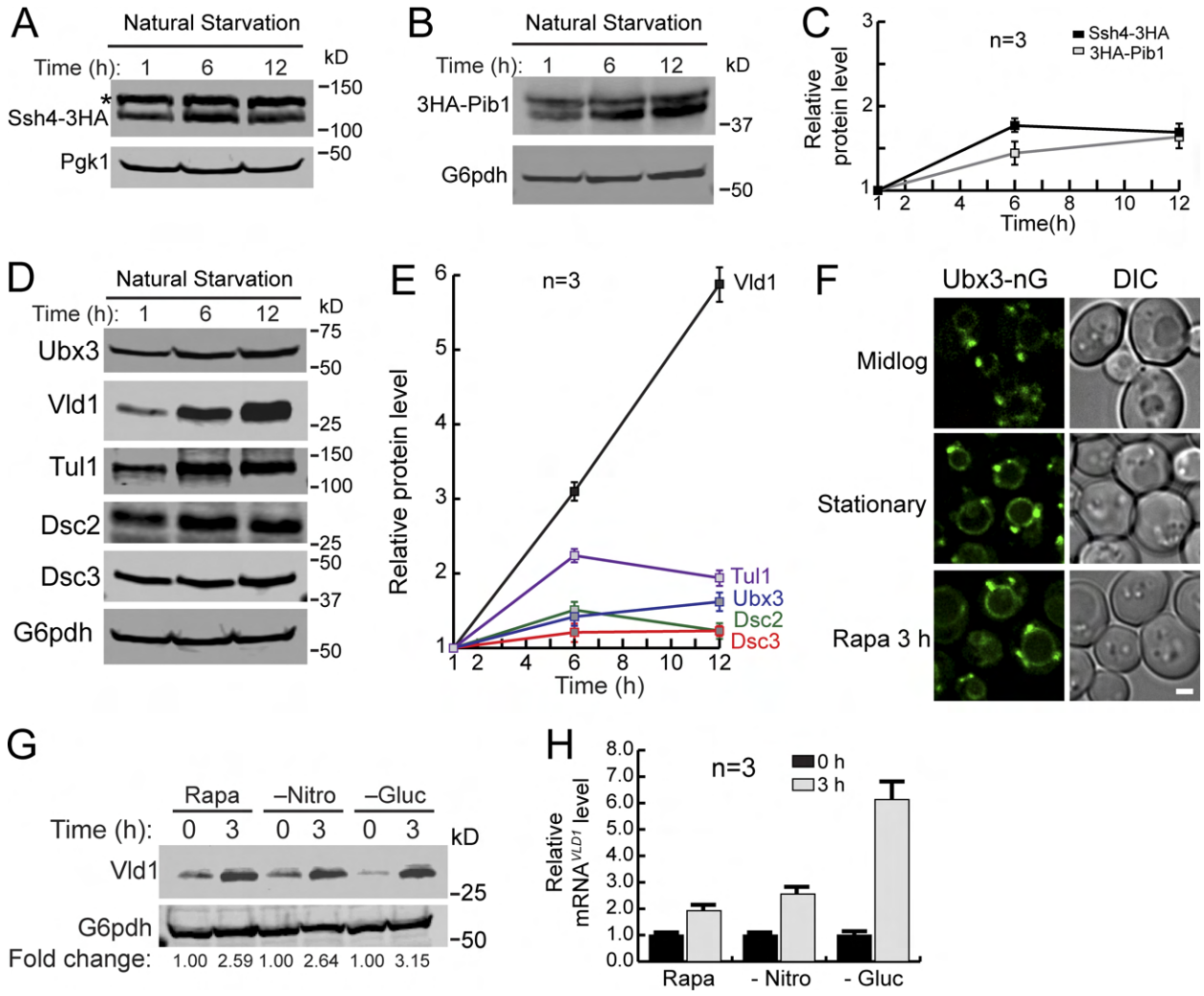

Figure 2.8: TORC1 regulates the activity of vacuole E3 ligases. (A) Western blot showing the protein level changes of Ssh4-mNeonGreen-3HA in stationary phase cells. The asterisk represents a non-specific band. **(B)** Western blot showing the protein level changes of 3HA-Pib1 in stationary phase cells. **(C)** Quantification of the protein levels in (A) and (B). **(D)** Western blots showing the protein level changes of different Dsc components in stationary phase cells. Samples were collected at the indicated time points and 1 OD_{600} units of cells were loaded in each lane. **(E)** Quantification of the protein levels in (D). **(F)** Subcellular localizations of Ubx3-mNeonGreen (Ubx3-nG) in mid-log phase, stationary phase, and rapamycin-treated cells. **(G)** A representative western blot (n=3) showing the level of Vld1-3HA after rapamycin treatment,

nitrogen starvation or glucose starvation. Samples were collected at the indicated time points and 1 OD_{600} unit of cells was loaded in each lane. **(H)** qRT-PCR showing the level of *VLD1* mRNA after rapamycin treatment, nitrogen starvation or glucose starvation. Scale bar: 2 μm.

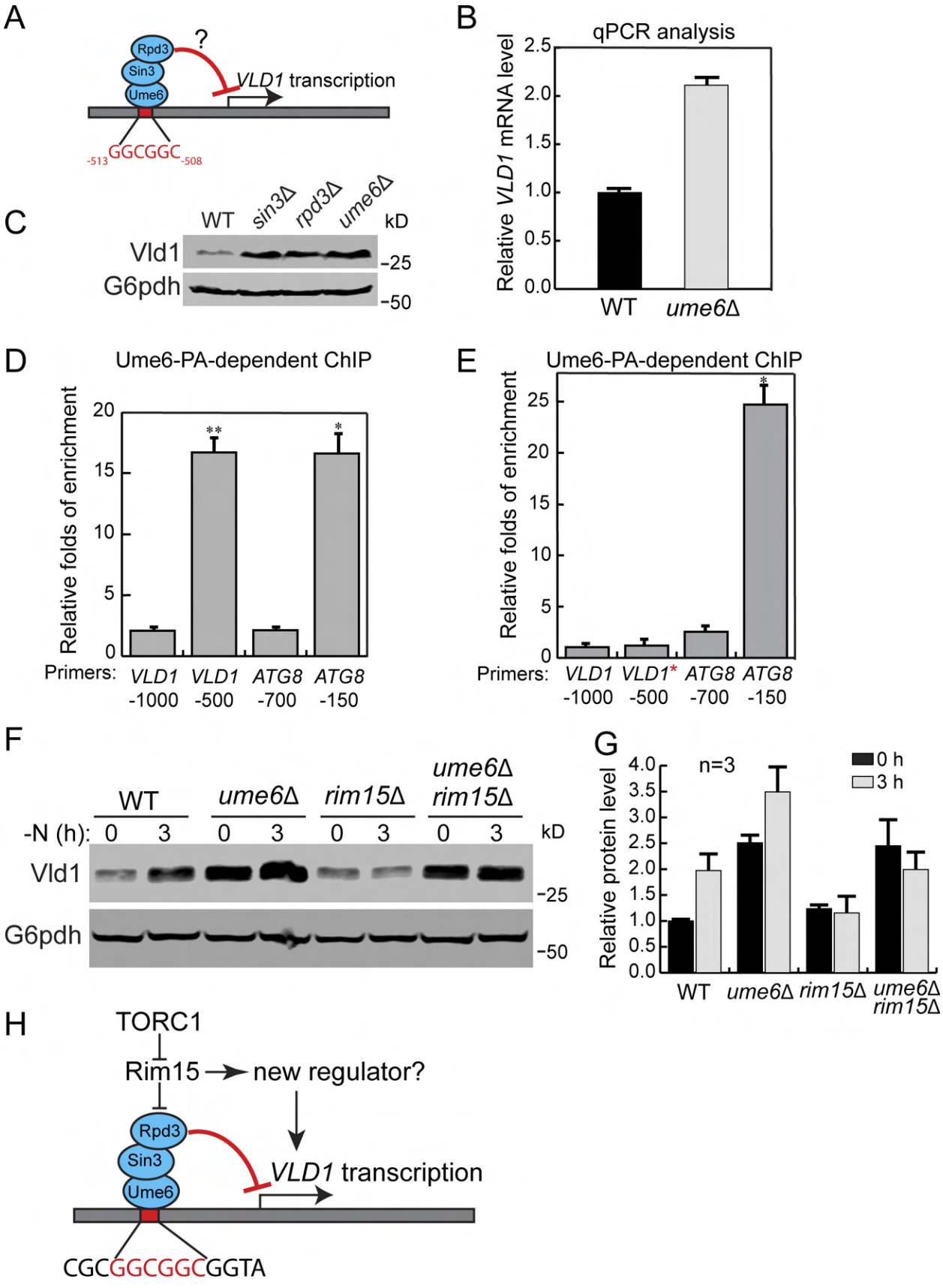
A
Rpd3
Sin3
Ume6
?
VLD1 transcription
-513 GGCGGC -508
B
qPCR analysis
Relative VLD1 mRNA level
2.5
2.0
1.5
1.0
0.5
0.0
WT
ume6Δ
C
WT
sin3Δ
rpd3Δ
ume6Δ
kD
Vld1
G6pdh
-25
-50
D
Ume6-PA-dependent ChIP
Relative folds of enrichment
20
15
10
5
0
**
*
Primers:
VLD1 -1000
VLD1 -500
ATG8 -700
ATG8 -150
E
Ume6-PA-dependent ChIP
Relative folds of enrichment
25
20
15
10
5
0
*
Primers:
VLD1 -1000
VLD1* -500
ATG8 -700
ATG8 -150
F
WT
ume6Δ
rim15Δ
ume6Δ rim15Δ
-N (h): 0 3 0 3 0 3 0 3
kD
Vld1
G6pdh
-25
-50
G
n=3
0 h
3 h
Relative protein level
4.0
3.5
3.0
2.5
2.0
1.5
1.0
0.5
0.0
WT
ume6Δ
rim15Δ
ume6Δ rim15Δ
H
TORC1
Rim15
new regulator?
Rpd3
Sin3
Ume6
VLD1 transcription
CGCGGCGGCGGTA

Figure 2.9: TORC1 regulates Vld1 through the Rim15-Ume6 signaling cascade. (A) A cartoon showing the interaction between the Ume6 complex with the putative binding motif in the *VLD1* promoter region. **(B)** qRT-PCR showing the *VLD1* mRNA level in WT and *ume6*Δ cells. **(C)** A representative western blot (n=3) showing the level of Vld1-3HA in WT, *ume6*Δ, *sin3*Δ, and *rpd3*Δ cells. **(D)** ChIP analysis showing the binding of Ume6 to the *VLD1* promoter region. **(E)** ChIP analysis showing the disruption of Ume6 binding to the *VLD1* promoter region after mutation. The enrichment values were normalized to the input DNA, and the error bars show the SEM of 3 independent experiments. The p-value is presented by stars: *<0.05, **<0.01. **(F)** Western blot showing the level of Vld1-3HA in WT, *ume6*Δ, *rim15*Δ, and *ume6*Δ *rim15*Δ cells after nitrogen starvation. Samples were collected at the indicated time points and 1 OD_{600} unit of cells was loaded in each lane. **(G)** Quantification of the protein levels in (F). **(H)** A cartoon model showing that TORC1 regulates Vld1 expression through a Rim15-mediated signaling cascade.

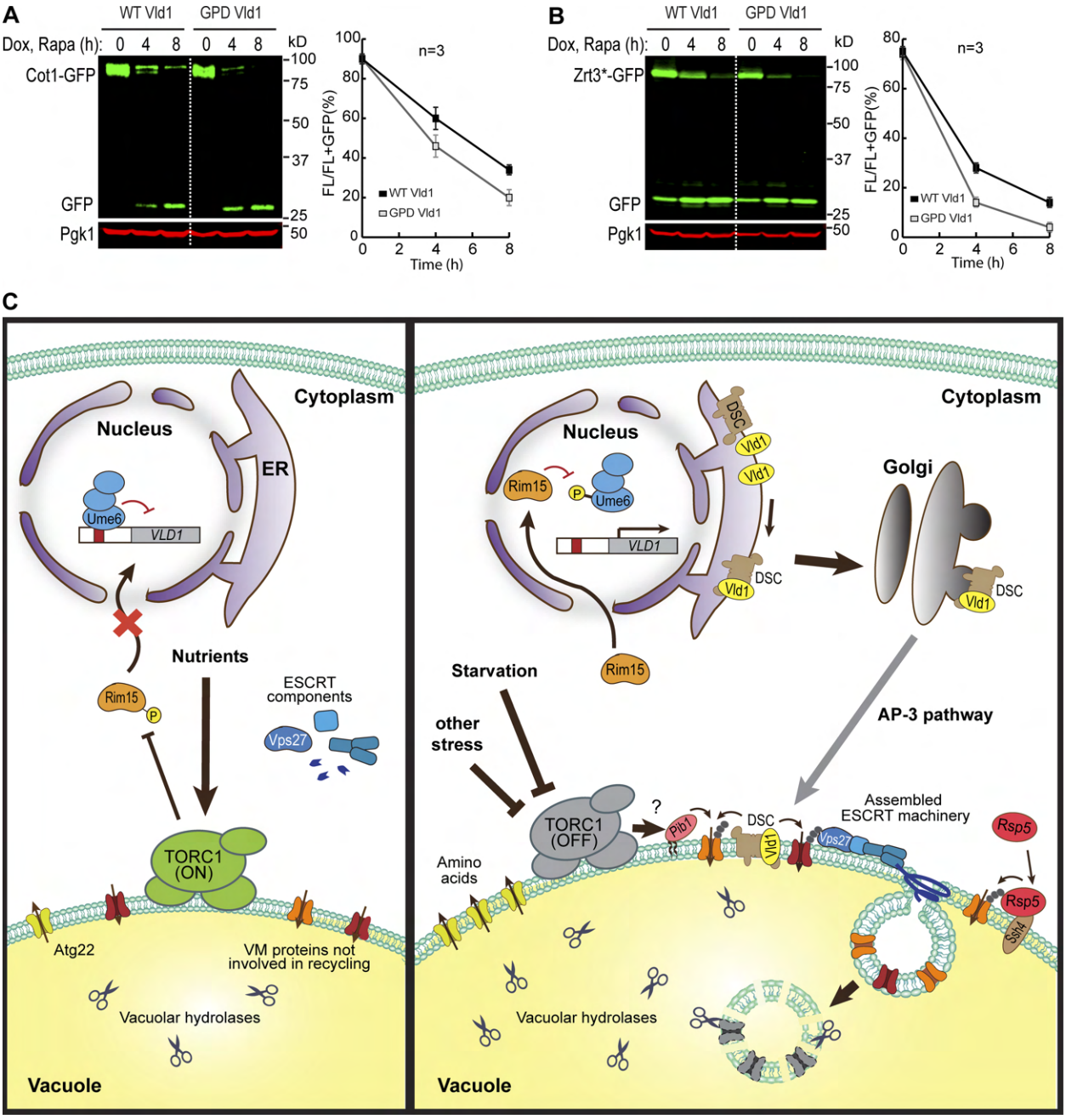

Figure 2.10: A model summarizing how TORC1 regulates the vacuole membrane composition via the ubiquitin- and ESCRT-dependent microautophagy. (A-B) Western blot (left) and quantification (right) showing the degradation of Cot1-GFP (A) or Zrt3*-GFP (B) in WT and Vld1 overexpression strains. The same volume of cells was loaded with 0.5 OD_{600} units of cells loaded at 0 h. **(C)** The model. For details, please see the Discussion.

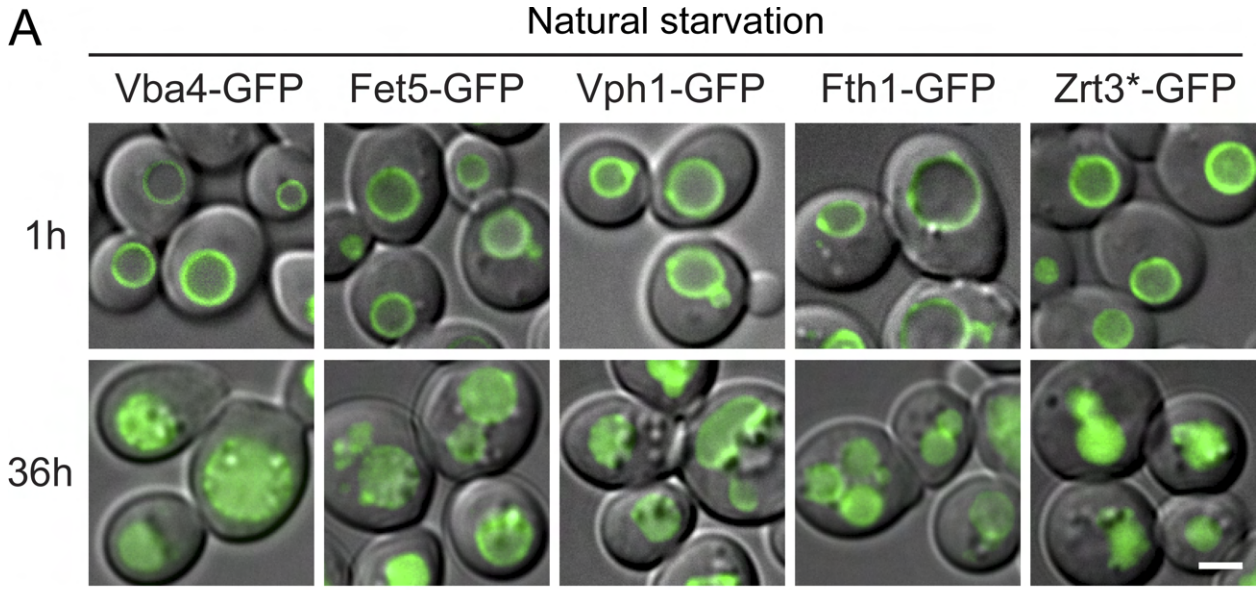
A
Natural starvation
Vba4-GFP
Fet5-GFP
Vph1-GFP
Fth1-GFP
Zrt3*-GFP
1h
36h

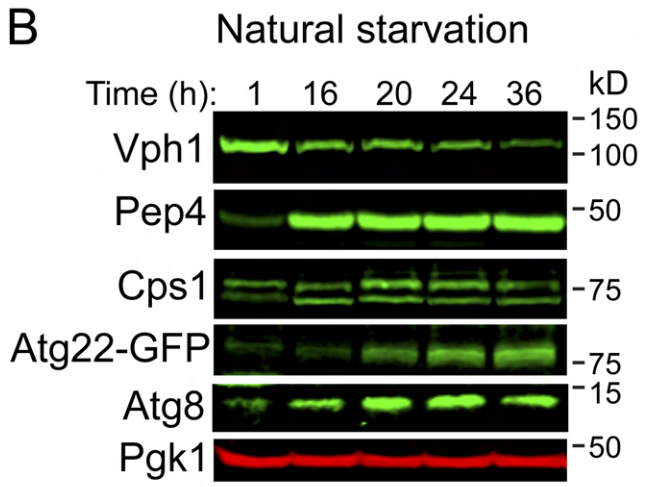
B
Natural starvation
Time (h): 1 16 20 24 36
kD
Vph1
Pep4
Cps1
Atg22-GFP
Atg8
Pgk1
150
100
50
75
75
15
50

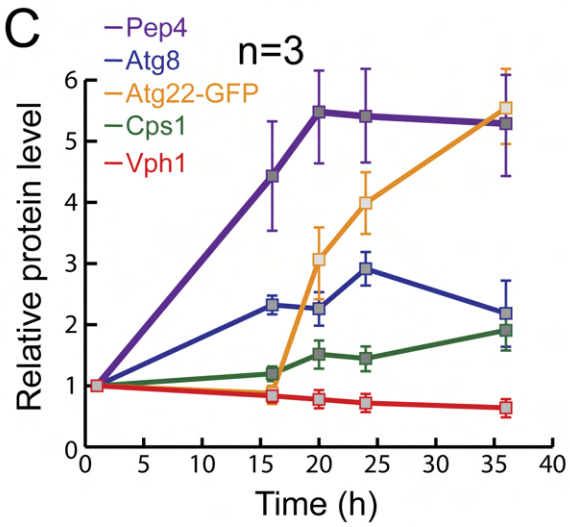
C
Pep4
Atg8
Atg22-GFP
Cps1
Vph1
n=3
Relative protein level
Time (h)
0
1
2
3
4
5
6
0
5
10
15
20
25
30
35
40

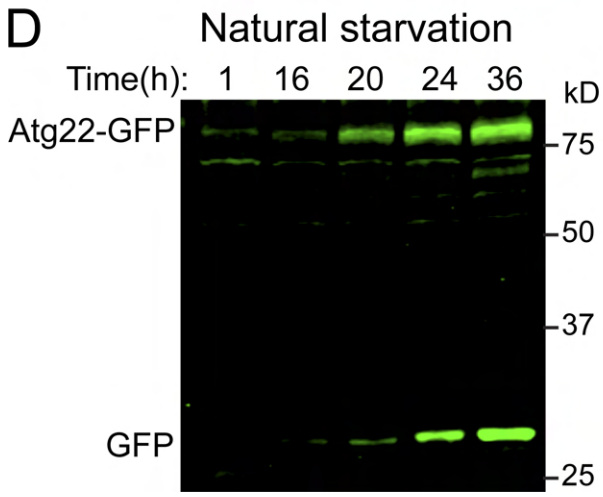
D
Natural starvation
Time(h): 1 16 20 24 36
kD
Atg22-GFP
GFP
75
50
37
25

Supplemental Figure 2.1: TORC1 inactivation triggers a global downregulation of vacuole membrane proteins. (A) Subcellular localization of vacuole membrane proteins in mid-log (1 h) or stationary phase (36 h) cells. **(B)** Western blots showing the changes of Vph1, Pep4, Cps1, Atg8, and Atg22-GFP in stationary phase cells. Samples were collected at the indicated time points and 1 OD_{600} unit of cells was loaded in each lane. **(C)** Quantification of the protein levels in (B). **(D)** Uncropped Atg22-GFP image from (B). Scale bar: 2 μm. Related to figure 1.

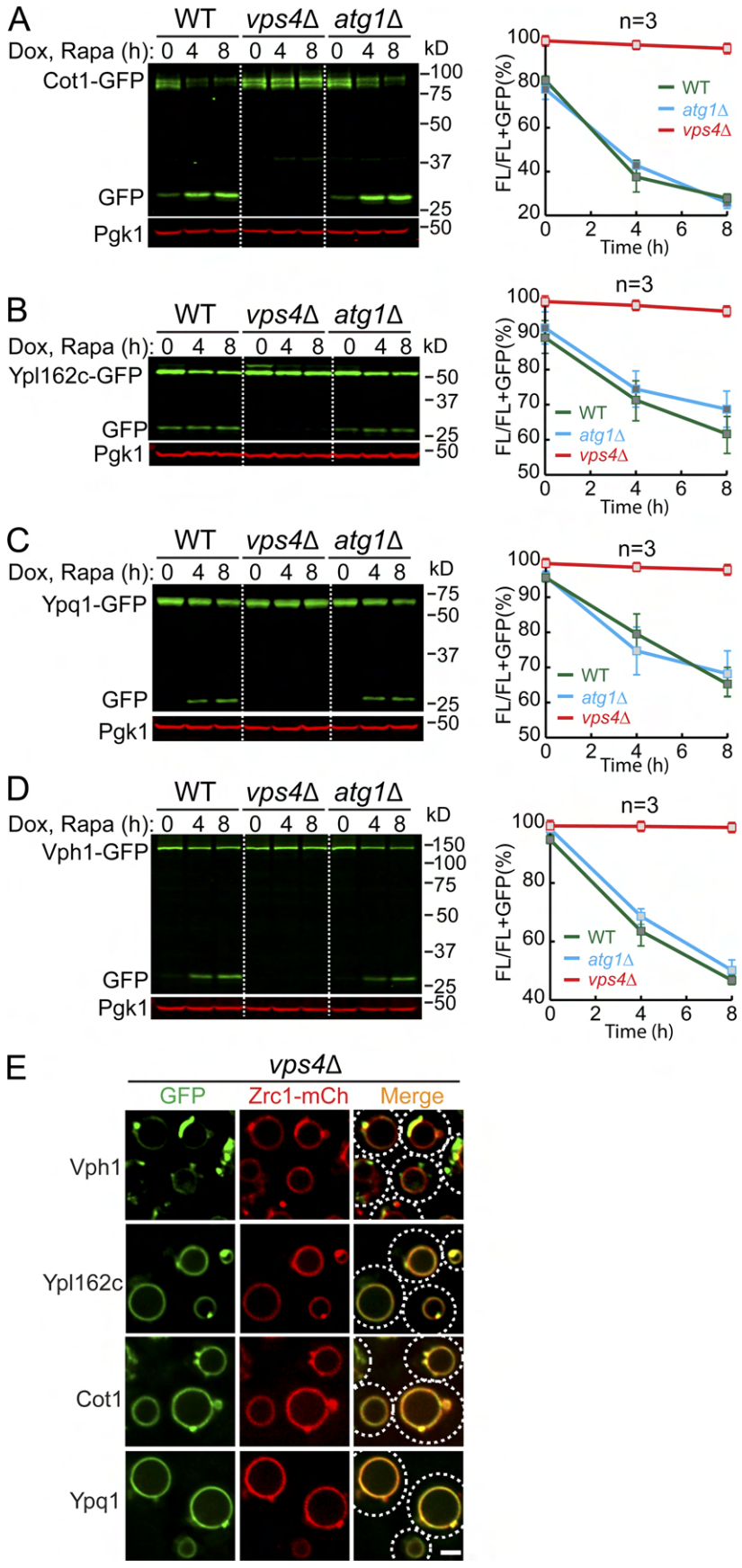
A
WT
vps4Δ
atg1Δ
Dox, Rapa (h): 0 4 8 0 4 8 0 4 8
kD
Cot1-GFP
GFP
Pgk1
100
75
50
37
25
50
n=3
FL/FL+GFP(%)
Time (h)
WT
atg1Δ
vps4Δ
B
Ypl162c-GFP
C
Ypq1-GFP
D
Vph1-GFP
150
E
vps4Δ
GFP
Zrc1-mCh
Merge
Vph1
Ypl162c
Cot1
Ypq1

Supplemental Figure 2.2: ESCRT machinery, but not macroautophagy, is responsible for the degradation of vacuole membrane proteins. (A-D) Western blots (left) and corresponding quantifications (right) showing the degradation of (A) Cot1-GFP, (B) Ypl162c-GFP, (C) Ypq1-GFP or (D) Vph1-GFP in WT, *vps4*Δ, and *atg1*Δ strain cells. The same volume of cells was loaded, with 0.5 OD_{600} units of cells loaded at 0 h. **(E)** Subcellular localization of vacuole membrane proteins in cells from the *vps4*Δ strain. White dotted circles highlight the yeast cell periphery. Scale bar: 2 μm. Related to figure 3.

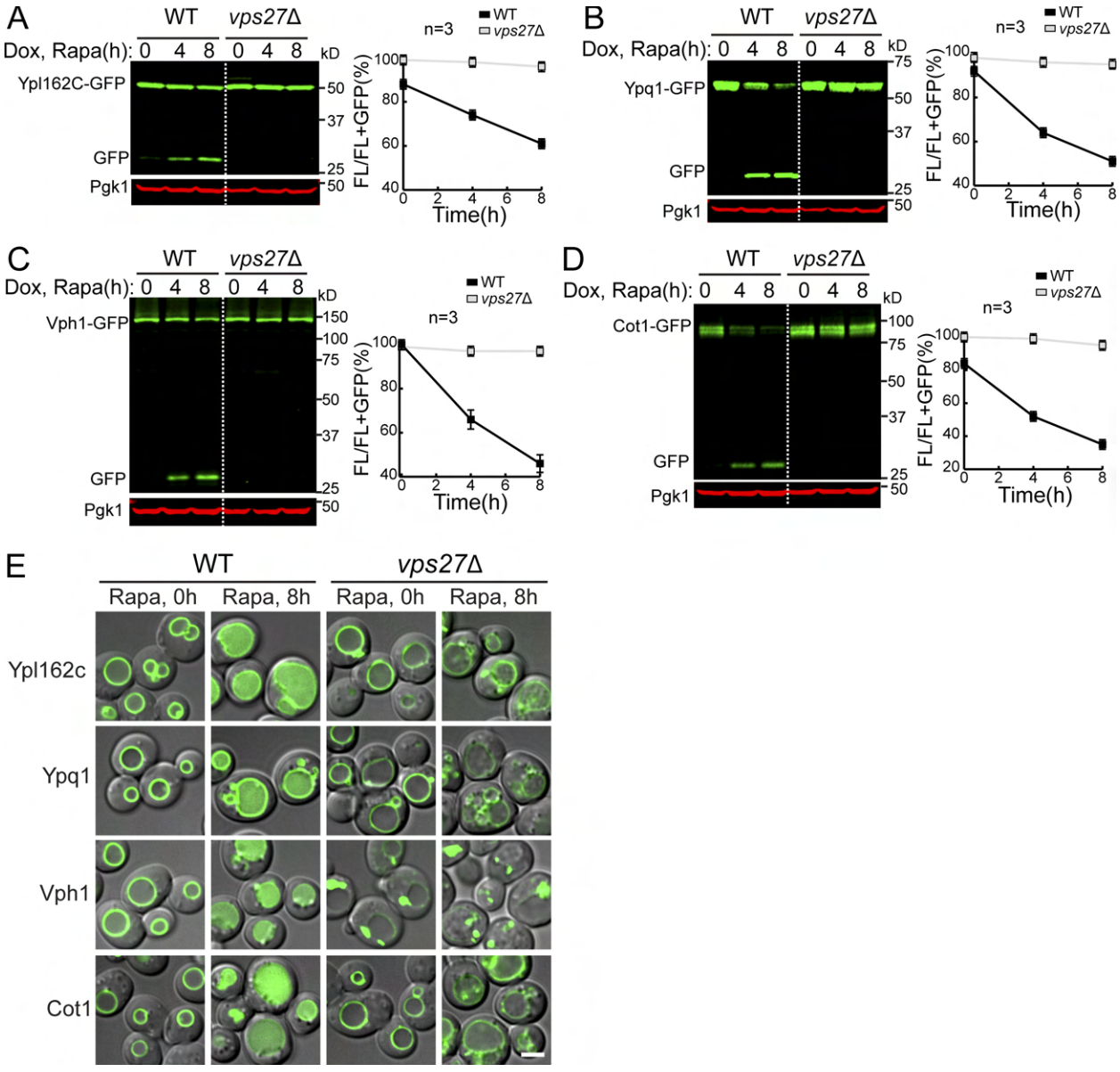

Supplemental Figure 2.3: ESCRT machinery is responsible for the degradation of vacuole membrane proteins. (A-D) Western blots (left) and corresponding quantifications (right) showing the degradation of (A) Ypl162c-GFP, (B) Ypq1-GFP, (C) Vph1-GFP or (D) Cot1-GFP in WT and *vps27*Δ strain cells. The same volume of cells was loaded, with 0.5 OD_{600} units of cells loaded at 0 h. **(E)** Subcellular localization of vacuole membrane proteins in WT and *vps27*Δ strain cells before (0 h) or after (8 h) rapamycin treatment. Scale bar: 2 μm. Related to figure 3.

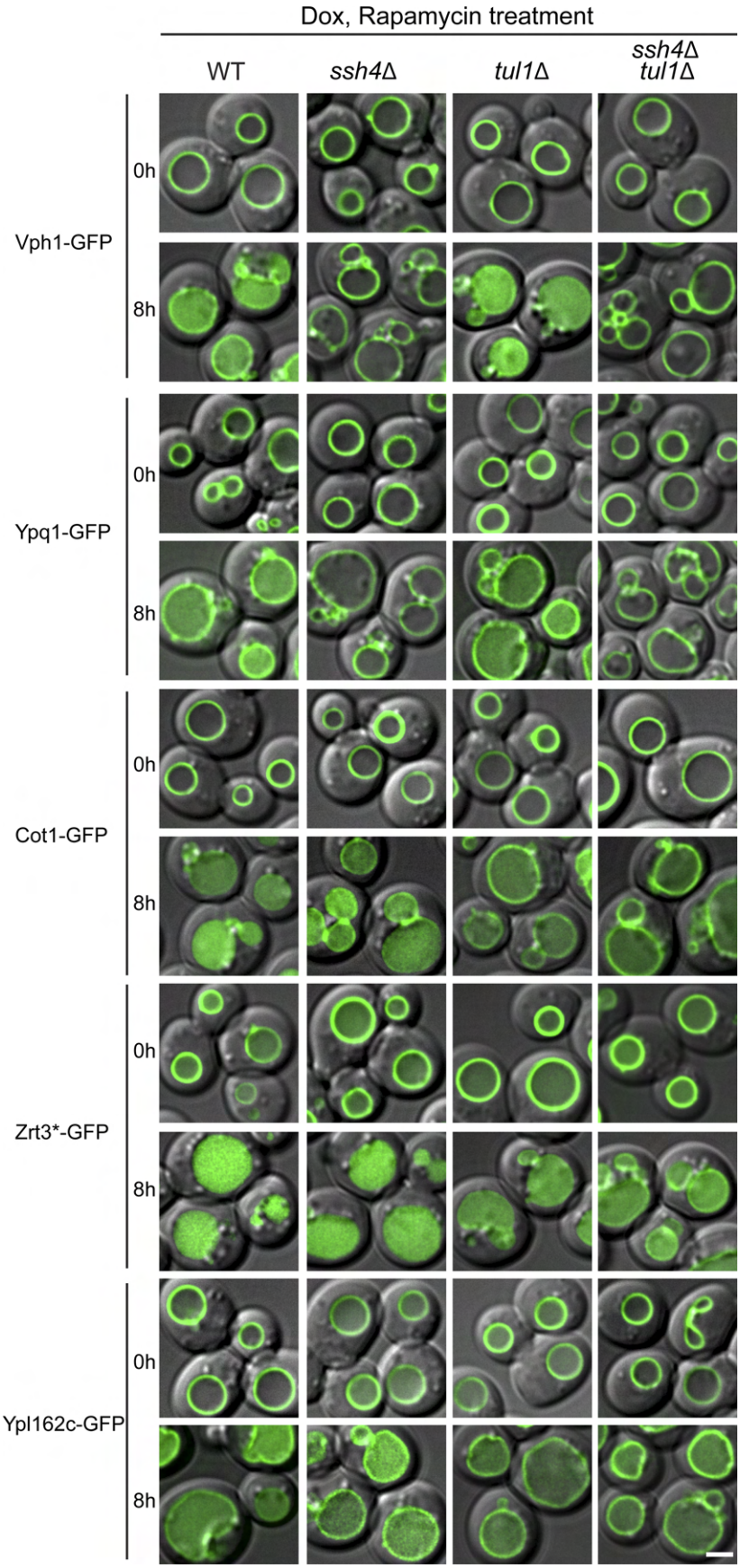
Dox, Rapamycin treatment
WT
ssh4Δ
tul1Δ
ssh4Δ tul1Δ
Vph1-GFP
Ypq1-GFP
Cot1-GFP
Zrt3*-GFP
Ypl162c-GFP
0h
8h

Supplemental Figure 2.4: Multiple vacuolar E3 ligases function downstream of the TORC1 kinase. Subcellular localization of vacuole membrane proteins in WT, *ssh4*Δ, *tul1*Δ, and *ssh4*Δ *tul1*Δ strain cells before (0 h) or after (8 h) rapamycin treatment. Scale bar: 2 μm. Related to figure 5.

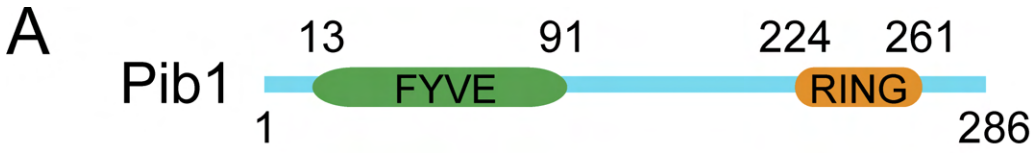
A
Pib1
13
91
224
261
FYVE
RING
1
286

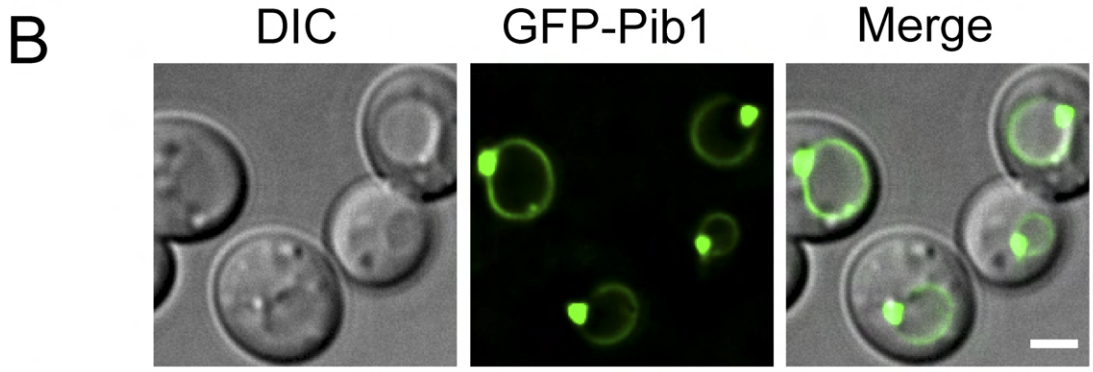
B
DIC
GFP-Pib1
Merge

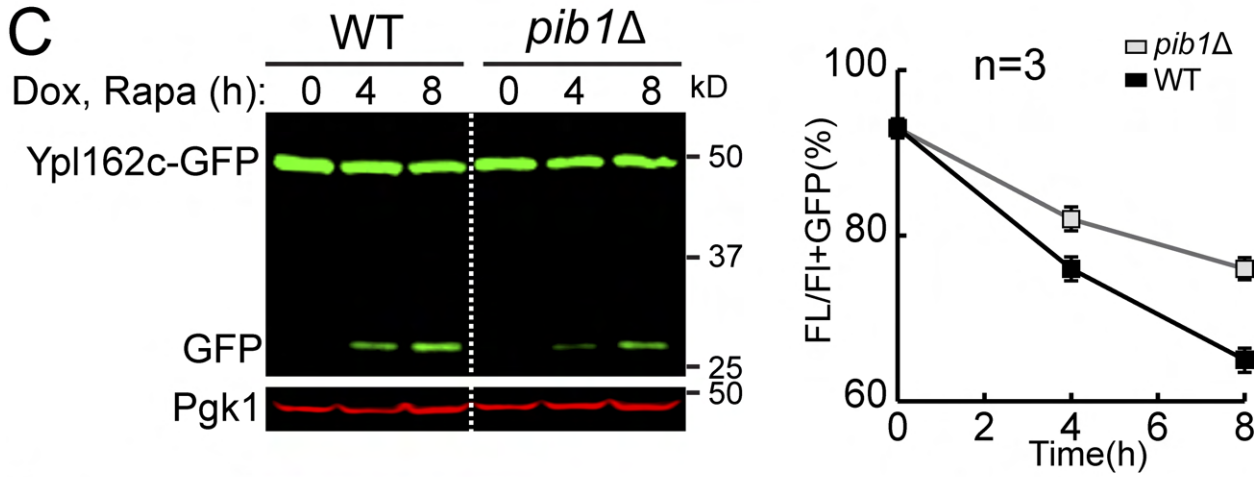
C
WT
pib1Δ
Dox, Rapa (h): 0 4 8 0 4 8 kD
Ypl162c-GFP
GFP
Pgk1
50
37
25
50
n=3
pib1Δ
WT
FL/FI+GFP(%)
100
80
60
0
2
4
6
8
Time(h)

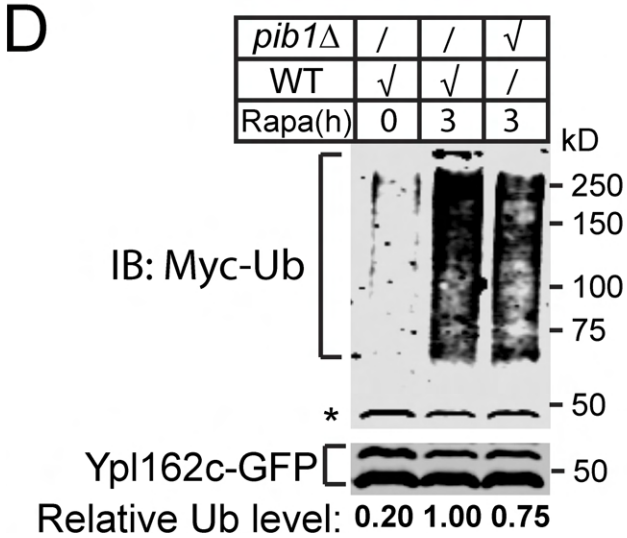
D
pib1Δ / / √
WT √ √ /
Rapa(h) 0 3 3
kD
IB: Myc-Ub
250
150
100
75
50
*
Ypl162c-GFP
50
Relative Ub level: 0.20 1.00 0.75

Supplemental Figure 2.5: Pib1 participates in the ubiquitination. (A) A schematic model to show the domain organization of Pib1. **(B)** Subcellular localization of GFP-Pib1. **(C)** Western blots (left) and quantification (right) comparing the degradation of Ypl162c-GFP in WT and *pib1*Δ strains. The same volume of cells was loaded, with 0.5 OD_{600} units of cells loaded at 0 h. **(D)** A representative western blot (n=3) showing the poly-ubiquitination of Ypl162c-GFP in WT and *pib1*Δ cells at 28^{o}C. The relative ubiquitin level was normalized to the Ypl162c-GFP level. The asterisk represents a background band. Scale bar: 2 μm. Related to figure 7.

Supplemental Table 2.1: Yeast strains and plasmids used in this study			
S. cerevisiae strains			
strain	***name***	***genotype***	***reference/source***
SEY6210	wild type	Matα*, leu1-3, 112 ura3-52 his3-200, trp1-901 lys2-801 suc2-D9*	(Robinson et al., 1988)
SEY6210.1	wild type	Mata*, leu1-3, 112 ura3-52 his3-200, trp1-901 lys2-801 suc2-D9*	(Robinson et al., 1988)
YML235	Vba4-GFP	6210, *VBA4-GFP::TRP1*	(Li et al., 2015a)
YML106	Fet5-GFP	6210.1, *FET5-GFP::HIS3*	(Li et al., 2015a)
YML169	Vph1-GFP	6210.1, *VPH1-GFP::KAN*	(Li et al., 2015a)
YML227	Zrt3*-GFP	6210.1, *ZRT3*-GFP::KAN*	(Li et al., 2015a)
YML1022	Ypq1-GFP	6210, *YPQ1-GFP::TRP1*	(Li et al., 2015a)
YML321	Ypl162c-GFP	6210.1, *YPL162C-GFP::KAN*	(Li et al., 2015a)
YML324	Cot1-GFP	6210.1, *COT1-GFP::KAN*	(Li et al., 2015a)
YML068	*vps4*Δ	6210.1, *vps4*Δ::*TRP1*	(Li et al., 2015a)
YML260	*atg1*Δ	6210, *atg1*Δ*::KAN*	(Li et al., 2015a)
YXY483	*vps4*Δ, Zrc1-mCh	6210.1, *vps4*Δ::TRP1, ZRC1-mCherry::HIS3	This study
YML100	*pep4*Δ	6210, *pep4Δ*::LEU2	(Li et al., 2015a)
YML208	$vps4^{ts}$	6210.1, *vps4Δ*::TRP1, $vps4^{ts}$::LEU2	(Li et al., 2015a)
YML354	*ssh4*Δ	6210, *ssh4Δ*::TRP1	(Li et al., 2015a)
YML489	*tul1*Δ	6210.1, *tul1Δ*::TRP1	(Li et al., 2015a)
YML505	*tul1*Δ*, ssh4*Δ	6210.1, *tul1Δ*::TRP1, *ssh4Δ*::TRP1	This study
YML629	*rsp5-1, tul1*Δ	6210, *rsp5-1*, *tul1Δ*::TRP1	This study
YXY464	*pib1*Δ*, rsp5-1, tul1*Δ	6210, *pib1Δ*::HYG, *rsp5-1*, *tul1Δ*::TRP1	This study
YXY492	*pep4*Δ*, rsp5-1, tul1*Δ	6210, *pib1Δ*::HYG, *rsp5-1*, *tul1Δ*::TRP1	This study
YXY307	Vld1-3HA,Gld1-3HA	6210.1, GLD1-3HA::HYG, VLD1-3HA::TRP1	This study
YXY266	Vld1-3HA	6210.1, VLD1-3HA::TRP1	This study
YML553	Ubx3-nG	6210.1, UBX3-neonGreen::TRP1	(Yang et al., 2018)
YML971	Ssh4-3HA	6210, SSH4-NeonGreen-3HA::TRP1	This study
YXY532	3HA-Pib1	3HA-PIB1::TRP1	This study
YXY331	Vld1-3HA, *ume6*Δ	6210.1, *ume6*Δ::HYG,Vld1-3HA::TRP1	This study

YXY333	Vld1-3HA, *sin3*Δ	6210.1, *sin3Δ*::HYG,Vld1-3HA::TRP1	This study
YXY334	Vld1-3HA, *rpd3*Δ	6210.1, *rpd3Δ*::HYG,Vld1-3HA::TRP1	This study
YXY457	Ume6-PA	6210.1, UME6-2PA::Kan, VLD1-3HA::TRP1	This study
YXY458	Ume6-PA, Vld1*	6210.1, UME6-2PA::Kan, VLD1^{mURS}-3HA::TRP1,	This study
YXY332	Vld1-3HA, *rim15*Δ	6210.1, *rim15Δ*::HYG,Vld1-3HA::TRP1	This study
YXY440	Vld1-3HA, *rim15*Δ*, ume6*Δ	6210.1, *rim15Δ*::HIS3, *ume6Δ*::HYG, Vld1-3HA::TRP1	This study
YXY480	Fth1 overexpression	6210.1, 305-pGPD-FTH1	This study
YML377	*vps27*Δ	6210, *vps27*Δ::HIS3	(Li et al., 2015a)
YXY676	Vph1-GFP, *doa4*Δ	6210.1, Vph1-GFP::KAN, *doa4*Δ::HIS3	This study
YXY673	Vph1-GFP, *doa4*Δ, *vld1*Δ	6210.1, Vph1-GFP::KAN, *vld1*Δ::TRP1, *doa4*Δ::HIS3	This study
YXY675	Vph1-GFP, *doa4*Δ, *ssh4*Δ	6210.1, Vph1-GFP::KAN, *ssh4*Δ::TRP1, *doa4*Δ::His3	This study
YXY671	Cot1-GFP, *doa4*Δ, *ssh4*Δ	6210.1, Cot1-GFP::KAN, *ssh4*Δ::TRP1, *doa4*Δ::HIS3	This study
YXY672	Cot1-GFP, *doa4*Δ, *vld1*Δ	6210.1, Cot1-GFP::KAN, *vld1*Δ::TRP1, *doa4*Δ::HIS3	This study
YXY764	Cot1-GFP, *doa4*Δ	6210.1, Cot1-GFP::KAN, ,*doa4*Δ::HIS3	This study
YXY767	Cot1-GFP, *doa4*Δ, *rsp5-1*	6210.1, Cot1-GFP::KAN, *rsp5-1*::TRP1, *doa4*Δ::HIS3	This study
YXY768	Cot1-GFP, *doa4*Δ, *rsp5-1*, *vld1* Δ	6210.1, Cot1-GFP::KAN, *vld1*Δ::NAT, *rsp5-1*::TRP1, *doa4*Δ::HIS3	This study
YXY755	Zrt3*-GFP, *doa4*Δ	6210.1, Zrt3*-GFP::KAN, *doa4*Δ::HIS3	This study
YXY754	Zrt3*-GFP, *doa4*Δ, *ssh4*Δ	6210.1, Zrt3*-GFP::KAN, *ssh4*Δ::TRP1, *doa4*Δ::HIS3,	This study
YXY753	Zrt3*-GFP, *doa4*Δ, *vld1*Δ	6210.1, Zrt3*-GFP::KAN, *vld1*Δ::TRP1, *doa4*Δ::HIS3	This study
YXY785	Zrt3*-GFP, *doa4*Δ, *rsp5-1*	6210.1, Zrt3*-GFP::KAN, *rsp5-1*::TRP1, *doa4*Δ::HIS3	This study
YXY786	Zrt3*-GFP, *doa4*Δ, *rsp5-1*, *vld1* Δ	6210.1, Zrt3*-GFP::KAN, *vld1*Δ::NAT, *rsp5-1*::TRP1, *doa4*Δ::HIS3	This study
YXY824	Ypl162c-GFP, *doa4*Δ	6210.1, Ypl162c-GFP::TRP1, *doa4*Δ::HIS3	This study

YXY825	Ypl162c-GFP, *doa4*Δ, *pib1*Δ	6210.1, Ypl162c-GFP::TRP1, *doa4*Δ::HIS3, *pib1*Δ::HYG	This study
YXY489	*pib1*Δ	6210.1, *pib1*Δ::HYG	This study
MAY143	Vps4-eGFP	6210.1, VPS4-3HA-GFP::TRP1	(Adell et al., 2017)
S. cerevisiae plasmids			
vector	***name***	***description***	***reference/source***
pCM189	VBA4-GFP	Tet-off vector, tet-O7+ endogenous promoter C-terminal GFP	This study
pCM189	VPH1-GFP	Tet-off vector, tet-O7+ endogenous promoter C-terminal GFP	This study
pCM189	ZRT3*-GFP	Tet-off vector, tet-O7+ endogenous promoter C-terminal GFP	This study
pCM189	FTH1-GFP	Tet-off vector, tet-O7+ endogenous promoter C-terminal GFP	This study
pCM189	FET5-GFP	Tet-off vector, tet-O7+ endogenous promoter C-terminal GFP	This study
pCM189	ZRC1-GFP	Tet-off vector, tet-O7+ endogenous promoter C-terminal GFP	This study
pCM189	COT1-GFP	Tet-off vector, tet-O7 promoter C-terminal GFP	(Li et al., 2015a)
pCM189	YPQ1-GFP	Tet-off vector, tet-O7+ endogenous promoter C-terminal GFP	This study
pCM189	YPQ2-GFP	Tet-off vector, tet-O7+ endogenous promoter C-terminal GFP	This study
pCM189	GFP-PIB1	Tet-off vector, tet-O7 promoter N-terminal GFP	This study
pRS425	pCu-myc-ub	Copper promoter, Myc-tagged Ubiquitin	(Li et al., 2015a)

Supplemental Table 2.2: Primers used in this study		
Primers	***sequence***	***purpose***
VLD1-500-For	ACTCGATGGCCCTTTCCATGGCAC	ChIP
VLD1-500-Rev	CAGAGATACTTGAATCTTAGGCACT	ChIP
VLD1-1000-For	TTTAGCAGCTGCTCTACCGAAGC	ChIP
VLD1-1000-Rev	GCCTGCTCGACCAAGAACGGGCAT	ChIP
ATG8-150-For	ATGTAATGCTAACTGTCTCCACC	ChIP
ATG8-150-Rev	CTCCTCAACCTTTAATGGTTCCC	ChIP
ATG8-700-For	GTTGGAGGTTGCCGGTATTGA	ChIP
ATG8-700-Rev	GTCGGTTCTGGTTTCTTGTCC	ChIP
VLD1-RT-For	AAAGGTCAGTGATAGCGAATTT	qPCR
VLD1-RT-Rev	AGTACGCTGTTTCTAGAAGTATTAG	qPCR
UBC6-RT-For	GATACTTGGAATCCTGGCTGGTCTGTCTC	qPCR
UBC6-RT-Rev	AAAGGGTCTTCTGTTTCATCACCTGTATTTGC	qPCR

2.5 References:

Adell MAY, Migliano SM, Upadhyayula S, et al. Recruitment dynamics of ESCRT-III and Vps4 to endosomes and implications for reverse membrane budding. *Elife*. 2017;6:e31652. Published 2017 Oct 11. doi:10.7554/eLife.31652

Ammerer G, Hunter CP, Rothman JH, Saari GC, Valls LA, Stevens TH. PEP4 gene of Saccharomyces cerevisiae encodes proteinase A, a vacuolar enzyme required for processing of vacuolar precursors. *Mol Cell Biol*. 1986;6(7):2490-2499. doi:10.1128/mcb.6.7.2490-2499.1986

Aparicio O, Geisberg JV, Struhl K. Chromatin immunoprecipitation for determining the association of proteins with specific genomic sequences in vivo. *Curr Protoc Cell Biol*. 2004;Chapter 17:. doi:10.1002/0471143030.cb1707s23

Babst M, Sato TK, Banta LM, Emr SD. Endosomal transport function in yeast requires a novel AAA-type ATPase, Vps4p. *EMBO J*. 1997;16(8):1820-1831. doi:10.1093/emboj/16.8.1820

Backues SK, Lynch-Day MA, Klionsky DJ. The Ume6-Sin3-Rpd3 complex regulates ATG8 transcription to control autophagosome size. *Autophagy*. 2012;8(12):1835-1836. doi:10.4161/auto.21845

Bartholomew CR, Suzuki T, Du Z, et al. Ume6 transcription factor is part of a signaling cascade that regulates autophagy. *Proc Natl Acad Sci U S A*. 2012;109(28):11206-11210. doi:10.1073/pnas.1200313109

Belle A, Tanay A, Bitincka L, Shamir R, O'Shea EK. Quantification of protein half-lives in the budding yeast proteome. *Proc Natl Acad Sci U S A*. 2006;103(35):13004-13009. doi:10.1073/pnas.0605420103

Burd CG, Emr SD. Phosphatidylinositol(3)-phosphate signaling mediated by specific binding to RING FYVE domains. *Mol Cell*. 1998;2(1):157-162. doi:10.1016/s1097-2765(00)80125-2

Fujioka Y, Suzuki SW, Yamamoto H, et al. Structural basis of starvation-induced assembly of the autophagy initiation complex. *Nat Struct Mol Biol*. 2014;21(6):513-521. doi:10.1038/nsmb.2822

Garí E, Piedrafita L, Aldea M, Herrero E. A set of vectors with a tetracycline-regulatable promoter system for modulated gene expression in Saccharomyces cerevisiae. *Yeast*. 1997;13(9):837-848. doi:10.1002/(SICI)1097-0061(199707)13:9<837::AID-YEA145>3.0.CO;2-T

Hariri H, Speer N, Bowerman J, et al. Mdm1 maintains endoplasmic reticulum homeostasis by spatially regulating lipid droplet biogenesis. *J Cell Biol*. 2019;218(4):1319-1334. doi:10.1083/jcb.201808119

Hecht KA, O'Donnell AF, Brodsky JL. The proteolytic landscape of the yeast vacuole. *Cell Logist*. 2014;4(1):e28023. doi:10.4161/cl.28023

Hecht KA, Wytiaz VA, Ast T, Schuldiner M, Brodsky JL. Characterization of an M28 metalloprotease family member residing in the yeast vacuole. *FEMS Yeast Res*. 2013;13(5):471-484. doi:10.1111/1567-1364.12050

Holz MK, Ballif BA, Gygi SP, Blenis J. mTOR and S6K1 mediate assembly of the translation preinitiation complex through dynamic protein interchange and ordered phosphorylation events. *Cell*. 2005;123(4):569-580. doi:10.1016/j.cell.2005.10.024

Jin N, Mao K, Jin Y, et al. Roles for PI(3,5)P2 in nutrient sensing through TORC1. *Mol Biol Cell*. 2014;25(7):1171-1185. doi:10.1091/mbc.E14-01-0021
Kane PM. Disassembly and reassembly of the yeast vacuolar H(+)-ATPase in vivo. *J Biol Chem*. 1995;270(28):17025-17032.
Kraft C, Kijanska M, Kalie E, et al. Binding of the Atg1/ULK1 kinase to the ubiquitin-like protein Atg8 regulates autophagy. *EMBO J*. 2012;31(18):3691-3703. doi:10.1038/emboj.2012.225
Laplante M, Sabatini DM. mTOR signaling at a glance. *J Cell Sci*. 2009;122(Pt 20):3589-3594. doi:10.1242/jcs.051011
Li M, Koshi T, Emr SD. Membrane-anchored ubiquitin ligase complex is required for the turnover of lysosomal membrane proteins. *J Cell Biol*. 2015;211(3):639-652. doi:10.1083/jcb.201505062
Li M, Rong Y, Chuang YS, Peng D, Emr SD. Ubiquitin-dependent lysosomal membrane protein sorting and degradation. *Mol Cell*. 2015;57(3):467-478. doi:10.1016/j.molcel.2014.12.012
Li SC, Kane PM. The yeast lysosome-like vacuole: endpoint and crossroads. *Biochim Biophys Acta*. 2009;1793(4):650-663. doi:10.1016/j.bbamcr.2008.08.003
Lim CY, Zoncu R. The lysosome as a command-and-control center for cellular metabolism. *J Cell Biol*. 2016;214(6):653-664. doi:10.1083/jcb.201607005
MacDonald C, Stringer DK, Piper RC. Sna3 is an Rsp5 adaptor protein that relies on ubiquitination for its MVB sorting. *Traffic*. 2012;13(4):586-598. doi:10.1111/j.1600-0854.2011.01326.x
Manolson MF, Proteau D, Preston RA, et al. The VPH1 gene encodes a 95-kDa integral membrane polypeptide required for in vivo assembly and activity of the yeast vacuolar H(+)-ATPase. *J Biol Chem*. 1992;267(20):14294-14303.
Martina JA, Diab HI, Lishu L, et al. The nutrient-responsive transcription factor TFE3 promotes autophagy, lysosomal biogenesis, and clearance of cellular debris. *Sci Signal*. 2014;7(309):ra9. Published 2014 Jan 21. doi:10.1126/scisignal.2004754
McNally EK, Karim MA, Brett CL. Selective Lysosomal Transporter Degradation by Organelle Membrane Fusion. *Dev Cell*. 2017;40(2):151-167. doi:10.1016/j.devcel.2016.11.024
Mellman I, Fuchs R, Helenius A. Acidification of the endocytic and exocytic pathways. *Annu Rev Biochem*. 1986;55:663-700. doi:10.1146/annurev.bi.55.070186.003311
Müller M, Schmidt O, Angelova M, et al. The coordinated action of the MVB pathway and autophagy ensures cell survival during starvation. *Elife*. 2015;4:e07736. Published 2015 Apr 22. doi:10.7554/eLife.07736
Noda T. Regulation of Autophagy through TORC1 and mTORC1. *Biomolecules*. 2017;7(3):52. Published 2017 Jul 7. doi:10.3390/biom7030052
Oku M, Maeda Y, Kagohashi Y, et al. Evidence for ESCRT- and clathrin-dependent microautophagy. *J Cell Biol*. 2017;216(10):3263-3274. doi:10.1083/jcb.201611029
Parzych KR, Klionsky DJ. Vacuolar hydrolysis and efflux: current knowledge and unanswered questions. *Autophagy*. 2019;15(2):212-227. doi:10.1080/15548627.2018.1545821
Pedruzzi I, Dubouloz F, Cameroni E, et al. TOR and PKA signaling pathways converge on the protein kinase Rim15 to control entry into G0. *Mol Cell*. 2003;12(6):1607-1613. doi:10.1016/s1097-2765(03)00485-4
Perera RM, Zoncu R. The Lysosome as a Regulatory Hub. *Annu Rev Cell Dev Biol*. 2016;32:223-253. doi:10.1146/annurev-cellbio-111315-125125

Rehli M, Den Elzen N, Cassady AI, Ostrowski MC, Hume DA. Cloning and characterization of the murine genes for bHLH-ZIP transcription factors TFEC and TFEB reveal a common gene organization for all MiT subfamily members. *Genomics*. 1999;56(1):111-120. doi:10.1006/geno.1998.5588

Richter C, West M, Odorizzi G. Dual mechanisms specify Doa4-mediated deubiquitination at multivesicular bodies. *EMBO J*. 2007;26(10):2454-2464. doi:10.1038/sj.emboj.7601692

Robinson JS, Klionsky DJ, Banta LM, Emr SD. Protein sorting in Saccharomyces cerevisiae: isolation of mutants defective in the delivery and processing of multiple vacuolar hydrolases. *Mol Cell Biol*. 1988;8(11):4936-4948. doi:10.1128/mcb.8.11.4936-4948.1988

Sardiello M, Palmieri M, di Ronza A, et al. A gene network regulating lysosomal biogenesis and function. *Science*. 2009;325(5939):473-477. doi:10.1126/science.1174447

Sekito T, Nakamura K, Manabe K, et al. Loss of ATP-dependent lysine uptake in the vacuolar membrane vesicles of Saccharomyces cerevisiae ypq1Δ mutant. *Biosci Biotechnol Biochem*. 2014;78(7):1199-1202. doi:10.1080/09168451.2014.918489

Settembre C, Di Malta C, Polito VA, et al. TFEB links autophagy to lysosomal biogenesis. *Science*. 2011;332(6036):1429-1433. doi:10.1126/science.1204592

Settembre C, Fraldi A, Medina DL, Ballabio A. Signals from the lysosome: a control centre for cellular clearance and energy metabolism. *Nat Rev Mol Cell Biol*. 2013;14(5):283-296. doi:10.1038/nrm3565

Settembre C, Zoncu R, Medina DL, et al. A lysosome-to-nucleus signalling mechanism senses and regulates the lysosome via mTOR and TFEB. *EMBO J*. 2012;31(5):1095-1108. doi:10.1038/emboj.2012.32

Shin ME, Ogburn KD, Varban OA, Gilbert PM, Burd CG. FYVE domain targets Pib1p ubiquitin ligase to endosome and vacuolar membranes. *J Biol Chem*. 2001;276(44):41388-41393. doi:10.1074/jbc.M105665200

Simm C, Lahner B, Salt D, et al. Saccharomyces cerevisiae vacuole in zinc storage and intracellular zinc distribution. *Eukaryot Cell*. 2007;6(7):1166-1177. doi:10.1128/EC.00077-07

Soulard A, Cremonesi A, Moes S, Schütz F, Jenö P, Hall MN. The rapamycin-sensitive phosphoproteome reveals that TOR controls protein kinase A toward some but not all substrates. *Mol Biol Cell*. 2010;21(19):3475-3486. doi:10.1091/mbc.E10-03-0182

Tong Z, Kim MS, Pandey A, Espenshade PJ. Identification of candidate substrates for the Golgi Tul1 E3 ligase using quantitative diGly proteomics in yeast. *Mol Cell Proteomics*. 2014;13(11):2871-2882. doi:10.1074/mcp.M114.040774

Urban J, Soulard A, Huber A, et al. Sch9 is a major target of TORC1 in Saccharomyces cerevisiae. *Mol Cell*. 2007;26(5):663-674. doi:10.1016/j.molcel.2007.04.020

Wanke V, Cameroni E, Uotila A, et al. Caffeine extends yeast lifespan by targeting TORC1. *Mol Microbiol*. 2008;69(1):277-285. doi:10.1111/j.1365-2958.2008.06292.x

Willett R, Martina JA, Zewe JP, Wills R, Hammond GRV, Puertollano R. TFEB regulates lysosomal positioning by modulating TMEM55B expression and JIP4 recruitment to lysosomes. *Nat Commun*. 2017;8(1):1580. Published 2017 Nov 17. doi:10.1038/s41467-017-01871-z

Williams RM, Primig M, Washburn BK, et al. The Ume6 regulon coordinates metabolic and meiotic gene expression in yeast. *Proc Natl Acad Sci U S A*. 2002;99(21):13431-13436. doi:10.1073/pnas.202495299

Woolford CA, Daniels LB, Park FJ, Jones EW, Van Arsdell JN, Innis MA. The PEP4 gene encodes an aspartyl protease implicated in the posttranslational regulation of Saccharomyces cerevisiae vacuolar hydrolases. *Mol Cell Biol*. 1986;6(7):2500-2510. doi:10.1128/mcb.6.7.2500-2510.1986

Wright R. Transmission electron microscopy of yeast. *Microsc Res Tech*. 2000;51(6):496-510. doi:10.1002/1097-0029(20001215)51:6<496::AID-JEMT2>3.0.CO;2-9

Yang X, Arines FM, Zhang W, Li M. Sorting of a multi-subunit ubiquitin ligase complex in the endolysosome system. *Elife*. 2018;7:e33116. Published 2018 Jan 22. doi:10.7554/eLife.33116

Yang Z, Huang J, Geng J, Nair U, Klionsky DJ. Atg22 recycles amino acids to link the degradative and recycling functions of autophagy. *Mol Biol Cell*. 2006;17(12):5094-5104. doi:10.1091/mbc.e06-06-0479

Zhu L, Jorgensen JR, Li M, Chuang YS, Emr SD. ESCRTs function directly on the lysosome membrane to downregulate ubiquitinated lysosomal membrane proteins. *Elife*. 2017;6:e26403. Published 2017 Jun 29. doi:10.7554/eLife.26403

Chapter 3: A Conserved Ubiquitin- and ESCRT-dependent Pathway Internalizes Human Lysosomal Membrane Proteins for Degradation

The lysosome is an essential organelle to recycle cellular materials and maintain nutrient homeostasis, but the mechanism to down-regulate its membrane proteins is poorly understood. In this study, we performed a cycloheximide chase assay to measure the half-lives of ~30 human lysosomal membrane proteins and identified RNF152 and LAPTM4A as short-lived membrane proteins. The degradation of both proteins is ubiquitin-dependent. RNF152 is a transmembrane E3 ligase that ubiquitinates itself, whereas LAPTM4A uses its C-terminal PY motifs to recruit NEDD4 for ubiquitination. After ubiquitination, they are internalized into the lysosome lumen by the ESCRT machinery for degradation. Strikingly, when ectopically expressed in budding yeast, human RNF152 is still degraded by the vacuole (yeast lysosome) in an ESCRT-dependent manner. Thus, our study uncovered a conserved mechanism to down-regulate lysosome membrane proteins.

3.1 Introduction

As an essential organelle, the lysosome is responsible for various cellular processes, including protein turnover and recycling, energy metabolism, intracellular signaling, and nutrient storage (Lawrence & Zoncu, 2019; Shin & Zoncu, 2020; Yang & Wang, 2021). The lysosome membrane contains hundreds of transmembrane proteins, many of which are transporters and channels that shuttle metabolites (ions, amino acids, cholesterol, etc.) across the membrane (Schröder et al., 2007; Chapel et al., 2013; Bissa et al., 2016; Wyant et al., 2018). Malfunction of these lysosomal membrane proteins (LMPs) can give rise to inherited genetic disorders called lysosomal storage diseases (LSDs). Many LSD patients will develop severe neurodegeneration symptoms (Marques & Saftig, 2019). Furthermore, growing evidence suggests that mutations in LMPs and other lysosome dysfunction are associated with age-related neurodegeneration such as Alzheimer's disease, frontotemporal dementia, and Parkinson's disease (Nixon & Cataldo, 2006; Amick & Ferguson, 2017; Cook et al., 2012). As we age, the lysosome membrane gradually accumulates damaged proteins and loses its integrity, which dampens the cell's ability to remove pathogenic protein aggregates and damaged organelles, eventually leading to cell death and inflammation (Carmona-Gutierrez et al., 2016; Cheon et al., 2019; Yambire et al., 2019; Nixon, 2020). Strategies to maintain the lysosome membrane integrity during aging will likely delay the onset of neurodegenerative symptoms.

Given the physiological importance and clinical implications of LMPs, we wonder how human LMPs are regulated and quality controlled. At the organelle level, if the lysosomal membrane is mildly damaged by insults like lysosomotropic compounds, such as LLOME or iron-dependent oxidative stress, the endosomal sorting complexes required for transport (ESCRT) machinery can be recruited to the lysosome surface to repair the membrane (Mittal et

al., 2018; Radulovic et al., 2018; Skowyra et al., 2018). If the damage is too severe to be repaired, ruptured lysosomes will be sequestered and degraded by selective autophagy, a process termed lysophagy (Maejima et al., 2013; Hung et al., 2013).

At the protein level, selective removal of proteins from the lysosome surface is essential for adjusting membrane composition in response to environmental cues. However, very little is known about its underlying mechanism. A process like lysophagy, which engulfs whole lysosomes, could not accomplish selectivity. This leads to important questions as to how human lysosomes selectively downregulate their membrane proteins and what machinery might be involved in the process.

In this study, we screened ~30 human LMPs using a cycloheximide chase assay and identified a few candidates with short half-lives. Among those candidates, we focused on RNF152 (a lysosome membrane-anchored E3 ligase) and LAPTM4A (a four-transmembrane LMP) as cargoes to examine the possible mechanisms of LMP turnover. We discovered that their degradation is both ubiquitination- and lysosome-dependent. Further, we showed that the conserved ESCRT machinery plays a vital role in cargo internalization. Collectively, our work suggests that the ubiquitin- and ESCRT-dependent degradation pathway is a conserved and general mechanism to downregulate LMPs.

3.2 Results

3.2.1 Cycloheximide (CHX) chase screen to determine the half-lives of LMPs

To identify fast-degrading lysosome membrane substrates, we collected more than 30 GFP- or mCherry-tagged human lysosome membrane proteins. These proteins were identified as lysosomal by either microscopy or Mass Spectrometry studies (Schröder et al., 2007; Chapel et al., 2013; Schwake et al., 2013; Bissa et al., 2016; Wyant et al., 2018). We transiently expressed

them in HEK293 cells and determined their half-lives using a cycloheximide chase assay (Kao et al., 2015). Here, we present some examples of the screen (Fig 1A-B, Fig S1, and Table S2). While most LMPs are very stable (TMEM175, PQLC2, CTNS, CLCN7, LAMP2, and TMEM192), a few LMPs have a relatively short half-life (LAPTM4A $t_{1/2}$=11.0 hrs, RNF152 $t_{1/2}$=6.7 hrs, and OCA2 $t_{1/2}$=5.6 hrs, Fig 1A-B). For LAPTM4A, RNF152, and OCA2, we confirmed their lysosome localization by co-staining with the lysosome-associated membrane protein 2 (LAMP2) (Fig 1C).

Although OCA2 has the fastest degradation, it is a melanosome protein absent in normal lysosomes (Sitaram et al., 2009). Studying the degradation of OCA2 in cells other than melanocytes may be physiologically irrelevant. Therefore, we focused on RNF152 and LAPTM4A to investigate the degradation pathway of lysosome membrane proteins.

3.2.2 RNF152 is a protein of short half-life

RNF152 is a single pass, Type-II transmembrane protein with 203 amino acids (Fig 2A). The predicted molecular weight is 23 kDa. It was recently characterized as a lysosome E3 ligase that negatively regulates MTORC1 activity by ubiquitinating RagA and Rheb (Deng et al., 2015; Deng et al., 2019). We generated an antibody to confirm that the overexpressed non-tagged RNF152 is also degraded (Fig 2B). However, this antibody failed to detect the endogenous RNF152 (Fig S2A). After slightly elevating the RNF152 level using a leaky TET-ON promoter, we were able to show the weakly expressed RNF152 is quickly degraded (Fig S2B). The BafA1 treatment can stabilize both endogenous and leaky expression RNF152 (Fig S2A-B). For further characterizing the mechanism of RNF152 degradation, we used the overexpressed GFP-RNF152. This fusion protein is still functional as it can interact and ubiquitinate RagA (Fig S2C).

The initial screen was conducted with transient transfection, which had a high variation of expression levels from cell to cell. Thus, we generated stable cell lines (HEK293 and HeLa) expressing GFP-RNF152 by lentivirus transduction. Repeating the CHX chase assay with these stable lines indicated that GFP-RNF152 is mostly degraded within 2 hours (Fig 2C), which was much faster than the transient system. Besides western blots, we also used flow cytometry to confirm the fast degradation of GFP-RNF152 in both cell lines (Fig 2D).

Interestingly, we observed a 27kDa band that is about the size of free GFP in the CHX chase assay (Fig 2C). Because GFP is fused to the cytosolic side of RNF152 (Fig 2A), there are two possibilities to generate the 27 kDa band. First, GFP-RNF152 may be internalized into the lysosome, and free GFP is the by-product of degradation. Second, free GFP may be cleaved off RNF152 due to the instability of the fusion protein. In this case, free GFP would be in the cytosol. To differentiate between these two possibilities, we adopted the Lyso-IP experiment developed by the Sabatini group (Abu-Remaileh et al., 2017). It uses TMEM192-3HA, a lysosome-specific membrane protein, as the bait to pull down intact lysosomes. As expected, full-length GFP-RNF152 and other lysosome proteins such as LAMP2 and cathepsin D (CTSD) were enriched by Lyso-IP. In contrast, PDI (ER), Golgin160 (Golgi), EEA1 (endosomes), and GAPDH (cytosol) were absent (Fig 2E). Importantly, we found the 27 kDa band was also enriched by Lyso-IP, indicating that free GFP is inside the lumen. Thus, RNF152 may be internalized and degraded in the lysosome.

Lastly, a small fraction of RNF152 was also reported to localize to endosomes (Xiong et al., 2020). To ensure that the lysosome population of RNF152 is fast-degrading, we performed the Lyso-IP experiment using cells collected before and after 2 hours of CHX treatment. Our

result confirmed that the lysosome population of GFP-RNF152 is rapidly turned over, while LAMP2 is very stable (Fig 2F).

3.2.3 RNF152 degradation is ubiquitination-dependent

Protein ubiquitination is the prerequisite for degradation in eukaryotic cells. Given that RNF152 has a short half-life, we hypothesized that RNF152 might be ubiquitinated. The full-length GFP-RNF152 migrates at 50 kDa. Interestingly, we observed a faint 60 kDa band that might be the mono-ubiquitinated form (Fig 3A, left panel). After longer exposure, a high-molecular-weight smear appeared on top of the full-length protein (Fig 3A, right panel). Could this smear be the poly-ubiquitinated GFP-RNF152? To answer this, we transfected HA-tagged ubiquitin into cells that stably express either GFP-RNF152 or GFP control, followed by immunoprecipitation using the GFP-TRAP nanobody. HA-ubiquitin was incorporated into the high-molecular-weight smear of GFP-RNF152, but not GFP control (Fig 3B). This result confirmed that a significant portion of GFP-RNF152 is poly-ubiquitinated.

To test if poly-ubiquitination is essential for the degradation, we mutated all eight lysines in the cytosolic domain of RNF152 to arginine (8K→R). As shown in Fig 3C-D, the 8K→R mutation increased the steady-state level of GFP-RNF152$_{8K\rightarrow R}$ (2.7 fold), and its degradation kinetics was significantly slower (Fig 3E).

Because RNF152 is a RING domain E3 ligase, we hypothesized that its degradation might be due to auto-ubiquitination. To test this, we mutated four cysteines of the RING finger motif to serines (4C→S mutant) (Deng et al. 2015). Similar to the 8K→R mutant, the steady-state protein level of GFP-RNF152$_{4C\rightarrow S}$ was increased by 2.8-fold (Fig 3C-3D), and the degradation kinetics was also significantly slower (Fig 3E). Lastly, the ubiquitin blots confirmed that both 8K→R and 4C→S mutants have reduced ubiquitination (Fig 3F).

Taken together, we concluded that the degradation of GFP-RNF152 is a ubiquitin-dependent process. The short half-life of GFP-RNF152 is likely due to auto-ubiquitination.

3.2.4 RNF152 is mainly degraded by the lysosome

In eukaryotic cells, there are two primary mechanisms to break down proteins: proteasome-dependent and lysosome-dependent proteolysis. The partial accumulation of GFP inside the lysosome suggests that RNF152 is degraded by the lysosome. To test this further, we treated cells with either lysosome v-ATPase inhibitor Bafilomycin A1 (BafA1) or proteasome inhibitor MG132. BafA1 treatment results in a rapid neutralization of lysosome pH and inhibition of the luminal proteases. After 6 hours of BafA1 treatment, the steady-state GFP-RNF152 level increased two-fold (Fig 4A-B). In contrast, MG132 treatment did not lead to a significant change in protein levels. The double treatment did not further increase the steady-state RNF152 than BafA1 alone.

We also observed an accumulation of a high-molecular-weight smear in the BafA1-treated sample and the double treatment sample (Fig 4A and 4C). Co-expressing HA-ubiquitin with GFP-RNF152 verified that they were poly-ubiquitinated (Fig 4D). These results suggest that the lysosome, but not proteasome, is the primary location to degrade RNF152.

We further confirmed our findings with both flow cytometry and microscopy. As shown in Fig 4E, the GFP intensity only increased slightly after MG132 treatment. In contrast, BafA1 treatment led to a major climb in GFP intensity. The BafA1+MG132 double treatment did not further increase the intensity. Consistently, under a microscope, we found the GFP signal was also much higher after BafA1 treatment (Fig 4F). Most of the GFP signal colocalized with LAMP2. Importantly, after deconvolving the imaging results (SoftWorx, GE Healthcare), we observed that much of the GFP signal was inside the lumen (line scan in Fig 4G). Similar results

were also obtained with a super resolution Leica Stimulated Emission Depletion (STED) microscope (Fig S3). The luminal GFP strongly supports a model that RNF152 is internalized into the lysosome and degraded by the luminal proteases.

Besides the steady-state protein levels, we also compared the degradation kinetics of GFP-RNF152. As shown in Fig S4, the degradation of GFP-RNF152 was blocked by BafA1 treatment, even after we extended the chase to 6 hours. In contrast, MG132 only delays the degradation of GFP-RNF152. Interestingly, we observed an increase of free GFP after both MG132 and BafA1 treatment. MG132 is known to partially inhibit some lysosome proteases such as Cathepsin A and Cathepsin B (Rock et al.; 1994; Shirley et al., 2005). The delayed degradation of GFP-RNF152 and increased free GFP signal in MG132 treated samples might be due to the reduced activity of some lysosome proteases.

Taken together, we concluded that RNF152 is degraded through lysosome-dependent proteolysis. For subsequent studies, we focused on identifying the machinery that delivers RNF152 into the lumen.

3.2.5 Macroautophagy machinery and CMA pathway are not involved in the degradation of GFP-RNF152

In mammalian cells, there are four possible mechanisms to deliver intracellular materials into lysosomes for degradation: macroautophagy, microautophagy, ESCRT-dependent formation of intraluminal vesicles, and chaperone-mediated autophagy (CMA) (Schuck et al., 2020). How is ubiquitinated RNF152 internalized into the lysosome then? Although lysophagy can deliver an entire damaged lysosome into other healthy lysosomes for degradation (Anding & Baehrecke, 2017), it cannot selectively turnover a particular membrane protein while leaving others intact. Recently, Overholzer and colleagues reported that glucose starvation and certain drug treatments

could trigger a microautophagy process to selectively turnover some LMPs. Although the mechanism remains to be identified, it was shown that the LC3 lipidation machinery, such as ATG5, is critical to initiate microautophagy (Lee et al., 2020). To test if this microautophagy is involved in RNF152 degradation, we knocked out either ATG5 or ATG7 using the CRISPR-Cas9 method (Ran et al., 2013; An et al., 2019). In wild-type cells, Atg5 forms a stable 55-kDa conjugate with Atg12 in an Atg7-dependent manner (Fig S5A, left three lanes) (Mizushima et al., 1998). After knocking out *ATG7*, the conjugate no longer forms, and ATG5 appears as a 33-kDa band (Fig S5A, last three lanes). However, neither *ATG5* nor *ATG7* knockout cells exhibited any defect in GFP-RNF152 degradation (Fig S5A-B).

Autophagy and the ubiquitin-proteasome system (UPS) are the two major pathways to degrade proteins in eukaryotic cells (Pohl & Dikic, 2019). There is mounting evidence to show that the two pathways can crosstalk. It is possible that the UPS pathway is upregulated to compensate for the loss of autophagy (Wang et al., 2013; Fan et al., 2018; Kocaturk & Gozuacik, 2018; Marshall & Vierstra, 2018). To rule out the possibility that GFP-RNF152 is re-directed to the proteasome after knocking out macroautophagy, we treated the *ATG7*KO cells with BafA1 and MG132. As shown in Fig S5C-D, GFP-RNF152 degradation is still mainly dependent on the lysosome in autophagy-deficient cells. Thus, the macroautophagy machinery and likely the LC3 lipidation-triggered microautophagy is not involved in RNF152 degradation.

We also examined whether chaperone-mediated autophagy is involved. In the CMA pathway, the chaperone Hsc70 recognizes a KFERQ-like motif of its substrates and delivers them to the lysosome for degradation (Cuervo & Wong, 2014). Using a web-based motif finder, we identified one putative KFERQ-like motif in the cytosolic domain of RNF152: ^{46}QKDVR^{50}

(Fig S5E) (Kirchner et al., 2019). However, mutating ^{46}QK^{47} to AA does not affect RNF152 degradation (Fig S5F-G), suggesting that the CMA pathway may not be involved.

3.2.6 The early-stage ESCRTs are less critical for GFP-RNF152 degradation

Next, we asked if ESCRT machinery is responsible for internalizing ubiquitinated GFP-RNF152. The ESCRT machinery is composed of several sub-complexes, including ESCRT-0, I, II, III, and the AAA-ATPase VPS4, all of which are conserved from yeast to human (Henne et al., 2011). ESCRTs usually function on the endosome surface to sort ubiquitinated cargoes into the lumen as intralumenal vesicles (ILVs) (Vietri et al., 2020). Besides the ILV formation, mammalian ESCRTs play diverse roles at different membrane compartments. Recently, it was demonstrated that the ESCRT machinery is involved in the repair of damaged lysosome membranes (Radulovic et al., 2018; Skowyra et al., 2018). However, whether the ESCRT machinery can internalize ubiquitinated lysosome membrane proteins remains an open question. To answer this, we knocked down different components of the ESCRT machinery and tested if they affect RNF152 degradation.

We first knocked down TSG101 (ESCRT-I, Vps23 in yeast) and PDCD6IP/ALIX (accessory unit, Bro1 in yeast) using siRNA because they are required to recruit ESCRT-III for lysosome membrane repair (Radulovic et al., 2018; Skowyra et al., 2018). Knocking down PDCD6IP/ALIX alone did not affect RNF152 degradation. However, knocking down either TSG101 or both TSG101 and PDCD6IP/ALIX had a slight impact on the degradation kinetics (Fig S6A-B). There was also a marginal increase of the ubiquitinated GFP-RNF152 in TSG101 knockdown and TSG101+ PDCD6IP/ALIX double knockdown groups (Fig S6A).

We then tested ESCRT-0 and ESCRT-II by knocking down HGS/HRS (Vps27 in yeast) and VPS22, respectively. Both knockdowns had a minor impact on the degradation of GFP-

RNF152 (Fig S6C-D). In the case of VPS22, there was a slight rise of the ubiquitinated GFP-RNF152 (Fig S6C).

To ensure the siRNA knockdown methods can disrupt the function of ESCRT machinery, we stained the cells with the FK2 antibody that specifically recognizes poly-ubiquitin (Firkowska et al., 2019). Since ESCRT machinery is responsible for internalizing ubiquitinated proteins from the endosome membrane, depleting ESCRTs will lead to the accumulation of poly-ubiquitinated proteins at the endosome surface. Indeed, after knocking down either TSG101+ PDCD6IP/ALIX or VPS22, we observed enlarged vacuole-like structures that stained positive for FK2 antibody (Fig S6E). In HGS/HRS knockdown, we did not observe the accumulation of poly-ubiquitin signals (Fig S6E) even though the western blot showed a pronounced reduction of the HGS/HRS level (Fig S6C).

Taken together, we concluded that early ESCRT components, especially TSG101, might play a role in RNF152 degradation. However, the relatively weak phenotypes suggested other redundant components might be involved to recruit the ESCRT-III.

3.2.7 The late-stage ESCRTs are important for GFP-RNF152 degradation

We then tested the ESCRT-III components, which polymerize into spiral filaments to drive the internalization of ubiquitinated membrane cargoes. After knocking down both CHMP4A and CHMP4B (Snf7 in yeast), the degradation of GFP-RNF152 is significantly delayed, as demonstrated by both western blots (Fig 5A-B) and flow cytometry (Fig 5C). Besides, we observed a substantial accumulation of ubiquitinated GFP-RNF152 (Fig 5A). We also used imaging to check the internalization of RNF152. In the siRNA control, GFP-RNF152 accumulated in the lumen after BafA1 treatment. However, it was stabilized on the membrane of vacuole-like structures after the double knockdown of CHMP4A and CHMP4B (Fig 5D-E).

Together, these results indicated that ESCRT-III plays a critical role in the degradation of GFP-RNF152.

Besides ESCRT-III, we also tested the AAA-ATPase VPS4 responsible for the disassembly of ESCRT-III filaments (Adell et al., 2017). Here, we used an inducible TET-ON system to overexpress either HA-VPS4A or its dominant-negative mutant E228Q (Takahashi et al., 2018). Overexpression of both wild-type HA-VPS4A and the E228Q mutant delayed the degradation of GFP-RNF152, with the EQ mutant having a more potent effect (Fig 5F-G). Consistent results were also observed by flow cytometry analysis (Fig 5H). Furthermore, for both WT and E228Q mutant, we observed the accumulation of poly-ubiquitinated GFP-RNF152 (Fig 5F). These results demonstrated that 1) VPS4 is important for RNF152 degradation, and 2) overexpression of wild-type HA-VPS4A also partially disrupts the ESCRT function, likely due to its HA tag.

To further confirm the importance of VPS4, we stained the cells with the FK2 antibody that recognizes poly-ubiquitin. Overexpression of both WT and the E228Q mutant showed an accumulation of FK2 positive signals, with the mutant having a much stronger effect (Fig S7). Specifically, after overexpressing WT HA-VPS4A, ~50% of cells displayed FK2 positive signals on enlarged vacuole-like structures. In contrast, with the E228Q mutant, more than 90% of cells were stained positive for FK2 antibody, and vacuoles were much more prominent. These results were consistent with the analysis using GFP-RNF152 in Fig 5F-H.

Taken together, our results strongly suggest that the late-stage ESCRT machinery, specifically ESCRT-III and VPS4, are critical for the degradation of GFP-RNF152.

3.2.8 Degradation of LAPTM4A depends on NEDD4 and the ESCRT machinery

To test if the ubiquitin- and ESCRT-dependent LMP degradation is a general mechanism, we characterized the turnover of LAPTM4A. It contains four transmembrane helices, with both N- and C- termini facing the cytoplasm (Fig 6A). Recent studies revealed that LAPTM4A is required for Gb3 (globotriaosylceramide) synthesis (Tian et al., 2018; Yamaji et al., 2019). However, its localization remains controversial. One study reported that overexpressed LAPTM4A localized to Golgi (Tian et al., 2018), which is inconsistent with our observation (Fig 1C). We first confirmed that endogenous LAPTM4A is lysosome-localized and quickly degraded (Fig 6B-C). As shown in fig 6B, the endogenous LAPTM4A was co-purified with lysosomes, whereas the Golgi marker Golgin 160 was absent. Besides the 22 kDa full-length LAPTM4A, we also observed a 17 kDa truncation product (asterisk, Fig 6B). Both bands were rapidly degraded after adding CHX (Fig 6C).

In addition to the endogenous protein, we also characterized stably expressed LAPTM4A-GFP. Consistently, LAPTM4A-GFP appeared as two major bands (50 and 45 kDa), and both bands decreased after CHX treatment (Fig 6D). Pretreating cells with BafA1, but not MG132, stabilized the protein by more than two-fold (Fig 6E-F). Besides, there was an accumulation of a high molecular weight smear in BafA1 treated samples (Fig 6F), which was confirmed as the polyubiquitinated LAPTM4A-GFP (Fig 6G). But what E3 ligase might be responsible for its ubiquitination?

Examining the protein sequence revealed that LAPTM4A contains three conserved PY motifs at its C-terminus (PPxY or LPxY, where x can be any amino acid, Fig 6A). The PY motif has been implicated in recruiting the NEDD4 family E3 ligases to various membrane compartments (Staub et al., 2000; Milkereit et al., 2011; Li et al., 2015b; Hirota et al., 2021;

Sardana & Emr, 2021). We confirmed that LAPTM4A does interact with NEDD4, which depends on its PY motifs (Fig 6H). Following this clue, we either mutated all three PY motifs or knocked down NEDD4. In both experiments, LAPTM4A was stabilized (Fig 6I-J). Together, they support a model where NEDD4 is recruited to the lysosome membrane to ubiquitinate LAPTM4A by interacting with its PY motifs (Fig 6K).

We then tested if the ESCRT machinery is essential for LAPTM4A degradation. Like RNF152, knocking down HGS/HRS and VPS22 had either no effect (HGS/HRS) or only a minor effect (VPS22) on the degradation. In contrast, the double silencing of both TSG101 and PDCD6IP/ALIX had a more substantial impact, and an accumulation of the ubiquitinated LAPTM4A was observed (Fig 7A-B). Knocking down the ESCRT-III (CHMP4A+CHMP4B) had an even stronger impact on LAPTM4A degradation and the accumulation of polyubiquitinated forms (Fig 7C-D). Similar strong effects were also observed when we overexpressed the dominant-negative E228Q mutant of VPS4A (Fig 7E-F). Lastly, we confirmed that endogenous LAPTM4A degradation also depends on late ESCRT, such as CHMP4A and CHMP4B (Fig 7G-H).

In summary, our analysis of LAPTM4A further supports that the ubiquitin- and ESCRT-dependent pathway is a general mechanism to degrade LMPs.

3.2.9 A conserved pathway from yeast to human

Fundamental biological processes are generally conserved. Here, our study uncovered a ubiquitin- and ESCRT- dependent pathway in humans to degrade lysosome membrane proteins. Is this pathway conserved in yeast? To directly answer the question, we expressed GFP-RNF152 in budding yeast. To our satisfaction, GFP-RNF152 is still correctly localized to the vacuole membrane (Fig 8). Strikingly, when protein synthesis was stopped by cycloheximide, GFP-

RNF152 was quickly internalized into the lumen and degraded (Fig 8A-B). Deletion of *PEP4*, the master vacuolar protease critical for activating other luminal proteases (Ammerer et al., 1986; Woolford et al., 1986), stopped the degradation (Fig 8A-B).

We then systematically deleted components of the ESCRT subcomplexes, including *VPS27* (ESCRT-0), *VPS23* (ESCRT-I), *VPS22* (ESCRT-II), *SNF7* (ESCRT-III), *VPS4* (AAA-ATPase), and *BRO1* (PDCD6IP/ALIX homolog). As shown in Fig 8C, deleting any ESCRT components stabilized GFP-RNF152 on the vacuole membrane. These results indicated that the ESCRT machinery is critical for the internalization and degradation of GFP-RNF152 in yeast. Unlike human cells, early-stage ESCRTs are just as crucial as the late-stage ESCRTs in yeast, suggesting that humans may have evolved an alternative mechanism to recruit late-stage ESCRTs onto the lysosome.

In summary, our investigation indicated that the ubiquitin- and ESCRT-dependent LMP turnover is a conserved mechanism from yeast to humans (Fig 8D).

3.3 Discussion

3.3.1 Different ESCRT requirements between yeast and human lysosomes

This study uncovered a ubiquitin and ESCRT- dependent pathway to down-regulate human LMPs such as RNF152 and LAPTM4A. Strikingly, when expressed in budding yeast, RNF152 is also degraded by a similar mechanism (Fig 8). Previously, we and others have demonstrated that yeast uses the same pathway to regulate vacuole membrane proteins (Li et al., 2015a; Li et al., 2015b; Oku et al., 2017; Yang e al., 2018; Yang et al., 2020). For example, the Ssh4-Rsp5 E3 ligase complex ubiquitinates Ypq1 (a vacuolar lysine transporter) when lysine is depleted from the media (Li et al., 2015b; Arines et al., 2021). After ubiquitination, vacuole

membrane proteins are internalized by the ESCRT machinery for degradation (Li et al., 2015a; Oku et al., 2017; Yang et al., 2018; Yang et al., 2020 Morshed et al., 2020; Yang et al., 2021).

Although the pathway is conserved, we noticed significant differences between yeast and human. In budding yeast, knocking out every sub-complex of the ESCRT machinery (ESCRT-0, I, II, III, and Vps4) stabilizes RNF152 on the membrane (Fig 8). But in humans, early ESCRTs seem to be less important (Fig S4 and 7A-B). Only ESCRT-III (CHMP4A and CHMP4B) and VPS4 are essential for the degradation (Fig 5 and 7C-F). Our results are consistent with a previous study showing that starvation-induced turnover of autophagy receptors by endosomal microautophagy depends on ESCRT-III and VPS4, but not early ESCRTs (ESCRT-0, -I, and –II) (Mejlvang et al, 2018).

One possible explanation could be the functional redundancy among early components. Interestingly, many early ESCRTs share functional domains or binding features. For example, both HGS/HRS (ESCRT-0) and VPS28 (ESCRT-II) contain PI3P binding domains (Christ et al., 2017). Also, many ESCRT components, including HGS/HRS, STAM and STAM2 (ESCRT-0), TSG101, MVB12A&B (ESCRT-I), Vps36 (ESCRT-II), and PDCD6IP/ALIX, are all ubiquitin-binding proteins (Haglund & Dikic, 2012). Therefore, it is possible that some early ESCRT components are functionally redundant.

Alternatively, it is also possible that human lysosomes may have evolved other ways to recruit the late-stage ESCRTs. Besides the classic role of ILV formation, ESCRTs have evolved a variety of functions on different membranes, such as plasma membrane repair, budding of viral particles, midbody formation during cytokinesis, and closure of the autophagosome. All these functions require ESCRT-III and VPS4, which are directly responsible for membrane deformation (Vietri et al., 2020). However, the corresponding proteins to recruit ESCRT-III at

different membranes are different. For example, ESCRT-0, CEP55, and viral Gag proteins can all recruit ESCRT-III to distinct membrane surfaces (Vietri et al., 2020). Identifying the new lysosome recruitment factors will require further investigation.

3.3.2 Multiple pathways may be involved in the selective turnover of LMPs

Besides the ESCRT-dependent pathway uncovered by this paper, recent studies have suggested other mechanisms might be involved in LMP degradation. First, Overholzer and colleagues showed that LC3 lipidation-triggered microautophagy is responsible for the selective turnover of several LMPs, including TRPML1 and SNAT7 (SLC38A7) (Lee et al., 2020). However, there are still many unanswered questions about this pathway. For example, how does ATG5-dependent microautophagy achieve its selectivity? It is unclear what machinery is responsible for selecting cargo proteins and how selected LMPs are sorted into microautophagy. Despite all these questions, ATG5-dependent microautophagy provides an exciting model for the selective turnover of some LMPs. Although our study did not find evidence that this microautophagy is responsible for the degradation of RNF152, it is still possible that these two pathways may operate in parallel to regulate different subsets of LMPs.

The proteasome-dependent degradation is another well-characterized and conserved pathway to down-regulate membrane proteins. The best-known example is the ER-associated degradation (ERAD) pathway, in which misfolded proteins were ubiquitinated by the E3 ligases at the endoplasmic reticulum, extracted by the AAA ATPase VCP/p97 (Cdc48 in yeast), and sent to the proteasome for degradation (Sun et al., 2019). Interestingly, several recent studies showed that p97 could be recruited to the lysosome to facilitate lysophagy (Papadopoulos et al., 2017; Koerver et al., 2019). It is possible that some LMPs extracted by p97 can be delivered to the proteasome for degradation (Papadopoulos & Mayer, 2017). As we are still at the early stage of

understanding lysosome membrane degradation, how ESCRTs, autophagy, and proteasome may coordinate to regulate its membrane composition remains an exciting puzzle.

3.4 Materials and Methods

Mammalian cell culture

All mammalian cell lines used in this study are listed in Table S1. The following cell lines were obtained from ATCC: HEK293 (CRL-1573), HEK293T (CRL-3216) and, HeLa (CCL-2). Cells were cultured in DMEM (Invitrogen) containing 10% Super Calf Serum (Gemini), 1% penicillin and streptomycin (Invitrogen) and 1μg/ml plasmocin (Invivogen) at 37°C, 5% CO_2. All cells were tested negative for mycoplasma contamination using Mycoalert mycoplasma detection kit (Lonza).

Plasmids

All mammalian plasmids used in this study are listed in Table S2. Most of the LMP overexpression plasmids were purchased from GeneCopoeia. The CDS of RNF152 was purchased from Horizon Discovery. The CDS of LAPTM4A was purchased from GeneCopoeia.The 4C→S and QK→AA mutants of RNF152 and 3 PY mutant of LAPTM4A were generated by PCR-based site-directed mutagenesis. The 8K→R mutant of RNF152 was synthesized as a gBlock gene fragment by Integrated DNA Technologies.

To generate transfer plasmids for GFP-RNF152 stable cell lines, EGFP was fused to the N-terminal of RNF152 (WT or mutants) using PCR-based overlapping extension, with 2X Gly-Gly-Gly-Ser linker in between. Then, EGFP-RNF152 was cloned into the pHAGE2-IRES-puro vector using restriction enzymes NotI and BamHI. For LAPTM4A-GFP (WT or mutants), GFP was fused to the C-terminal of the LAPTM4A, and then cloned into pHAGE2-IRES-puro vector. To generate mCherry selection transfer plasmids, mCherry was amplified from the pmCherry-N1 (Clontech) vector and cloned into a pHAGE2 vector to replace the puromycin-resistant gene using restriction enzymes NdeI and ClaI. To generate transfer plasmids for 3XFLAG-RNF152

stable cell lines, RNF152 (WT or mutants) was cloned into the pBICEP-CMV2-3XFLAG (Millipore-Sigma) vector using restriction enzymes SalI and BamHI. Then, 3XFLAG-RNF152 was cloned into pHAGE2-IRES-Puro vector using restriction enzymes NcoI and BamHI.

The CDS of Vps4A E228Q was purchased from Addgene (80351). Vps4A E228Q was cloned into the pCMV-HA (Clontech) vector using restriction enzymes EcoRI and NotI. The WT HA-Vps4A was obtained by using PCR-based site-directed mutagenesis. Then the WT HA-Vps4A and HA-Vps4A E228Q were cloned into pCW57.1 (Addgene 41393) using restriction enzymes NheI and AgeI.

Transfection and cycloheximide chase screen

HEK293 cells were cultured in DMEM containing 10% serum-only media for at least 4 days before transfection. Cells were transfected with individual overexpression plasmids (2.4 µg DNA for a 3.5cm dish) using Lipofectamine 2000 (Invitrogen) according to the manufacturer's instruction. After 20-24 hours of transfection, cells were treated with 100 µg/ml cycloheximide (Millipore-Sigma). At indicated chase time, cell samples were collected in ice-cold 1XPBS, pelleted at 800xg for 1 minute, and stored at -80°C before subsequent western blot analysis.

Generation of Lentiviral stable cell lines and shRNA knockdown

Stable cell lines were generated as described in Abu-Remaileh et al. 2017 with some modifications. HEK293T cells were transfected with transfer plasmid, psPAX2 (Addgene 12260), and pMD2.G (Addgene 12259) at 3.5:3.5:1 ratio using Lipofectamine 2000 according to the manufacturer's instruction. Three days after transfection, the virus-containing supernatant was collected using a 5ml syringe and applied through a 0.45 µm filter. To generate stable cell lines, HEK293, HEK293T or HeLa cells were seeded in 3.5cm dishes and infected with the infectious media (DMEM containing 10% super calf serum, 10 µg/ml polybrene, MOI between

0.3 to 0.4). For puromycin selection, the media was refreshed with DMEM containing 10% super calf serum and 1 μg/ml puromycin. The selection lasted for at least 7 days before subsequent analysis. For mCherry selection cells (pHAGE2-GFP-RNF152-IRES-mCherry and pHAGE2-LAPTM4A-GFP-IRES-mCherry), the media was refreshed with DMEM containing 10% super calf serum. Three days after transduction, cells with proportional GFP vs. mCherry expression were enriched by FACS. Sorting was repeated 7 days after the first round of FACS.

For shRNA knockdown, the shRNA was cloned into pLKO.1 (Addgene 8453). HEK293 cells were infected with infectious media DMEM containing 10% super calf serum, 10 μg/ml polybrene. After 72 hours, cells were subjected to subsequent cycloheximide chase and western blotting analysis,

The following shRNA sequence for NEDD4 knockdown was used in this study: NEDD4: 5'- CCGGGCTGAACTATACGGTTCAAATCTCGAGATTTGAACCGTATAGTTCAGCTTTTTG-3'

siRNA knockdown

HEK293 cells were cultured in DMEM containing 10% serum only media for at least 4 days before siRNA knockdown. Cells were transfected with siRNAs using Lipofectamine RNAimax (Invitrogen) according to the manufacturer's instruction. After 24 hours, cells were transfected with the same amount of siRNA again. Seventy-two hours after the first round of transfection, cells were subjected to subsequent western blotting, immunostaining, or flow cytometry analysis.

The following siRNA sequences were used in this study at indicated concentration: TSG101 (50nM): 5'-CCUCCAGUCUUAUCUCGUC-dTdT-3' (Skowyra et al., 2018)

PDCD6IP/ALIX (50nM): 5’-CCUGGAUAAUGAUGAAGGATT-dTdT-3’ (Skowyra et al., 2018)

VPS22 (50nM): 5'-CUUGCAGAGGCCAAGUAUA-dTdT-3' (Christ et al., 2017)

HGS/HRS (50nM): 5’-CGACAAGAACCCACACGU-dTdT-3’ (Bache et al., 2003)

CHMP4A (100nM): 5’-GGCACAAACUGACGGGACA-dTdT-3’ (Maminska et al., 2016)

CHMP4B (100nM): 5’-CGAUAAAGUUGAUGAGUUA-dTdT-3’ (Mejlvang et al., 2018)

ON-TARGETplus Non-targeting Pool (50nM, Dharmacon): 5’-UGGUUUACAUGUCGACUAA-3’, 5’-UGGUUUACAUGUUGUGUGA-3’, 5’-UGGUUUACAUGUUUUUCUGA-3’, 5’-UGGUUUACAUGUUUUCCUA-3’.

Generation of CRISPR-Cas9 KO cell lines

ATG5 and *ATG7* knockout HEK293 cells were generated as described (Ran et al., 2013). The sgRNA guides for ATG5 and ATG7 CRISPR-Cas9 knockout were described in An et al., 2019: 5’-GATCACAAGCAACTCTGGAT-3' for ATG5, and 5’-ATCCAAGGCACTACTAAAAG-3' for ATG7 (An et al., 2019). In brief, sgRNA guides were ligated into pspCas9(BB)-2A-Puro (Addgene, 48139) plasmid. HEK293 cells were transfected with CRISPR-Cas9 knockout plasmids using Lipofectamine 2000 according to the manufacturer's instruction. After 24 hours of transfection, cells were treated with 1μg/ml puromycin (Invitrogen) for 72 hours. Single cells were isolated into 96-well plates using limited dilution to a final concentration of 0.5 cell per well. The knockout colonies were screened by western blot analysis using antibodies against ATG5 and/or ATG7. The KO cell lines were further verified by sequencing analysis to confirm the indels at target sites.

Yeast strains, plasmids, media, and growth conditions

All yeast strains and plasmids used in this study are listed in Table S3. Difco Yeast Nitrogen Base (YNB) w/o amino acids were purchased from Millipore-Sigma. Yeast strains were grown in YNB at 26°C before further analysis.

Mammalian sample preparation and western blotting

Cells were collected in ice-cold 1XPBS, pelleted at 800xg for 1 minute, and lysed in lysis buffer (20mM Tris pH=8.0, 150mM NaCl, 1% Triton) containing 1Xprotease inhibitor cocktail (Biotool) at 4°C for 20 minutes. Cell lysates were centrifuged at 18,000 g for 15 minutes at 4°C. The protein concentration of the supernatant was measured by Bradford assay (Bio-rad) and normalized. After adding 2X urea sample buffer (150mM Tris pH 6.8, 6M Urea, 6% SDS, 40% glycerol, 100mM DTT, 0.1% Bromophenol blue), samples were heated at 65°C for 8 minutes. 20μg of each lysate was loaded and separated on 11% SDS-PAGE gel. Protein samples were transferred to nitrocellulose membrane for western blot analysis. After incubated with primary and secondary antibodies, membranes were scanned using the Odyssey CLx imaging system (LI-COR).

The following primary antibodies were used for western blotting in this study: rabbit anti-GFP (1:3000, TP401, Torrey Pines Biolabs), mouse anti-actin (1:5000, Proteintech), mouse anti-LAMP1 (1:1000, H4A3, DHSB), mouse anti-LAMP2 (1:1000, H4B4, DHSB), rabbit anti-CTSD (1:1000, Cell Signaling Technology), mouse anti-PDI (1:2000, BD Biosciences), rabbit anti-Golgin160 (1:1000, Proteintech), mouse-anti-EEA (1:500, G-4, Santa Cruz Biotechnology), rabbit-GAPDH (1:2000, Proteintech), mouse anti-ubiquitin (1:100, P4D1, Santa Cruz Biotechnology), rabbit anti-ATG5 (1:2000, D5FF5U, Cell Signaling Technology), rabbit anti-ATG7 (1:2000, D12B11, Cell Signaling Technology), rabbit anti-FLAG (1:2000, Millipore-Sigma), mouse anti-TSG101 (1:200, C-2, Santa Cruz Biotechnology), mouse anti-

PDCD6IP/ALIX (1:500, 1A12, Santa Cruz Biotechnology), mouse anti-Vps22 (1:500, C-11, Santa Cruz Biotechnology), rabbit anti-HGS/HRS (1:2000, D7T5N, Cell Signaling Technology), mouse anti-HA (1:1000, 16B12, BioLegend), rabbit anti-CHMP4B (1:2000, Proteintech), rabbit anti-LAPTM4A (1:1000, HPA, Millipore-Sigma).

The rabbit anti-RNF152 antibody was raised against the cytosolic domain of RNF152 (amino acid 1-166) expressed in BL21 Competent *E. coli*. The antibody was generated in rabbits by Covance Inc. The immunoreactive sera were further affinity-purified against immobilized RNF152 (1-166). This antibody was used at 1:500 dilution in western blot analysis.

The following secondary antibodies were used in this study: goat anti-mouse IRDye 680LT, goat anti-mouse IRDye 800CW, goat anti-rabbit IRDye 680LT, goat anti-rabbit IRDye 800CW. All secondary antibodies were purchased from LI-COR Biosciences and used at 1:10,000 dilution.

To detect the endogenous ubiquitin using a anti-Ub (P4D1, Santa Cruz) antibody, antigen retrieval was performed by boiling the membrane in 1XTBS for 30 minutes before blocking.

Yeast sample preparation and western blotting

Typically, 7 OD_{600} unit yeast cells were collected for sample preparation at each timepoint. The cells were first resuspended with 10% ice-cold TCA and incubated on ice for at least 1 hr. After washing with 0.1% TCA, the cell pellets were then resuspended in 70 µl 2× boiling buffer (150 mM Tris, pH 6.8; 6 M urea; 6% SDS; 10% glycerol; 100 mM DTT), lysed by bead beating for 5 minutes, and heat-treated at 65°C for another 5 minutes. After the addition of 70 µl 2 × urea sample buffer (50 mM Tris, pH 7.5; 6 M urea; 10 mM EDTA; 2% SDS; 100 mM DTT, and 0.1% bromophenol blue), samples were treated for another round of bead beating and 65°C heating for 5 minutes, respectively. After spinning at 13,000 g for 5 minutes, the

supernatant was collected, subjected to SDS-PAGE, and transferred to nitrocellulose membranes for western blotting analysis. One OD_{600} unit (20 µl) of yeast cells was loaded in each lane.

The following primary antibodies were used in this study: mouse anti-Pgk1 (1:5,000, 22C5D8; Invitrogen) and rabbit anti-GFP (1:3000, TP401, Torrey Pines Biolabs).

Immunostaining for mammalian samples

All incubation processes were performed in the dark. Cells grown on 1.5 circular glass coverslips were washed with ice-cold 1XPBS and fixed in cold 100% methanol for 8 minutes at -20°C. The fixed samples were blocked in 3% BSA (in 1XPBS) for 30 minutes at room temperature, followed by incubating with primary and secondary antibodies. The cell nucleus was stained using Hoechst (1:8000, Invitrogen). Coverslips were mounted in Fluoromount-G (SouthernBiotech) and cured for at least 24 hours before imaging.

The following primary antibodies were used for immunostaining in this study: mouse anti-LAMP2 (1:100, H4B4, DHSB), mouse anti-ubiquitin (1:100, FK2, Millipore-Sigma).

The following secondary antibodies were used in this study: FITC goat anti-mouse (1:100, Jackson ImmunoReseach) and TRITC goat anti-mouse (1:100, Jackson ImmunoResearch).

Microscopy and image processing

Samples were imaged with either a DeltaVision system (GE Healthcare Life Sciences) or a Leica SP8 confocal microscope system (Yang et al., 2018). The DeltaVision microscope was equipped with a scientific CMOS camera and an Olympus UPLXAP0100X objective. The filter sets FITC (excitation, 475/28; emission, 525/48), TRITC (excitation 542/27; emission 594/45), and DAPI (excitation 390/18; emission 435/48) were used for GFP, mCherry, and DAPI, respectively. Image acquisition and deconvolution were performed with the softWoRx program.

The Leica SP8 confocal microscope system was equipped with a Lecia PMT (photomultiplier tube) and a HyD (hybrid detector) light-detecting sensor systems. The Leica HC PL APO63X/1.40 Oil CS2 and HC PL APO100X/1.40 Oil STED White objectives were used in this study. Image acquisition was performed with the LAS X Life Science imaging software.

Images were further cropped or adjusted using ImageJ (National Institutes of Health).

Ubiquitin immunoprecipitation with GFP-Trap A nanobody

The HA-Ubiquitin plasmid was transfected into HEK293 cells that either stably express free GFP control, GFP-RNF152, or LAPTM4A-GFP. Immunoprecipitation was performed 48 hours post-transfection according to the manufacturer's instruction with some modifications. In brief, cells (one 10 cm dish of near-confluent cells per IP group) were collected in ice-cold 1XPBS, pelleted at 1000 g for 1 minute, and lysed in 300 µl of lysis buffer (20mM Tris pH=8.0, 150mM NaCl, 1% Triton) containing 100 mM of N-Ethylmaleimide (Millipore-Sigma) and 1Xprotease inhibitor cocktail (Biotool) at 4°C for 20 minutes. Cell lysates were centrifuged at 18,000 g for 15 minutes at 4°C. The concentration of the supernatant was measured by Bradford assay (Bio-rad) and normalized. 15 µl of GFP-Trap A (pre-equilibrated with lysis buffer, Chromotek) was added to 285µl of normalized cell lysate and incubated at 4°C for 2 hours with gentle rocking. The resin was then washed once with lysis buffer, three times with stringent washing buffer (8M Urea, 1%SDS in 1XPBS), and once with 1%SDS in 1XPBS. To elute bound proteins, the resin was incubated with 2X Urea sample buffer (150mM Tris pH 6.8, 6M Urea, 6% SDS, 40% glycerol, 100mM DTT, 0.1% Bromophenol blue) at 65°C for 10 minutes. The resulting eluates were analyzed by western blotting.

Lyso-IP

LysoIP was conducted as described before with some modifications (Abu-Remaileh et al., 2017). About $2X10^7$ cells in a 15cm dish were used for each LysoIP experiment. Cells were rinsed twice with cold PBS, scraped, and collected with 1ml KPBS (136 mM KCl, 10 mM KH_2PO_4, pH=7.25). Cells were centrifuged at 1000 g for 2 minutes at 4℃. Pelleted cells were resuspended in 1ml of KPBS with protease inhibitor and homogenized. The homogenate was then centrifuged at 1000 g for 2 minutes at 4℃. For input, 40µl of supernatant was taken (about 5% to the total amount) and mixed with 2X Urea sample buffer (150mM Tris pH 6.8, 6M Urea, 6% SDS, 40% glycerol, 100mM DTT, 0.1% Bromophenol blue). For IP, 800µl supernatant was incubated with 20µl anti-HA beads (Millipore-Sigma) and rotated for 20 minutes. The beads were washed with KPBS 6 times. To eluate bound lysosomes, the beads were resuspended in 40µl KPBS and 2X Urea sample buffer (150mM Tris pH 6.8, 6M Urea, 6% SDS, 40% glycerol, 100mM DTT, 0.1% Bromophenol blue). Samples were heated at 65°C for 10 minutes, followed by western blot analysis.

Flow cytometry analysis and FACS

Cells were washed with 1XPBS and trypsinized until all cells are dissociated from the dishes. Dissociated cells were neutralized with DMEM containing 10% serum media and pelleted at 300xg for 3 minutes. Cells were resuspended in ice-cold 1XPBS and analyzed using either an LSR Fortessa (BD Biosciences) or a Ze5 (Bio-rad) flow cytometer. For FACS, cells were sorted using FACSAria III cell sorter (BD Biosciences). Flow cytometry analysis and FACS were performed by technicians from the Flow Cytometry Core at the University of Michigan. The data were analyzed using FlowJo software.

Quantification and statistical analysis

The band intensity for western blot was quantified using Image Studio software (LI-COR). To calculate protein half-lives, the data were fitted to the first-order decay and the rate constant (k) was generated using Excel. The half-lives were calculated using the following equation: $t_{(1/2)} = \ln 2 / k$. Graphs were generated using Prism (GraphPad). Statistical analysis was performed with the two-tailed unpaired t-test or one-way ANOVA. Error bars represent the standard deviation. *: ≤0.05, **: ≤0.01, ***: ≤0.001.

Acknowledgments:

We thank the Li laboratory members, including F. Arines, G. Shi, A. Hamlin, and J. Zhang from the Wang laboratory, for their technical support. This research is supported by a startup fund, the MCubed 3.0 fund from the University of Michigan, and NIH grants GM133873 and GM133873-01S2 to ML, R35GM130331 to YW, R01GM122434 to PH.

Author contributions:

Conceptualization, WZ and ML; Methodology, WZ and ML; Investigation, WZ, XY, LC,YL, VV, LR, and ML; Some critical reagents, PH, HX, and YW, Writing & Editing, WZ, XY, and ML; Funding Acquisition, Resources, & Supervision, ML.

Declaration of interests

The authors declare no competing interests.

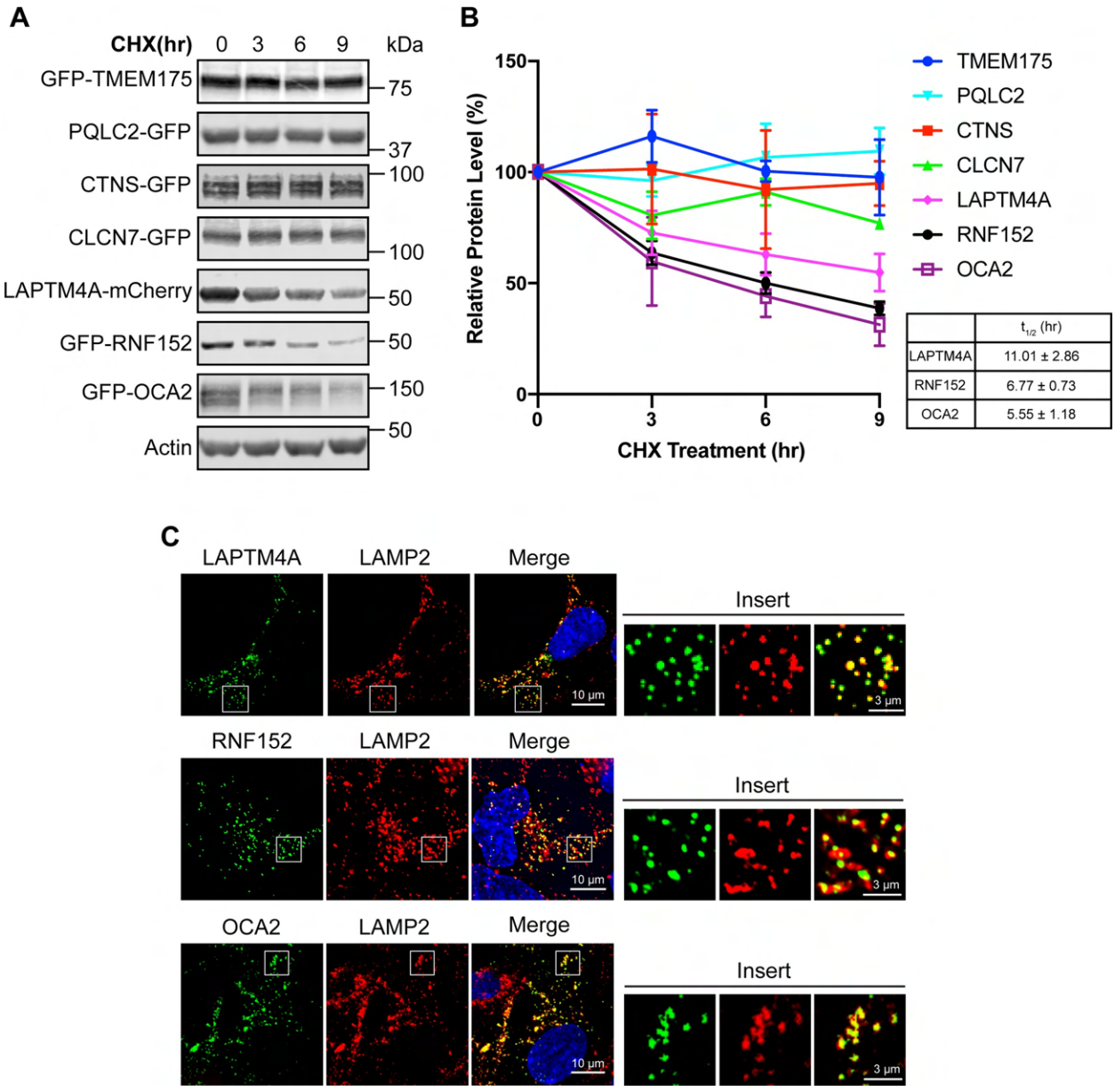

Figure 3.1: Cycloheximide chase assay to determine the stability of LMPs. (A) CHX chase assay to determine the stability of transiently expressed LMPs in HEK293 cells. **(B)** Quantification of the protein levels in A, n=3. Error bars represent standard deviation. The half-lives ($t_{1/2}$) of LAPTM4A, RNF152, and OCA2 were listed in the table. **(C)** Immunofluorescence showing the localization of LAPTM4A-mCherry, GFP-RNF152, and GFP-OCA2 in HEK293 cells co-stained with LAMP2.

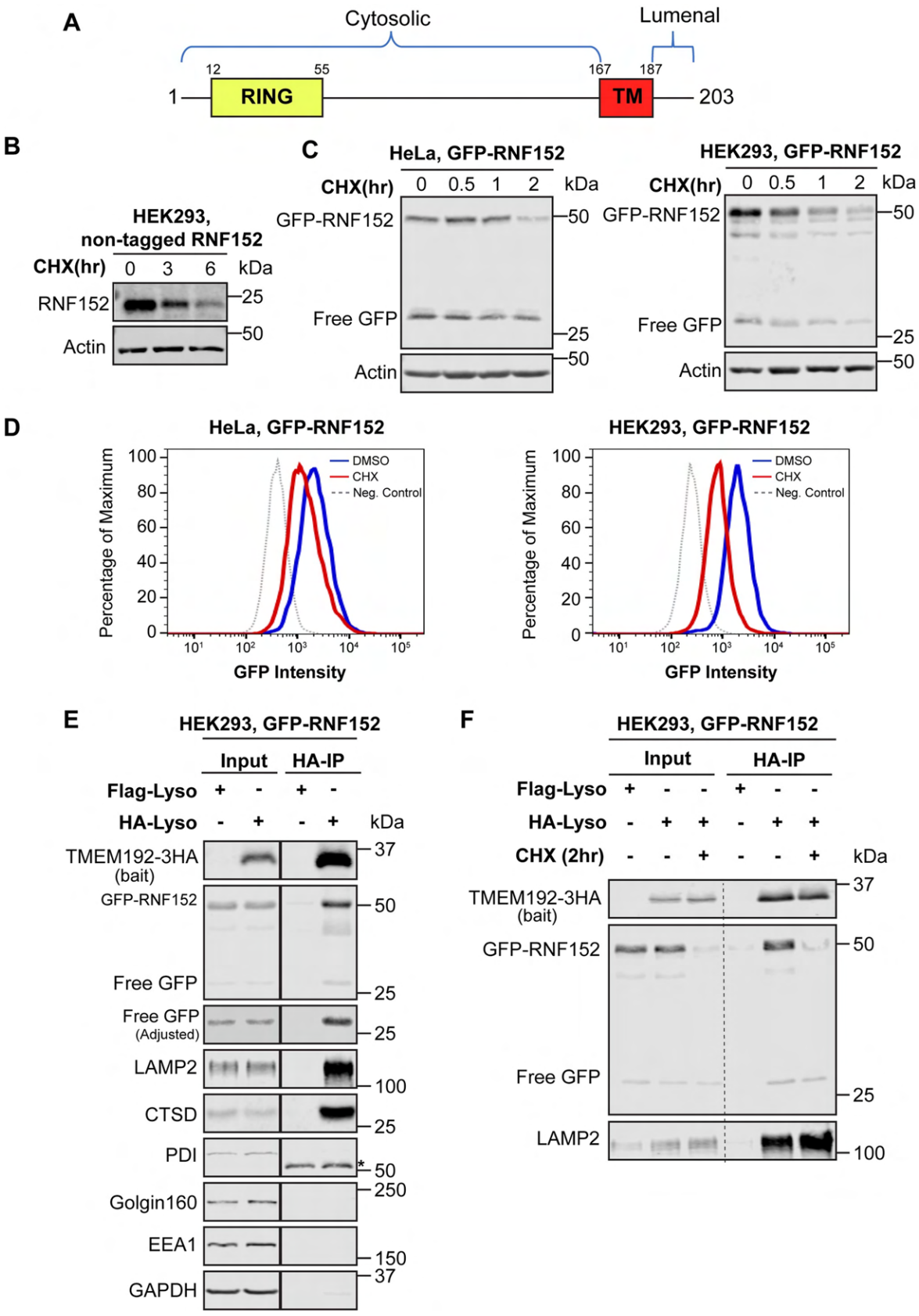
A
Cytosolic
Lumenal
12
55
167
187
1
RING
TM
203
B
HEK293,
non-tagged RNF152
CHX(hr) 0 3 6 kDa
RNF152
25
Actin
50
C
HeLa, GFP-RNF152
CHX(hr) 0 0.5 1 2 kDa
GFP-RNF152
50
Free GFP
25
Actin
50
HEK293, GFP-RNF152
CHX(hr) 0 0.5 1 2 kDa
GFP-RNF152
50
Free GFP
25
Actin
50
D
HeLa, GFP-RNF152
HEK293, GFP-RNF152
Percentage of Maximum
DMSO
CHX
Neg. Control
GFP Intensity
E
HEK293, GFP-RNF152
Input
HA-IP
Flag-Lyso + - + -
HA-Lyso - + - + kDa
TMEM192-3HA
(bait)
37
GFP-RNF152
50
Free GFP
25
Free GFP
(Adjusted)
25
LAMP2
100
CTSD
25
PDI
*
50
Golgin160
250
EEA1
150
GAPDH
37
F
HEK293, GFP-RNF152
Input
HA-IP
Flag-Lyso + - - + - -
HA-Lyso - + + - + +
CHX (2hr) - - + - - + kDa
TMEM192-3HA
(bait)
37
GFP-RNF152
50
Free GFP
25
LAMP2
100

Figure 3.2: RNF152 is a fast-degrading LMP. (A) A schematic representation of RNF152. **(B)** CHX chase assay of transiently expressed, non-tagged RNF152 in HEK293 cells. **(C)** CHX chase assay of stably expressed GFP-RNF152 in both HeLa and HEK293 cells. **(D)** Flow cytometry analysis of stably expressed GFP-RNF152. Cells were pretreated with either CHX or DMSO for 2 hours. Non-infected cells served as negative controls. **(E)** Both full-length GFP-RNF152 (50kDa) and free GFP (27kDa) were enriched by Lyso-IP. Flag-Lyso: cells stably expressing TMEM192-2XFLAG; HA-Lyso: cells stable expressing TMEM192-3HA. Both cells were stably expressing GFP-RNF152. Asterisk: mouse heavy chain. **(F)** Lysosome-localized GFP-RNF152 was degraded after 2 hours of CHX treatment. LAMP2 serves as an internal control.

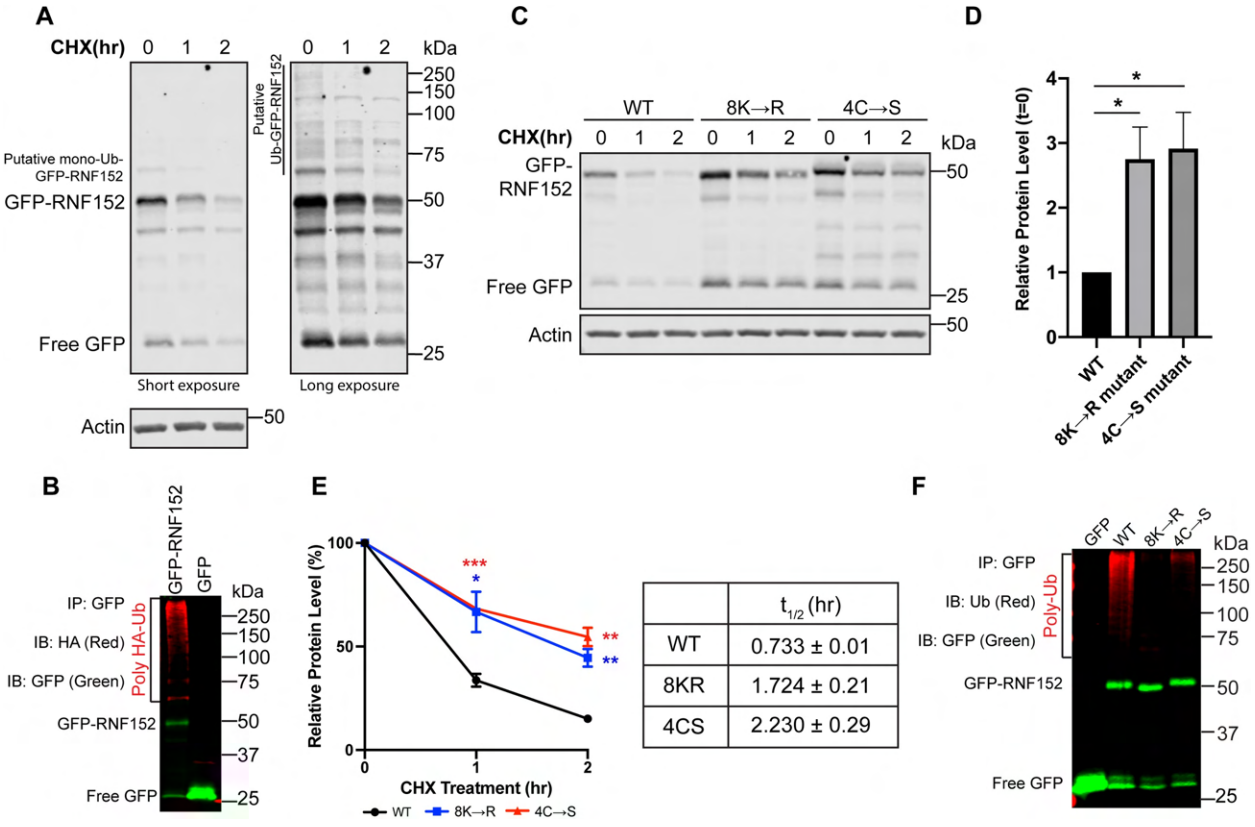

	$t_{1/2}$ (hr)
WT	0.733 ± 0.01
8KR	1.724 ± 0.21
4CS	2.230 ± 0.29

Figure 3.3: RNF152 degradation is ubiquitin-dependent. (A) Left: CHX chase assay of stably expressed GFP-RNF152. Right: long exposure. **(B)** GFP-RNF152, but not free GFP, is poly-ubiquitinated. **(C)** CHX chase assay of stably expressed WT, 8K→R, and 4C→S mutants of GFP-RNF152. **(D)** Steady-state (0hr) full-length protein levels in C, n=3. Error bars represent standard deviation. *: p≤0.05. **(E)** Left: Quantification of GFP-RNF152 degradation in C, n=3. Error bars represent standard deviation. *: p≤0.05, **:p≤0.01, ***:p≤0.001. Table: Calculated protein half-lives. **(F)** 8K→R and 4C→S mutants have impaired poly-ubiquitination.

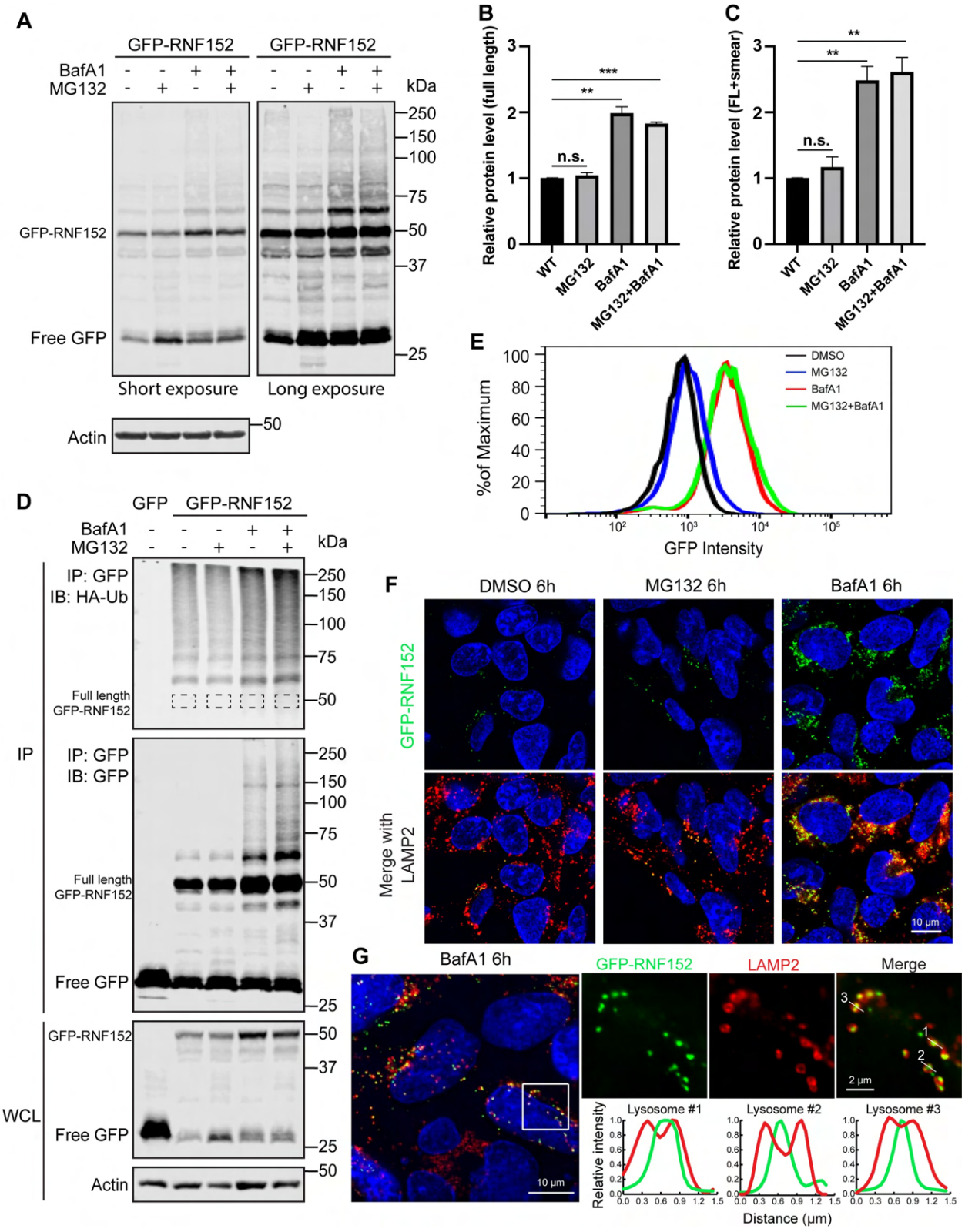
A
GFP-RNF152
GFP-RNF152
BafA1
MG132
kDa
250
150
100
75
50
37
25
GFP-RNF152
Free GFP
Short exposure
Long exposure
Actin
50
B
Relative protein level (full length)
n.s.
**
***
WT
MG132
BafA1
MG132+BafA1
C
Relative protein level (FL+smear)
n.s.
**
**
WT
MG132
BafA1
MG132+BafA1
D
GFP
GFP-RNF152
BafA1
MG132
kDa
IP: GFP
IB: HA-Ub
Full length GFP-RNF152
IP
IP: GFP
IB: GFP
Full length GFP-RNF152
Free GFP
WCL
GFP-RNF152
Free GFP
Actin
E
%of Maximum
GFP Intensity
DMSO
MG132
BafA1
MG132+BafA1
F
DMSO 6h
MG132 6h
BafA1 6h
GFP-RNF152
Merge with LAMP2
10 μm
G
BafA1 6h
GFP-RNF152
LAMP2
Merge
2 μm
Lysosome #1
Lysosome #2
Lysosome #3
Relative intensity
Distance (μm)

Figure 3.4: RNF152 is degraded in the lysosome. (A) Left: GFP-RNF152 protein levels after MG132 (50 μM), BafA1 (400 nM), and double treatment for 6 hours. Right: long exposure. **(B)** Quantification of the full-length GFP-RNF152 protein level in A, n=3. Error bars represent standard deviation. n.s.: not significant. ** $p \leq 0.01$, *** $p \leq 0.001$. **(C)** Quantification of the total GFP-RNF152 protein level, including full-length and the high-molecular-weight smear in A, n=3. **(D)** Accumulation of poly-ubiquitinated GFP-RNF152 after the BafA1 and BafA1+MG132 treatments. **(E)** Flow cytometry analysis of stably express GFP-RNF152 in HEK293 cells after 6 hours of indicated treatments. **(F)** Localization of GFP-RNF152 and LAMP2 after indicated treatments. Images were taken by a confocal microscope. **(G)** Localization of GFP-RNF152 and LAMP2 after BafA1 (400 nM) treatment. The image was taken by a DeltaVision deconvolution microscope. Line scan analysis highlighted the lumenal localization of GFP-RNF152.

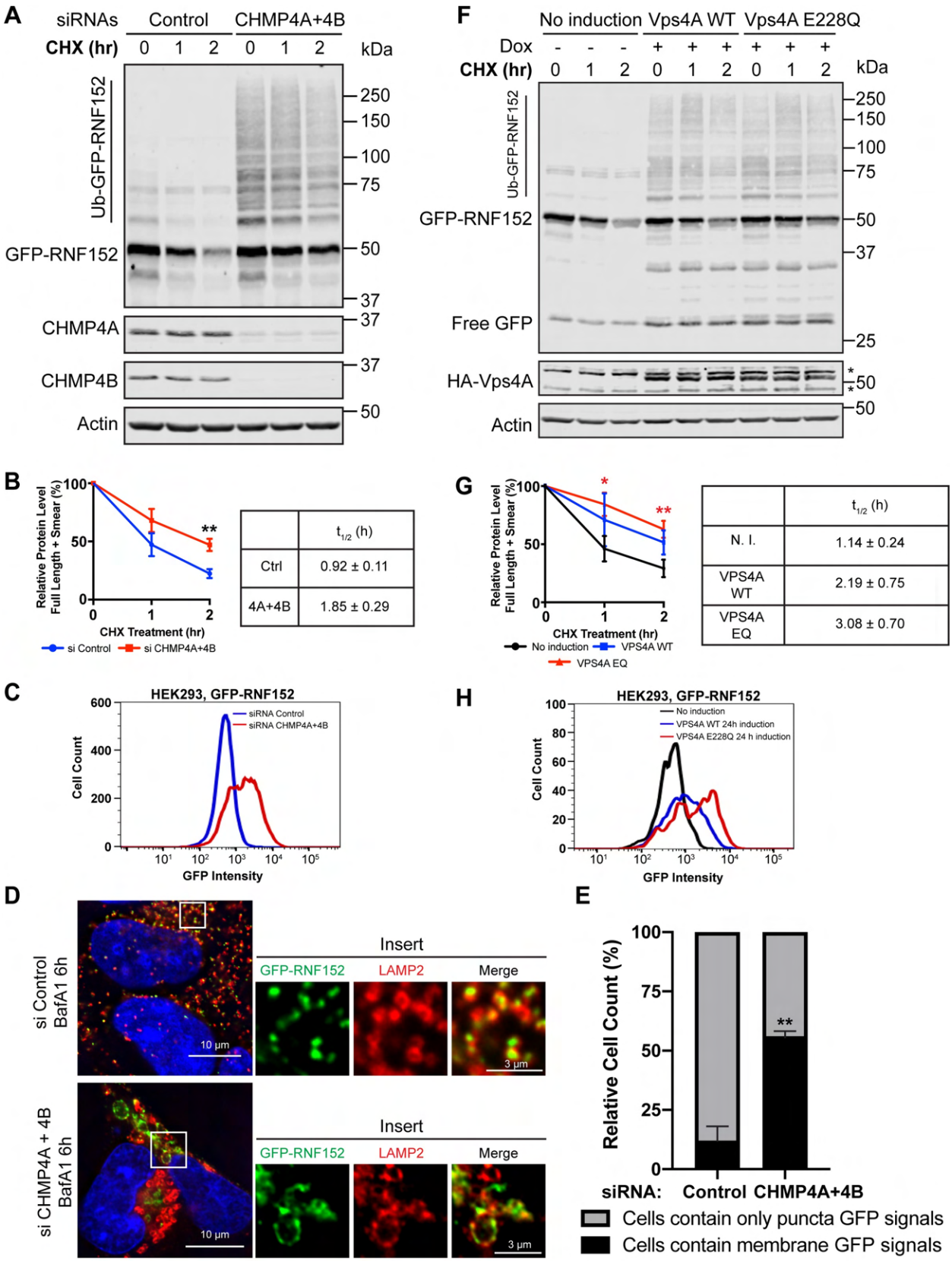
A
siRNAs
Control
CHMP4A+4B
CHX (hr)
0 1 2 0 1 2
kDa
Ub-GFP-RNF152
GFP-RNF152
CHMP4A
CHMP4B
Actin
250
150
100
75
50
37
37
37
50
F
No induction
Vps4A WT
Vps4A E228Q
Dox
- - - + + + + + +
CHX (hr)
0 1 2 0 1 2 0 1 2
kDa
Ub-GFP-RNF152
GFP-RNF152
Free GFP
HA-Vps4A
Actin
250
150
100
75
50
37
25
50
50
B
Relative Protein Level
Full Length + Smear (%)
CHX Treatment (hr)
si Control
si CHMP4A+4B
**
t1/2 (h)
Ctrl
0.92 ± 0.11
4A+4B
1.85 ± 0.29
G
Relative Protein Level
Full Length + Smear (%)
CHX Treatment (hr)
No induction
VPS4A WT
VPS4A EQ
*
**
t1/2 (h)
N. I.
1.14 ± 0.24
VPS4A WT
2.19 ± 0.75
VPS4A EQ
3.08 ± 0.70
C
HEK293, GFP-RNF152
siRNA Control
siRNA CHMP4A+4B
Cell Count
GFP Intensity
H
HEK293, GFP-RNF152
No induction
VPS4A WT 24h induction
VPS4A E228Q 24 h induction
Cell Count
GFP Intensity
D
si Control
BafA1 6h
si CHMP4A + 4B
BafA1 6h
Insert
GFP-RNF152
LAMP2
Merge
10 μm
3 μm
E
Relative Cell Count (%)
**
siRNA:
Control
CHMP4A+4B
Cells contain only puncta GFP signals
Cells contain membrane GFP signals

Figure 3.5: ESCRT-III and VPS4 are important for the degradation of RNF152. (A) CHX chase assay of GFP-RNF152 in siRNA control and CHMP4A + CHMP4B double knockdown cells. **(B)** Left: Total GFP-RNF152 protein levels in A. n=3. Error bars represent standard deviation. ** $p \leq 0.01$. Right: Half-lives of GFP-RNF152 in A. **(C)** Flow cytometry analysis of GFP-RNF152 in siRNA control and CHMP4A + CHMP4B double knockdown cells. **(D)** Localization of GFP-RNF152 and LAMP2 in siRNA control and CHMP4A +CHMP4B double knockdown cells after BafA1 (400nM) treatment. **(E)** Quantification of D counting the percentage of cells that contain either punctate or membrane GFP signals. **(F)** CHX chase assay of GFP-RNF152 in indicated cells. **(G)** Left: Total GFP-RNF152 protein levels in G, n=3. Error bars represent standard deviation. * $p \leq 0.05$, ** $p \leq 0.01$. Right: Half-lives of GFP-RNF152 in F. **(H)** Flow cytometry analysis of GFP-RNF152 in indicated cells.

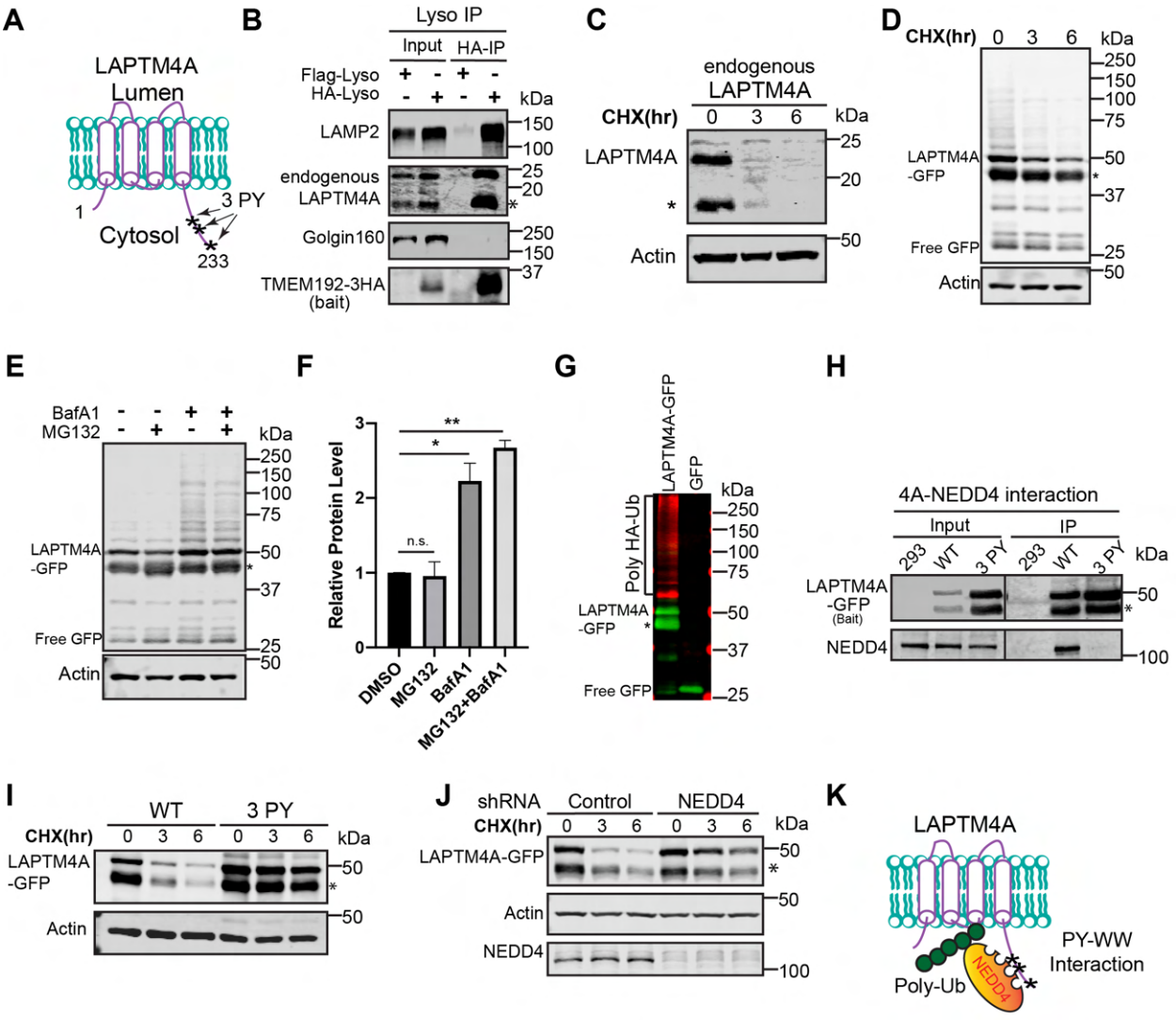

Figure 3.6: LAPTM4A degradation depends on NEDD4. (A) A cartoon showing LAPTM4A with three PY motifs at its C terminus. **(B)** Endogenous LAPTM4A is enriched by Lyso-IP. Flag-Lyso: cells stably expressing TMEM192-2XFLAG; HA-Lyso: cells stable expressing TMEM192-3HA. **(C)** Endogenous LAPTM4A is quickly degraded. The asterisk highlights a protease cleavage product. **(D)** CHX chase assay of stably expressed LAPTM4A-GFP in HEK293 cells. **(E)** LAPTM4A-GFP protein levels after MG132 (50 μM), BafA1 (400 nM), and double treatment for 6 hours. **(F)** Total LAPTM4A-GFP protein levels in E, n=3. Error bars represent standard deviation. n.s.: not significant. *: p≤0.05, **: p≤0.01. **(G)** LAPTM4A-GFP,

but not GFP, is poly-ubiquitinated. **(H)** Co-IP showing a PYmotif-dependent interaction between LAPTM4A-GFP and NEDD4. **(I)** CHX chase assay of stably expressed WT LAPTM4A-GFP and 3PY mutant. **(J)** CHX chase assay of stably expressed LAPTM4A-GFP in shRNA control and NEDD4 knockdown cells. **(K)** A cartoon showing the association of LAPTM4A with NEDD4 leads to its polyubiquitination.

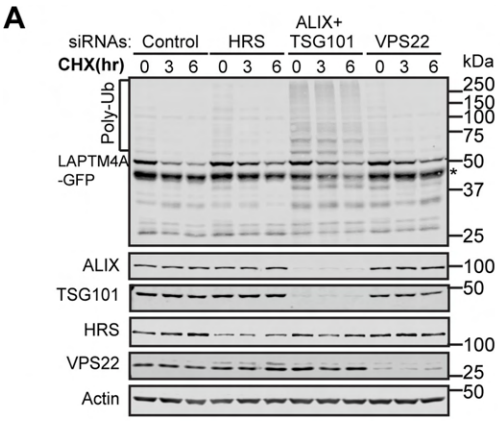

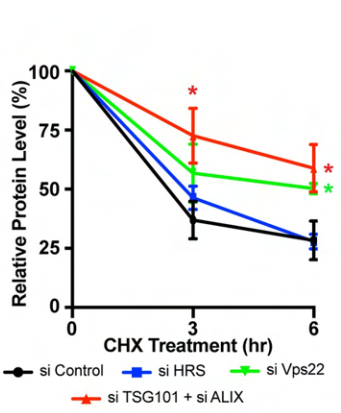

	$t_{1/2}$ (h)
Ctrl	3.10 ± 0.52
HRS	3.27 ± 0.31
VPS22	6.06 ± 0.39
TSG + ALIX	8.24 ± 2.49

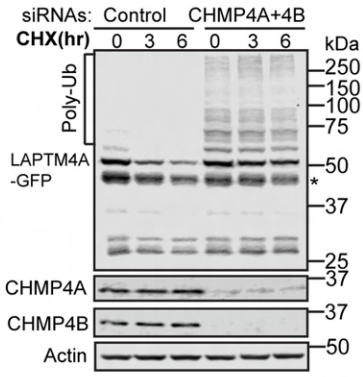

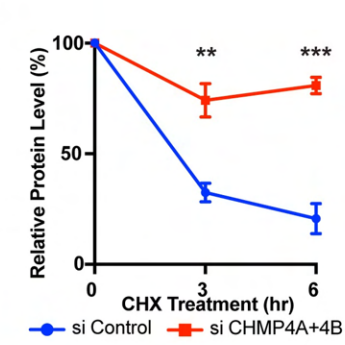

	$t_{1/2}$ (h)
Ctrl	2.65 ± 0.56
4A + 4B	20.14 ± 4.14 #

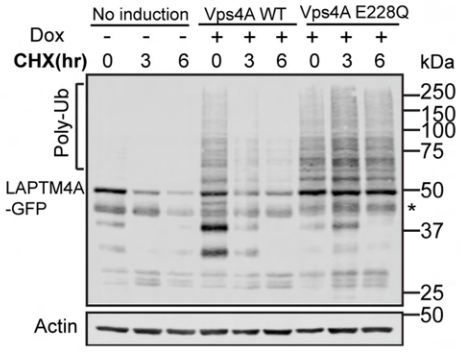

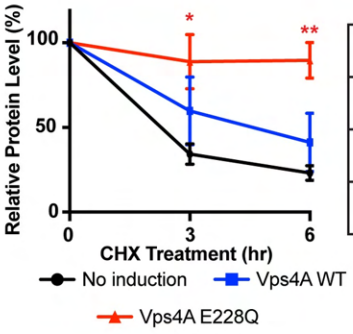

	$t_{1/2}$ (h)
N.I.	2.84 ± 0.36
Vps4A WT	5.15 ± 2.66
Vps4A EQ	26.12 ± 10.87 #

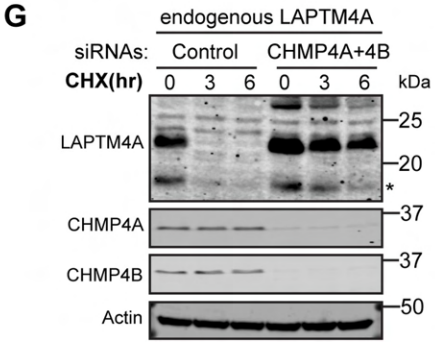

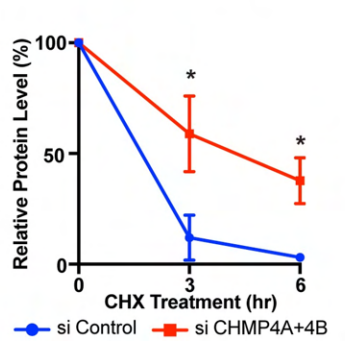

	$t_{1/2}$ (h)
Ctrl	1.26 ± 0.12
4A + 4B	4.15 ± 1.50

Figure 3.7: LAPTM4A degradation is ESCRT-dependent. (A) CHX chase assay of stably expressed LAPTM4A-GFP in siRNA control, HGS/HRS knockdown, TSG101 + PDCD6IP/ALIX double knockdown, and VPS22 knockdown cells. **(B)** Left: Total LAPTM4A-GFP protein levels in A, n=3. Error bars represent standard deviation. *: $p \leq 0.05$, **: $p \leq 0.01$, ***: $p \leq 0.001$. Right: Half-lives of LAPTM4A-GFP in A. **(C)** CHX chase assay of stably expressed LAPTM4A-GFP in siRNA control and CHMP4A + CHMP4B double knockdown cells. **(D)** Left: Total LAPTM4A-GFP protein levels in C, n=3. Right: Half-lives of LAPTM4A-GFP in C. #: one of the degradation data sets is too stable to fit with the first-order decay. The average $t_{1/2}$ is calculated based on the other two data sets. **(E)** CHX chase assay of stably expressed LAPTM4A-GFP in cells overexpressing either WT HA-VPS4A or its dominant-negative mutant (E228Q). **(F)** Left: Total LAPTM4A-GFP protein levels in E, n=3. Right: Half-lives of LAPTM4A-GFP in E. **(G)** CHX chase assay of endogenous LAPTM4A in siRNA control and CHMP4A + CHMP4B double knockdown cells. **(H)** Left: Endogenous LAPTM4A protein levels in G, n=3. Right: Half-lives of the endogenous LAPTM4A in G.

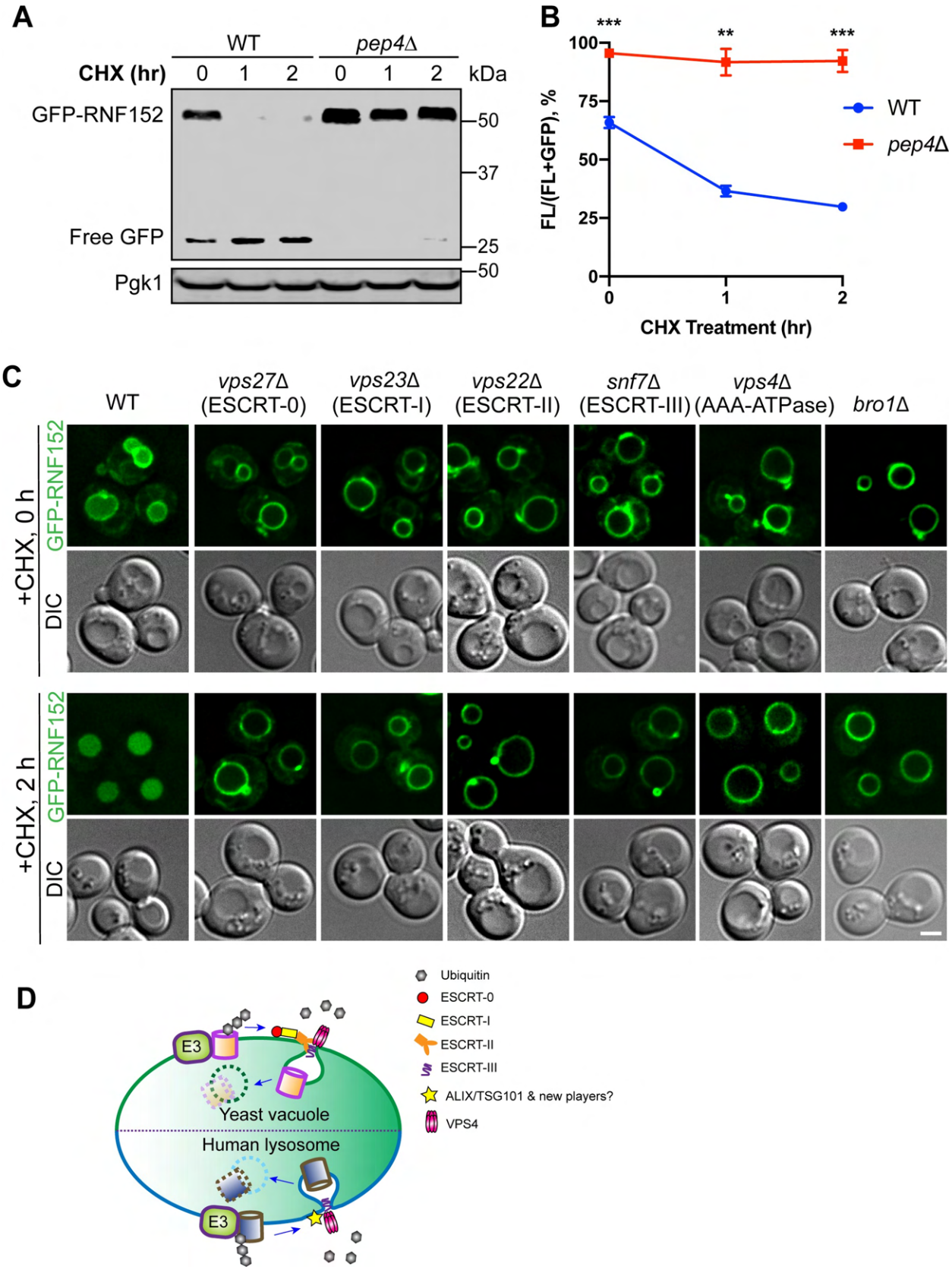
A
WT
pep4Δ
CHX (hr)
0 1 2 0 1 2 kDa
GFP-RNF152
Free GFP
Pgk1
50
37
25
50
B
***
**
***
100
75
50
25
0
FL/(FL+GFP), %
WT
pep4Δ
0
1
2
CHX Treatment (hr)
C
WT
vps27Δ (ESCRT-0)
vps23Δ (ESCRT-I)
vps22Δ (ESCRT-II)
snf7Δ (ESCRT-III)
vps4Δ (AAA-ATPase)
bro1Δ
+CHX, 0 h
+CHX, 2 h
GFP-RNF152
DIC
D
E3
Yeast vacuole
Human lysosome
E3
Ubiquitin
ESCRT-0
ESCRT-I
ESCRT-II
ESCRT-III
ALIX/TSG101 & new players?
VPS4

Figure 3.8: The degradation of RNF152 is ESCRT-dependent in budding yeast. (A) CHX chase assay of GFP-RNF152 in WT and *pep4*Δ yeast strains. **(B)** GFP-RNF152 protein levels in A, n=3. Error bars represent standard deviation. ** p≤0.01, *** p≤0.001. **(C)** Subcellular localization of GFP-RNF152 in WT, *vps27*Δ , *vps23*Δ, *vps22*Δ, *snf7*Δ, *vps4*Δ ,and *bro1*Δ yeast strains before (0hr) and after (2hr) cycloheximide treatment. Scale bar=2µm. DIC: differential interference contrast. **(D)** A model showing the conserved ubiquitin- and ESCRT-dependent mechanism to degrade LMPs in yeast and humans.

Figure S1

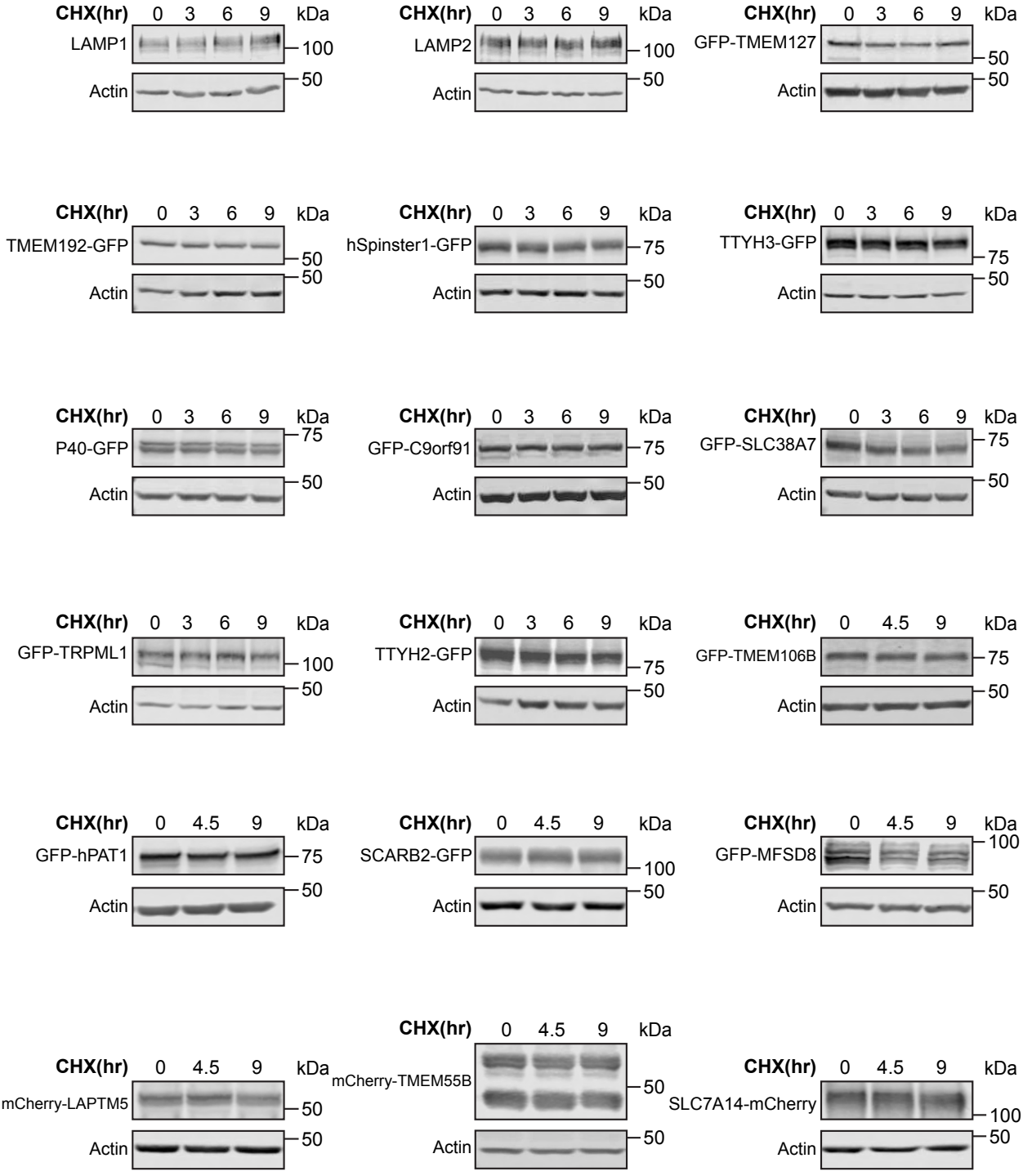

Supplemental Figure 3.1: Cycloheximide chase assay to measure half-lives of LMPs. Some examples of the CHX chase screen in HEK293 cells. LAMP1 and LAMP2 were detected with

endogenous antibodies. For other LMPs, HEK293 cells were transiently transfected with indicated overexpression plasmids and detected by either GFP or mCherry antibodies. The majority of the tested LMPs are very stable. Related to figure 1.

Figure S2

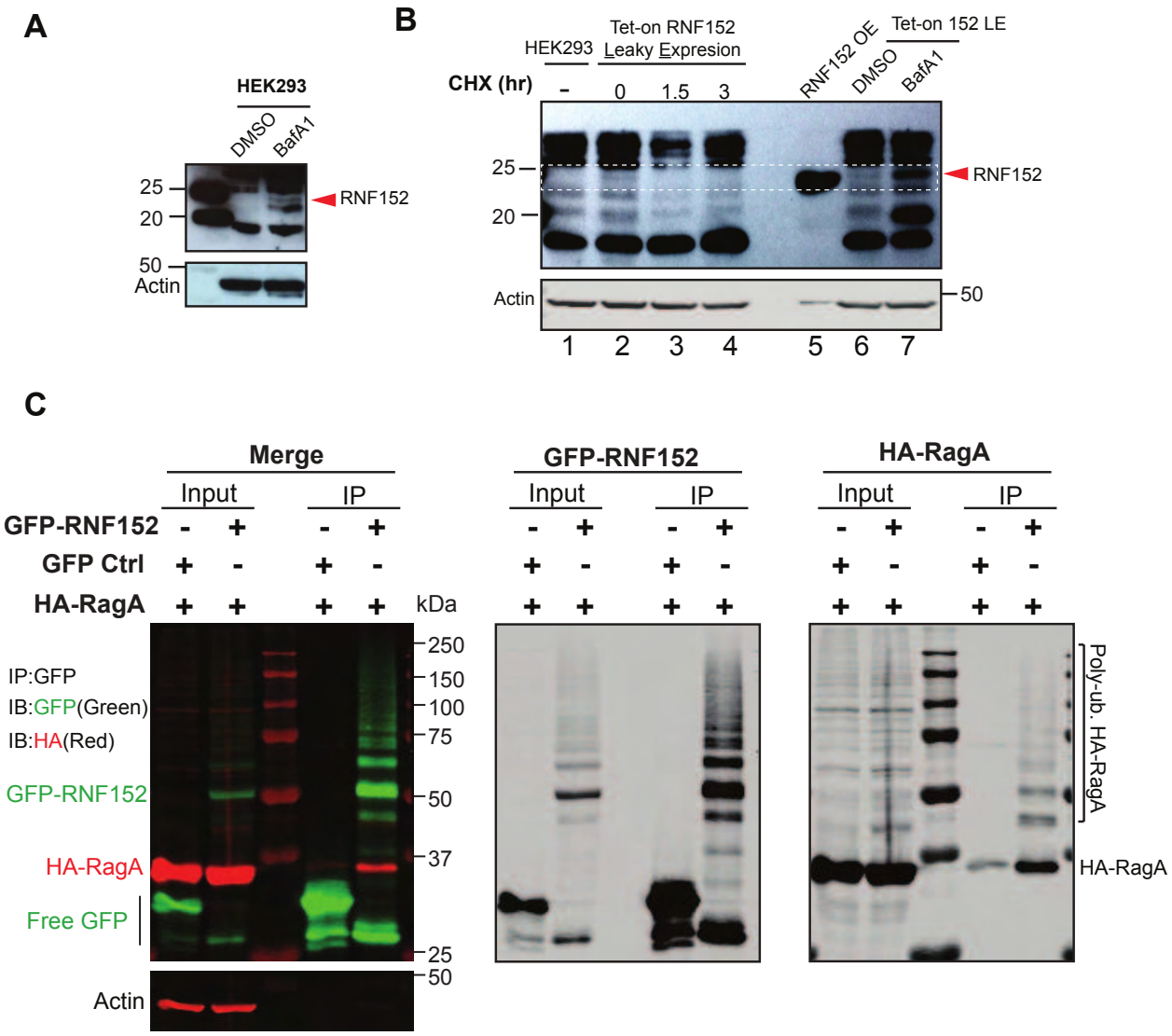

Supplemental Figure 3.2: Endogenous RNF152 is too low to be detected by a homemade antibody. (A) Endogenous RNF152 (~23 kDa) can only be detected after BafA1 treatment. **(B)** Lanes 2-4: CHX chase assay of RNF152 expressed from a leaky TET-ON promoter. Lane 5: RNF152 after the doxycycline induction, only 10% lysate was loaded. Lanes 6-7: BafA1 treatment stabilized RNF152 from the leaky TET-ON promoter. The White dashed box highlights the position of RNF152. **(C)** Overexpressed GFP-RNF152 can still interact and ubiquitinate its substrate RagA. Related to Figure 2.

Figure S3

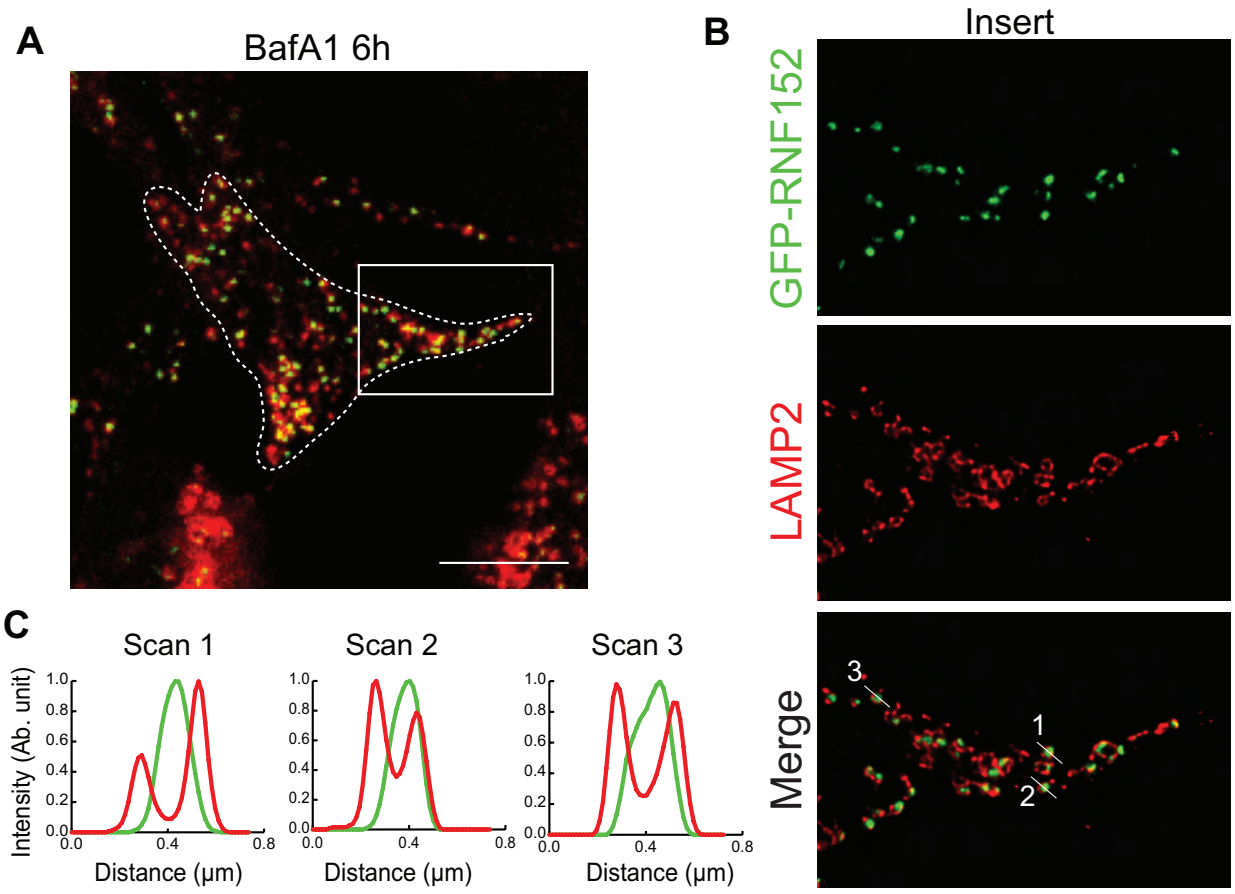

Supplemental Figure 3.3: GFP-RNF152 accumulates in the lysosome lumen after BafA1 treatment. (A) Localization of GFP-RNF152 and LAMP2 after 6h BafA1 treatment. The image was taken by a Leica Stimulated Emission Depletion (STED) microscope. Scale bar: 10 μm. **(B)** Zoomed-in pictures of A. **(C)** Line scan analysis highlighted the lumenal localization of GFP-RNF152. Related to figure 4.

Figure S4

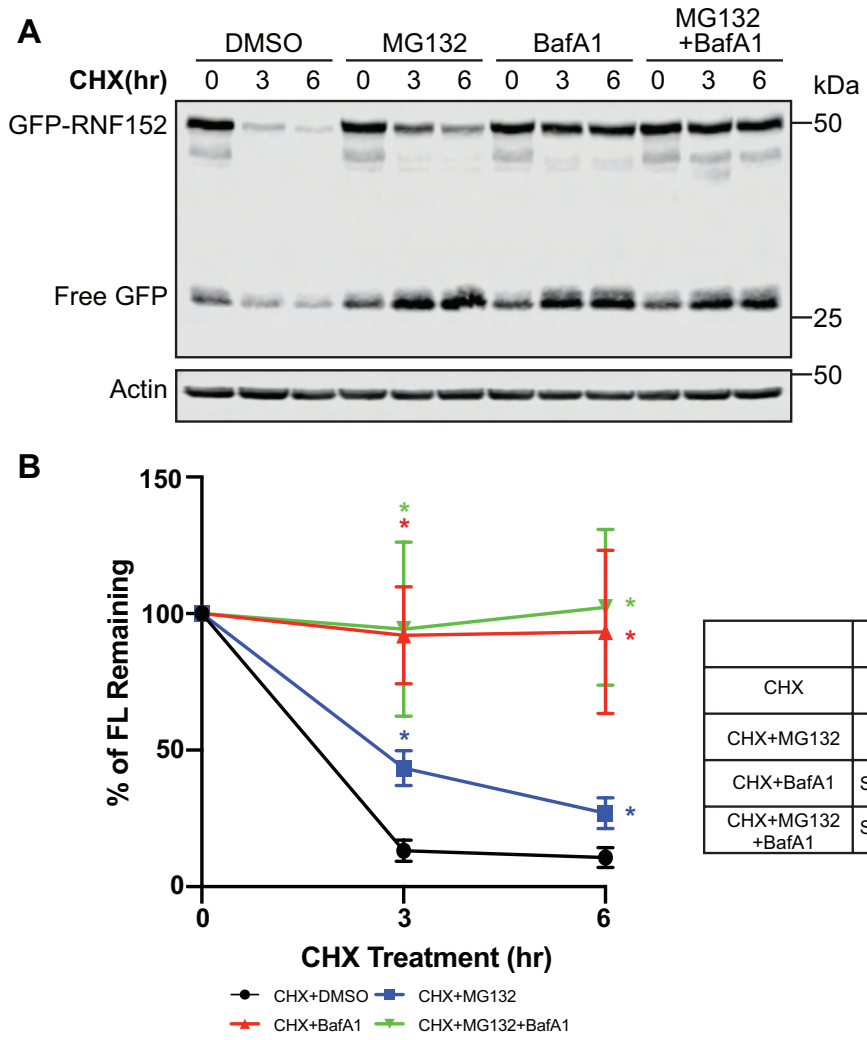

	$t_{1/2}$ (h)
CHX	1.03 ± 0.15
CHX+MG132	3.03 ± 0.50
CHX+BafA1	Stablized, do not fit with first-order decay
CHX+MG132 +BafA1	Stablized, do not fit with first-order decay

Supplemental Figure 3.4: GFP-RNF152 is mainly degraded by lysosome-dependent proteolysis. (A) CHX chase assay of stably expressed GFP-RNF152 after MG132 (50μM), BafA1 (400nM), and double treatment. **(B)** Left: Full-length GFP-RNF152 levels in A, n=3. Error bars represent standard deviation. *: p≤0.05, **: p≤0.01. Right: Half-lives of GFP-RNF152 in A. Related to figure 4.

Figure S5

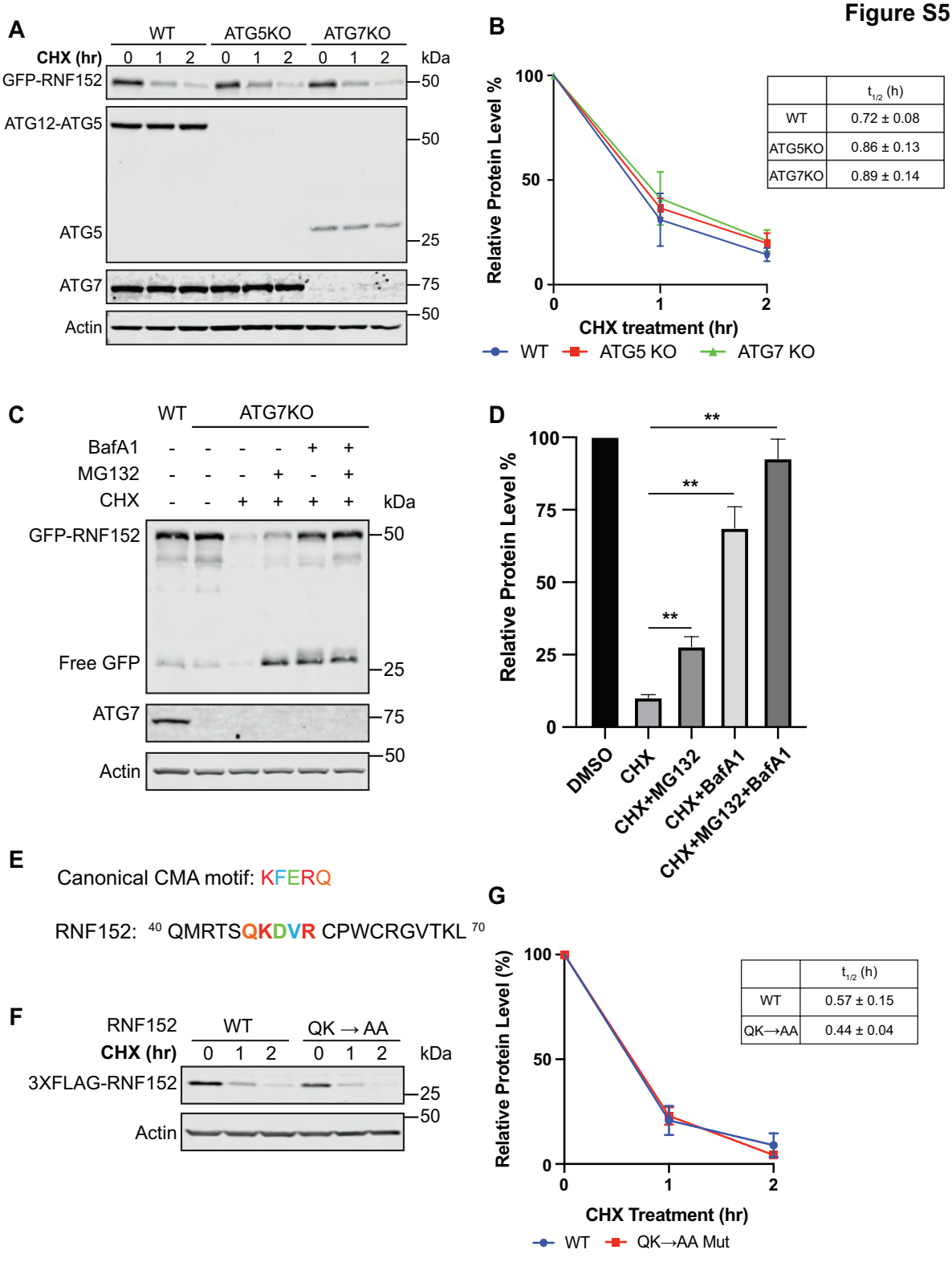

Supplemental Figure 3.5: Macroautophagy and CMA pathways are not involved in the degradation of RNF152. (A) CHX chase assay of stably expressed GFP-RNF152 in WT,

ATG5KO, and ATG7KO cell lines. **(B)** Left: Full-length GFP-RNF152 protein levels in A, n=3. Error bars represent standard deviation. Right: Half-lives of GFP-RNF152 in A. **(C)** western blots showing stably expressed GFP-RNF152 protein levels in ATG7KO cells after indicated treatment for 4 hours. **(D)** GFP-RNF152 protein levels in C, n=3. **: $p \leq 0.01$. **(E)** Identifying KFERQ-like CMA motif in RNF152. **(F)** CHX chase assay of WT 3XFLAG-RNF152 and QK→AA mutant. **(G)** Left: Quantification of F, n=3. Right: Half-lives of 3xFLAG-RNF152 in F.

Figure S6

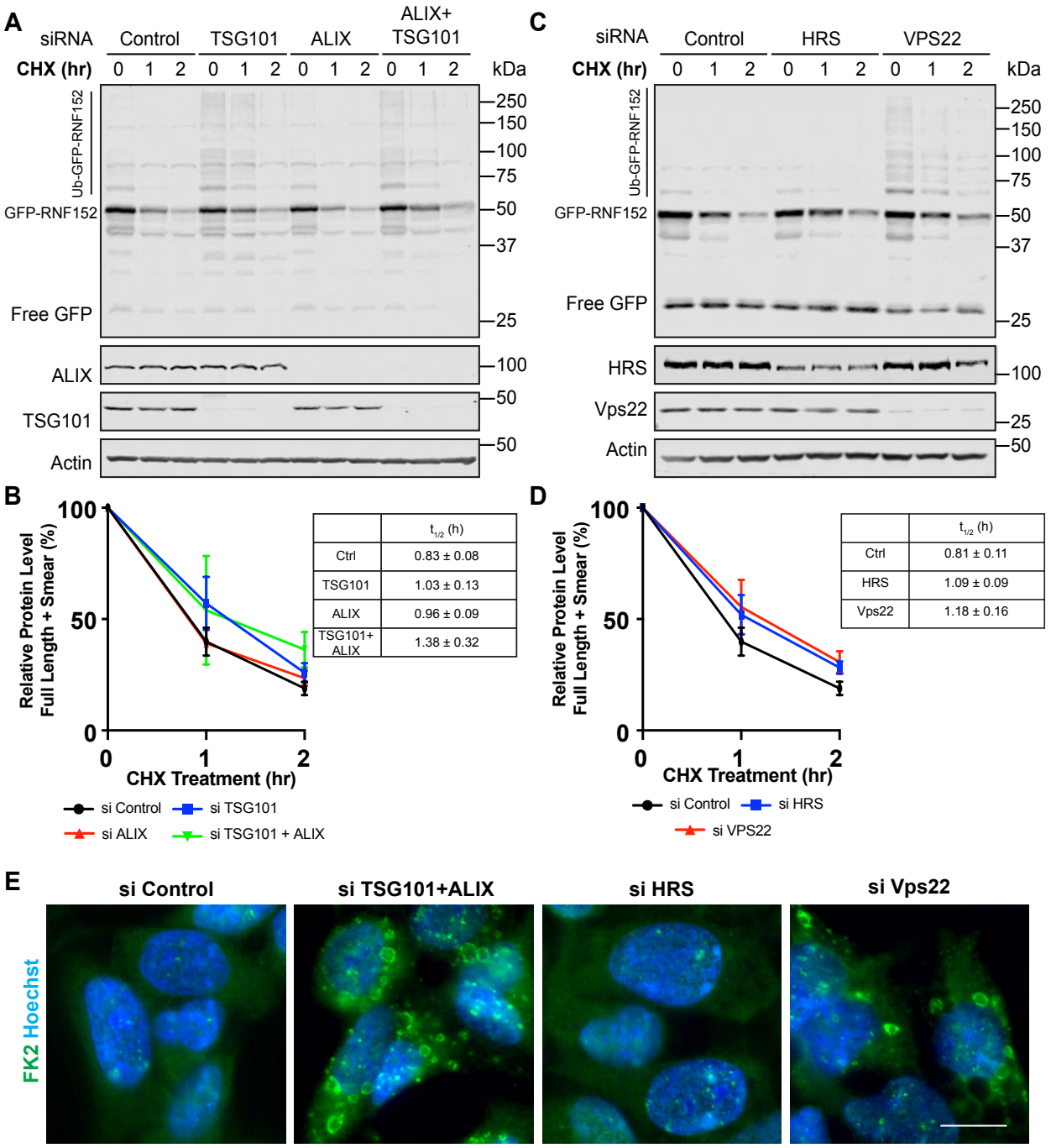

Supplemental Figure 3.6: Early ESCRT components are less important for the degradation of RNF152. (A) CHX chase assay of stably expressed GFP-RNF152 in indicated knockdown cells. **(B)** Left: Total GFP-RNF152 protein levels in A, n=3. Right: Half-lives of GFP-RNF152 in A. Error bars represent standard deviation. **(C)** CHX chase assay of stably expressed GFP-

RNF152 in siRNA control, HGS/HRS knockdown, and Vps22 knockdown cells. **(D)** Left: Total GFP-RNF152 protein levels in C, n=3. Right: Half-lives of GFP-RNF152 in C. **(E)** FK2 antibody staining of poly-ubiquitinated proteins in indicated knockdown cells. Nuclei were labeled with Hoechst. Scale bar=10μm. Related to figure 5.

Figure S7

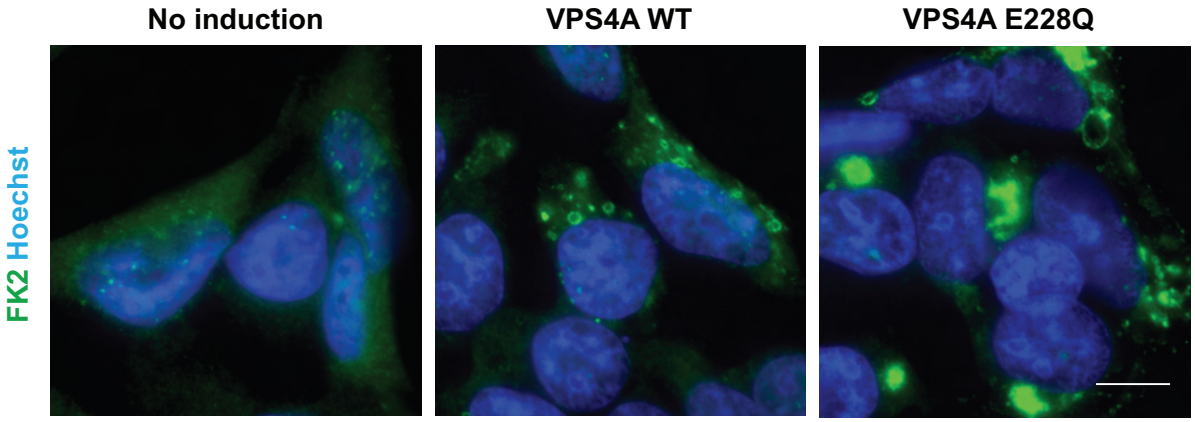

Supplemental Figure 3.7: Cells overexpressing VPS4A EQ mutant accumulate poly-ubiquitinated proteins. FK2 antibody staining of poly-ubiquitinated proteins in indicated cells. The overexpression of HA-VPS4A was induced by 1µg/ml of doxycycline treatment for 24 hours. Nuclei were labeled with Hoechst. Scale bar=10µm. Related to figure 5.

Supplemental Table 3.1: Mammalian cell lines used in this study		
Cell lines	***Description***	***reference/source***
Human HEK293	CRL-1573	ATCC
Human HEK293T	CRL-3216	ATCC
Human HeLa	CCL-2	ATCC
Human HEK293, GFP-RNF152	pHAGE2-EF1α-EGFP-RNF152-IRES-Puro	This study
Human HEK293, GFP-RNF152 (4C→S)	pHAGE2-EF1α-EGFP-RNF152 (4C→S)-IRES-Puro	This study
Human HEK293, GFP-RNF152 (8K→R)	pHAGE2-EF1α-EGFP-RNF152 (8K→R)-IRES-Puro	This study
Human HEK293, ATG5KO, GFP-RNF152	ATG5 CRISPR-Cas9 knockout, pHAGE2-EF1α-EGFP-RNF152-IRES-Puro	This study
Human HEK293, ATG7KO, GFP-RNF152	ATG7 CRISPR-Cas9 knockout, pHAGE2-EF1α-EGFP-RNF152-IRES-Puro	This study
Human HEK293, GFP-RNF152, FLAG-Lyso	pHAGE2-EF1α-EGFP-RNF152-IRES-mCherry, pLJC5-TMEM192-2XFLAG-Puro (Addgene 102929)	This study (Abu-Remaileh et al. 2017)
Human HEK293, GFP-RNF152, HA-Lyso	pHAGE2-EF1α-EGFP-RNF152-IRES-mCherry, pLJC5-TMEM192-3XHA-Puro (Addgene 102930)	This study (Abu-Remaileh et al. 2017)
Human HEK293, GFP-RNF152, HA-Vps4A	pHAGE2-EF1α-EGFP-RNF152-IRES-mCherry, pCW57.1-HA-Vps4A-Puro	This study
Human HEK293, GFP-RNF152, HA-Vps4A E228Q	pHAGE2-EF1α-EGFP-RNF152-IRES-mCherry, pCW57.1-HA-Vps4A (E228Q)-Puro	This study
Human HEK293, 3XFLAG-RNF152	pHAGE2-EF1α-3XFLAG-RNF152-IRES-Puro	This study
Human HEK293, 3XFLAG-RNF152 (QK→AA)	pHAGE2-EF1α-3XFLAG-RNF152 (QK→AA)-IRES-Puro	This study
Human HEK293, LAPTM4A-GFP	pHAGE2-EF1α-LAPTM4A-EGFP-IRES-Puro	This study

Human HEK293, LAPTM4A (3PY)-GFP	pHAGE2-EF1α-LAPTM4A (3PY)-EGFP-IRES-Puro	This study
Human HEK293, LAPTM4A-GFP, HA-Vps4A	pHAGE2-EF1α-LAPTM4A-EGFP-IRES-mCherry, pCW57.1-HA-Vps4A (E228Q)-Puro	This study
Human HEK293, LAPTM4A-GFP, HA-Vps4A E228Q	pHAGE2-EF1α-LAPTM4A-EGFP-IRES-mCherry, pCW57.1-HA-Vps4A (E228Q)-Puro	This study
Human HEK293T, FLAG-Lyso	pLJC5-TMEM192-2XFLAG-Puro (Addgene 102929)	This study (Abu-Remaileh et al. 2017)
Human HEK293T, HA-Lyso	pLJC5-TMEM192-3XHA-Puro (Addgene 102930)	This study (Abu-Remaileh et al. 2017)
Human HeLa, GFP-RNF152	pHAGE2-EF1α-EGFP-RNF152-IRES-Puro	This study

Supplemental Table 3.2: Mammalian plasmids used in this study			
Vector	***Insert***	***description***	***reference/source***
pEGFP-C1	RNF152	CMV promoter, N-terminal GFP	This study
pBICEP-CMV2-3XFLAG	RNF152	CMV promoter, N-terminal 3XFLAG	This study
pcDNA3.1(-)	RNF152	CMV promoter	This study
pHAGE2-IRES-Puro	EGFP	EF1α promoter, puromycin selection	This study
pHAGE2-IRES-Puro	EGFP-RNF152	EF1α promoter, puromycin selection	This study
pHAGE2-IRES-Puro	LAPTM4A-EGFP	EF1α promoter, puromycin selection	This study
pHAGE2-IRES-Puro	LAPTM4A (3PY)-EGFP	EF1α promoter, puromycin selection	This study
pHAGE2-IRES-Puro	EGFP-RNF152 (4C→S)	EF1α promoter, puromycin selection	This study
pHAGE2-IRES-Puro	EGFP-RNF152 (8K→R)	EF1α promoter, puromycin selection	This study
pHAGE2-IRES-Puro	3XFLAG-RNF152	EF1α promoter, puromycin selection	This study
pHAGE2-IRES-Puro	3XFLAG-RNF152 (QK→AA)	EF1α promoter, puromycin selection	This study
pHAGE2-IRES-mCherry	EGFP-RNF152	EF1α promoter, mCherry selection	This study
pHAGE2-IRES-mCherry	LAPTM4A-EGFP	EF1α promoter, mCherry selection	This study
pEGFP-C1	Vps4 E228Q	CMV promoter, N-terminal GFP	Votteler et al. 2016 Addgene 80351
pCMV-HA	HA-Vps4A E228Q	CMV promoter, N-terminal HA	This study
pCW57.1	HA-Vps4A WT	Tet-on promoter	This study
pCW57.1	HA-Vps4A E228Q	Tet-on promoter	This study

pCMV-HA-Ub		CMV promoter, three repeats of HA-Ub	This study
pLJC5	TMEM192-2XFLAG	UbC promoter	Abu-Remaileh et al. 2017 Addgene 102929
pLJC5	TMEM192-3XHA	UbC promoter	Abu-Remaileh et al. 2017 Addgene 102930
pSpCas9(BB)-2A-Puro (PX459)		CRISPR-Cas9 knockout	Ran et al. 2013 Addgene, 48139
psPAX2		Lentiviral packaging plasmid	Addgene 12260
pMD2.G		VSV-G envelope	Addgene 12259
pLKO.1		shRNA knockdown	Addgene 8453
Overexpression plasmids used in the cycloheximide chase screen			
pcDNA3-EGFP	CLCN7	CMV promoter, C-terminal GFP	This study. CDS from Origene.
pCMV6-AC-GFP	OSTM1	CMV promoter, C-terminal turboGFP	This study, Origene
pCMV-SPORT6	p40-EGFP	CMV promoter, C-terminal GFP	Gift from Dr. M Boonen. (Boonen et al. 2006)
pEGFP-C1	hPAT1 (SLC36A1)	CMV promoter, N-terminal GFP	This study, CDS from Origene
pEGFP-C1	TMEM192	CMV promoter, N-terminal GFP	Gift from B. Schröder. (Schröder et al. 2010)
pEGFP-C2	TRPML1	CMV promoter, N-terminal GFP	Dong et al. 2008.
pEGFP-N1	CTNS	CMV promoter, C-terminal GFP	This study, CDS from DNASU.
pEGFP-N1	hSpinster1	CMV promoter, C-terminal GFP	This study. (Rong et al. 2011)
pEGFP-N1	SCARB2	CMV promoter, C-terminal GFP	This study, CDS from DNASU.
pReceiver-M03-EGFP	PQLC2	CMV promoter, C-terminal GFP	This study GeneCopoeia
pReceiver-M03-EGFP	TTYH2	CMV promoter, C-terminal GFP	This study GeneCopoeia
pReceiver-M03-EGFP	TTYH3	CMV promoter, C-terminal GFP	This study GeneCopoeia
pReceiver-M29-EGFP	C9orf91	CMV promoter, N-terminal GFP	This study GeneCopoeia

pReceiver-M29-EGFP	ITM2C	CMV promoter, N-terminal GFP	This study GeneCopoeia
pReceiver-M29-EGFP	MFSD8	CMV promoter, N-terminal GFP	This study GeneCopoeia
pReceiver-M29-EGFP	OCA2	CMV promoter, N-terminal GFP	This study GeneCopoeia
pReceiver-M29-EGFP	SLC38A7	CMV promoter, N-terminal GFP	This study GeneCopoeia
pReceiver-M29-EGFP	STARD3	CMV promoter, N-terminal GFP	This study GeneCopoeia
pReceiver-M29-EGFP	TMEM106B	CMV promoter, N-terminal GFP	This study GeneCopoeia
pReceiver-M29-EGFP	TMEM127	CMV promoter, N-terminal GFP	This study GeneCopoeia
pReceiver-M29-EGFP	TMEM175	CMV promoter, N-terminal GFP	This study GeneCopoeia
pReceiver-M55-mCherry	LAPTM5	CMV promoter, N-terminal mCherry	This study GeneCopoeia
pReceiver-M55-mCherry	TMEM55B	CMV promoter, N-terminal mCherry	This study GeneCopoeia
pReceiver-M56-mCherry	LAPTM4A	CMV promoter, C-terminal mCherry	This study GeneCopoeia
pReceiver-M56-mCherry	SLC7A14	CMV promoter, C-terminal mCherry	This study GeneCopoeia

Supplemental Table 3.3: Yeast strains and Plasmids used in this study			
S. cerevisiae strains			
strain	***name***	***genotype***	***reference/source***
SEY6210	wild type	Matα*, leu1-3, 112 ura3-52 his3-200, trp1-901 lys2-801 suc2-D9*	Robinson et al., 1988
SEY6210.1	wild type	Matα*, leu1-3, 112 ura3-52 his3-200, trp1-901 lys2-801 suc2-D9*	Robinson et al., 1988
YXY813	*pep4*Δ	6210.1, *pep4*Δ::KAN	This study
YML377	*vps27*Δ	6210, *vps27*Δ::HIS3	Li et al., 2015
YML068	*vps4*Δ	6210.1, *vps4*Δ::TRP1	Li et al., 2015
YXY624	*vps23*Δ	6210.1, *vps23*Δ::TRP1	This study
YXY1031	*vps22*Δ	6210, *vps22*Δ::KAN	This study
YXY625	*snf7*Δ	6210.1, *snf7*Δ::TRP1	This study
YXY1030	*bro1*Δ	6210, *bro1*Δ::KAN	This study
S. cerevisiae expression plasmids			
vector	***Insert***	***description***	***reference/source***
pRS415	GFP-RNF152	ADH1 promoter, N-terminal GFP	This study

3.5 References:

Abu-Remaileh M, Wyant GA, Kim C, et al. Lysosomal metabolomics reveals V-ATPase- and mTOR-dependent regulation of amino acid efflux from lysosomes. *Science*. 2017;358(6364):807-813. doi:10.1126/science.aan6298

Adell MAY, Migliano SM, Upadhyayula S, et al. Recruitment dynamics of ESCRT-III and Vps4 to endosomes and implications for reverse membrane budding. *Elife*. 2017;6:e31652. Published 2017 Oct 11. doi:10.7554/eLife.31652

Amick J, Ferguson SM. C9orf72: At the intersection of lysosome cell biology and neurodegenerative disease. *Traffic*. 2017;18(5):267-276. doi:10.1111/tra.12477

Ammerer G, Hunter CP, Rothman JH, Saari GC, Valls LA, Stevens TH. PEP4 gene of Saccharomyces cerevisiae encodes proteinase A, a vacuolar enzyme required for processing of vacuolar precursors. *Mol Cell Biol*. 1986;6(7):2490-2499. doi:10.1128/mcb.6.7.2490-2499.1986

An H, Ordureau A, Paulo JA, Shoemaker CJ, Denic V, Harper JW. TEX264 Is an Endoplasmic Reticulum-Resident ATG8-Interacting Protein Critical for ER Remodeling during Nutrient Stress. *Mol Cell*. 2019;74(5):891-908.e10. doi:10.1016/j.molcel.2019.03.034

Anding AL, Baehrecke EH. Cleaning House: Selective Autophagy of Organelles. *Dev Cell*. 2017;41(1):10-22. doi:10.1016/j.devcel.2017.02.016

Arines FM, Hamlin AJ, Yang X, Liu YJ, Li M. A selective transmembrane recognition mechanism by a membrane-anchored ubiquitin ligase adaptor. *J Cell Biol*. 2021;220(1):e202001116. doi:10.1083/jcb.202001116

Bache KG, Brech A, Mehlum A, Stenmark H. Hrs regulates multivesicular body formation via ESCRT recruitment to endosomes. *J Cell Biol*. 2003;162(3):435-442. doi:10.1083/jcb.200302131

Bissa B, Beedle AM, Govindarajan R. Lysosomal solute carrier transporters gain momentum in research. *Clin Pharmacol Ther*. 2016;100(5):431-436. doi:10.1002/cpt.450

Carmona-Gutierrez D, Hughes AL, Madeo F, Ruckenstuhl C. The crucial impact of lysosomes in aging and longevity. *Ageing Res Rev*. 2016;32:2-12. doi:10.1016/j.arr.2016.04.009

Chapel A, Kieffer-Jaquinod S, Sagné C, et al. An extended proteome map of the lysosomal membrane reveals novel potential transporters. *Mol Cell Proteomics*. 2013;12(6):1572-1588. doi:10.1074/mcp.M112.021980

Cheon SY, Kim H, Rubinsztein DC, Lee JE. Autophagy, Cellular Aging and Age-related Human Diseases. *Exp Neurobiol*. 2019;28(6):643-657. doi:10.5607/en.2019.28.6.643

Cook C, Stetler C, Petrucelli L. Disruption of protein quality control in Parkinson's disease. *Cold Spring Harb Perspect Med*. 2012;2(5):a009423. doi:10.1101/cshperspect.a009423

Christ L, Raiborg C, Wenzel EM, Campsteijn C, Stenmark H. Cellular Functions and Molecular Mechanisms of the ESCRT Membrane-Scission Machinery. *Trends Biochem Sci*. 2017;42(1):42-56. doi:10.1016/j.tibs.2016.08.016

Christ L, Wenzel EM, Liestøl K, Raiborg C, Campsteijn C, Stenmark H. ALIX and ESCRT-I/II function as parallel ESCRT-III recruiters in cytokinetic abscission. *J Cell Biol*. 2016;212(5):499-513. doi:10.1083/jcb.201507009

Cuervo AM, Wong E. Chaperone-mediated autophagy: roles in disease and aging. *Cell Res*. 2014;24(1):92-104. doi:10.1038/cr.2013.153

Deng L, Chen L, Zhao L, et al. Ubiquitination of Rheb governs growth factor-induced mTORC1 activation. *Cell Res*. 2019;29(2):136-150. doi:10.1038/s41422-018-0120-9

Deng L, Jiang C, Chen L, et al. The ubiquitination of rag A GTPase by RNF152 negatively regulates mTORC1 activation. *Mol Cell*. 2015;58(5):804-818. doi:10.1016/j.molcel.2015.03.033

Dong XP, Cheng X, Mills E, et al. The type IV mucolipidosis-associated protein TRPML1 is an endolysosomal iron release channel. *Nature*. 2008;455(7215):992-996. doi:10.1038/nature07311

Fan T, Huang Z, Wang W, et al. Proteasome inhibition promotes autophagy and protects from endoplasmic reticulum stress in rat alveolar macrophages exposed to hypoxia-reoxygenation injury. *J Cell Physiol*. 2018;233(10):6748-6758. doi:10.1002/jcp.26516

Firkowska M, Macias M, Jaworski J. ESCRT Proteins Control the Dendritic Morphology of Developing and Mature Hippocampal Neurons. *Mol Neurobiol*. 2019;56(7):4866-4879. doi:10.1007/s12035-018-1418-9

Haglund K, Dikic I. The role of ubiquitylation in receptor endocytosis and endosomal sorting. *J Cell Sci*. 2012;125(Pt 2):265-275. doi:10.1242/jcs.091280

Henne WM, Buchkovich NJ, Emr SD. The ESCRT pathway. *Dev Cell*. 2011;21(1):77-91. doi:10.1016/j.devcel.2011.05.015

Hirota Y, Hayashi M, Miyauchi Y, Ishii Y, Tanaka Y, Fujimoto K. LAPTM4α is targeted from the Golgi to late endosomes/lysosomes in a manner dependent on the E3 ubiquitin ligase Nedd4-1 and ESCRT proteins. *Biochem Biophys Res Commun*. 2021;556:9-15. doi:10.1016/j.bbrc.2021.03.151

Hung YH, Chen LM, Yang JY, Yang WY. Spatiotemporally controlled induction of autophagy-mediated lysosome turnover. *Nat Commun*. 2013;4:2111. doi:10.1038/ncomms3111

Kao SH, Wang WL, Chen CY, et al. Analysis of Protein Stability by the Cycloheximide Chase Assay. *Bio Protoc*. 2015;5(1):e1374. doi:10.21769/BioProtoc.1374

Kirchner P, Bourdenx M, Madrigal-Matute J, et al. Proteome-wide analysis of chaperone-mediated autophagy targeting motifs [published correction appears in PLoS Biol. 2022 Feb 4;20(2):e3001550]. *PLoS Biol*. 2019;17(5):e3000301. Published 2019 May 31. doi:10.1371/journal.pbio.3000301

Kocaturk NM, Gozuacik D. Crosstalk Between Mammalian Autophagy and the Ubiquitin-Proteasome System. *Front Cell Dev Biol*. 2018;6:128. Published 2018 Oct 2. doi:10.3389/fcell.2018.00128

Koerver L, Papadopoulos C, Liu B, et al. The ubiquitin-conjugating enzyme UBE2QL1 coordinates lysophagy in response to endolysosomal damage. *EMBO Rep*. 2019;20(10):e48014. doi:10.15252/embr.201948014

Lawrence RE, Zoncu R. The lysosome as a cellular centre for signalling, metabolism and quality control. *Nat Cell Biol*. 2019;21(2):133-142. doi:10.1038/s41556-018-0244-7

Lee C, Lamech L, Johns E, Overholtzer M. Selective Lysosome Membrane Turnover Is Induced by Nutrient Starvation. *Dev Cell*. 2020;55(3):289-297.e4. doi:10.1016/j.devcel.2020.08.008

Li M, Koshi T, Emr SD. Membrane-anchored ubiquitin ligase complex is required for the turnover of lysosomal membrane proteins. *J Cell Biol*. 2015;211(3):639-652. doi:10.1083/jcb.201505062

Li M, Rong Y, Chuang YS, Peng D, Emr SD. Ubiquitin-dependent lysosomal membrane protein sorting and degradation. *Mol Cell*. 2015;57(3):467-478. doi:10.1016/j.molcel.2014.12.012

Maejima I, Takahashi A, Omori H, et al. Autophagy sequesters damaged lysosomes to control lysosomal biogenesis and kidney injury. *EMBO J*. 2013;32(17):2336-2347. doi:10.1038/emboj.2013.171

Mamińska A, Bartosik A, Banach-Orłowska M, et al. ESCRT proteins restrict constitutive NF-κB signaling by trafficking cytokine receptors. *Sci Signal*. 2016;9(411):ra8. Published 2016 Jan 19. doi:10.1126/scisignal.aad0848

Marques ARA, Saftig P. Lysosomal storage disorders - challenges, concepts and avenues for therapy: beyond rare diseases. *J Cell Sci*. 2019;132(2):jcs221739. Published 2019 Jan 16. doi:10.1242/jcs.221739

Marshall RS, Vierstra RD. Proteasome storage granules protect proteasomes from autophagic degradation upon carbon starvation. *Elife*. 2018;7:e34532. Published 2018 Apr 6. doi:10.7554/eLife.34532

Mejlvang J, Olsvik H, Svenning S, et al. Starvation induces rapid degradation of selective autophagy receptors by endosomal microautophagy. *J Cell Biol*. 2018;217(10):3640-3655. doi:10.1083/jcb.201711002

Mittal E, Skowyra ML, Uwase G, et al. Mycobacterium tuberculosis Type VII Secretion System Effectors Differentially Impact the ESCRT Endomembrane Damage Response. *mBio*. 2018;9(6):e01765-18. Published 2018 Nov 27. doi:10.1128/mBio.01765-18

Mizushima N, Noda T, Yoshimori T, et al. A protein conjugation system essential for autophagy. *Nature*. 1998;395(6700):395-398. doi:10.1038/26506

Milkereit R, Rotin D. A role for the ubiquitin ligase Nedd4 in membrane sorting of LAPTM4 proteins. *PLoS One*. 2011;6(11):e27478. doi:10.1371/journal.pone.0027478

Morshed S, Sharmin T, Ushimaru T. TORC1 regulates ESCRT-0 complex formation on the vacuolar membrane and microautophagy induction in yeast. *Biochem Biophys Res Commun*. 2020;522(1):88-94. doi:10.1016/j.bbrc.2019.11.064

Nixon RA. The aging lysosome: An essential catalyst for late-onset neurodegenerative diseases. *Biochim Biophys Acta Proteins Proteom*. 2020;1868(9):140443. doi:10.1016/j.bbapap.2020.140443

Nixon RA, Cataldo AM. Lysosomal system pathways: genes to neurodegeneration in Alzheimer's disease. *J Alzheimers Dis*. 2006;9(3 Suppl):277-289. doi:10.3233/jad-2006-9s331

Oku M, Maeda Y, Kagohashi Y, et al. Evidence for ESCRT- and clathrin-dependent microautophagy. *J Cell Biol*. 2017;216(10):3263-3274. doi:10.1083/jcb.201611029

Papadopoulos C, Kirchner P, Bug M, et al. VCP/p97 cooperates with YOD1, UBXD1 and PLAA to drive clearance of ruptured lysosomes by autophagy. *EMBO J*. 2017;36(2):135-150. doi:10.15252/embj.201695148

Papadopoulos C, Meyer H. Detection and Clearance of Damaged Lysosomes by the Endo-Lysosomal Damage Response and Lysophagy. *Curr Biol*. 2017;27(24):R1330-R1341. doi:10.1016/j.cub.2017.11.012

Pohl C, Dikic I. Cellular quality control by the ubiquitin-proteasome system and autophagy. *Science*. 2019;366(6467):818-822. doi:10.1126/science.aax3769

Radulovic M, Schink KO, Wenzel EM, et al. ESCRT-mediated lysosome repair precedes lysophagy and promotes cell survival. *EMBO J*. 2018;37(21):e99753. doi:10.15252/embj.201899753

Ran FA, Hsu PD, Wright J, Agarwala V, Scott DA, Zhang F. Genome engineering using the CRISPR-Cas9 system. *Nat Protoc*. 2013;8(11):2281-2308. doi:10.1038/nprot.2013.143

Robinson JS, Klionsky DJ, Banta LM, Emr SD. Protein sorting in Saccharomyces cerevisiae: isolation of mutants defective in the delivery and processing of multiple vacuolar hydrolases. *Mol Cell Biol*. 1988;8(11):4936-4948. doi:10.1128/mcb.8.11.4936
Rock KL, Gramm C, Rothstein L, et al. Inhibitors of the proteasome block the degradation of most cell proteins and the generation of peptides presented on MHC class I molecules. *Cell*. 1994;78(5):761-771. doi:10.1016/s0092-8674(94)90462-6
Rong Y, McPhee CK, Deng S, et al. Spinster is required for autophagic lysosome reformation and mTOR reactivation following starvation [published correction appears in Proc Natl Acad Sci U S A. 2011 Jul 5;108(27):11297. McPhee, Christina [corrected to McPhee, Christina K]; Baehreck, Eric H [corrected to Baehrecke, Eric H]]. *Proc Natl Acad Sci U S A*. 2011;108(19):7826-7831. doi:10.1073/pnas.1013800108
Sardana R, Emr SD. Membrane Protein Quality Control Mechanisms in the Endo-Lysosome System. *Trends Cell Biol*. 2021;31(4):269-283. doi:10.1016/j.tcb.2020.11.011
Schröder B, Wrocklage C, Pan C, et al. Integral and associated lysosomal membrane proteins. *Traffic*. 2007;8(12):1676-1686. doi:10.1111/j.1600-0854.2007.00643.x
Schuck S. Microautophagy - distinct molecular mechanisms handle cargoes of many sizes. *J Cell Sci*. 2020;133(17):jcs246322. Published 2020 Sep 9. doi:10.1242/jcs.246322
Schröder B, Wrocklage C, Hasilik A, Saftig P. Molecular characterisation of 'transmembrane protein 192' (TMEM192), a novel protein of the lysosomal membrane. *Biol Chem*. 2010;391(6):695-704. doi:10.1515/BC.2010.062
Schwake M, Schröder B, Saftig P. Lysosomal membrane proteins and their central role in physiology. *Traffic*. 2013;14(7):739-748. doi:10.1111/tra.12056
Shin HR, Zoncu R. The Lysosome at the Intersection of Cellular Growth and Destruction. *Dev Cell*. 2020;54(2):226-238. doi:10.1016/j.devcel.2020.06.010
Shirley RB, Kaddour-Djebbar I, Patel DM, Lakshmikanthan V, Lewis RW, Kumar MV. Combination of proteasomal inhibitors lactacystin and MG132 induced synergistic apoptosis in prostate cancer cells. *Neoplasia*. 2005;7(12):1104-1111. doi:10.1593/neo.05520
Sitaram A, Piccirillo R, Palmisano I, et al. Localization to mature melanosomes by virtue of cytoplasmic dileucine motifs is required for human OCA2 function. *Mol Biol Cell*. 2009;20(5):1464-1477. doi:10.1091/mbc.e08-07-0710
Skowyra ML, Schlesinger PH, Naismith TV, Hanson PI. Triggered recruitment of ESCRT machinery promotes endolysosomal repair. *Science*. 2018;360(6384):eaar5078. doi:10.1126/science.aar5078
Staub O, Abriel H, Plant P, et al. Regulation of the epithelial Na+ channel by Nedd4 and ubiquitination. *Kidney Int*. 2000;57(3):809-815. doi:10.1046/j.1523-1755.2000.00919.x
Sun Z, Brodsky JL. Protein quality control in the secretory pathway. *J Cell Biol*. 2019;218(10):3171-3187. doi:10.1083/jcb.201906047
Takahashi Y, He H, Tang Z, et al. An autophagy assay reveals the ESCRT-III component CHMP2A as a regulator of phagophore closure. *Nat Commun*. 2018;9(1):2855. Published 2018 Jul 20. doi:10.1038/s41467-018-05254-w
Tian S, Muneeruddin K, Choi MY, et al. Genome-wide CRISPR screens for Shiga toxins and ricin reveal Golgi proteins critical for glycosylation. *PLoS Biol*. 2018;16(11):e2006951. Published 2018 Nov 27. doi:10.1371/journal.pbio.2006951
Vietri M, Radulovic M, Stenmark H. The many functions of ESCRTs. *Nat Rev Mol Cell Biol*. 2020;21(1):25-42. doi:10.1038/s41580-019-0177-4

Votteler J, Ogohara C, Yi S, et al. Designed proteins induce the formation of nanocage-containing extracellular vesicles. *Nature*. 2016;540(7632):292-295. doi:10.1038/nature20607

Wang XJ, Yu J, Wong SH, et al. A novel crosstalk between two major protein degradation systems: regulation of proteasomal activity by autophagy. *Autophagy*. 2013;9(10):1500-1508. doi:10.4161/auto.25573

Woolford CA, Daniels LB, Park FJ, Jones EW, Van Arsdell JN, Innis MA. The PEP4 gene encodes an aspartyl protease implicated in the posttranslational regulation of Saccharomyces cerevisiae vacuolar hydrolases. *Mol Cell Biol*. 1986;6(7):2500-2510. doi:10.1128/mcb.6.7.2500-2510.1986

Wyant GA, Abu-Remaileh M, Frenkel EM, et al. NUFIP1 is a ribosome receptor for starvation-induced ribophagy. *Science*. 2018;360(6390):751-758. doi:10.1126/science.aar2663

Xiong MG, Xu ZS, Li YH, Wang SY, Wang YY, Ran Y. RNF152 positively regulates TLR/IL-1R signaling by enhancing MyD88 oligomerization. *EMBO Rep*. 2020;21(3):e48860. doi:10.15252/embr.201948860

Yamaji T, Sekizuka T, Tachida Y, et al. A CRISPR Screen Identifies LAPTM4A and TM9SF Proteins as Glycolipid-Regulating Factors. *iScience*. 2019;11:409-424. doi:10.1016/j.isci.2018.12.039

Yambire KF, Rostosky C, Watanabe T, et al. Impaired lysosomal acidification triggers iron deficiency and inflammation in vivo. *Elife*. 2019;8:e51031. Published 2019 Dec 3. doi:10.7554/eLife.51031

Yang C, Wang X. Lysosome biogenesis: Regulation and functions. *J Cell Biol*. 2021;220(6):e202102001. doi:10.1083/jcb.202102001

Yang X, Arines FM, Zhang W, Li M. Sorting of a multi-subunit ubiquitin ligase complex in the endolysosome system. *Elife*. 2018;7:e33116. Published 2018 Jan 22. doi:10.7554/eLife.33116

Yang X, Reist L, Chomchai DA, Chen L, Arines FM, Li M. ESCRT, not intralumenal fragments, sorts ubiquitinated vacuole membrane proteins for degradation. *J Cell Biol*. 2021;220(8):e202012104. doi:10.1083/jcb.202012104

Yang X, Zhang W, Wen X, et al. TORC1 regulates vacuole membrane composition through ubiquitin- and ESCRT-dependent microautophagy. *J Cell Biol*. 2020;219(3):e201902127. doi:10.1083/jcb.201902127

Chapter 4: A Genome-wide CRISPR-Cas9 Screen Reveals a Novel Factor Essential for Lysosome Biogenesis

Lysosomes contain acidic hydrolases critical for digesting macromolecules and maintaining nutrient homeostasis in the cell. The GlcNAc-1-phosphotransferase (GNPT) catalyzes the first-step reaction of the mannose-6-phosphate (M6P) modification of lysosomal soluble proteins. M6P is essential for the proper targeting of acidic hydrolases to lysosomes. In this study, we performed a genome-wide CRISPR-Cas9 screen to identify essential factors for lysosome function. Our screen results highlight the importance of M6P biogenesis, endosomal membrane trafficking pathway, and lysosomal v-ATPase to maintain lysosome function. In addition, we identified TMEM251, a functionally uncharacterized gene, as a top hit. We showed that ablation of TMEM251 leads to lysosome dysfunction due to hypersecretion of lysosomal hydrolases. Notably, these secreted lysosome hydrolases do not contain M6P modifications, suggesting a defect in M6P biogenesis. Our investigation further indicated that TMEM251 is required for the cleavage and activation of GNPT α/ β precursor by MBTPS1. Lastly, in zebrafish, we showed that TMEM251 deficiency leads to severe heart edema and maldevelopments of cartilage and bone tissues, which phenocopies mucolipidosis-II (*gnptab*KO) *in vivo*. Thus, our study uncovered a novel critical factor that regulated lysosome biogenesis.

4.1 Introduction

N-acetylglucosamine-1-phosphotransferase (GlcNAc-1-phosphotransferase) is essential for lysosome biogenesis by catalyzing the formation of mannose-6-phosphate (M6P) modifications on lysosomal luminal proteins (Qian et al., 2010). The M6P receptors recognize M6P residues at the trans-Golgi network (TGN) and deliver lysosomal enzymes to the endo-lysosomal compartment (Dahms et al., 1987; Oshima et al., 1988; Ghosh et al., 2003; McCormick et al., 2008). GlcNAc-1-phosphotransferase (GNPT) is a $\alpha_2\beta_2\gamma_2$ hexamer (Bao et al., 1996). The *GNPTAB* gene encodes the catalytic α and β subunits, and the *GNPTG* gene encodes the soluble γ subunit (Raas-Rothschild et al., 2000; Kudo et al., 2005; Tiede et al., 2005). Mutations in the *GNPTAB* gene lead to inherited metabolic disorders mucolipidosis (ML) type II and type III α/β. At the cellular level, defective GNPT activity leads to mistargeting and hypersecretion of the lysosomal enzymes, and thus, lysosomal dysfunction (Wiesmann et al., 1971). Consequently, undigested substrates, including lipids, glycosaminoglycans, and protein aggregates, accumulate in lysosomes, resulting in severe damages to cells (Kollmann et al., 2012; Coutinho et al., 2012; Mareninova et al., 2021). Clinically, MLII and MLIIIα/β are characterized by coarse facial features, short stature, skeletal abnormalities, and delayed physical and mental development (Cathey et al., 2010; Khan & Tomatsu, 2020; Dogterom et al., 2021). In addition, patients with MLII or MLIIIα/β suffer prolonged respiratory infections and severe cardiac complications (Otomo et al., 2009; Edmiston et al., 2018; Kwak et al., 2018). MLIIIγ, caused by mutations in the *GNPTG* gene, often leads to milder symptoms compared to MLII (Oussoren et al. 2018).

The α and β subunits of GNPT is transcribed and translated as an α/ β precursor form. At the cis-Golgi, membrane bound transcription factor peptidase, site-1 (MBTPS1) cleaves the α/ β

precursor; therefore, activates its transferase function (Marschner et al., 2011). Interestingly, MBTPS1 was originally discovered as one of the key regulators for unfolded protein response (UPR) and sterol synthesis. Under certain cellular stress (e.g., ER stress or low sterol level), ATF6 (activating transcription factor 6) and SREBPs (Sterol regulatory element-binding proteins) are sequentially cleaved by MBPTS1 and MBTPS2, releasing the active transcriptional factors to control gene expression in specific cellular pathways (Yokoyama et al. 1993; Haze et al, 1999; Ye et al. 2000; Yoshida et al. 2001; Pedersen et al. 2007). As MBTPS1 regulates diverse cellular events through its proteolytic activity, a mystery remains for more than a decade: how MBTPS1 achieves its selectivity against GNPT to regulate lysosome biogenesis.

In this study, we conducted a genome-wide CRISPR-Cas9 screen to identify genes essential for lysosome function. Our screen revealed a functionally uncharacterized gene, TMEM251, required for lysosome biogenesis. Ablation of this novel factor causes hypersecretion of lysosomal enzymes, and thus, defects in lysosome-related pathways. We further demonstrated that TMEM251 is critical for M6P biogenesis by selectively promoting the processing and activation of GNPT by MBTPS1. Using a zebrafish model, we showed that TMEM251 deficiency phenocopies MLII *in vivo* (Qian et al. 2013; Qian et al. 2015). Collectively, our work suggested a conserved role of TMEM251 in regulating lysosome biogenesis.

4.2 Results

4.2.1 A genome-wide CRISPR-Cas9 screen reveals essential components for lysosomal function.

Lysosomes play essential roles in maintaining cellular nutrient homeostasis. It is important and intriguing to understand how cells regulate lysosomal membrane protein (LMP)

composition in response to environmental cues. Previously, we and others demonstrated a conserved ubiquitin- and ESCRT-dependent mechanism that turns over LMPs in yeast and human cells (Li et al., 2015, Oku et al., 2017; Yang et al., 2018; Yang et al., 2020; Morshed et al., 2020; Arines et al., 2021; Zhang et al., 2021). In our recent study, we characterized two human lysosomal membrane proteins, RNF152 and LAPTM4A, are internalized and degraded inside the lysosome (Chapter 3, Zhang et al., 2021).

To further investigate how human cells regulate lysosomal function and LMP turnover, we aimed to screen for novel factors involved in this process. First, we generated a reporter cell line that stably expressed both GFP-RNF152 and mCherry. After cycloheximide (CHX) treatment to inhibit protein synthesis, GFP-RNF152 is quickly degraded and mCherry remains stable in the cytosol (Fig. 1A-B, 1D). To conduct the CRISPR screen, we sequentially transduced the reporter cells with Lenti-Cas9 and the human CRISPR Brunello pooled libraries (Fig. 1C) (Doench et al., 2016). For genes essentials for the degradation of LMP, we predicted that CRISPR knockout would stabilize the GFP-RNF152 signal, leading to a relatively high GFP/mCherry ratio after CHX chase. After two consecutive rounds of FACS, we enriched a population with >90% high GFP/mCherry ratio at the steady-state, and the GFP signal is resistant to the CHX treatment (Fig. 1D). Through Next-Generation Sequencing and bioinformatic analysis, we identified 193 enriched genes from the first-round sorting and 27 genes from the second-round sorting with FDR<10^{-5} and $\log_2|FC|>1$ (Fig. 1E, Table 1). Notably, our screen results highlight the following functional groups: 1) M6P modification at the Golgi Apparatus (*GNPTAB, GNPTG,* and *MBTPS1*), (2) endosomal sorting machinery (HOPS & CORVET components: *VPS11/16/18/33A/39/41, LRRK2*, and *PIKFYVE*), and (3) v-ATPase components on the lysosomes (*ATP6V0B/C/D1, ATP6V1A/B2/C1/D/G1, ATP6AP1/2, WDR7,*

and *VMA21*) (Fig. 1F). These functional groups represent key compartments of membrane trafficking and lysosome biogenesis which further supported and validated our previous finding that the degradation of RNF152 is lysosome dependent (Zhang et al., 2021).

Our screen also reveals a few uncharacterized genes, among which *TMEM251* is the strongest hit. *TMEM251* encodes two transcriptional variants through alternative splicing: a long isoform (18.7kDa) and a short isoform (15.2kDa) (Fig. 1E, Fig S1A). To verify the expression of each isoform at the protein level, we first used CRISPR-Cas9 technique to knockout TMEM251 in HEK293 cells and then overexpressed each isoform, respectively. Our results suggest that the short isoform is the predominantly variant at the endogenous level, and the long isoforms can be further processed into short isoforms (Fig. S1B).

4.2.2 TMEM251 is essential for lysosome function

To investigate the cellular function of TMEM251, we transduced HEK293 cells that stably expressed GFP-RNF152 with Cas9 and two independent sgRNAs against TMEM251. Both sgRNAs achieved high KO efficiency at the polyclonal level (Fig. 2A). Consistent with our screen results, TMEM251 deficiency blocks the degradation of GFP-RNF152, and the protein level of GFP-RNF152 increases two-fold at the steady-state (Fig 2A-C).

In our previous study, we identified another LMP, LAPTM4A, which is also constitutively degraded by lysosomes (Zhang et al., 2021). To verify the functional role of TMEM251 in regulating LMP degradation, we monitored the protein level and degradation kinetics of the endogenous LAPTM4A. As expected, TMEM251 deficiency leads to a drastic increase of LAPTM4A protein level by 8 to 10-fold and significantly slower degradation kinetics (Fig 2D-F).

To test if TMEM251 is also involved in other lysosome-dependent cellular processes, such as cell surface receptor endocytosis and degradation, we generated two independent TMEM251KO colonies of HeLa cells and evaluated the degradation of epidermal growth factor receptor (EGFR) induced by EGF (Chen et al., 1989). Our data show that TMEM251KO leads to a significant delay of EGFR turnover after EGF treatment, suggesting the degradation of EGFR is impaired (Fig S2A-B).

Previously, an autophagy reporter based CRISPR-Cas9 screen has identified TMEM251 as one of the top hits, suggesting its role in regulating autophagy (Shoemaker et al., 2019). To test this hypothesis, we investigated the protein level of p62/SQSTM1 (an autophagy receptor) and LC3B-II (a maker for autophagosome) in HEK293 and HeLa cells. Indeed, TMEM251 deficiency leads to a two-fold increase of p62/SQSTM1 protein level and ~6-fold increase of the lipidated LC3B-II level under the growth condition (Fig 2G-I, Fig S2C). These results suggest TMEM251 is also an important autophagy factor.

We further ruled out the off-target effects of CRISPR-Cas9 KO by stably overexpressing either the long or short isoform in the TMEM251KO cells, respectively. About 10 days post-transduction, both long and short isoforms rescued the accumulation of LAPTM4A and LC3B-II (Fig S3A-C). As TMEM251 deficiency impairs various lysosome-dependent pathways, including LMP degradation, EGFR endocytosis and degradation, and autophagy, we concluded that TMEM251 is a master regulator of lysosome function.

4.2.3 Ablation of TMEM251 upregulates lysosome biogenesis

How does TMEM251 deficiency lead to lysosomal dysfunction? We envision two scenarios that might explain this observation: (1) lysosomes might have an acidification defect, which inactivates luminal hydrolases that depend on the low pH to be functional, or (2) the

luminal hydrolases might be absent from lysosomes. To test the first hypothesis, we stained cells with lysotracker that labels the acidic endo-lysosomes and analyzed them by flow cytometry. Instead of lowering the fluorescent intensity, TMEM251KO led to a drastic increase of the lysotracker signal in both HeLa and HEK293 cells (Fig. 2J). Using transmission electron microscopy, we observed a massive increase of electron-dense lysosomes with numerous undigested materials accumulating inside after knocking out TMEM251 (Fig. 2K-L). The average lysosome radius also increases by 10%, corresponding to a ~30% increase in volume (Fig. 2L-M). Together, these results indicated that TMEM251 deficiency increases lysosome biogenesis and does not impair the v-ATPase function.

Intrigued by the increase of lysosome numbers, we analyzed the knockout cells with RNA sequencing (Fig. S4A). Transcriptome analysis reveals 211 differential expressed genes (DEGs) with $p<0.05$ and $\log_2|FC|>0.263$ (Fig. S4D). The gene ontology (GO) analysis confirmed the upregulation of lysosome pathways at the transcriptional level (Fig. 2N-P). In addition, the transcription of genes involved in extracellular matrix formation and focal adhesion was reduced (Fig. 2N). When categorizing these DEGs into biological processes, we noticed that genes involved in the lipid metabolism pathways, autophagy, UDP-GlcNAc biosynthetic processes were also upregulated (Fig. S4B-C). These findings are consistent with recent CRISPR-Cas9 KO screens suggesting that TMEM25KO leads to increased lipid/cholesterol biosynthesis (van den Boomen et al., 2020; Lu et al., 2021). As lysosome plays a critical role in regulating lipid homeostasis, these transcriptional activations may be due to feedback from lysosome dysfunction in TMEM251 deficient cells. On the other hand, the expression of genes involved in wound healing and development of the urogenital system, sensory organ, and epidermis decreases. These imply that TMEM251 deficiency may lead to severe developmental defects.

Taken together, our results indicated that TMEM251 deficiency resulted in lysosome dysfunction. Presumably, as a feedback response, cells upregulated lysosomal and lipid metabolic pathways.

4.2.4 TMEM251 deficiency leads to the secretion of many lysosomal hydrolases

After ruling out the acidification defect, we tested if luminal hydrolases can still properly target to the lysosome using Cathepsin D and C (CTSD and CTSC) as proxies. Both enzymes are sorted at the trans-Golgi network (TGN) and undergo sequential cleavage into mature forms when reaching the lysosome. Strikingly, depleting TMEM251 abolished the mature forms of both CTSD and CTSC in the cell, and only the pro-enzymes were detected (Fig. 3A-C). Analyzing the conditioned culture media indicated that a significant portion of the ProCTSD and ProCTSC were also secreted out of the cell (Fig. 3A-C).

To obtain a holistic view of how many lysosomal enzymes are secreted after knocking out TMEM251, we compared the conditioned media from TMEM251 deficient cells to WT cells using quantitative mass spectrometry. Our analysis uncovered 39 lysosome luminal proteins exhibiting significantly increased secretion in TMEM251 deficient cells ($\log_2|FC|>1$ and $p<0.05$) (Fig. 3D-E). This comprehensive secretome analysis confirms that many luminal proteins are mistargeted to the secretory pathway after knocking out TMEM251.

4.2.5 TMEM251 is essential for the M6P biogenesis of lysosome enzymes

To understand how TMEM251 deficiency leads to hypersecretion of lysosome enzymes, we first determined the subcellular localization of TMEM251. Using an antibody that recognizes the C-terminus of the protein, we observed that both long and short isoforms of TMEM251 colocalized with the cis-Golgi marker GM130 (Fig. S5A-B). Interestingly, a small fraction of TMEM251 also colocalized with the early endosome marker EEA1 and the lysosome marker

LAMP2 (Fig. S5A-B). At the endogenous level, TMEM251 is highly enriched in the rat liver Golgi extract (Fig. S5C) and shows slight enrichment in the purified lysosomes (Fig. S5D). Altogether, we concluded that TMEM251 is mainly localized to Golgi with a small population also localized to the later endo-lysosome compartments.

Besides TMEM251, our CRISPR screen also identified three other Golgi factors essential for lysosome function, including GNPTAB, GNPTG, and MBTPS1 (Fig. 1E-F). *GNPTAB* and *GNPTG* encode the three subunits of GlcNAc-1-phosphotransferase (GNPT), the enzyme responsible for M6P modification of lysosomal hydrolases (Kudo et al., 2005). *GNPTAB* encodes α- and β-subunits, whereas *GNPTG* encodes the γ-subunit. The complete GNPT enzyme is an α2β2γ2 hexamer, which is assembled at the ER before its trafficking to the Golgi (Bao et al., 1996). Upon arrival at the Golgi, the GNPT α/β precursor is cleaved by the membrane bound transcription factor peptidase, site 1 (MBTPS1) and activated (Marschner et al., 2011; Velho et al., 2017). At the cis-Golgi, GNPT utilizes UDP-GlcNAc as a substrate to transfer GlcNAc-phosphate onto the mannose group of lysosomal enzymes (Qian et al., 2010). The uncovering enzyme (UCE) then removes the GlcNAc group to expose the M6P (Rohrer & Kornfeld, 2001). At the trans-Golgi network, the M6P receptors (CI/CD-MPRs) recognize the M6P signal of luminal enzymes and sort them to lysosomes (Fig. 4A) (Kang et al., 2010; Coutinho et al., 2012b). Mutations in either *GNPTAB* or *MBTPS1* that lead to the GNPT cleavage deficiency will result in the M6P biogenesis defect and secretion of most luminal enzymes. Interestingly, published bioinformatic analysis indicated a high co-dependency (Pearson correlation 0.26, https://www.depmap.org) between *TMEM251* and *GNPTAB* from large-scale CRISPR knockout screen datasets, suggesting a genetic correlation between the two genes. Because of the similar

localization, consistent secretion phenotypes for luminal enzymes, and the genetic correlation, we hypothesized that TMEM251 is also a critical factor in the M6P biogenesis pathway.

As the first step to assess the role of TMEM251 in M6P biogenesis, we studied the processing and secretion of proCTSD in TMEM251 KO, GNPTAB KO, and CI-MPR (cation-independent mannose-6-phosphate receptor) KO cells. TMEM251 KO phenocopies GNPTAB deficiency as evidenced by the absence of mature CTSD and the accumulation of ProCTSD. CI-MPR KO cells showed a mild phenotype with a small amount of proCTSD being delivered to the lysosome and processed to the mature form (Fig. 4B). Importantly, all three KO lines exhibit strong secretion of ProCTSD into the conditioned media (Fig 4B). To directly evaluate the M6P modification state of secreted lysosome enzymes, we used purified biotinylated M6P receptors to detect the presence of M6P in the conditioned media (Sleat et al., 2005; Sleat et al., 2008). Our results indicated that only the conditioned media from CI-MPR KO cells contains M6P-tagged glycoproteins, whereas condition media from the TMEM251 KO and GNPTAB KO cells do not (Fig. 4C). Further, knocking out TMEM251 in CI-MPR KO cells abolished the binding of biotinylated M6P receptors, suggesting that TMEM251 functions upstream of the M6P sorting step and is likely involved in the M6P modification (Fig. 4C).

We also verified our results by examining the M6P modification of individual enzymes, including Lipase A (LIPA), CTSD, and cathepsin Z (CTSZ). After immunoprecipitation, we detected the M6P modifications using a single-chain antibody against M6P (Müller-Loennies et al., 2010; Blacker et al., 2016). As shown in Figure 4D-F, TMEM251 deficiency abolished the M6P modification of all three tested lysosome enzymes.

As TMEM251 deficiency leads to lysosome dysfunction due to the absence of M6P modifications, we ask if we can use conditioned media from CI-MPR KO cells that contain M6P

tagged lysosome enzymes to rescue the TMEM251 deficient cells (Neufeld, 2006). Early studies demonstrated that MPRs also localize to the cell surface to endocytose secreted lysosome enzymes and deliver them to the lysosome through receptor-mediated endocytosis (Geuze et al., 1984). Indeed, feeding TMEM251 knockout cells with conditioned media from CI-MPR KO cells partially rescued lysosome function, as evidenced by reduction of full-length LAPTM4A and LC3B-II (Fig. 4G-J). In addition, we also observed a significant increase of mature enzymes such as mCTSC and mCTSD (Fig. 4G, 4K-L), indicating that M6P-tagged enzymes have reached the lysosome. These rescued phenotypes can be abolished by adding free M6P to saturate the M6P receptors at the cell surface (Fig. 4G-L). Lastly, the conditioned media from GNPTAB KO cells did not rescue the lysosome defects in TMEM251 deficient cells (Fig. 4G-L). These results demonstrated that the lysosome defects in TMEM251 knockout cells are due to the lack of M6P on its luminal enzymes because they can be rescued by exogenous addition of M6P containing enzymes.

Taken together, we concluded that TMEM251 is essential for the M6P biogenesis of lysosome enzymes. It acts upstream of the MPR sorting and likely functions at the step of M6P modification.

4.2.6 TMEM251 is required for the efficient processing of GNPT α/β precursor

Next, we set out to resolve the relationship among TMEM251, GNPT, and MBTPS1. To this end, we knocked in a 3xHA tagged at the C-terminus of the *GNPTAB* gene in HEK293T cells using the CRISPR-Cas9 technique (Ran et al., 2013). At the endogenous level, a majority of GNPT α/β precursor is processed into the active form, as indicated by the strong signal of 3xHA-tagged β subunit at ~48kDa (Fig. 5A). We also observed a small amount of the unprocessed α/β precursor at ~200 kDa. Knocking out TMEM251 abolished the β subunit in cells. Interestingly,

we noticed the accumulation of a new band slightly larger than the α/β precursors after knocking out TMEM251 (Fig. 5A). To verify our results, we generated a cell line that stably overexpresses GNPTAB-3xV5. Consistently, ablation of TMEM251 nearly abolished the processing of GNPTAB-3xV5 (Fig. 5B). On the other hand, overexpressing the short isoform of TMEM251 promoted the processing, indicated by the increase of the β subunits (Fig. 5B). These results suggested that TMEM251 is required for the cleavage of GNPT α/β precursor by MBTPS1 and explained why knocking out TMEM251 leads to lysosome dysfunction and secretion of many luminal enzymes. Notably, TMEM251 KO does not impair the processing of SREBF2/SREBP2 trigger by sterol depletion (Fig. 5C-E), suggesting TMEM251 selectively promote the cleavage of the GNPT α/β precursors by MBTPS1.

We further assessed the interaction among GNPT, MBTPS1, and TMEM251. First, we confirmed that TMEM251 interacts with MBTPS1 (Fig. 5F). Moreover, using catalytic-defective mutant (S414) of MBTPS1, we can pull down both GNPTAB α/β precursors and the active β subunit, suggesting MBTPS1 interacts with both precursor and active forms (Fig. 5G). Interestingly, this interaction is not affected in TMEM251-null cells, suggesting TMEM251 does not bridge the interaction between GNPT and MBTPS1 (Fig. 5G).

Taken together, our results demonstrated that TMEM251 is required for GNPT activation through selectively promoting its processing by MBTPS1.

4.2.7 TMEM251 deficiency phenocopies MLII *in vivo*

TMEM251 is conserved in the metazoan (Ain et al., 2021). The amino acid sequences of TMEM251 in Zebrafish (*Danio rerio*) and the human short isoform share 69.7% identity (Fig. 6A). Previous studies have successfully established a zebrafish model to study human lysosomal storage diseases, including mucolipidosis type II (MLII) (Qian et al., 2013; Qian et al., 2015;

Flanagan-Steet et al., 2016; Lu et al., 2020). As our data indicated that TMEM251 is required for the processing and activation of GNPT α/β precursor, we anticipated similar developmental phenotypes between *tmem251* KO and *gnptab* KO (MLII) in zebrafish. Using the CRISPR-Cas9 technique, we generated *tmem251* and *gnptab*-deficient mutants in the F0 generation (Kroll et al., 2021). For both mutants, we observed that >50% of the population elicited aberrant morphology at 5-7 dpf (Fig. 5B-D). We further categorized these defective phenotypes into two groups: 1) severe edema in the heart, trunk, or whole-body without tail abnormities, 2) severe edema with curly tail or no tail (Fig. 5B-D). These phenotypes were consistent with the clinical observations that MLII was commonly associated with cardiovascular abnormalities and defects in body development (Kwak et al., 2018; Dogterom et al., 2021).

Clinically, MLII is characterized by short stature and skeletal deformities (Cathey et al., 2010; Khan & Tomatsu, 2020; Dogterom et al., 2021). To further assess the relationship between TMEM251 and ML-like disorder, we examined the cartilage development using Alcian blue staining (Walker & Kimmel 2007). As shown in Fig. 6E, the Group 1(edema only) *tmem251*- and *gnptab*-deficient embryos exhibit significant dysmorphogenesis of the jaw. The Group 2 (edema + curly tail) embryos displayed more severe mal-development in the cartilage, indicated by the loss of the majority of the cartilage structures (Fig. 6E). Further, Alizarin red staining showed a remarkable reduction of the calcified bone structures in the *tmem251*- and *gnptab*-deficient zebrafish with aberrant morphology (Fig. 6F).

Together, our *in vivo* study indicated that TMEM251 deficiency phenocopies MLII as evidenced by cardiac abnormalities and mal-development in cartilage and bone tissues.

4.3 Discussion

In this study, we performed a genome-wide CRISPR-Cas9 screen to identify uncharacterized factors essential for LMP degradation and lysosomal function. Our study uncovered that TMEM251 promotes the processing of GNPT α/β precursor by MBTPS1 (Figure 7). Ablation of TMEM251 impairs the cleavage and activation of GNPT, thus, resulting in M6P biogenesis defects. In TMEM251 deficient cells, lysosomal enzymes lacking the M6P modifications are mis-sorted into the secretory pathway and no longer reach lysosomes, leading to severe lysosomal dysfunction. In a zebrafish model, *tmem251*-defeicient mutant resembled MLII phenotypes, indicated by severe cardiac and skeletal abnormalities. These results together suggested that TMEM251 plays a critical role in regulating lysosomal biogenesis and function.

MLs are classified into four subtypes according to the genes/enzymes that are affected. MLI (sialidosis) results from the deficiency of lysosomal sialidase, which removes sialic acid from glycoproteins, leading to the accumulation of toxic complex carbohydrates in the body (d'Azzo et al., 2015). MLII and MLIII are both associated with GNPT. MLII, also known as I-cell (inclusion-cell) disease, is characterized by the build-up of waste products called inclusion bodies. MLII patients often die early in their lifetime due to heart failure or respiratory tract infection (Otomo et al., 2009; Edmiston et al., 2018; Kwak et al., 2018). In contrast, MLIII manifests less severe symptoms and progresses slower (Oussoren et al., 2018). Lastly, pathogenic mutations of MCOLN1 cause MLIV, which is characterized by delayed psychomotor development and progressive visual impairment (Bach, 2001). MCOLN1 encodes a cation channel that releases Ca^{2+} from endo-lysosomal compartments, which regulates lysosome-related events such as fusion and trafficking (Bassi et al., 2000; Cheng et al., 2010; Venkatachalam et al., 2015). However, the underlining mechanism of how MCOLN1 mutations lead to

neurodevelopment disorder remains unclear. In this study, we characterized a new type of ML associated with mutations in *TMEM251*. Mechanistically, TMEM251 is essential for the processing and activation of GNPT. Symptomatically, individuals who carried the pathogenic *TMEM251* mutations displayed severe skeletal disorder reminiscent of MLII, including coarse facial features, skeletal dysplasia, and short stature (Ain et al., 2021). Therefore, we propose to classify this MLII-liked inherited metabolic disorder caused by pathogenic *TMEM251* mutation as ML type V (MLV).

MBTPS1 controls a variety of biological pathways via its proteolytic activities. One mechanism to regulate MBTPS1 processing is to modulate the subcellular localization of its substrates in response to cellular stress and environmental cues. For example, MBTPS1 regulates lipid homeostasis through the processing of SREBP1/2. When cholesterol is present in the ER, the SREBPs/SCAP complex interacts with INSIG1/2 causing its ER retention (Yang e al., 2002). Cholesterol depletion leads to dissociation of SREBPs/SCAP from INSIGs and transport to the Golgi via COP-II vesicles (Espenshade et al., 2002). Similarly, ATF6 forms complex with BIP at the ER (Shen et al., 2005). ER stresses trigger the dissociation of ATF6 from BIP and its translocation to the Golgi. At the cis-Golgi, SREBPs and ATF6 are sequentially processed by MBTPS1 and MBTPS2, and the N-terminal transcription factor domains enter the nucleus and activate cellular lipid/ biogenesis and ER stress responses, respectively (Yokoyama et al., 1993; Haze et al., 1999; Ye et al., 2000; Yoshida et al., 2001; Pedersen et al., 2007). On the other hand, the ER-Golgi trafficking of the GNPT α/β precursor is mediated by its N-terminal dileucine motif and C-terminal dibasic motif (Franke et al., 2013). As lysosomes are essential organelles to maintain cellular homeostasis, it is unclear, or probably even unlikely, that any cellular factors might retain the GNPT α/β precursor in the ER in healthy cells (Velho et al., 2017).

A second possible mechanism is to modulate the substrate specificity of MBTPS1. Recently, multiple studies uncovered a novel factor, C12orf49/POST1/SPRING1, that positively regulated SREBPs signaling by promoting MBTPS1 proteolytic activities (Aregger et al., 2020; Bayraktar et al., 2020; Loregger et al., 2020; Xiao et al., 2021). However, this novel factor does not provide specificities against various substrates of MBTPS1 (Bayrakar et al., 2020; Xiao et al., 2021). Instead, it is required for the maturation of MBTPS1 (Xiao et al., 2021). In our study, we discovered that TMEM251 selectivity promoted the processing and activation of GNPT. Moreover, ablation of TMEM251 did not interfere with other MBTPS1-dependent processing, such as SREBF2/SREBP2 cleavage in response to cholesterol deprivation, indicating that this processing is unique to the GNPT α/β precursor at the substrate level. Thus, our study unveiled a novel mechanism for cells to regulate MBTPS1 selectivity and lysosome biogenesis.

To date, it is unclear how exactly TMEM251 selectively promotes the processing of GNPT α/β precursor MBTPS1. We first speculated that TMEM251 may serve as an adaptor to recruit MBTPS1 to GNPT α/β precursor. However, our IP analysis showed that knocking out TMEM251 does not interfere with the interaction between GNPT and MBTPS1, which does not favor the adaptor hypothesis. Interestingly, recent studies implicated that some pathogenic mutations of GNPTAB (ex: Y937-M972 deletion) and N-terminal truncation of the GNPT-α subunits (lacking the spacer-1 domain) both led to abnormal processing of GNPT α/β precursor, producing non-functional enzyme (Velho et al., 2015). Therefore, it is possible that TMEM251 might engage MBTPS1 and GNPT α/β precursor in a correct conformation for efficient and precise cleavage. As we are still at the early stage of exploring the function of TMEM251, future investigations on understanding how TMEM251, and potentially other uncharacterized factors, may regulate MBTPS1 specificity would be important and exciting.

4.4. Materials and Methods

Mammalian cell culture

Cell lines used in this study are listed in Table S1. HEK293 (CRL-1573), HEK293T (CRL-3216) and, HeLa (CCL-2) were purchased from ATCC. Cells were cultured in DMEM (Invitrogen) containing 10% Super Calf Serum (Gemini), 1% penicillin and streptomycin (Invitrogen) and 1µg/ml plasmocin (Invivogen) at 37°C, 5% CO_2. All cells were tested negative for mycoplasma.

Plasmids

Plasmids used in this study are listed in Table S2. The CDS of TMEM251 was purchased from DNASU plasmid Repository (Arizona State University). The CDS of GNPTAB is a generous gift from Dr. Stuart Kornfeld at the Washington University in St. Louis.

Transfection

HEK293 cells were cultured in DMEM containing 10% serum-only media for at least 4 days before transfection. Cells were transfected with individual overexpression plasmids (2.4 µg DNA for a 3.5cm dish) using Lipofectamine 2000 (Invitrogen) according to the manufacturer's instruction.

Generation of lentiviral stable cell lines

Stable cell lines were generated as described in Zhang et al, 2021. In Brief, HEK293T cells were transfected with transfer plasmid, psPAX2 (Addgene 12260), and pMD2.G (Addgene 12259) at 3.5:3.5:1 ratio using Lipofectamine 2000 according to the manufacturer's instruction. 72 hours after transfection, the supernatant was collected and applied through a 0.45 µm filter. To generate stable cell lines, HEK293, HEK293T or HeLa cells were seeded in 3.5cm or 6cm dishes and infected with the infectious media (DMEM containing 10% super calf serum, 10

μg/ml polybrene, MOI between 0.3 to 0.5). The puromycin selection was used at 1 μg/ml, and the blasticidin selection was used at 10 μg/ml. The selection lasted for at least 10 days before subsequent analysis.

Generation of CRISPR-Cas9 KO and KI cell lines

TMEM251, *GNPTAB*, and *CI-MPR* knockout HEK293 or HeLa cells were generated as described in Ran et al., 2013. In brief, sgRNA guides were ligated into pspCas9(BB)-2A-Puro (Addgene, 48139) or Lenti-multi-CRISPR (Addgene 85402) plasmids. For single colonies, cells were transfected with CRISPR-Cas9 knockout plasmids using Lipofectamine 2000 according to the manufacturer's instruction. After 24 hours of transfection, cells were treated with 1μg/ml puromycin (Invitrogen) for 48 hours. Single cells were isolated into 96-well plates using limited dilution to a final concentration of 0.5 cell per well. The knockout colonies were screened by western blot analysis. The KO cell lines were verified by sequencing analysis to confirm the indels at target sites. For polyclonal KO cell lines, cells were transduced with Lentivirus-based CRISPR-Cas9 plasmids. After 24 hours, cells were treated with 1μg/ml puromycin for 7 days.

To generate the template for CRISPR-Cas9 KI of GNPTAB, the 300bp homology arms (upstream and downstream from the stop codon) were amplified from the genomic DNA. The 3HA coding sequence was inserted in between the homology arms by overlapping extension. The resulted DNA fragment was ligated into the pGEM-T Easy vector. To generate the GNPTAB-3HA KI cells, HEK293T cells from a 6 cm dish were transfected with 4 μg of template plasmid and 2 μg CRISPR-Cas9 plasmid using Lipofectamine 2000 according to the manufacturer's instruction. After 24 hours of transfection, cells were treated with 1μg/ml puromycin (Invitrogen) for 48 hours. Single cells were isolated into 96-well plates using limited dilution to a final concentration of 0.5 cell per well. The knockin colonies were screened by PCR

using a 3HA internal forward primer and a reverse primer located 600 bp downstream of the stop codon. The KI colonies were further verified by western blot and sequencing analysis.

The following sgRNAs were used in this study (Doench et al., 2016):

TMEM251 sgRNA1: 5' – ATGAACTTCCGTCAGCGGAT – 3',

TMEM251 sgRNA2: 5' – TGTCCACACCCAAAAAGGCA – 3',

TMEM251 sgRNA3: 5' – ATAGTAAAATGCTGCTGCAC – 3',

GNPTAB sgRNA1: 5' – ACTCATTGCGATCTATCGAG – 3',

GNPTAB sgRNA2 (KI): 5' – CTTCTATACTCTGATTCGAT – 3',

CI-MPR sgRNA: 5' – GCTCAAAGATCCATTCGCCG– 3'

CRISPR-Cas9 knockout screen

The FACS-based CRISPR-Cas9 knockout screen were performed according to Joung et al., 2017 and Lenk et al., 2019. The human Brunello CRISPR knockout pooled library was purchased from Addgene (73179) and amplified according to manufactory instructions. Lentiviral particles were produced by the Vector Core at the University of Michigan.

HEK293 cells that stably expresses GFP-RNF152-IRES-mCherry and Cas9 were cultured in twenty 15 cm dishes to reach 50% confluency. Viral containing DMEM were added to reach MOI=0.25. After 24 h, cells were treated with 1μg/ml puromycin for 7 days.

About 1.5 x 10^8 Transduced cells were subjected to FACS using FACSAria III cell sorter (BD Biosciences). The top 1-1.5% cells with high GFP/mCherry ratio were collected. About 6 x 10^5 of such events/cells were captured, plated and expanded for 18 days. About 10^8 cells were subjected to a second round of FACS, and 3.2 x 10^5 events/cells were captured, plated and expanded for 7 days. The genomic DNA of presorted and sorted cells were purified using the Gentra Purogene kit (Qiagen) according to manufactory instructions. For sgRNA sequencing, the

integrated sgRNAs were enriched by PCR amplification. The Illumina adaptor sequences and barcodes were added to libraries by a second round of PCR. The libraries were pooled and sequenced on MiSeq and HiSeq instruments using 50-bp single-end reads.

Sample preparation and western blotting

Cells were collected in ice-cold 1XPBS, pelleted at 2700xg for 2 min, and lysed in lysis buffer (20mM Tris pH=8.0, 150mM NaCl, 1% Triton) containing protease inhibitor cocktail (Bimake) at 4°C for 20 minutes. Cell lysates were centrifuged at 18,000 g for 15 minutes at 4°C. The protein concentration of the supernatant was measured by Bradford assay (Bio-rad) and normalized. After adding 2X urea sample buffer (150mM Tris pH 6.8, 6M Urea, 6% SDS, 40% glycerol, 100mM DTT, 0.1% Bromophenol blue), samples were heated at 65°C for 10 minutes. 30μg of each lysate was loaded and separated on SDS-PAGE gels. Protein samples were transferred to nitrocellulose membrane for western blot analysis. After incubated with primary and secondary antibodies, membranes were scanned using the Odyssey CLx imaging system (LI-COR) or developed with CL-XPosure film (Thermo Scientific).

The following primary antibodies were used for western blotting in this study: rabbit anti-GFP (1:3000, TP401, Torrey Pines Biolabs), mouse anti-actin (1:5000, Proteintech), mouse anti-GAPDH (1:2000, Proteintech), rabbit anti-CTSD (1:1000, Proteintech), rabbit anti-Golgin160 (1:1000, Proteintech), rabbit anti-p62 (1:2000, Proteintech), rabbit anti-LC3 (1:2000, Proteintech), rabbit anti-IGF2R (CI-MPR) (1:2000, Proteintech), mouse anti-HA (1:500, 16B12, BioLegend), mouse anti-CTSC (1:500, D-6, Santa Cruz Biotechnology), mouse anti-SREBF2/SREBP2 (1:500, 1C6, Santa Cruz Biotechnology), rabbit anti-FLAG (1:2000, Millipore-Sigma), rabbit anti-LAPTM4A (1:1000, HPA, Millipore-Sigma), rabbit anti-

TMEM251 (1:1000, Millipore-Sigma), rabbit anti-EGFR (1:2000, a generous gift from Dr. Stuart Decker at the University of Michigan).

The plasmid for single-chain antibody against M6P (scFv M6P) was purchased from the Geneva Antibody Facility (AG949, University of Geneva). The full construct contains a N-terminal IL-2 signal sequence and a C-terminal Fc region from the rabbit IgG. To produce this scFv M6P, HEK293T cells were transfected with AG949 plasmid. After 48 hours, cells were washed with serum free DMEM and incubated with serum free DMEM for 24 hours. The supernatant is filtered with a 0.45 μm filter. This filtered supernatant is directed used as a primary antibody (without dilution) to detect M6P.

The following secondary antibodies were used in this study: goat anti-mouse IRDye 680LT, goat anti-mouse IRDye 800CW, goat anti-rabbit IRDye 680LT, goat anti-rabbit IRDye 800CW. These secondary antibodies were purchased from LI-COR Biosciences and used at 1:10,000 dilution.

To detect TMEM251 and M6P (scFv M6P), the anti-protein A HRP secondary antibody was used at 1:10,000 dilution. The signal is detected with the Pierce ECL kit (Thermo Scientific).

EGFR degradation assay

HeLa cells were cultured to 70-80% confluency in 6 cm dishes. Cells were washed with serum free DMEM twice and incubated with serum free DMEM. After 14 h, 100ng/ml of EGF (Invitrogen) was added to cells. Cells were collected in ice-cold PBS at indicated time, pelleted at 2700 g for 2 min and stored in -80°C before subsequent western blot analysis.

Membrane isolation

The membrane isolation protocol was adapted from Shao and Espenshade, 2014, with some modifications. Cells with 70-80% confluency from a 10cm dish were collected in ice-cold 1X PBS, pelleted at 2700 g for 2 min. The pelleted cells were resuspended in 1 ml ice-cold membrane isolation buffer (1 mM EDTA and 1 mM EGTA in 1X PBS, with protease inhibitor) and homogenized. The homogenate was centrifuged at 900 g for 5 min at 4˚C, and the supernatant was transferred to a new tube and centrifuged at 20,000 g for 20 min at 4 °C to collect membranes. After centrifugation, the membrane pellet was further dissolved in lysis buffer (20 mM Tris pH = 8.0, 150 mM NaCl, and 1% Triton) containing 1X protease inhibitor cocktail (Biomake) at 4˚C for 20 minutes. The undissolved membranes were removed by another round of centrifugation at 20,000 g for 15 minutes at 4˚C, and the protein concentration from the supernatant was measured by Bradford assay and normalized. Samples were incubated with 2X urea sample buffer samples at 65˚C for 8 minutes before western blot analysis.

SREBF2/SREBP2 processing assay

The SREBF2/SREBP2 processing assay was adapted from Shao et al., 2016. with some modifications. Cells were cultured to 50% confluency, treated with 50 μM sodium compactin (Millipore-Sgima) and 50 μM sodium mevalonate (Millipore-Sgima) in the presence or absence of sterols (1 μg/ml 25-Hydroxycholesterol [25-HC, Millipore-Sgima], 10 μg/ml cholesterol (Millipore-Sgima). After 16 h, N-acetyl-leucinyl-leucinyl-norleucinal (ALLN, Millipore-Sgima) was added to a final concentration of 25 μg/ml and cells were harvested 1 h later for membrane isolation and western blot analysis.

CI-MPR binding assay

Cells with 70-80% confluency in a 10 cm dish were washed twice with serum free DMEM and then incubated with serum free DMEM for secretion. After 16h, conditioned media

from were collected and transferred to a 50 ml conical tube. The media was centrifuged at 500 x g for 5 min to remove cell debris, filtered with a 0.45 μm filter, and concentrated to ~200ul using 10kDa cutoff Amicon Centrifugal filters (Millipore-Sigma). The protein concentration from the concentrated media was measured by Bradford assay and normalized. After adding 2X urea sample buffer, samples were heated at 65˚C for 8 minutes and loaded onto SDS-PAGE gel for western blot analysis. After transfer, the nitrocellulose membrane was blocked with 3% BSA, and incubated with biotinylated CIMPR protein (0.25 ug/ml in 3% BSA, a generous gift from Dr. Peter Lobel, Rutgers University) as primary antibodies at 4˚C. After 14h incubation, the membrane was further incubated with Streptavidin secondary antibodies (IRDye® 800CW Streptavidin, LI-COR Biosciences) and scanned using the Odyssey CLx imaging system.

TMEM251 KO cells rescue with conditioned media.

CI-MPR KO and GNPTAB KO cells were cultured to reach 70-80% confluency. Cells were washed twice with serum free DMEM and then incubated with serum free DMEM for secretion. After 16h, the conditioned media from different cell lines were collected and transferred to a 50 ml conical tube. The media was centrifuged at 500 g for 5 min to remove cell debris, filtered with a 0.45 μm filter, and concentrated to ~500μl using 10kDa cutoff Amicon Centrifugal filters (Millipore-Sgima). The concentrated conditioned were added to TMEM251KO cells (~5% confluency, 4ml complete media in 6 cm dishes). For the mannose-6-phosphate (M6P) competition experiment, 10mM of M6P (Millipore-Sigma) was added to the TMEM251KO cells 3 hours before the addition of concentrated conditioned media from the CI-MPR KO cells.

During cell growth, new conditioned media from fresh CI-MPR KO and GNPTAB KO cells were concentrated every the other day and fed to TMEM251KO cells. For the M6P

competition dish, TMEM251 cells were always pre-treated with 10mM M6P for three hours before adding the new conditioned media. After 7 days, cells were harvested for analysis.

Secretome analysis

HEK293 WT and sgTMEM251 cells were culture in 15 cm dishes to reach 70-80% confluency. Cells were washed with serum free DMEM three times and incubated with 20ml serum free DMEM for 14 hours. The conditioned media were collected and transferred to a 50 ml conical tube. The media was centrifuged at 500 g for 5 min to remove cell debris, filtered with a 0.45 µm filter, and concentrated to ~200µl using 3kDa cutoff Amicon Centrifugal filters (Millipore-Sigma). The protein concentration from the concentrated media was measured by Bradford assay and normalized. Samples were mixed with 2XUrea buffer and heated at 65˚C for 8 minutes.

About ~70µg of protein samples were loaded onto SDS-PAGE gel and run for 4.5cm into the gel. Samples were stained with Sypro Ruby gel stain (Invitrogen) and excised for MS analysis. The Mass spectrometry (MS) analysis was performed by the Taplin Mass Spectrometry Facility at the Harvard Medical School.

Statistically significantly proteins were determined as having absolute log-fold change larger than 2 and a p-value less than 0.05. Gene ontology enrichment analyses were perform using Metascape, a web-based and updated biological annotation database (Zhou et al., 2019)

Immunostaining, microscopy and image processing

Immunostaining was performed as described in Zhang et al, 2021., with some modifications. Cells grown on 1.5 circular glass coverslips were washed with ice-cold 1XPBS and fixed in 4% paraformaldehyde for 10 minutes at room temperature. Cells were permeabilized with 0.3% Triton in PBS for 15 minutes. For immunostaining of LAMP2, cells were fixed and

permeabilized in cold 100% methanol for 8 minutes at -20°C. The samples were blocked in 3% BSA (in 1XPBS) for 30 minutes at room temperature, followed by incubating with primary and secondary antibodies. The cell nucleus was stained using Hoechst (1:8000, Invitrogen). Coverslips were mounted in Fluoromount-G (SouthernBiotech) and cured for 24 hours before imaging.

The following primary antibodies were used for immunostaining in this study: mouse anti-LAMP2 (1:100, H4B4, DHSB), rabbit anti-TMEM251 (1:100, Millipore-Sigma), anti-EEA1 (1:50, Santa Cruz Biotechnology), mouse anti-GM130 (1:200, BD Biosciences).

The following secondary antibodies were used at 1:100: FITC goat anti-mouse and TRITC goat anti-rabbit (Jackson ImmunoReseach).

Microscopy is performed with a DeltaVision system (GE Healthcare Life Sciences). The DeltaVision microscope was equipped with a scientific CMOS camera and an Olympus UPLXAP0100X objective. The following filter sets were used: FITC (excitation, 475/28; emission, 525/48), TRITC (excitation 542/27; emission 594/45), and DAPI (excitation 390/18; emission 435/48). Image acquisition and deconvolution were performed with the softWoRx program.

Images were further cropped or adjusted using ImageJ (National Institutes of Health).

Immunoprecipitation.

MBTPS1-FLAG plasmids were transfected into HEK293T. Immunoprecipitation was performed 48 hours post-transfection according to the manufacturer's instruction with some modifications. In brief, cells (one 15 cm dish of near-confluent cells per IP group) were collected in ice-cold 1XPBS, pelleted at 2700 g for 2 min, and lysed in 1 ml of lysis buffer (20mM Tris pH=8.0, 150mM NaCl, 1% Triton) containing protease inhibitor cocktail (Biomake) at 4°C for

20 minutes. Cell lysates were centrifuged at 18,000 g for 15 minutes at 4°C. The concentration of the supernatant was measured by Bradford assay (Bio-rad) and normalized. 30 µl of anti-FLAG M2 beads (pre-equilibrated with lysis buffer, Millipore-Sigma) was added to the normalized cell lysate and incubated at 4°C for 2 hours with gentle rocking. The resin was then washed 4 times with lysis buffer. The bound proteins on the anti-FLAG M2 beads were eluted with 3xFLAG peptides and precipitated by 10% TCA precipitation for 1 hours. The pellet was washed with 0.1% TCA, resuspended with 2X Urea sample buffer (150mM Tris pH 6.8, 6M Urea, 6% SDS, 40% glycerol, 100mM DTT, 0.1% Bromophenol blue). Sample was treated with beat beating for 10 min and heated at 65°C for 10 minutes. The resulting eluates were analyzed by western blot.

Lyso-IP

LysoIP was conducted as described before (Abu-Remaileh et al., 2017; Zhang et al., 2021). Briefly, ~8X10^6 HEK293T cells that stably expressed TMEM192-3HA or TMEM192-2FLAG were collected in ice-cold PBS. ~2.5% of the cells were used as input and further processed for western blot. The rest of cells were spined down at 1000g for 2 min, resuspended with ice cold PBS containing protease inhibitor cocktail and homogenized. The samples were then centrifuged at 1000xg for 2 min. Supernatant was incubated with 20µl of anti-HA magnetic beads (Millipore-Sigma) for 20min at 4℃. The beads were washed with PBS for five times and then heated at 65℃ for 10min in 2xUrea sample buffer (150mM Tris pH 6.8, 6M Urea, 6% SDS, 40% glycerol, 100mM DTT, 0.1% Bromophenol blue). Samples were further analyzed by western blot.

Preparation of Golgi membranes from rat liver

Golgi membranes were prepared from fresh liver tissues of female Sprague–Dawley rats as described previously (Wang et al., 2006; Tang et al., 2010). Briefly, rats were euthanized by

carbon dioxide (CO_2) inhalation followed by cervical dislocation after 24-hour food starvation. Liver tissues were rapidly washed in PBS and transferred into ice-cold buffer C (0.5 M sucrose, 5 mM $MgCl_2$, 0.1 M phosphate buffer pH 6.7) with EDTA-free protease inhibitors and pepstatin A. Liver tissues were cut by a pair of surgical scissors into 1-2 mm pieces and homogenized by gentle pressing through a 150-µm mesh stainless-steel sieve with the bottom of a 250 ml conical flask in a rolling action. To prepare the sucrose gradients, place 6 ml of buffer D (0.86 M sucrose, 5 mM $MgCl_2$, 0.1 M phosphate buffer pH 6.7) in Beckman SW-41 Ultraclear tubes and overlay 5 ml of homogenate and 1 ml of buffer B (0.25 M sucrose, 5 mM $MgCl_2$, 0.1 M phosphate buffer pH 6.7). After centrifugation at 103,800 *g* (29,000 rpm) in an SW-41 rotor for 60 min at 4°C, the lipid at the top was aspirated and the Golgi fractions accumulated at the 0.5/0.86 M sucrose interfaces were collected. The Golgi fractions were adjusted to 0.25 M sucrose concentration (refractive index, 1.3456) using buffer A (5 mM $MgCl_2$, 0.1 M phosphate buffer pH 6.7). Pooled Golgi fractions were loaded onto the second gradient in the same centrifuge tube by adding 1 ml buffer E (1.3 M sucrose, 5 mM $MgCl_2$, 0.1 M phosphate buffer pH 6.7), 2 ml buffer C and 9 ml diluted Golgi fractions. After centrifugation at 7,900 *g* (8,000 rpm) in an SW-41 rotor for 30 min, Golgi membranes concentrated at the 0.5 M/1.3 M sucrose interface were collected and gently mixed with 1 volume buffer A. Purified Golgi membranes were aliquoted and snap-frozen in liquid nitrogen and stored at -80°C.

RNA-sequencing

Total RNA samples were extracted from either WT or 251KO HEK293 cells using TRIzol (Thermo Fisher Scientific) and the PureLink RNA Mini Kit (Invitrogen). For each sample (three WT and three TMEM251KO using different sgRNAs), around 3µg of total RNA was submitted to the Advanced Genomics Core at the University of Michigan. After quality

control, the mRNAs from total RNAs were enriched with a poly-A based selection method prior to cDNA synthesis, and the sequencing was then performed on the NovaSeq with 150bp paired end reads (PE150) to target 30-40 million reads/sample.

The raw reads were filtered using RSeQC with default parameters by removing low-quality bases (> Q30) and adapter contaminated reads. The resulting high-quality clean reads in fastq format were trimmed using Trim Galore (v 0.5.0) and aligned to the human genome (Sequence: ENSEMBL-GRCh38) using STAR (v 2.6.0) (Dobin et al., 2013). After mapping, read counts were generated by HTSeq-count (v.0.11.3) (Anders et al., 2015). The read counts were used for a differential expression analysis between wild-type control cells and TMEM251 knockout cells using R package DESeq2 (v.1.28.1) (Love et al., 2014). Statistically significantly expressed genes were determined as having absolute log-fold change larger than 1.2 and a p-value less than 0.05 based on the Benjamini-Hochberg procedure, which controls the false discovery rate (FDR). Principal component analysis (PCA) and heatmaps of differentially expressed genes (DEGs) were generated using ClustVis (https://biit.cs.ut.ee/clustvis/). DEGs were processed for gene ontology enrichment analyses using Metascape.

Lysotracker staining and flow cytometry analysis

Cells were treated with 50nM lysotracker Red DND-99 (Thermo Fisher Scientific) for 30 minutes. Cells were washed with 1XPBS and trypsinized until all cells are dissociated from the dishes. Dissociated cells were neutralized with DMEM containing 10% serum media and pelleted at 300 g for 3 minutes. Cells were resuspended in ice-cold 1XPBS and analyzed by a Ze5 (Bio-rad) flow cytometer. The data were analyzed using FlowJo software.

Transmission electron microscopy

HeLa cells were culture on an 8 mm (diameter) Thermanox coverslip to 80-90% confluency and fixed in 1.25% glutaraldehyde at 37 °C for 5 min. Samples were further processed and imaged at the Microscopy core at the University of Michigan.

Zebrafish husbandry

Zebrafish were raised following standard zebrafish husbandry guidelines (Westerfield, 2000). Embryos were obtained by natural crosses and raised in standard E3 embryo medium (Westerfield, 2000). Embryos were staged as described previously (Kimmel et al., 1995). To inhibit pigmentation, 0.003% (w/v) N-phenylthiourea (PTU) was added. All experiments were conducted in accordance with the guidelines approved by the University of Michigan Institutional Committee on the Use and Care of Animals.

Alcian blue and Alizarin red Staining

Alizarin red staining was performed following a published protocol (Du et al., 2001; Xin et al., 2019). Alcian blue staining was previously described in Walker & Kimmel, 2007. Images were captured with a stereomicroscope (Leica MZ16F) equipped with a QImaging QICAM camera.

The F0 knockout of *tmem251* and *gnptab* in zebrafish

Cas9 mRNA was synthesized by *in vitro* transcription using the pT3.Cas9-UTRglobin plasmid (a kind gift from Prof. Yonghua Sun from the Institute of Hydrobiology, Chinese Academy of Sciences) as the template. Four sgRNAs targeting tmem251 were designed using CHOPCHOP (Labun et al., 2019). The primers used to synthesize gRNAs which target *tmem251* and *gnptab* were listed in Supplementary Table 3. The sgRNAs were synthesized by *in vitro* transcription following a published method (Xin & Duan, 2018). Once synthesized, the sgRNAs (40 ng/μl) were mixed with Cas9 mRNA (400 ng/μl) and co-injected into WT embryos at the

one-cell stage. The injected embryos were raised in E3 embryo medium, with PTU added at 1 dpf.

Quantification and statistical analysis

The band intensity for western blot was quantified using Image Studio software (LI-COR). The rate constants (k) of GFP-RNF152, LAPTM4A and EGFR were calculated by fitting the data toto the first-order decay and the rate constant in Excel. The half-lives were calculated by $t_{(1/2)} = \ln 2 / k$. Graphs were generated using Prism (GraphPad). Statistical analysis was performed with the two-tailed unpaired t-test or one-way ANOVA. Error bars represent the standard deviation. *: ≤0.05, **: ≤0.01, ***: ≤0.001, ****:≤0.0001.

Acknowledgment:

We thank Dr. Jacob Kitzman for helping us plan the CRISPR-Cas9 screen and analyze the Next-Generation Sequencing data. Dr. Jianchao Zhang from the Wang laboratory provided us with rat liver Golgi samples. Dr. Sarah Bui from the Wang laboratory analyzed our RNA-sequencing data. The microinjection of zebrafish embryo and Alizarin red staining were performed by Yingxiang Li from the Duan laboratory.

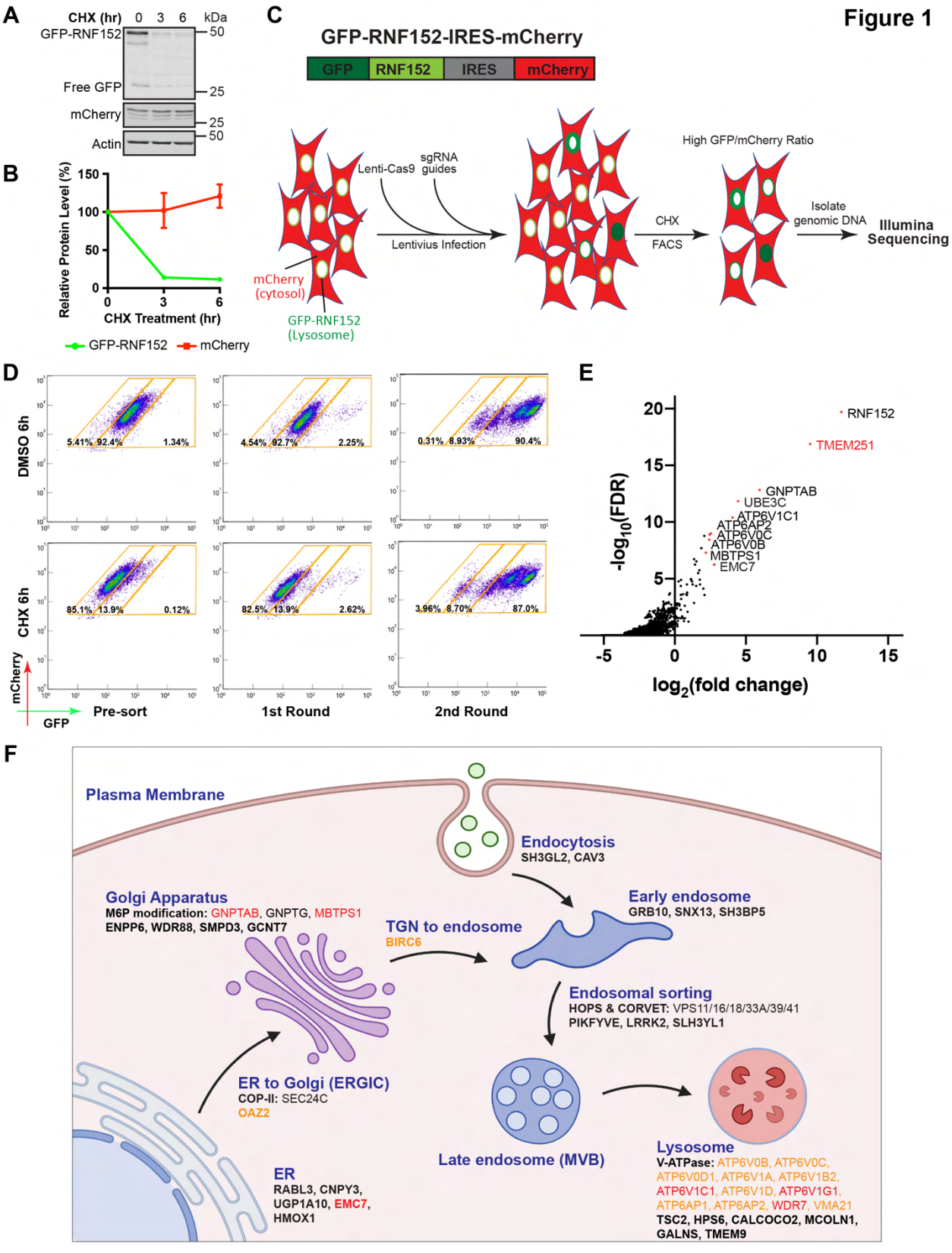
Figure 1
A
CHX (hr) 0 3 6 kDa
GFP-RNF152
Free GFP
mCherry
Actin
50
25
25
50
B
Relative Protein Level (%)
150
100
50
0
0 3 6
CHX Treatment (hr)
GFP-RNF152
mCherry
C
GFP-RNF152-IRES-mCherry
GFP
RNF152
IRES
mCherry
Lenti-Cas9
sgRNA guides
Lentivius Infection
mCherry (cytosol)
GFP-RNF152 (Lysosome)
CHX
FACS
High GFP/mCherry Ratio
Isolate genomic DNA
Illumina Sequencing
D
DMSO 6h
CHX 6h
5.41% 92.4% 1.34%
4.54% 92.7% 2.25%
0.31% 8.93% 90.4%
85.1% 13.9% 0.12%
82.5% 13.9% 2.62%
3.96% 8.70% 87.0%
mCherry
GFP
Pre-sort
1st Round
2nd Round
E
-log10(FDR)
log2(fold change)
RNF152
TMEM251
GNPTAB
UBE3C
ATP6V1C1
ATP6AP2
ATP6V0C
ATP6V0B
MBTPS1
EMC7
F
Plasma Membrane
Endocytosis
SH3GL2, CAV3
Golgi Apparatus
M6P modification: GNPTAB, GNPTG, MBTPS1
ENPP6, WDR88, SMPD3, GCNT7
TGN to endosome
BIRC6
Early endosome
GRB10, SNX13, SH3BP5
Endosomal sorting
HOPS & CORVET: VPS11/16/18/33A/39/41
PIKFYVE, LRRK2, SLH3YL1
ER to Golgi (ERGIC)
COP-II: SEC24C
OAZ2
Late endosome (MVB)
Lysosome
V-ATPase: ATP6V0B, ATP6V0C, ATP6V0D1, ATP6V1A, ATP6V1B2, ATP6V1C1, ATP6V1D, ATP6V1G1, ATP6AP1, ATP6AP2, WDR7, VMA21
TSC2, HPS6, CALCOCO2, MCOLN1, GALNS, TMEM9
ER
RABL3, CNPY3, UGP1A10, EMC7, HMOX1

Figure 4.1: A genome-wide CRISPR-Cas9 screen to identify genes essential for LMP degradation and lysosome function. (A) CHX chase assay of stably expressed GFP-RNF152 and mCherry in HEK293 cells. **(B)** Quantification of the protein levels in A, n=3. Error bars represent standard deviation. **(C)** A schematic representation of the CRISPR-Cas9 screen to identify genes essential for LMP degradation and lysosome function. **(D)** Flow cytometry profiles of pre-sorted and sorted cells from the CRISPR-Cas9 screen. **(E)** Top 10 hits of Illumina sequencing of sgRNAs from the second round of sorting. **(F)** A schematic representation of hits from the CRISPR-Cas9 screen that highlights the membrane trafficking pathways. Black: hits from the first-round sorting. Orange: hits from the second-round sorting. Red: hits appeared in both rounds sorting.

Figure 2

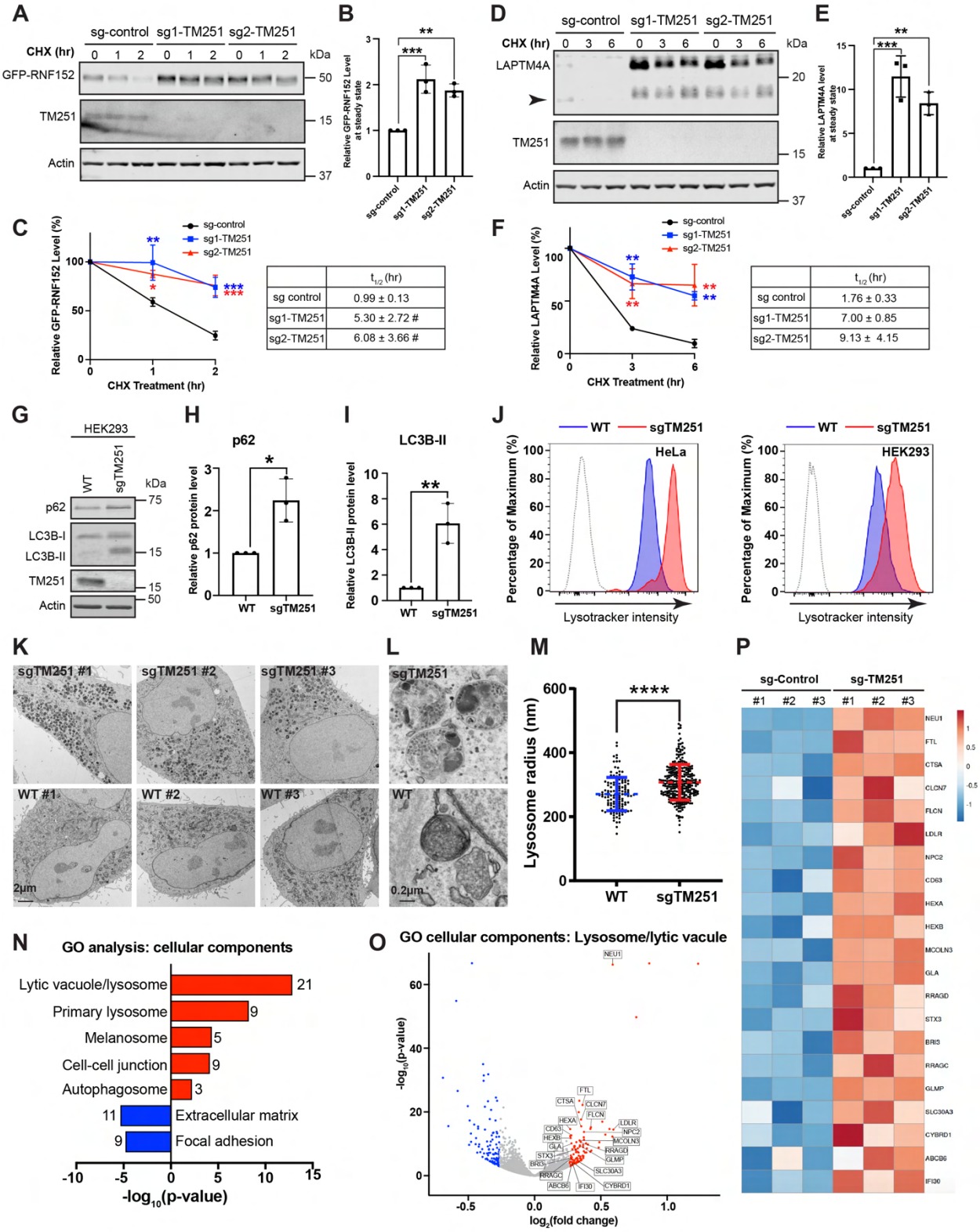
A
sg-control
sg1-TM251
sg2-TM251
CHX (hr)
0 1 2 0 1 2 0 1 2
kDa
GFP-RNF152
50
TM251
15
Actin
37
B
Relative GFP-RNF152 Level at steady state
**
***
sg-control
sg1-TM251
sg2-TM251
C
Relative GFP-RNF152 Level (%)
sg-control
sg1-TM251
sg2-TM251
CHX Treatment (hr)
t1/2 (hr)
sg control 0.99 ± 0.13
sg1-TM251 5.30 ± 2.72 #
sg2-TM251 6.08 ± 3.66 #
D
sg-control
sg1-TM251
sg2-TM251
CHX (hr)
0 3 6 0 3 6 0 3 6
kDa
LAPTM4A
20
TM251
15
Actin
37
E
Relative LAPTM4A level at steady state
**
***
sg-control
sg1-TM251
sg2-TM251
F
Relative LAPTM4A Level (%)
sg-control
sg1-TM251
sg2-TM251
CHX Treatment (hr)
t1/2 (hr)
sg control 1.76 ± 0.33
sg1-TM251 7.00 ± 0.85
sg2-TM251 9.13 ± 4.15
G
HEK293
WT
sgTM251
kDa
p62
75
LC3B-I
LC3B-II
15
TM251
15
Actin
50
H
p62
Relative p62 protein level
WT
sgTM251
I
LC3B-II
Relative LC3B-II protein level
WT
sgTM251
J
WT
sgTM251
HeLa
HEK293
Percentage of Maximum (%)
Lysotracker intensity
K
sgTM251 #1
sgTM251 #2
sgTM251 #3
WT #1
WT #2
WT #3
2μm
L
sgTM251
WT
0.2μm
M
Lysosome radius (nm)
****
WT
sgTM251
P
sg-Control
sg-TM251
#1 #2 #3 #1 #2 #3
NEU1
FTL
CTSA
CLCN7
FLCN
LDLR
NPC2
CD63
HEXA
HEXB
MCOLN3
GLA
RRAGD
STX3
BRI3
RRAGC
GLMP
SLC30A3
CYBRD1
ABCB6
IFI30
N
GO analysis: cellular components
Lytic vacuole/lysosome 21
Primary lysosome 9
Melanosome 5
Cell-cell junction 9
Autophagosome 3
11 Extracellular matrix
9 Focal adhesion
-log10(p-value)
O
GO cellular components: Lysosome/lytic vacule
-log10(p-value)
log2(fold change)

Figure 4.2: TMEM251 deficiency leads to lysosome dysfunction. (A) CHX chase assay of stably expressed GFP-RNF152 in sgRNA control, sgRNA-1 TMEM251, and sgRNA-2 TMEM251 cells. **(B)** Steady-state (0h) protein levels in A, n=3. Error bars represent standard deviation. **: p≤0.01, *** p≤0.001. **(C)** Quantification of GFP-RNF152 degradation in A, n=3. Error bars represent standard deviation. *: p≤0.05, **:p≤0.01, ***:p≤0.001. Table: Calculated protein half-lives. **(D)** CHX chase assay of endogenous LAPTM4A in sgRNA control, sgRNA-1 TMEM251, and sgRNA-2 TMEM251 cells. Arrowhead: cleavage product of LAPTM4A. **(E)** Steady-state (0h) protein levels in A, n=3. Error bars represent standard deviation. **: p≤0.01, *** p≤0.001. **(F)** Quantification of LAPTM4A degradation in A, n=3. Error bars represent standard deviation. **: p≤0.01. Table: Calculated protein half-lives. **(G)** p62 and LC3B protein levels in HEK293 WT and sgTMEM251 cells. **(H)** Quantification of p62 protein level in G. n=3. Error bars represent standard deviation. *: p≤0.05. **(I)** Quantification of LC3B-II level in G. n=3. Error bars represent standard deviation. **: p≤0.01. **(J)** Lysotracker intensity of WT vs. sgTMEM251 in HeLa and HEK293 cells. **(K)** Representative TEM images of HeLa WT and sgTMEM251 cells. Scale bar: 2 μm. **(L)** Representative TEM images of lysosomes in HeLa WT and sgTMEM251 cells. Scale bar: 0.2 μm. **(M)** Quantification of lysosome radius in HeLa WT and sgTMEM251 cells. Error bars represent standard deviation. ****: p≤0.0001. **(N)** Metascape Gene Ontology (GO) cellular component analysis of differentially expressed genes (DEGs) altered in sgTMEM251 vs. control cells. The number of genes in each pathway is indicated. **(O)** Volcano plot of RNA-seq analysis of sgTMEM251 vs. control cells. Annotated genes are classified in lysosome/lytic vacuole components. **(P)** Heatmap of genes annotated in O.

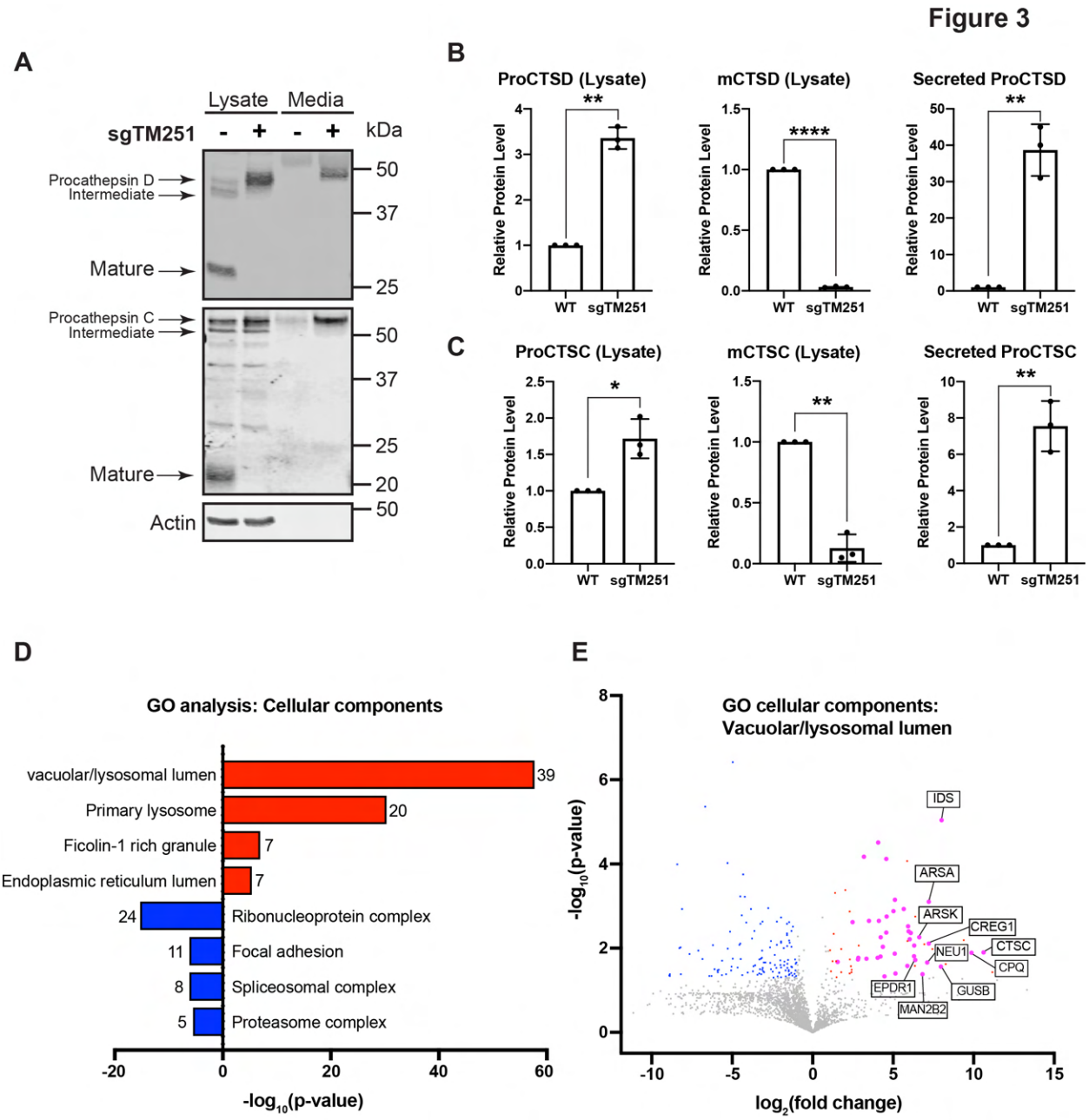

Figure 4.3: TMEM251 deficiency leads to hypersecretion of lysosome enzymes. (A) CTSC and CTSD protein level in HEK293 WT and sgTMEM251 whole cell lysate and conditioned media. **(B-C)** Quantification of protein levels in A. n=3. Error bars represent standard deviation. *: p≤0.05, **: p≤0.01, **** p≤0.0001. **(D)** GO enrichment analysis of secreted proteins altered in sgTMEM251 vs. control cells. The number of proteins in each pathway is indicated. **(E)**

Volcano plot of secretome analysis of sgTMEM251 vs. control cells. Annotated genes are the top 10 candidates in vacuolar/lysosomal lumen components.

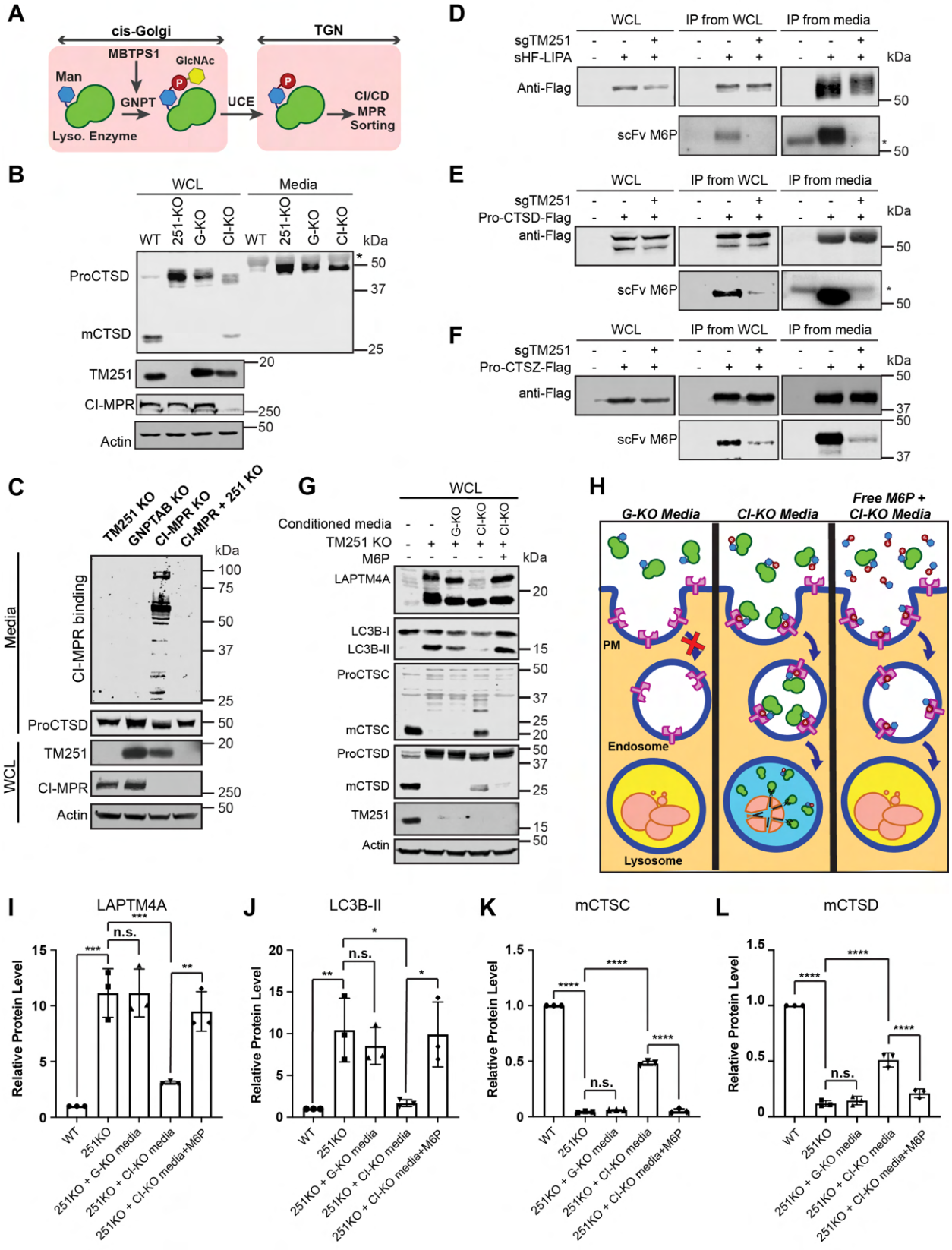
A
cis-Golgi
TGN
MBTPS1
GlcNAc
Man
GNPT
UCE
CI/CD MPR Sorting
Lyso. Enzyme
B
WCL
Media
WT
251-KO
G-KO
CI-KO
kDa
ProCTSD
mCTSD
TM251
CI-MPR
Actin
C
TM251 KO
GNPTAB KO
CI-MPR KO
CI-MPR + 251 KO
Media
CI-MPR binding
ProCTSD
WCL
TM251
CI-MPR
Actin
D
WCL
IP from WCL
IP from media
sgTM251
sHF-LIPA
Anti-Flag
scFv M6P
E
Pro-CTSD-Flag
anti-Flag
F
Pro-CTSZ-Flag
G
Conditioned media
TM251 KO
M6P
LAPTM4A
LC3B-I
LC3B-II
ProCTSC
mCTSC
ProCTSD
mCTSD
TM251
Actin
H
G-KO Media
CI-KO Media
Free M6P + CI-KO Media
PM
Endosome
Lysosome
I
LAPTM4A
J
LC3B-II
K
mCTSC
L
mCTSD
Relative Protein Level
WT
251KO
251KO + G-KO media
251KO + CI-KO media
251KO + CI-KO media+M6P
n.s.

Figure 4.4: TMEM251 deficiency leads to defects of M6P modification of lysosomal enzymes. (A) A schematic representation of mannose-6-phosphate (M6P) modification of lysosomal enzymes. **(B)** CTSD protein level in HEK293T WT, TMEM251KO, GNPTABKO, CI-MPRKO whole cell lysate and conditioned media. Asterisk: non-specific band. **(C)** CI-MPR binding assay of conditioned media from TMEM251KO, GNPTABKO, CI-MPRKO and CIMPR, TMEM251 double KO cells. **(D)** Detection of M6P modification of LIPA in HEK293T sgTMEM251 cells using single-chain antibodies against M6P (scFv M6P). Asterisk: non-specific band. **(E)** Detection of M6P modification of CTSD in HEK293T sgTMEM251 cells. Asterisk: non-specific band. **(F)** Detection of M6P modification of CTSZ in HEK293T sgTMEM251 cells. **(G)** Rescue of TMEM251KO with conditioned media from GNPTABKO and CI-MPR KO cells. **(H)** A schematic representation of the rescue experiment in G. **(I-L)** Quantification of the full-length LAPTM4A, LC3B-II, mature CTSC, and mature CTSD protein levels in G. n=3. Error bars represent standard deviation. *: $p \leq 0.05$, **: $p \leq 0.01$, *** $p \leq 0.001$, **** $p \leq 0.0001$.

Figure 5

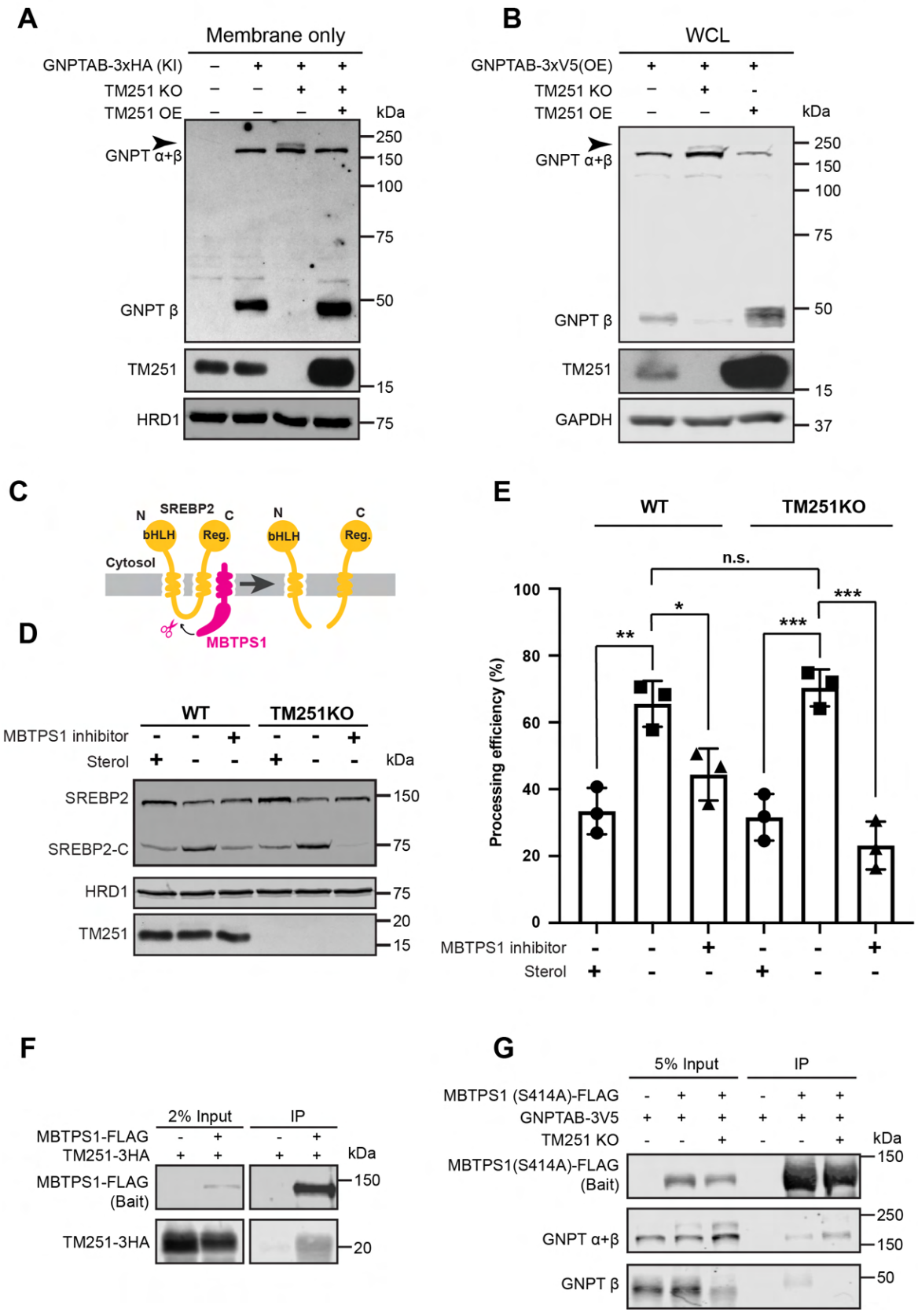
A
Membrane only
GNPTAB-3xHA (KI)
TM251 KO
TM251 OE
kDa
GNPT α+β
GNPT β
TM251
HRD1
250
150
100
75
50
15
75
B
WCL
GNPTAB-3xV5(OE)
TM251 KO
TM251 OE
kDa
GNPT α+β
GNPT β
TM251
GAPDH
250
150
100
75
50
15
37
C
SREBP2
N
C
bHLH
Reg.
Cytosol
MBTPS1
D
WT
TM251KO
MBTPS1 inhibitor
Sterol
kDa
SREBP2
SREBP2-C
HRD1
TM251
150
75
75
20
15
E
WT
TM251KO
n.s.
***
*
***
**
Processing efficiency (%)
100
80
60
40
20
0
MBTPS1 inhibitor
Sterol
F
2% Input
IP
MBTPS1-FLAG
TM251-3HA
kDa
MBTPS1-FLAG
(Bait)
TM251-3HA
150
20
G
5% Input
IP
MBTPS1 (S414A)-FLAG
GNPTAB-3V5
TM251 KO
kDa
MBTPS1(S414A)-FLAG
(Bait)
GNPT α+β
GNPT β
150
250
150
50

Figure 4.5: TMEM251 is required for the cleavage and activation of GNPT α/ β precursor by MBTPS1. (A) The processing of the endogenous GlcNAc-1-phosphotransferase (GNPT) in TMEM251KO and TMEM251 overexpression (OE) cells. HEK293T cells were knocked-in with a 3xHA tag at the C-terminus of the *GNPTAB* gene. **(B)** The processing of overexpressed GNPTAB-3xV5 in TMEM251KO and TMEM251OE cells. **(C)** A schematic representation of SREBF2/SREBP2 processing by MBTPS1. **(D)** The processing of SREBF2/SREBP2 in HEK293T WT and TMEM251KO cells. **(E)** Quantification of protein levels in D. n=3. Error bars represent standard deviation. *: $p \leq 0.05$, **: $p \leq 0.01$, *** $p \leq 0.001$. **(F)** Immunoprecipitation (IP) analysis showing an interaction between MBTPS1 and TMEM251. **(G)** IP analysis showing interactions between MBTPS1 and GNPTAB in WT and TMEM251KO cells.

Figure 6

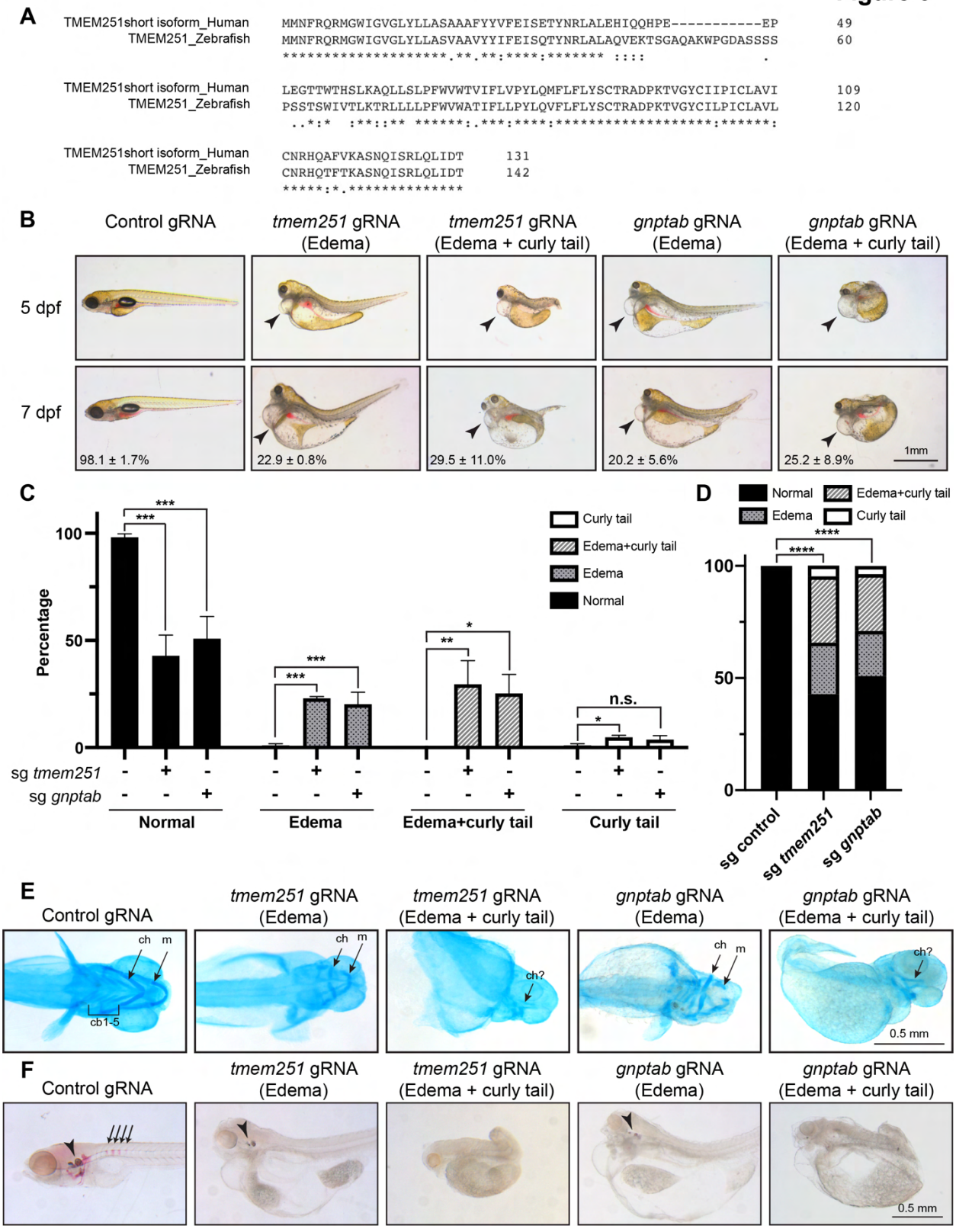
A
TMEM251short isoform_Human MMNFRQRMGWIGVGLYLLASAAAFYYVFEISETYNRLALEHIQQHPE----------EP 49
TMEM251_Zebrafish MMNFRQRMGWIGVGLYLLASVAAVYYIFEISQTYNRLALAQVEKTSGAQAKWPGDASSSS 60
TMEM251short isoform_Human LEGTTWTHSLKAQLLSLPFWVWTVIFLVPYLQMFLFLYSCTRADPKTVGYCIIPICLAVI 109
TMEM251_Zebrafish PSSTSWIVTLKTRLLLLPFWVWATIFLLPYLQVFLFLYSCTRADPKTVGYCILPICLAVL 120
TMEM251short isoform_Human CNRHQAFVKASNQISRLQLIDT 131
TMEM251_Zebrafish CNRHQTFTKASNQISRLQLIDT 142
B
Control gRNA
tmem251 gRNA (Edema)
tmem251 gRNA (Edema + curly tail)
gnptab gRNA (Edema)
gnptab gRNA (Edema + curly tail)
5 dpf
7 dpf
98.1 ± 1.7%
22.9 ± 0.8%
29.5 ± 11.0%
20.2 ± 5.6%
25.2 ± 8.9%
1mm
C
Percentage
Curly tail
Edema+curly tail
Edema
Normal
sg tmem251
sg gnptab
Normal
Edema
Edema+curly tail
Curly tail
n.s.
D
Normal
Edema+curly tail
Edema
Curly tail
sg control
sg tmem251
sg gnptab
E
Control gRNA
tmem251 gRNA (Edema)
tmem251 gRNA (Edema + curly tail)
gnptab gRNA (Edema)
gnptab gRNA (Edema + curly tail)
ch
m
cb1-5
ch?
0.5 mm
F
Control gRNA
tmem251 gRNA (Edema)
tmem251 gRNA (Edema + curly tail)
gnptab gRNA (Edema)
gnptab gRNA (Edema + curly tail)
0.5 mm

Figure 4.6: TMEM251-defefiency phenocopies ML-II *in vivo*. (A) Sequence alignments of human TMEM251 short isoform and zebrafish TMEM251. **(B)** Morphology of the F0 *tmem251*KO and *gnptab*KO zebrafish embryos at 5dpf and 7 dpf. Arrowheads point to heart edema. **(C)** Quantification of morphological phenotypes observed in B. n=3. Error bars represent standard deviation. *: $p \leq 0.05$, **: $p \leq 0.01$, *** $p \leq 0.001$. **(D)** χ^2 test to compare control, *tmem251*KO, and *gnptab*KO. **** $p \leq 0.0001$. **(E)** Ventral view of alcian blue stained zebrafish embryos at 4 dpf. ch: ceratohyal, m: Meckel's cartilage; cb: ceratobranchials. **(F)** Alizarin red staining of zebrafish embryos at 7 dpf. Arrowheads: ear stones. Arrows: segmentation.

Figure 7

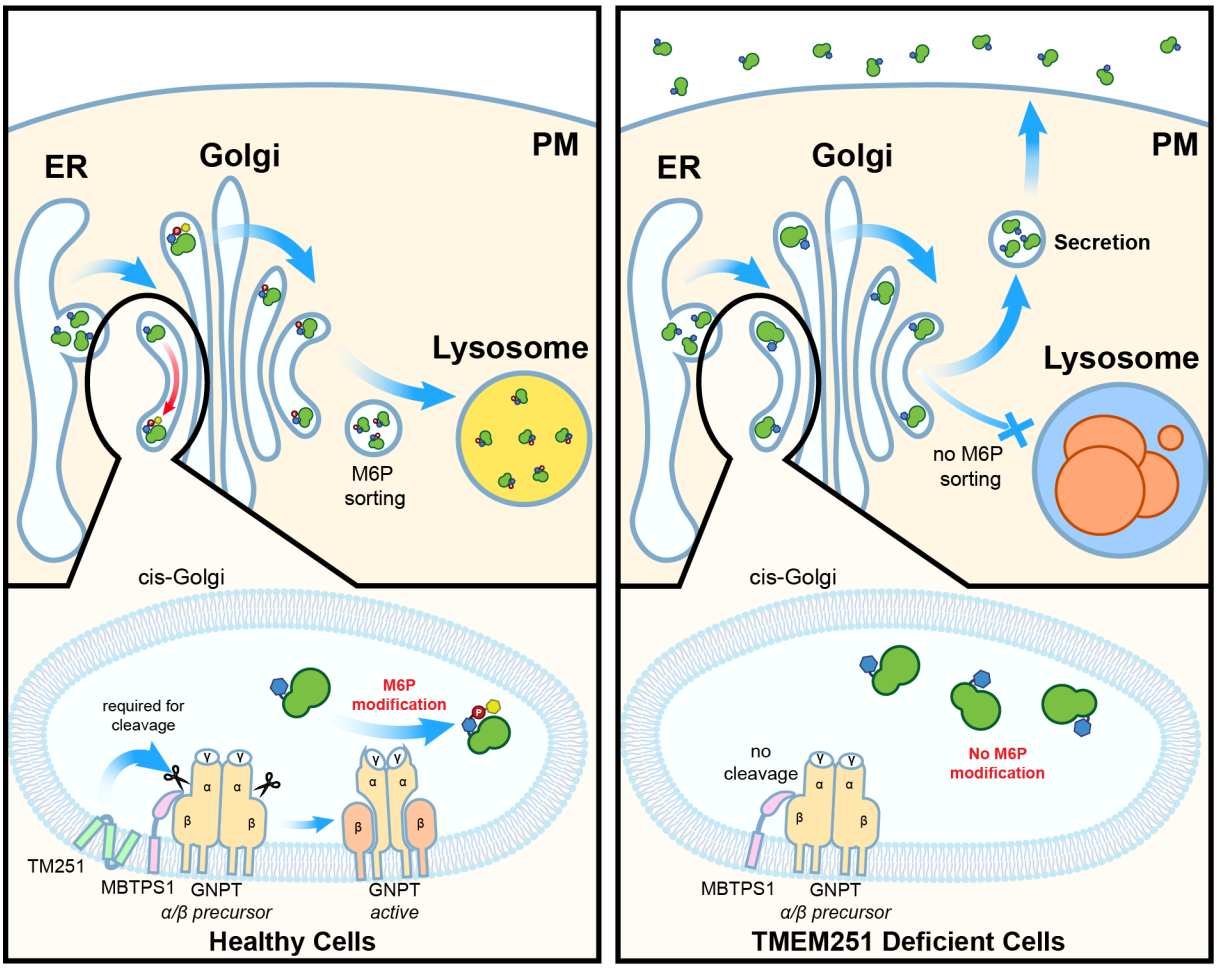

Figure 4.7: A model showing TMEM251 is required for the cleavage and activation of GNPT α/ β precursor. TMEM251 deficiency leads to defects in M6P modification of lysosomal enzymes at the cis-Golgi. Lysosomal enzymes without M6P are targeted to the secretory pathway, resulting in lysosome dysfunction.

Figure S1

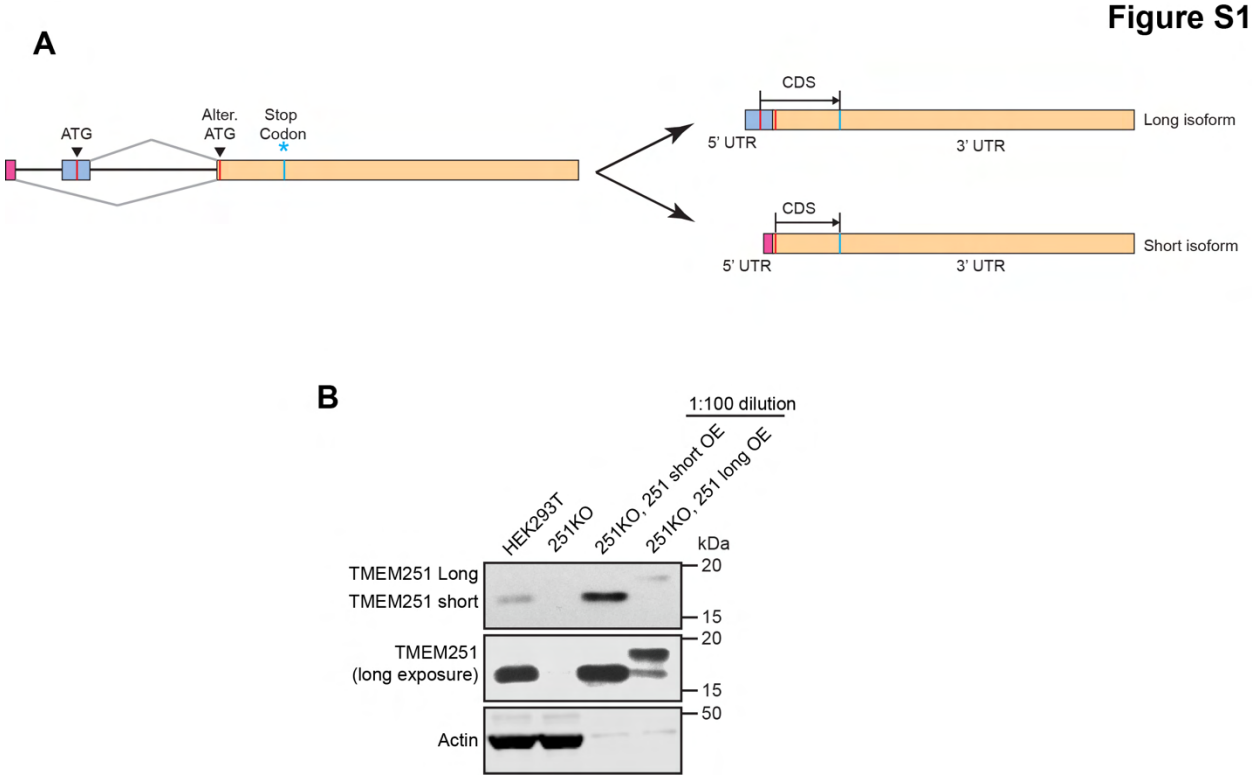

Supplemental Figure 4.1: Transcriptional variants of TMEM251. (A) A schematic representation of the alternative splicing of TMEM251 mRNA. **(B)** Protein expression of endogenous TMEM251 and overexpression of different isoforms of TMEM251 in HEK293T cells. Related to figure 1.

Figure S2

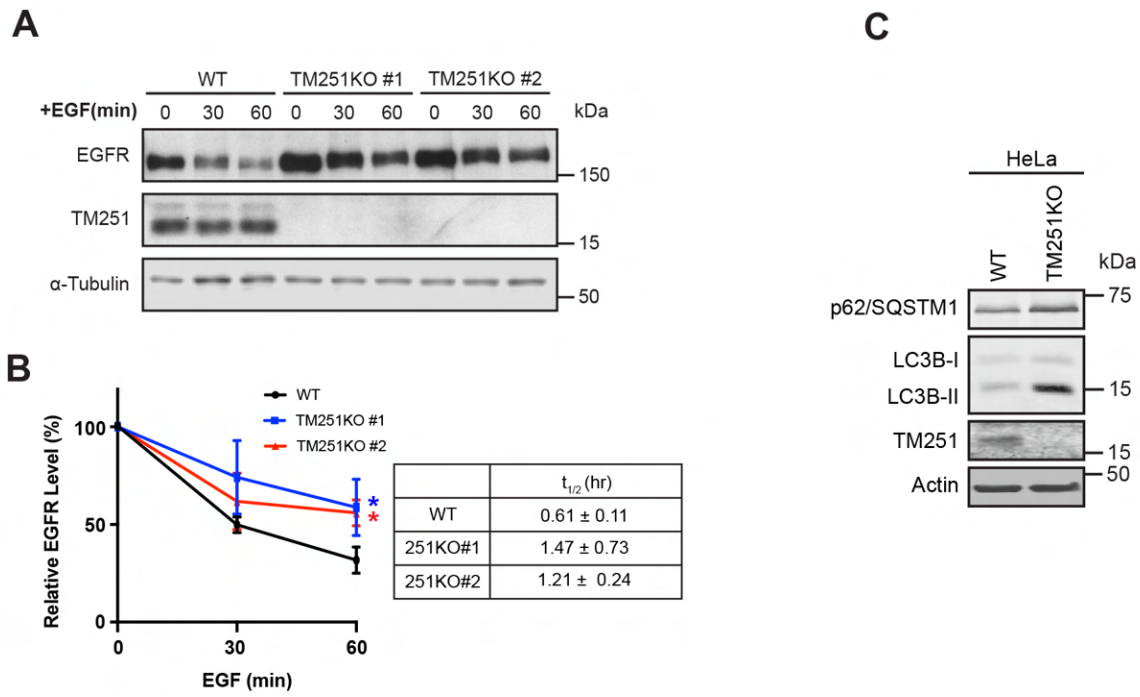

Supplemental Figure 4.2: TMEM251KO leads to defects in EGFR degradation and autophagy in HeLa cells. (A) EGFR degradation assay in HeLa WT and TMEM251KO cells. **(B)** Quantification of EGFR degradation in A, n=3. Error bars represent standard deviation. *: p≤0.05. Table: Calculated protein half-lives. **(C)** p62 and LC3B protein levels in HeLa WT and TMEM251KO cells.

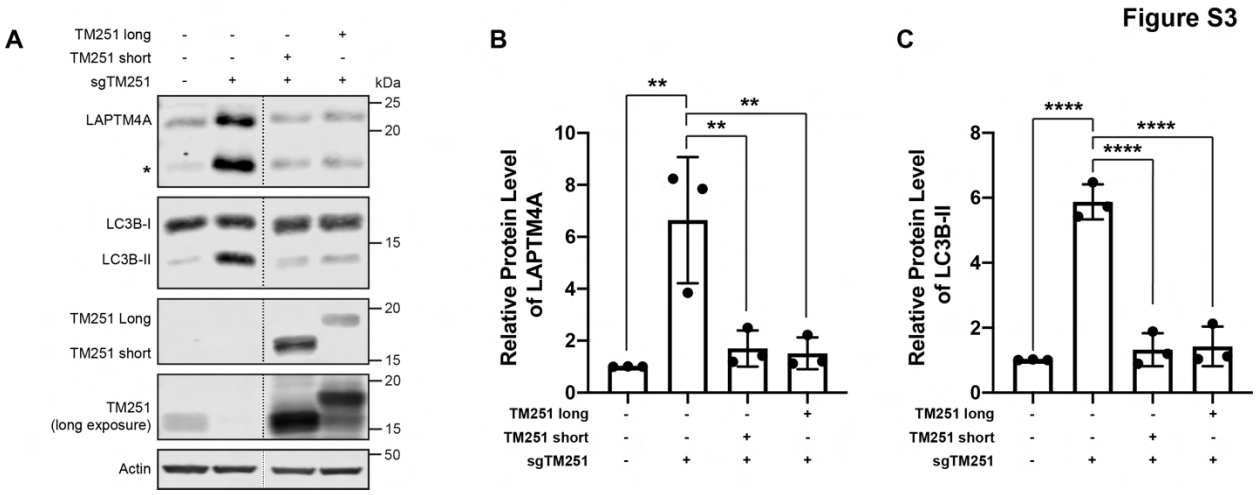

Supplemental Figure 4.3: Both long and short isoforms of TMEM251 are functional. (A) Overexpression of either short or long isoform of TMEM251 rescues LAPTM4A and LC3B-II protein levels in TMEM251-deficient cells. **(B)** Quantification of LAPTM4A protein level in A. n=3. Error bars represent standard deviation. **: p≤0.01. **(C)** Quantification of LC3B-II protein level in A. n=3. Error bars represent standard deviation. ****: p≤0.0001. Related to figure 2.

Figure S4

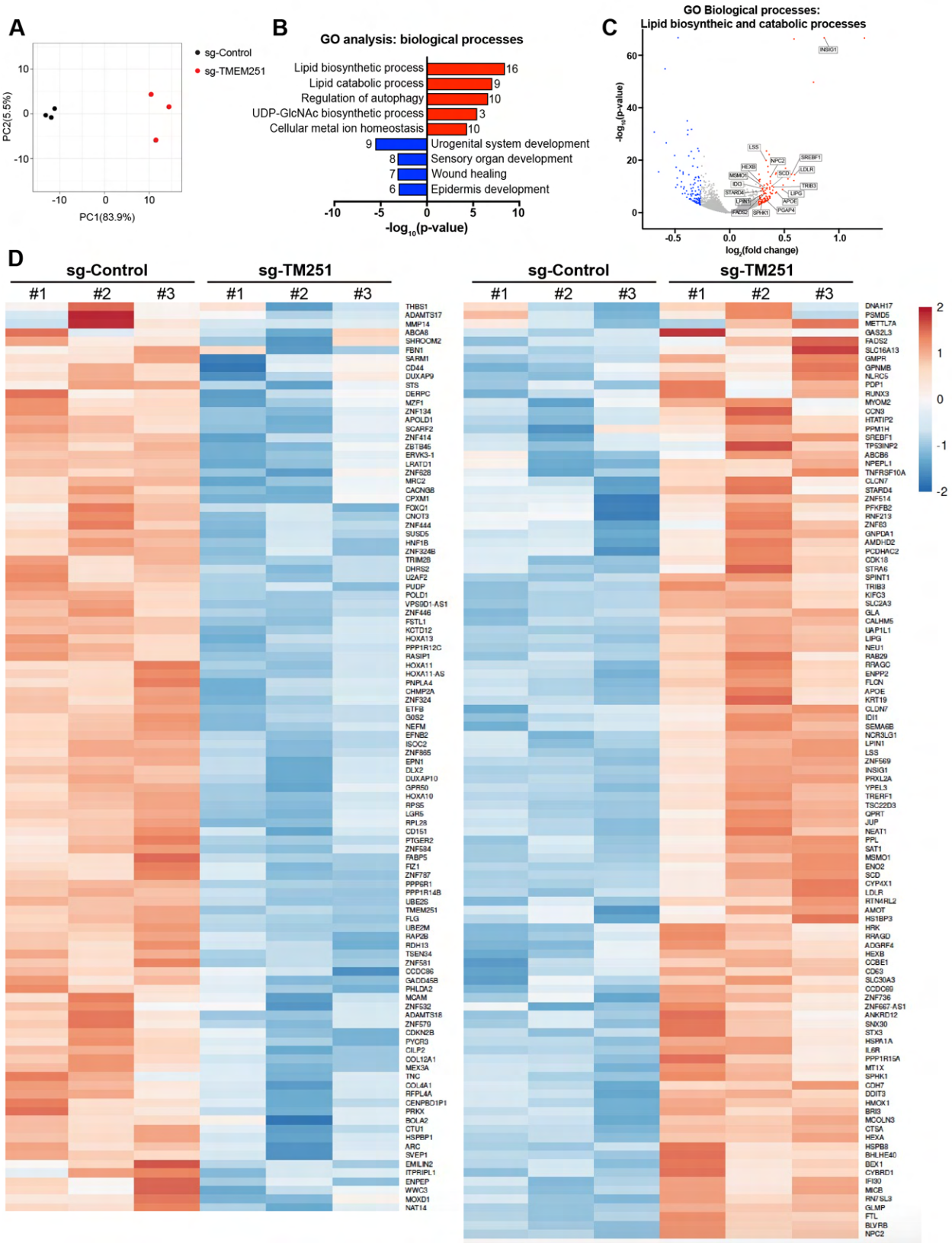
A
sg-Control
sg-TMEM251
PC2(5.5%)
PC1(83.9%)
B
GO analysis: biological processes
Lipid biosynthetic process
Lipid catabolic process
Regulation of autophagy
UDP-GlcNAc biosynthetic process
Cellular metal ion homeostasis
Urogenital system development
Sensory organ development
Wound healing
Epidermis development
-log10(p-value)
C
GO Biological processes:
Lipid biosyntheic and catabolic processes
-log10(p-value)
log2(fold change)
D
sg-Control
sg-TM251
#1
#2
#3

Supplemental Figure 4.4: RNA sequencing analysis of sgTMEM251 cells vs. control cells. **(A)** Principal component analysis (PCA) of RNA-sequencing. **(B)** GO biological processes analysis of DEGs altered in sgTMEM251 vs. control cells. The number of genes in each pathway is indicated. **(C)** A Volcano plot of RNA-seq analysis of sgTMEM251 vs. control cells. Annotated genes are classified in lipid biosynthetic and catabolic processes. **(D)** A heatmap of 211 DEGs altered in sgTMEM251 vs. control cells. Related to figure 2.

Figure S5

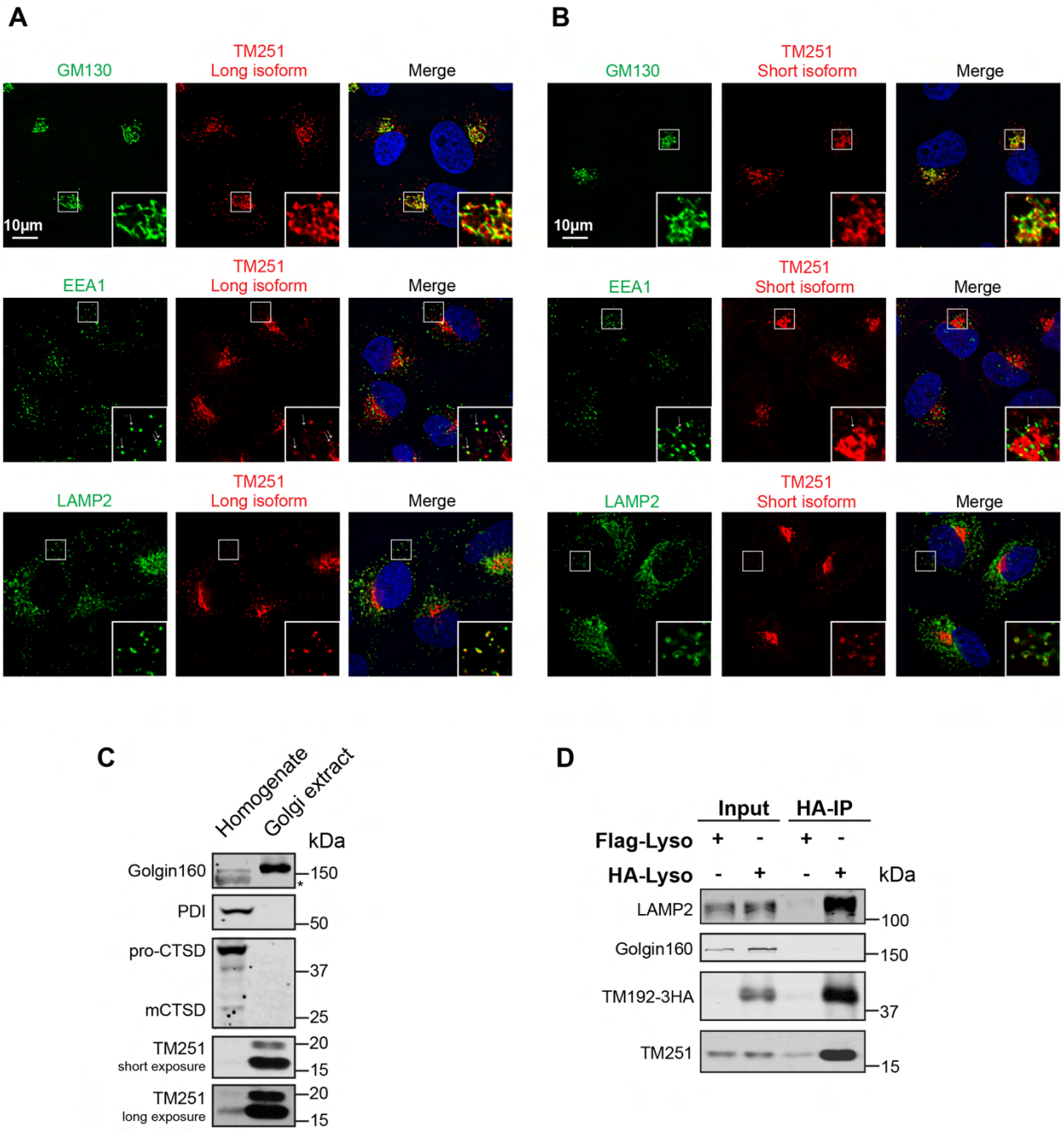

Supplemental Figure 4.5: Subcellular localization of TMEM251. (A) Immunofluorescence showing the localization of the long isoform of TMEM251 in HeLa cells co-stained with GM130, EEA1, and LAMP2. Scale bar: 10 μm. **(B)** Immunofluorescence showing the localization of the short isoform of TMEM251 in HeLa cells co-stained with GM130, EEA1, and

LAMP2. Scale bar: 10 μm. **(C)** Expression of the endogenous TMEM251 in rat liver Golgi extract. **(D)** Expression of the endogenous TMEM251 in purified lysosomes room HEK293T cells. Related to figure 4.

Table 4.1: Hits from CRISPR-Cas9 screen $Log_2FC>1$, $p<0.05$

Hits from the first round of sorting:				
RNF152	TMEM251	UBE3C	VPS18	VPS16
VPS41	VPS33A	GNPTAB	VPS11	DIO
MBTPS1	TSC2	CNTF	ZNF426	TLCD2
TAF1L	SLC1A1	GRB10	WDR87	PLIN5
ENPP6	NEK6	TMPRSS6	ARX	FAM174A
DPP4	MTERF1	ATP6V1C1	GDI2	RBM20
RHBDL1	VSX1	HPS6	DCUN1D3	WDR88
MMP19	HES5	HSFY1	OR10G8	PIKFYVE
RAD54L2	REG3A	MPEG1	LRRC23	SPRED2
ERICH6B	PDCD2L	SSTR3	PTBP3	XPNPEP3
CXXC5	ZNF765	CALCOCO2	MLF1	ZNF549
F13B	PA2G4	SH3GL2	OR4Q3	RABL3
MCOLN1	OR1J4	TNFAIP8L1	LYPD4	SRGAP2
TRIM48	GNAT2	EBF1	GAGE12H	SLC8B1
MRGPRX3	UNC13A	ERI2	VGLL2	VIL1
SPDYA	CCDC157	ABCB8	PCDHA7	CAPN3
CAPN3	NQO2	ANKRD55	ARL6IP1	NECAB1
MAP9	ZMYM3	PTCHD4	ATP6V1G1	ZSCAN5B
GNPTG	TMEM185C	C8orf58SMPD3	HMP19	CAV3
PCDHA1	EMC7	UBTFL1	SNX13	GALNS
INFA10	EDA	SLC26A9	CC2D1B	DRD5

RNF113B	ZP2	SIGLEC14	TMEM9	CECR1
FLYWCH2	PHEX	MSANTD4	TAC3	CNPY3
CCDC182	NKX6-1	HRH4	UBE2F	PDE7A
AGBL4	CCDC77	PDE10A	UGT1A10	KLHDC10
SEC24C	PWWP2B	BCAS4	TSPY3	C7orf77
TMSB4Y	SH3YL1	FRMD3	WDR7	CORT
RDH14	MAGED1	USP18	KRTAP22-2	MRVI1
FBXO16	MPDZ	HTR2B	ZEP36	CEBPA
HPGDS	GSR	SMIM9	ANKRD18A	LRRK2
FCHSD2	AMZ2	SERPINA3	ZNF10	TMPRSS11D
VPS39	MPC1	WFDC11	DOK2	DOK6
HBA2	APBB1IP	XKR3	ZNF275	GNGT1
STAG1	C1QTNF9	OARD1	ADGRE2	GCNT7
HMOX1	CDH1	KDM4D	OSR2	C22orf46
NPW	PAOX	MAP1A	C14orf105	HRASLS2
LRFN5	FBN1	MYOC	TYW3	OSR1
SCGB2A2	IRF4	RBP5	C16orf96	GABARAPL2
SH3BP5	IL5	SRA1		
Hits from the second round of sorting:				
RNF152	TMEM251	GNPTAB	UBE3C	ATP6V1C1
EMC7	ATP6V0C	ATP6V0B	ATP6AP2	MBTPS1
BRI3BP	ATP6V1A	BIRC6	ATP6V1D	SSTR3

ATP6V1B2	ATP6V0D1	ATP6V1G1	WDR7	KCNN1
RNASEK	ATP6AP1	GAS1	OR5B12	OAZ2
VAM21	LRRC16A			

Table 4.2: Hypersecreted lysosomal enzymes in TMEM251-deficient cells. $Log_2FC>1$, $p<0.05$.

AGA	ARSA	ARSK	C3	CPQ
CREG1	CTSA	CTSB	CTSC	CTSH
CTSL	CTSV	DNASE2	EPDR1	GAA
GBA	GGH	GLB1	GNS	GRN
GUSB	HEXA	HEXB	IDS	LGMN
LIPA	MAN2B1	MAN2B2	MANBA	NAGLU
NEU1	NPC2	PLBD2	PRCP	PSAP
RNASET2	SGSH	SIAE	TPP1	

Supplemental Table 4.1: Mammalian cell lines used in this study		
Cell lines	***Description***	***reference/source***
Human HEK293	CRL-1573	ATCC
Human HEK293T	CRL-3216	ATCC
Human HeLa	CCL-2	ATCC
Human HEK293, GFP-RNF152	pHAGE2-EF1α-EGFP-RNF152-IRES-Puro	Zhang et al., 2021
Human HEK293, GFP-RNF152	pHAGE2-EF1α-EGFP-RNF152-IRES-mCherry	Zhang et al., 2021
Human HEK293, GFP-RNF152, Cas9	pHAGE2-EF1α-EGFP-RNF152-IRES-mCherry, LentiCas9-Blast	This study
Human HEK293, sg1-TMEM251	Polyclonal TMEM251 CRISPR-Cas9 KO with sgRNA-1	This study
Human HEK293, sg2-TMEM251	Polyclonal TMEM251 CRISPR-Cas9 KO with sgRNA-1	This study
Human HEK293, sg3-TMEM251 (for RNA-seq)	Polyclonal TMEM251 CRISPR-Cas9 KO with sgRNA-3	This study
Human HEK293, sg1-TMEM251, TMEM251 long isoform	Polyclonal TMEM251 CRISPR-Cas9 KO with sgRNA-1, pLenti6.3-TMEM251(long)-BLAST	This study
Human HEK293 sg1-TMEM251, TMEM251 short isoform	Polyclonal TMEM251 CRISPR-Cas9 KO with sgRNA-1, pLenti6.3-TMEM251(short)-BLAST	This study
Human HEK293T, TMEM251KO	CRISPR-Cas9 KO of TMEM251, sgRNA-1, single colony.	This study
Human HEK293T, sg-TMEM251	Polyclonal TMEM251 CRISPR-Cas9 KO with sgRNA-1	This study
Human HEK293T, TMEM251KO, TMEM251 long isoform	TMEM251 CRISPR-Cas9 KO, pLenti6.3-TMEM251(long)-BLAST	This study
Human HEK293T, TMEM251KO, TMEM251 short isoform	TMEM251 CRISPR-Cas9 KO, pLenti6.3-TMEM251(short)-BLAST	This study

Human HEK293T, FLAG-Lyso	pLJC5-TMEM192-2XFLAG-Puro (Addgene 102929)	This study (Abu-Remaileh et al. 2017)
Human HEK293T, HA-Lyso	pLJC5-TMEM192-3XHA-Puro (Addgene 102930)	This study (Abu-Remaileh et al. 2017)
Human HEK293T, GNPTAB KO	CRISPR-Cas9 KO of GNPTAB, single colony.	This study
Human HEK293T, CI-MPR KO	CRISPR-Cas9 KO of CI-MPR, single colony.	This study
Human HEK293T, CI-MPR KO, TMEM251KO	CRISPR-Cas9 KO of CI-MPR and TMEM251, single colony.	This study
Human HEK293T, GNPTAB-3HA knockin	CRISPR-Cas9 knockin of 3HA tag the C-terminus of GNPTAB	This study
Human HEK293T, GNPTAB-3HA knockin, TMEM251KO	CRISPR-Cas9 knockin of 3HA tag the C-terminus of GNPTAB, CRISPR-Cas9 KO of TMEM251	This study
Human HEK293T, GNPTAB-3HA knockin, TMEM251KO, TMEM251OE	CRISPR-Cas9 knockin of 3HA tag the C-terminus of GNPTAB, CRISPR-Cas9 KO of TMEM251, pLenti6.3-TMEM251(short)	This study
Human HeLa, TMEM251KO #1	CRISPR-Cas9 KO of TMEM251, sgRNA-1, single colony #1	This study
Human HeLa, TMEM251KO #2	CRISPR-Cas9 KO of TMEM251, sgRNA-2, single colony #2	This study
Human HeLa, sgTMEM251	Polyclonal TMEM251 CRISPR-Cas9 KO with sgRNA-1	This study
Human HeLa, TMEM251 long isoform	pLenti6.3-TMEM251(long)-BLAST	This study
Human HeLa, TMEM251 short isoform	pLenti6.3-TMEM251(short)-BLAST	This study

Supplemental Table 4.2: Mammalian plasmids used in this study			
Vector	***Insert***	***description***	***reference/source***
pHEK293Ultra	sHF-LIPA	CMV promoter, N-terminal His_6-FLAG	Jin et al., 2018
pcDNA3.1(-)	CTSD-3FLAG	CMV promoter, C-terminal 3FLAG	This study
pcDNA3.1(-)	CTSZ-3FLAG	CMV promoter, C-terminal 3FLAG	This study
pcDNA4.0	MBTPS1-FLAG	CMV promoter, C-terminal FLAG	Chen et al., 2021
pcDNA4.0	MBTPS1 (S414A)-FLAG	CMV promoter, C-terminal FLAG	Chen et al., 2021
pLenti6.3-BLAST	TMEM251 long isoform	CMV promoter, Blasticidin selection	This study
pLenti6.3-BLAST	TMEM251 short isoform	CMV promoter, Blasticidin selection	This study
pLenti6.3-BLAST	TMEM251 (short)-3HA	CMV promoter, Blasticidin selection	This study
pHAGE2-IRES-mCherry	EGFP-RNF152	EF1α promoter, mCherry selection	Zhang et al., 2021
pLJC5	TMEM192-2XFLAG	UbC promoter	Abu-Remaileh et al., 2017 Addgene 102929
pLJC5	TMEM192-3XHA	UbC promoter	Abu-Remaileh et al., 2017 Addgene 102930
pSpCas9(BB)-2A-Puro (PX459)		CRISPR-Cas9 knockout	Ran et al., 2013 Addgene, 48139
Lenti-multi-CRISPR		CRISPR-Cas9 knockout	Cao et al., 2016 Addgene 85402
psPAX2		Lentiviral packaging plasmid	Addgene 12260
pMD2.G		VSV-G envelope	Addgene 12259
AG949	scFv M6P	N-terminal IL-2 signal sequence and C-terminal Fc region of Rabbit IgG	University of Geneva, This Study

Supplemental Table 4.3: primers used for F0 knockout in zebrafish	
Names	***Sequences***
tmem251 sgRNA-1	GAAATTAATACGACTCACTATATGAATTTCCGTCAGCGGATGGTTTTAGAGCTAGAAAT
tmem251 sgRNA-2	GAAATTAATACGACTCACTATAGGAGCGCAGGCAAAATGGCCGTTTTAGAGCTAGAAAT
tmem251 sgRNA-3	GAAATTAATACGACTCACTATAGAAACACCTGCAGATAGGGAGTTTTAGAGCTAGAAAT
tmem251 sgRNA-4	GAAATTAATACGACTCACTATATGATTGACACCTGAAGATGTGTTTTAGAGCTAGAAAT
gnptab sgRNA-1	GAAATTAATACGACTCACTATAGGGCTTTACCTGTGTTTCGGGTTTTAGAGCTAGAAAT
gnptab sgRNA-2	GAAATTAATACGACTCACTATAGAAGGGACTCACCGCCCTTTGTTTTAGAGCTAGAAAT
gnptab sgRNA-3	GAAATTAATACGACTCACTATAGGGCTGTGCTAACTCTTGGTGTTTTAGAGCTAGAAAT
gnptab sgRNA-4	GAAATTAATACGACTCACTATAGGAGAGGGATTCAGACTCCGGTTTTAGAGCTAGAAAT

4.5 References:

Abu-Remaileh M, Wyant GA, Kim C, et al. Lysosomal metabolomics reveals V-ATPase- and mTOR-dependent regulation of amino acid efflux from lysosomes. *Science*. 2017;358(6364):807-813. doi:10.1126/science.aan6298

Ain NU, Muhammad N, Dianatpour M, et al. Biallelic TMEpM251 variants in patients with severe skeletal dysplasia and extreme short stature. *Hum Mutat*. 2021;42(1):89-101. doi:10.1002/humu.24139

Anders S, Pyl PT, Huber W. HTSeq--a Python framework to work with high-throughput sequencing data. *Bioinformatics*. 2015;31(2):166-169. doi:10.1093/bioinformatics/btu638

Aregger M, Lawson KA, Billmann M, et al. Systematic mapping of genetic interactions for de novo fatty acid synthesis identifies C12orf49 as a regulator of lipid metabolism. *Nat Metab*. 2020;2(6):499-513. doi:10.1038/s42255-020-0211-z

Arines FM, Hamlin AJ, Yang X, Liu YJ, Li M. A selective transmembrane recognition mechanism by a membrane-anchored ubiquitin ligase adaptor. *J Cell Biol*. 2021;220(1):e202001116. doi:10.1083/jcb.202001116

Bach G. Mucolipidosis type IV. *Mol Genet Metab*. 2001;73(3):197-203. doi:10.1006/mgme.2001.3195

Bao M, Booth JL, Elmendorf BJ, Canfield WM. Bovine UDP-N-acetylglucosamine:lysosomal-enzyme N-acetylglucosamine-1-phosphotransferase. I. Purification and subunit structure. *J Biol Chem*. 1996;271(49):31437-31445. doi:10.1074/jbc.271.49.31437

Bassi MT, Manzoni M, Monti E, Pizzo MT, Ballabio A, Borsani G. Cloning of the gene encoding a novel integral membrane protein, mucolipidin-and identification of the two major founder mutations causing mucolipidosis type IV. *Am J Hum Genet*. 2000;67(5):1110-1120. doi:10.1016/S0002-9297(07)62941-3

Bayraktar EC, La K, Karpman K, et al. Metabolic coessentiality mapping identifies C12orf49 as a regulator of SREBP processing and cholesterol metabolism. *Nat Metab*. 2020;2(6):487-498. doi:10.1038/s42255-020-0206-9

Blackler RJ, Evans DW, Smith DF, et al. Single-chain antibody-fragment M6P-1 possesses a mannose 6-phosphate monosaccharide-specific binding pocket that distinguishes N-glycan phosphorylation in a branch-specific manner†. *Glycobiology*. 2016;26(2):181-192. doi:10.1093/glycob/cwv093

Cao J, Wu L, Zhang SM, et al. An easy and efficient inducible CRISPR/Cas9 platform with improved specificity for multiple gene targeting. *Nucleic Acids Res*. 2016;44(19):e149. doi:10.1093/nar/gkw660

Cathey SS, Leroy JG, Wood T, et al. Phenotype and genotype in mucolipidoses II and III alpha/beta: a study of 61 probands. *J Med Genet*. 2010;47(1):38-48. doi:10.1136/jmg.2009.067736

Chen WS, Lazar CS, Lund KA, et al. Functional independence of the epidermal growth factor receptor from a domain required for ligand-induced internalization and calcium regulation. *Cell*. 1989;59(1):33-43. doi:10.1016/0092-8674(89)90867-2

Chen X, Zhang J, Liu P, et al. Proteolytic processing of secretory pathway kinase Fam20C by site-1 protease promotes biomineralization. *Proc Natl Acad Sci U S A*. 2021;118(32):e2100133118. doi:10.1073/pnas.2100133118

Coutinho MF, Lacerda L, Alves S. Glycosaminoglycan storage disorders: a review. *Biochem Res Int*. 2012a;2012:471325. doi:10.1155/2012/471325

Coutinho MF, Prata MJ, Alves S. Mannose-6-phosphate pathway: a review on its role in lysosomal function and dysfunction. *Mol Genet Metab*. 2012b;105(4):542-550. doi:10.1016/j.ymgme.2011.12.012

d'Azzo A, Machado E, Annunziata I. Pathogenesis, Emerging therapeutic targets and Treatment in Sialidosis. *Expert Opin Orphan Drugs*. 2015;3(5):491-504. doi:10.1517/21678707.2015.1025746

Dahms NM, Lobel P, Breitmeyer J, Chirgwin JM, Kornfeld S. 46 kd mannose 6-phosphate receptor: cloning, expression, and homology to the 215 kd mannose 6-phosphate receptor. *Cell*. 1987;50(2):181-192. doi:10.1016/0092-8674(87)90214-5

Di Lorenzo G, Velho RV, Winter D, et al. Lysosomal Proteome and Secretome Analysis Identifies Missorted Enzymes and Their Nondegraded Substrates in Mucolipidosis III Mouse Cells. *Mol Cell Proteomics*. 2018;17(8):1612-1626. doi:10.1074/mcp.RA118.000720

Dobin A, Davis CA, Schlesinger F, et al. STAR: ultrafast universal RNA-seq aligner. *Bioinformatics*. 2013;29(1):15-21. doi:10.1093/bioinformatics/bts635

Doench JG, Fusi N, Sullender M, et al. Optimized sgRNA design to maximize activity and minimize off-target effects of CRISPR-Cas9. *Nat Biotechnol*. 2016;34(2):184-191. doi:10.1038/nbt.3437

Dogterom EJ, Wagenmakers MAEM, Wilke M, et al. Mucolipidosis type II and type III: a systematic review of 843 published cases. *Genet Med*. 2021;23(11):2047-2056. doi:10.1038/s41436-021-01244-4

Du SJ, Frenkel V, Kindschi G, Zohar Y. Visualizing normal and defective bone development in zebrafish embryos using the fluorescent chromophore calcein. *Dev Biol*. 2001;238(2):239-246. doi:10.1006/dbio.2001.0390

Edmiston R, Wilkinson S, Jones S, Tylee K, Broomfield A, Bruce IA. I-Cell Disease (Mucolipidosis II): A Case Series from a Tertiary Paediatric Centre Reviewing the Airway and Respiratory Consequences of the Disease. *JIMD Rep*. 2019;45:1-8. doi:10.1007/8904_2018_130

Espenshade PJ, Li WP, Yabe D. Sterols block binding of COPII proteins to SCAP, thereby controlling SCAP sorting in ER. *Proc Natl Acad Sci U S A*. 2002;99(18):11694-11699. doi:10.1073/pnas.182412799

Flanagan-Steet H, Aarnio M, Kwan B, et al. Cathepsin-Mediated Alterations in TGFß-Related Signaling Underlie Disrupted Cartilage and Bone Maturation Associated With Impaired Lysosomal Targeting. *J Bone Miner Res*. 2016;31(3):535-548. doi:10.1002/jbmr.2722

Geuze HJ, Slot JW, Strous GJ, Hasilik A, Von Figura K. Ultrastructural localization of the mannose 6-phosphate receptor in rat liver. *J Cell Biol*. 1984;98(6):2047-2054. doi:10.1083/jcb.98.6.2047

Ghosh P, Dahms NM, Kornfeld S. Mannose 6-phosphate receptors: new twists in the tale. *Nat Rev Mol Cell Biol*. 2003;4(3):202-212. doi:10.1038/nrm1050

Gieselmann V, Hasilik A, von Figura K. Processing of human cathepsin D in lysosomes in vitro. *J Biol Chem*. 1985;260(5):3215-3220.

Haze K, Yoshida H, Yanagi H, Yura T, Mori K. Mammalian transcription factor ATF6 is synthesized as a transmembrane protein and activated by proteolysis in response to endoplasmic reticulum stress. *Mol Biol Cell*. 1999;10(11):3787-3799. doi:10.1091/mbc.10.11.3787

Jin ZC, Kitajima T, Dong W, et al. Genetic disruption of multiple α1,2-mannosidases generates mammalian cells producing recombinant proteins with high-mannose-type *N*-glycans. *J Biol Chem*. 2018;293(15):5572-5584. doi:10.1074/jbc.M117.813030

Joung J, Konermann S, Gootenberg JS, et al. Genome-scale CRISPR-Cas9 knockout and transcriptional activation screening [published correction appears in Nat Protoc. 2019 Jul;14(7):2259]. *Nat Protoc*. 2017;12(4):828-863. doi:10.1038/nprot.2017.016

Kang C, Riazuddin S, Mundorff J, et al. Mutations in the lysosomal enzyme-targeting pathway and persistent stuttering. *N Engl J Med*. 2010;362(8):677-685. doi:10.1056/NEJMoa0902630

Khan SA, Tomatsu SC. Mucolipidoses Overview: Past, Present, and Future. *Int J Mol Sci*. 2020;21(18):6812. Published 2020 Sep 17. doi:10.3390/ijms21186812

Kimmel CB, Ballard WW, Kimmel SR, Ullmann B, Schilling TF. Stages of embryonic development of the zebrafish. *Dev Dyn*. 1995;203(3):253-310. doi:10.1002/aja.1002030302

Kollmann K, Damme M, Markmann S, et al. Lysosomal dysfunction causes neurodegeneration in mucolipidosis II 'knock-in' mice. *Brain*. 2012;135(Pt 9):2661-2675. doi:10.1093/brain/aws209

Kollmann K, Pohl S, Marschner K, et al. Mannose phosphorylation in health and disease. *Eur J Cell Biol*. 2010;89(1):117-123. doi:10.1016/j.ejcb.2009.10.008

Kroll F, Powell GT, Ghosh M, et al. A simple and effective F0 knockout method for rapid screening of behaviour and other complex phenotypes. *Elife*. 2021;10:e59683. Published 2021 Jan 8. doi:10.7554/eLife.59683

Kudo M, Bao M, D'Souza A, et al. The alpha- and beta-subunits of the human UDP-N-acetylglucosamine:lysosomal enzyme N-acetylglucosamine-1-phosphotransferase [corrected] are encoded by a single cDNA [published correction appears in J Biol Chem. 2005 Dec 23;280(51):42476]. *J Biol Chem*. 2005;280(43):36141-36149. doi:10.1074/jbc.M509008200

Kwak MJ, Lee HW, Kim YM, Cho SY, Park HD, Jin DK. Rare Association of Mucolipidosis III alpha/beta with Dilated Cardiomyopathy. *Ann Clin Lab Sci*. 2018;48(6):785-789.

Labun K, Montague TG, Krause M, Torres Cleuren YN, Tjeldnes H, Valen E. CHOPCHOP v3: expanding the CRISPR web toolbox beyond genome editing. *Nucleic Acids Res*. 2019;47(W1):W171-W174. doi:10.1093/nar/gkz365

Lenk GM, Park YN, Lemons R, et al. CRISPR knockout screen implicates three genes in lysosome function. *Sci Rep*. 2019;9(1):9609. Published 2019 Jul 3. doi:10.1038/s41598-019-45939-w

Li M, Rong Y, Chuang YS, Peng D, Emr SD. Ubiquitin-dependent lysosomal membrane protein sorting and degradation. *Mol Cell*. 2015;57(3):467-478. doi:10.1016/j.molcel.2014.12.012

Liu L, Lee WS, Doray B, Kornfeld S. Role of spacer-1 in the maturation and function of GlcNAc-1-phosphotransferase. *FEBS Lett*. 2017;591(1):47-55. doi:10.1002/1873-3468.12525

Loregger A, Raaben M, Nieuwenhuis J, et al. Haploid genetic screens identify SPRING/C12ORF49 as a determinant of SREBP signaling and cholesterol metabolism. *Nat Commun*. 2020;11(1):1128. Published 2020 Feb 28. doi:10.1038/s41467-020-14811-1

Love MI, Huber W, Anders S. Moderated estimation of fold change and dispersion for RNA-seq data with DESeq2. *Genome Biol*. 2014;15(12):550. doi:10.1186/s13059-014-0550-8
Lu A, Hsieh F, Sharma BR, Vaughn SR, Enrich C, Pfeffer SR. CRISPR screens for lipid regulators reveal a role for ER-bound SNX13 in lysosomal cholesterol export. *J Cell Biol*. 2022;221(2):e202105060. doi:10.1083/jcb.202105060
Lu PN, Moreland T, Christian CJ, Lund TC, Steet RA, Flanagan-Steet H. Inappropriate cathepsin K secretion promotes its enzymatic activation driving heart and valve malformation. *JCI Insight*. 2020;5(20):e133019. Published 2020 Oct 15. doi:10.1172/jci.insight.133019
Mareninova OA, Vegh ET, Shalbueva N, et al. Dysregulation of mannose-6-phosphate-dependent cholesterol homeostasis in acinar cells mediates pancreatitis. *J Clin Invest*. 2021;131(15):e146870. doi:10.1172/JCI146870
Marschner K, Kollmann K, Schweizer M, Braulke T, Pohl S. A key enzyme in the biogenesis of lysosomes is a protease that regulates cholesterol metabolism. *Science*. 2011;333(6038):87-90. doi:10.1126/science.1205677
McCormick PJ, Dumaresq-Doiron K, Pluviose AS, Pichette V, Tosato G, Lefrancois S. Palmitoylation controls recycling in lysosomal sorting and trafficking. *Traffic*. 2008;9(11):1984-1997. doi:10.1111/j.1600-0854.2008.00814.x
Morshed S, Sharmin T, Ushimaru T. TORC1 regulates ESCRT-0 complex formation on the vacuolar membrane and microautophagy induction in yeast. *Biochem Biophys Res Commun*. 2020;522(1):88-94. doi:10.1016/j.bbrc.2019.11.064
Muno D, Ishidoh K, Ueno T, Kominami E. Processing and transport of the precursor of cathepsin C during its transfer into lysosomes. *Arch Biochem Biophys*. 1993;306(1):103-110. doi:10.1006/abbi.1993.1486
Müller-Loennies S, Galliciotti G, Kollmann K, Glatzel M, Braulke T. A novel single-chain antibody fragment for detection of mannose 6-phosphate-containing proteins: application in mucolipidosis type II patients and mice. *Am J Pathol*. 2010;177(1):240-247. doi:10.2353/ajpath.2010.090954
Neufeld EF. Enzyme replacement therapy – a brief history. In: Mehta A, Beck M, Sunder-Plassmann G, eds. *Fabry Disease: Perspectives from 5 Years of FOS*. Oxford: Oxford PharmaGenesis; 2006.
Oku M, Maeda Y, Kagohashi Y, et al. Evidence for ESCRT- and clathrin-dependent microautophagy. *J Cell Biol*. 2017;216(10):3263-3274. doi:10.1083/jcb.201611029
Oshima A, Nolan CM, Kyle JW, Grubb JH, Sly WS. The human cation-independent mannose 6-phosphate receptor. Cloning and sequence of the full-length cDNA and expression of functional receptor in COS cells. *J Biol Chem*. 1988;263(5):2553-2562.
Otomo T, Muramatsu T, Yorifuji T, et al. Mucolipidosis II and III alpha/beta: mutation analysis of 40 Japanese patients showed genotype-phenotype correlation. *J Hum Genet*. 2009;54(3):145-151. doi:10.1038/jhg.2009.3
Oussoren E, van Eerd D, Murphy E, et al. Mucolipidosis type III, a series of adult patients. *J Inherit Metab Dis*. 2018;41(5):839-848. doi:10.1007/s10545-018-0186-z
Pedersen TA, Bereshchenko O, Garcia-Silva S, et al. Distinct C/EBPalpha motifs regulate lipogenic and gluconeogenic gene expression in vivo. *EMBO J*. 2007;26(4):1081-1093. doi:10.1038/sj.emboj.7601563
Qian Y, Flanagan-Steet H, van Meel E, Steet R, Kornfeld SA. The DMAP interaction domain of UDP-GlcNAc:lysosomal enzyme N-acetylglucosamine-1-phosphotransferase is a

substrate recognition module. *Proc Natl Acad Sci U S A*. 2013;110(25):10246-10251. doi:10.1073/pnas.1308453110
Qian Y, Lee I, Lee WS, et al. Functions of the alpha, beta, and gamma subunits of UDP-GlcNAc:lysosomal enzyme N-acetylglucosamine-1-phosphotransferase. *J Biol Chem*. 2010;285(5):3360-3370. doi:10.1074/jbc.M109.068650
Qian Y, van Meel E, Flanagan-Steet H, Yox A, Steet R, Kornfeld S. Analysis of mucolipidosis II/III GNPTAB missense mutations identifies domains of UDP-GlcNAc:lysosomal enzyme GlcNAc-1-phosphotransferase involved in catalytic function and lysosomal enzyme recognition. *J Biol Chem*. 2015;290(5):3045-3056. doi:10.1074/jbc.M114.612507
Raas-Rothschild A, Cormier-Daire V, Bao M, et al. Molecular basis of variant pseudo-hurler polydystrophy (mucolipidosis IIIC). *J Clin Invest*. 2000;105(5):673-681. doi:10.1172/JCI5826
Ran FA, Hsu PD, Wright J, Agarwala V, Scott DA, Zhang F. Genome engineering using the CRISPR-Cas9 system. *Nat Protoc*. 2013;8(11):2281-2308. doi:10.1038/nprot.2013.143
Rohrer J, Kornfeld R. Lysosomal hydrolase mannose 6-phosphate uncovering enzyme resides in the trans-Golgi network. *Mol Biol Cell*. 2001;12(6):1623-1631. doi:10.1091/mbc.12.6.1623
Shao W, Espenshade PJ. Sterol regulatory element-binding protein (SREBP) cleavage regulates Golgi-to-endoplasmic reticulum recycling of SREBP cleavage-activating protein (SCAP). *J Biol Chem*. 2014;289(11):7547-7557. doi:10.1074/jbc.M113.545699
Shao W, Machamer CE, Espenshade PJ. Fatostatin blocks ER exit of SCAP but inhibits cell growth in a SCAP-independent manner. *J Lipid Res*. 2016;57(8):1564-1573. doi:10.1194/jlr.M069583
Shen J, Snapp EL, Lippincott-Schwartz J, Prywes R. Stable binding of ATF6 to BiP in the endoplasmic reticulum stress response. *Mol Cell Biol*. 2005;25(3):921-932. doi:10.1128/MCB.25.3.921-932.2005
Shoemaker CJ, Huang TQ, Weir NR, Polyakov NJ, Schultz SW, Denic V. CRISPR screening using an expanded toolkit of autophagy reporters identifies TMEM41B as a novel autophagy factor. *PLoS Biol*. 2019;17(4):e2007044. Published 2019 Apr 1. doi:10.1371/journal.pbio.2007044
Sleat DE, Della Valle MC, Zheng H, Moore DF, Lobel P. The mannose 6-phosphate glycoprotein proteome. *J Proteome Res*. 2008;7(7):3010-3021. doi:10.1021/pr800135v
Sleat DE, Lackland H, Wang Y, et al. The human brain mannose 6-phosphate glycoproteome: a complex mixture composed of multiple isoforms of many soluble lysosomal proteins [published correction appears in Proteomics. 2005 May;5(8):2272]. *Proteomics*. 2005;5(6):1520-1532. doi:10.1002/pmic.200401054
Tang D, Xiang Y, Wang Y. Reconstitution of the cell cycle-regulated Golgi disassembly and reassembly in a cell-free system. *Nat Protoc*. 2010;5(4):758-772. doi:10.1038/nprot.2010.38
Tiede S, Storch S, Lübke T, et al. Mucolipidosis II is caused by mutations in GNPTA encoding the alpha/beta GlcNAc-1-phosphotransferase. *Nat Med*. 2005;11(10):1109-1112. doi:10.1038/nm1305
van den Boomen DJH, Sienkiewicz A, Berlin I, et al. A trimeric Rab7 GEF controls NPC1-dependent lysosomal cholesterol export. *Nat Commun*. 2020;11(1):5559. Published 2020 Nov 3. doi:10.1038/s41467-020-19032-0

Venkatachalam K, Wong CO, Zhu MX. The role of TRPMLs in endolysosomal trafficking and function. *Cell Calcium*. 2015;58(1):48-56. doi:10.1016/j.ceca.2014.10.008
Velho RV, De Pace R, Klünder S, et al. Analyses of disease-related GNPTAB mutations define a novel GlcNAc-1-phosphotransferase interaction domain and an alternative site-1 protease cleavage site. *Hum Mol Genet*. 2015;24(12):3497-3505. doi:10.1093/hmg/ddv100
Velho RV, De Pace R, Klünder S, et al. Site-1 protease and lysosomal homeostasis. *Biochim Biophys Acta Mol Cell Res*. 2017;1864(11 Pt B):2162-2168. doi:10.1016/j.bbamcr.2017.06.023
Walker MB, Kimmel CB. A two-color acid-free cartilage and bone stain for zebrafish larvae. *Biotech Histochem*. 2007;82(1):23-28. doi:10.1080/10520290701333558
Wang L, Wang S, Li W. RSeQC: quality control of RNA-seq experiments. *Bioinformatics*. 2012;28(16):2184-2185. doi:10.1093/bioinformatics/bts356
Wang Y, Taguchi T, Warren G (2006) Purification of Rat Liver Golgi Stacks. In: Celis J (ed) Cell Biology: A Laboratory Handbook, 3rd Edition. Elsevier Science (USA), San Diego, pp 33-39.
Westerfield M. 2000. The Zebrafish Book: A Guide for the Laboratory Use of Zebrafish
Wiesmann U, Vassella F, Herschkowitz N. "I-cell" disease: leakage of lysosomal enzymes into extracellular fluids. *N Engl J Med*. 1971;285(19):1090-1091. doi:10.1056/NEJM197111042851922
Xiao J, Xiong Y, Yang LT, et al. POST1/C12ORF49 regulates the SREBP pathway by promoting site-1 protease maturation. *Protein Cell*. 2021;12(4):279-296. doi:10.1007/s13238-020-00753-3
Xin Y, Duan C. Microinjection of Antisense Morpholinos, CRISPR/Cas9 RNP, and RNA/DNA into Zebrafish Embryos. *Methods Mol Biol*. 2018;1742:205-211. doi:10.1007/978-1-4939-7665-2_18
Yang T, Espenshade PJ, Wright ME, et al. Crucial step in cholesterol homeostasis: sterols promote binding of SCAP to INSIG-1, a membrane protein that facilitates retention of SREBPs in ER. *Cell*. 2002;110(4):489-500. doi:10.1016/s0092-8674(02)00872-3
Yang X, Arines FM, Zhang W, Li M. Sorting of a multi-subunit ubiquitin ligase complex in the endolysosome system. *Elife*. 2018;7:e33116. Published 2018 Jan 22. doi:10.7554/eLife.33116
Yang X, Reist L, Chomchai DA, Chen L, Arines FM, Li M. ESCRT, not intralumenal fragments, sorts ubiquitinated vacuole membrane proteins for degradation. *J Cell Biol*. 2021;220(8):e202012104. doi:10.1083/jcb.202012104
Yang X, Zhang W, Wen X, et al. TORC1 regulates vacuole membrane composition through ubiquitin- and ESCRT-dependent microautophagy. *J Cell Biol*. 2020;219(3):e201902127. doi:10.1083/jcb.201902127
Ye J, Rawson RB, Komuro R, et al. ER stress induces cleavage of membrane-bound ATF6 by the same proteases that process SREBPs. *Mol Cell*. 2000;6(6):1355-1364. doi:10.1016/s1097-2765(00)00133-7
Yokoyama C, Wang X, Briggs MR, et al. SREBP-1, a basic-helix-loop-helix-leucine zipper protein that controls transcription of the low density lipoprotein receptor gene. *Cell*. 1993;75(1):187-197.
Yoshida H, Matsui T, Yamamoto A, Okada T, Mori K. XBP1 mRNA is induced by ATF6 and spliced by IRE1 in response to ER stress to produce a highly active transcription factor. *Cell*. 2001;107(7):881-891. doi:10.1016/s0092-8674(01)00611-0

Zaidi N, Maurer A, Nieke S, Kalbacher H. Cathepsin D: a cellular roadmap. *Biochem Biophys Res Commun*. 2008;376(1):5-9. doi:10.1016/j.bbrc.2008.08.099

Zhang W, Yang X, Chen L, et al. A conserved ubiquitin- and ESCRT-dependent pathway internalizes human lysosomal membrane proteins for degradation. *PLoS Biol*. 2021;19(7):e3001361. Published 2021 Jul 23. doi:10.1371/journal.pbio.3001361

Zhou Y, Zhou B, Pache L, et al. Metascape provides a biologist-oriented resource for the analysis of systems-level datasets. *Nat Commun*. 2019;10(1):1523. Published 2019 Apr 3. doi:10.1038/s41467-019-09234-6

Chapter 5: Summary and Future Directions

The Lysosome is the central organelle to digest and recycle cellular materials and maintain homeostasis. It also serves as a signaling hub to control cellular activities in response to environmental cues. Lysosome dysfunction leads to inherited lysosomal storage diseases. Lysosome dysregulation is often associated with the early onset of neurodegeneration disorders and cancer. Therefore, the discovery and characterization of novel mechanisms of lysosome biogenesis and regulation will contribute a better understanding of the field and provide therapeutic insights to treat lysosome-associated diseases.

5.1 Regulation of LMPs in response to environmental cues

Using budding yeast as a model organism, Dr. Ming Li unveiled a novel mechanism to precisely turn over a vacuolar membrane protein (VMP) in response to its substrate level (Li et al., 2015a; Li et al., 2015b). In Chapter 2, we further characterized that TORC1 inactivation triggered a broad down-regulation of VMPs in yeast. Mechanistically, VMPs are ubiquitinated by a group of E3 ligases, including ssh4-Rsp5, vDSC, and Pib1, and internalized by the ESCRT-dependent microautophagy. Together, these studies provide a complete picture of how yeast cells regulate VMP composition in response to environmental cues.

In Chapter 3, we sought to explore the mechanism of lysosome membrane protein (LMP) regulation in human cells. Using cycloheximide chase assay, we identified two fast-degrading LMPs, RNF152 and LAPTM4A. We showed that the degradation of RNF152 was trigged by autoubiquitination, and the LAPTM4A was ubiquitinated by NEDD4. Further, the ESCRT

machinery internalized the ubiquitinated RNF152 and LAPTM4A for degradation. This study demonstrated a conserved ubiquitin- and ESCRT-dependent mechanism to turn over LMP in human cells.

In this study, we performed our experiments under the cycloheximide chase condition or at the steady-state, when MTORC1 is active. However, it is unclear how cells regulate LMPs in response to other environmental conditions. Recently, two independent studies suggested that the lysosomal localized E3 ligase RNF167 regulates the stability of amino acid sensors SESN2 (Wang et al., 2022) and CASTOR1 (Li et al., 2021) in response to cellular leucine and arginine level, respectively. Similarly, future studies may explore how lysosomal transports and channels are regulated in response to their substrate levels and MTORC1 activities.

5.2 Mechanisms of how TMEM251 promotes GNPT cleavage and activation

In Chapter 4, we generated a GFP-RNF152 reporter cell line and performed a genome-wide CRISPR-Cas9 screen to identify uncharacterized genes involved in the LMP degradation and lysosome function. Our screen results further emphasized the importance of lysosome biogenesis, endosomal trafficking system, and lysosomal v-ATPase in LMP degradation. From this screen, we also identified TMEM251, an uncharacterized gene, as a top hit. Our investigation indicated that TMEM251 deficiency leads to hypersecretion of lysosome hydrolases, resulting in lysosome dysfunction. We further demonstrated that TMEM251 is required for the processing and activation of GlcNAc-1 phosphotransferase (GNPT) by the membrane bound transcription factor peptidase, site-1 (MBTPS1). Ablation of TMEM251 causes defects in mannose-6-phosphate modification on lysosomal hydrolases and their hypersecretion. Therefore, our study characterized TMEM251 as a novel essential factor for lysosome biogenesis.

In this study, we demonstrated that TMEM251 selectively promoted the cleavage of GNPT α/β precursor by MBPTS1. Meanwhile, the processing of SREBF2/SREBP2 in response to sterol depletion is not affected by TMEM251 KO. We further confirmed the interaction between TMEM251 and MBPTS1. We also showed that the interaction between MBTPS1 and GNPTAB is not affected In TMEM251-null cells. This raises an intriguing question: how TMEM251 selectively promotes the processing of GNPT by MBTPS1?

We speculated that TMEM251 might serve as an adaptor to recruit MBTPS1 to GNPT α/β precursor. However, this model was not favored by our interaction analysis. Alternatively, TMEM251 might interact with MBTPS1 and/or GNPTAB to ensure an optimal conformation for a precise and efficient cleavage. Further, we have consistently observed that MBTPS1 is more sensitive to its inhibitor in *TMEM251*-null cells (indicated by SREBF2/SREBP2 processing). Therefore, TMEM251 may protect the MBTPS1 active site, or TMEM251 interacts with residues close to the active site of MBTPS1. Nevertheless, more biochemistry analysis is required to test these hypotheses. It is important to pinpoint the amino acid residues/motifs that mediate the interaction among TMEM251, MBPTS1, and GNPT. In addition, future studies may explore the X-ray crystallography or Cryo-EM structure of TMEM251 to resolve these questions.

5.3 Disease models of TMEM251

In Chapter 4, we established a zebrafish model to investigate the physiological impact of TMEM251 deficiency. The *tmem251*-deficient zebrafish exhibits heart edema and maldevelopment of cartilage and bone tissue, which phenocopies Mucolipidosis type II (*gnptab*-deficiency). Our results are consistent with the recent clinical observations that pathogenic mutations of TMEM251 lead to severe skeletal dysplasia and short stature (Ain et al., 2020).

In humans, two pathogenic mutations of TMEM251 were identified: c.133C>T and c.215dupA. The c.133C>T variant leads to a missense mutation R7W in the short isoform of TMEM251 (R39W in the long isoform). Notably, this is a substitution of a positive charge side chain to a large hydrophobic side chain. This mutation might lead to a destabilization of TMEM251. Interestingly, our recent topology study (fluorescence proteinase K protection assay) suggested that TMEM251 contains three transmembrane domains, with N-terminus facing the Golgi lumen and C-terminus in the cytosolic (data not shown) (White et al., 2015), which is consistent with the AlphaFold prediction (Jumper et al., 2021). This Arg7 residue (plus the Arg5 residue) is located near the membrane surface in the Golgi lumen. Interestingly, this observation is contradictory to the "positive inside rule" stating that more positive residues are located near the cytosolic side of the membrane (Heijne, 1986). A future study might generate site-direct mutagenesis using the CRISPR-Cas9 technique and explore how these positive residues (R5 and R7) affect the stability and function of TMEM251. On the other hand, the c.215dupA variant causes a fragment shift of the protein from the Try28 residue. One would predict that this truncated variant (only <25% preserved) may not be fully functional. Nevertheless, further investigation is required to characterize this mutation in more detail.

At the organism level, TMEM251 deficiency leads to severe cardiovascular dysfunction and skeletal anomalies. Furthermore, our RNA-seq analysis suggested that TMEM251 may also be involved in wound healing and the development of urogenital, sensory organs, and epidermis. However, given the limitation of the zebrafish model, it would be challenging to investigate the physiological impacts in such organs and tissues. Future studies may establish a mouse model to investigate the physiological impact of tmem251 deficiency. In addition, as lysosome storage diseases are frequently associated with neurological manifestations, it would be interesting to

explore the connection between TMEM251 and neurodegeneration (Hoffmann and Mayatepek, 2005). Together, these investigations will provide a further understanding of the regulation of lysosomal biogenesis and lysosome-related diseases.

5.4 References

Ain NU, Muhammad N, Dianatpour M, et al. Biallelic TMEM251 variants in patients with severe skeletal dysplasia and extreme short stature. *Hum Mutat*. 2021;42(1):89-101. doi:10.1002/humu.24139

Heijne G. The distribution of positively charged residues in bacterial inner membrane proteins correlates with the trans-membrane topology. *EMBO J*. 1986;5(11):3021-3027.

Hoffmann B, Mayatepek E. Neurological manifestations in lysosomal storage disorders - from pathology to first therapeutic possibilities. *Neuropediatrics*. 2005;36(5):285-289. doi:10.1055/s-2005-872810

Jumper J, Evans R, Pritzel A, et al. Highly accurate protein structure prediction with AlphaFold. *Nature*. 2021;596(7873):583-589. doi:10.1038/s41586-021-03819-2

Li M, Rong Y, Chuang YS, Peng D, Emr SD. Ubiquitin-dependent lysosomal membrane protein sorting and degradation. *Mol Cell*. 2015;57(3):467-478. doi:10.1016/j.molcel.2014.12.012

Li M, Koshi T, Emr SD. Membrane-anchored ubiquitin ligase complex is required for the turnover of lysosomal membrane proteins. *J Cell Biol*. 2015;211(3):639-652. doi:10.1083/jcb.201505062

Li T, Wang X, Ju E, et al. RNF167 activates mTORC1 and promotes tumorigenesis by targeting CASTOR1 for ubiquitination and degradation. *Nat Commun*. 2021;12(1):1055. Published 2021 Feb 16. doi:10.1038/s41467-021-21206-3

Wang D, Xu C, Yang W, et al. E3 ligase RNF167 and deubiquitinase STAMBPL1 modulate mTOR and cancer progression. *Mol Cell*. 2022;82(4):770-784.e9. doi:10.1016/j.molcel.2022.01.002

White C, Nixon A, Bradbury NA. Determining Membrane Protein Topology Using Fluorescence Protease Protection (FPP). *J Vis Exp*. 2015;(98):52509. Published 2015 Apr 20. doi:10.3791/52509